Modelling and control of a high performance electro-hydraulic test bench

Yaozhong Xu

UNIVERSITY OF LYON

DOCTORAL SCHOOL E.E.A.

P H D T H E S I S

to obtain the title of

PhD of Science

of the Institut National des Sciences Appliquées de Lyon - INSA Lyon

Speciality : Energy and Systems

defended by

Yaozhong XU

Modelling and Control of a High Performance Electro-Hydraulic Test Bench

Thesis Advisor: Eric Bideaux and Sylvie Sesmat

prepared at

Laboratoire AMPÈRE (UMR CNRS 5005)

Département Méthodes pour l'Ingénierie des Systèmes

June 11, 2013

Jury :

Reviewers :	Andrew Plummer	-	University of Bath (CPTMC)
	Rachid Outbib	-	Univ. d'Aix-Marseille (LSIS)
Examinators :	Jean-Pierre Barbot	-	ENSEA (ECS)
	Jean-Charles Maré	-	INSA de Toulouse (Inst. Clément Ader)
	Edouard Richard	-	Univ. Henri Poincare de LONGWY (CRAN)
Invited :	Ludovic Boisse	-	Moog France
	Daniel Thomasset	-	INSA de Lyon (AMPÈRE)
Advisor :	Eric Bideaux	-	INSA de Lyon (AMPÈRE)
	Sylvie Sesmat	-	INSA de Lyon (AMPÈRE)

INSA Direction de la Recherche - Ecoles Doctorales – Quinquennal 2011-2015

SIGLE	ECOLE DOCTORALE	NOM ET COORDONNEES DU RESPONSABLE
CHIMIE	**CHIMIE DE LYON** **http://www.edchimie-lyon.fr** Insa : R. GOURDON	M. Jean Marc LANCELIN Université de Lyon – Collège Doctoral Bât ESCPE 43 bd du 11 novembre 1918 69622 VILLEURBANNE Cedex Tél : 04.72.43 13 95 directeur@edchimie-lyon.fr
E.E.A.	**ELECTRONIQUE, ELECTROTECHNIQUE, AUTOMATIQUE** **http://edeea.ec-lyon.fr** Secrétariat : M.C. HAVGOUDOUKIAN eea@ec-lyon.fr	M. Gérard SCORLETTI Ecole Centrale de Lyon 36 avenue Guy de Collongue 69134 ECULLY Tél : 04.72.18 60 97 Fax : 04 78 43 37 17 Gerard.scorletti@ec-lyon.fr
E2M2	**EVOLUTION, ECOSYSTEME, MICROBIOLOGIE, MODELISATION** **http://e2m2.universite-lyon.fr** Insa : H. CHARLES	Mme Gudrun BORNETTE CNRS UMR 5023 LEHNA Université Claude Bernard Lyon 1 Bât Forel 43 bd du 11 novembre 1918 69622 VILLEURBANNE Cédex Tél : 04.72.43.12.94 e2m2@biomserv.univ-lyon1.fr
EDISS	**INTERDISCIPLINAIRE SCIENCES-SANTE** **http://ww2.ibcp.fr/ediss** Sec : Safia AIT CHALAL Insa : M. LAGARDE	M. Didier REVEL Hôpital Louis Pradel Bâtiment Central 28 Avenue Doyen Lépine 69677 BRON Tél : 04.72.68 49 09 Fax :04 72 35 49 16 Didier.revel@creatis.uni-lyon1.fr
INFOMATHS	**INFORMATIQUE ET MATHEMATIQUES** http://infomaths.univ-lyon1.fr	M. Johannes KELLENDONK Université Claude Bernard Lyon 1 INFOMATHS Bâtiment Braconnier 43 bd du 11 novembre 1918 69622 VILLEURBANNE Cedex Tél : 04.72. 44.82.94 Fax 04 72 43 16 87 infomaths@univ-lyon1.fr
Matériaux	**MATERIAUX DE LYON** Secrétariat : M. LABOUNE PM : 71.70 –Fax : 87.12 Bat. Saint Exupéry Ed.materiaux@insa-lyon.fr	M. Jean-Yves BUFFIERE INSA de Lyon MATEIS Bâtiment Saint Exupéry 7 avenue Jean Capelle 69621 VILLEURBANNE Cédex Tél : 04.72.43 83 18 Fax 04 72 43 85 28 Jean-yves.buffiere@insa-lyon.fr
MEGA	**MECANIQUE, ENERGETIQUE, GENIE CIVIL, ACOUSTIQUE** Secrétariat : M. LABOUNE PM : 71.70 –Fax : 87.12 Bat. Saint Exupéry mega@insa-lyon.fr	M. Philippe BOISSE INSA de Lyon Laboratoire LAMCOS Bâtiment Jacquard 25 bis avenue Jean Capelle 69621 VILLEURBANNE Cedex Tél :04.72.43.71.70 Fax : 04 72 43 72 37 Philippe.boisse@insa-lyon.fr
ScSo	**ScSo*** M. OBADIA Lionel Sec : Viviane POLSINELLI Insa : J.Y. TOUSSAINT	M. OBADIA Lionel Université Lyon 2 86 rue Pasteur 69365 LYON Cedex 07 Tél : 04.78.69.72.76 Fax : 04.37.28.04.48 Lionel.Obadia@univ-lyon2.fr

*ScSo : Histoire, Geographie, Aménagement, Urbanisme, Archéologie, Science politique, Sociologie, Anthropologie

INSTITUT NATIONAL DES SCIENCES APPLIQUÉES DE LYON

Abstract

École Doctorale Électronique, Électrotechnique, Automatique
Laboratoire AMPÈRE (UMR CNRS 5005)

PhD of Science

by Yaozhong XU

Hydraulic systems have been widely applied in industry for position or force control. However, due to hydraulic system nonlinearities, it is difficult to achieve a precise model valid over a large range of frequency and movement. The work in this dissertation focuses on a high performance hydraulic test bench which involves three main hydraulic components, i.e. two high performance servovalves, a double rod actuator, and a specific manifold connecting the servovalves and actuator. This rig has been designed for testing aerospace or automotive components in real conditions (e.g. wear and ageing effects). The main objectives of this dissertation are first the development of a virtual prototype based on a precise model which is derived from the physical principles and experimental works, and then second the synthesis of several nonlinear control laws of this actuation system in a large operating range with a good robustness to the perturbations. The proposed model based on Bond Graph shows a very good agreement with experimental results not only at low frequencies, but also at high frequencies. Moreover, its performances are improved at high frequencies by introducing the dynamic effects due to the manifold. Besides, multivariable and monovariable control strategies, based on respectively the backstepping and the model-free method, are developed and implemented on the test bench. All the control strategies proposed are validated by simulations and experiments. Results show they lead to better tracking precision and robustness performance compared to the conventional control techniques.

Keywords: Electro-hydraulic system, High performance, Modelling, Bond Graph, Multivariable control, Nonlinear system control, Backstepping, Model-free control, Robustness performance.

Acknowledgements

Over three years of doctoral research in France, this dissertation is the end of the indelible journey. The completion of the work involves the support and encouragement of numerous people including my professors, friends, and colleagues. It is a pleasure for me to have the opportunity to express my gratitude to all those people.

First and foremost, I would like to express my deepest gratitude to my advisor, Professor Eric Bideaux, for his continuous support of my Ph.D study and research, for his patience, motivation, enthusiasm, and immense knowledge. Without his guidance and persistent help, this dissertation would not have been possible. This acknowledgement is addressed to him, not only for his guidance of my dissertation, but also for directing my study and research career. Through these three years, he introduced me step by step into the domain of fluid power. He provided me with many opportunities to get in touch with other knowledgeable persons and to extend my perspective in the hydraulic system control community.

My co-advisor, Mrs. Sylvie Sesmat, has always kindly been there to listen and give me advice. I am deeply grateful to her for the valuable discussions, suggestions, comments and ideas for my work. I thank her for all her support, and also for her kindness and friendship during these years.

It gives me great pleasure in acknowledging the support and help of Professor Xavier Brun, who gave me invaluable guidance in the hydraulic system control and the implementation of control strategies on the test bench.

My sincere thanks also goes to Professor Daniel Thomasset, who gave me numerous encouragement for my work and lots of advices on the model-free control design.

I would like also to thank Mr. Mohamed Smaoui who shared valuable insights in the backstepping multivariable control.

I would like to thank Miss Lilia Sidhom for her inspiring discussions and warm friendship.

I gratefully acknowledge all members of the committee, Prof. Jean-Charles Maré, Prof. Andrew Plummer, Prof. Rachid Outbib, Prof. Jean-Pierre Barbot, Dr. Edouard Richard, and Mr. Ludovic Boisse, for providing me with invaluable

suggestions and comments on my work. They have clearly helped me to increase the quality of this thesis.

I would like to thank all my friends in Lyon and all members of Laboratory AMPERE, with whom I shared many good and bad moments during my study here. I consider it an honour to be friends and work with them.

Last but not the least, I would like to thank all my family for their love and encouragement in my pursuit of this research.

Contents

List of Figures

List of Tables

Abbreviations

ABM	**A**bacus-**B**ased **M**ethod
CFD	**C**omputational **F**luid **D**ynamics
CRM	**C**ontrol with **R**estricted **M**odel
DAO2	Adaptive 2nd-order Sliding Modes Differentiator
MFC	**M**odel-**F**ree **C**ontrol
SNR	**S**ignal-to-**N**oise **R**atio
STD	**S**tandard **D**eviation

Symbols

a	Actuator acceleration	m/s^2
a^d	Desired acceleration	m/s^2
a_m	Length of the lever arm of the armature	m
A	Piston active area	m^3
$A_0, A_d, A_{fL(R)}$	Areas of the upstream orifices, the drain orifices, and the nozzles	m^2
A_{si}	Area of the spool piston	m^2
b	Viscous coefficient between the actuator piston and barrel	N/(m/s)
b_m	Gap diameter of the torque motor	m
B_s	Spool viscous damping coefficient	N/(m/s)
B_f	Flapper viscous damping coefficient	Nm/(rad/s)
C	Friction index	
$C_{di}, C_{di\infty}$	Discharge coefficients of the orifice i of the spool valve, and discharge coefficient at wide opening	
C_{d0}, C_{df}, C_{dd}	Discharge coefficients of the upstream orifice, the nozzles, and the drain orifice	
d_0, d_n, d_d	Diameters of the upstream orifice, the nozzles, and the drain orifice	m
d_r, d_i, d_0, d_s	Diameters of rounded edges, orifice i, initial orifice opening and spool	m
e_s	Radius of radial clearance of the spool valve	m

E_t, E_r	Young's modulus of flexible tube and feedback spring	Pa
F_C	Coulomb friction	N
F_{ext}	External force	N
F_{fs}	Dry friction	N
F_{fhs}, F_{fhd}	Hydrostatic an hydrodynamic forces in the flapper valve	N
F_{sdyn}	Dynamic dry friction	N
F_{shs}, F_{shd}	Hydrostatic an hydrodynamic forces in spool valve	N
g	Gravity	m/s^2
i	Input current to the torque motor	A
I_t, I_r	Moment of area of flexible tube and feedback spring	m^4
J_f	Flapper inertia	$kg.m^2$
k_I	Energy losses constant due to fluid inertia	m
k_s	Equivalent overlap diameter	m
k_t	Transitional constant	
K_r, K_t	Feedback spring and flexible tube constant	N/m
l_t, l_r, l_f	Length of flexible tube, feedback spring, flapper	m
l_{re}, l_{fe}	Distance from flexible point of spring (flapper) to pivot center	m
M	Mass of the moving part of the actuator	kg
m_s, m_f	Spool and flapper/armature mass	kg
n	Number of the slits	
$P_{L(R)}, P_E, P_{A(B)}$	Servovalve pressures	Pa
P_0	Reference pressure	Pa
P_1, P_2	Actuator chamber pressures	Pa
P_1^d	Desired pressure of P_1	Pa
P_P	Pump pressure	Pa
P_T	Tank pressure	Pa
ΔP_n	Rated valve pressure drop	Pa
$Q_{PL(R)}$	Upstream orifice flow rates of the flapper valve	m^3/s

$Q_{L(R)E}$	Flow rates through nozzles	m^3/s
$Q_E, Q_{L(R)}$	Total drain orifice flow rate, pilot flow rates on left (right) side	m^3/s
$Q_{si,\text{underlap}}$	Flow rates of port i of spool valve at underlap position	m^3/s
$Q_{si,\text{overlap}}$	Flow rates of port i of spool valve at overlap position	m^3/s
$Q_{A(B)}$	Output flow rates from the spool valve	m^3/s
Q_n	Rated flow	m^3/s
Q_1, Q_2	Input flow rates to the actuator	m^3/s
Re, Re_t	Reynolds number and transitional Reynolds number	
$u_{1,2}$	Control inputs	V
u_n	Rated control input	V
v	Actuator velocity	m/s
v^d	Desired velocity	m/s
V_1, V_2	Volume in actuator chamber 1 & 2	m^3
w_s	Width of the slits of the spool valve	m
x_s, x_f, x_{f0}	Spool and flapper position, initial distance between the flapper and nozzle	m
x_{fG}, x_r	Position of flapper/armature gravity center, feedback spring deformation	m
x_{si}, x_{si0}	Total and initial underlap diameters of orifice i	m
y	Actuator piston position	m
y^d	Desired position	m
β	Bulk modulus	Pa
δ_{Re}	Asymptote slope	
θ_f	Angular position of the flapper/armature	rad
θ_i	Jet angular of orifice i	rad
μ	Dynamic viscosity	Pa.s
ν	Kinematic viscosity	m^2/s
ρ	Density of hydraulic oil	kg/m^3

Chapter 1

General introduction

Contents

1.1 Context

A hydraulic system is a system working with compressible fluid to accomplish mechanical transmission and automatic control. The hydraulic technology has been well developed in industry since its first application at the end of the 18th century. This type of system is widely used in automobile, aerospace, architecture and mine machines, etc., due to its advantages over electro-mechanical systems [Merritt 1967]:

1) The hydraulic system can realize a larger power transmission than other equipments with the same volume as the fluid carries away the heat generated by

internal losses which is the main limitation to machines with high power. The volume and weight of hydraulic pumps and motors are currently about 12% of electric ones [Chen 2007].

2) The hydraulic system has a good working stability. Due to the high natural frequency of the second-order from flow to speed of hydraulic actuators, this leads to a high response speed, which makes it possible to achieve fast starts, brakes, and speed reversals. Meanwhile, hydraulic actuators have a high stiffness, which provides a precise position control along with the change of loads.

3) The hydraulic system has a large operating range. Without the saturation problem as in the electro-magnetic motors, the torque developed by hydraulic actuators can reach a large amplitude which is only limited by safe stress levels. While applying a hydraulic actuator with a large torque to inertia ratio, a high acceleration is hence available. Besides, a large range of speed regulation is possible with proper hydraulic actuators which can reach a range of 1 to 2000.

4) Thanks to direct drive to the load, linear or rotary motion controls are more easily achieved by applying linear or rotary actuators than other machines.

However, there are some disadvantages in the hydraulic applications. More energy losses exists in hydraulic systems than in others because of the inevitable fluid leakage, particularly when the system breaks. It requires a higher cost to meet the high precision because of the fabrication of hydraulic components. Besides, the working temperature has great effect on the system performance since the fluid viscosity varies as a function of the temperature. In addition, there is a lack of convenient and accurate methods to deal with the complex nonlinear phenomena of hydraulic components; this makes difficult the control of hydraulic systems when precision and large operating range are required.

For over 25 years, one of the research domains of the Ampere laboratory was focused on the modelling and control design of fluid power systems (hydraulic and pneumatic). The objective of this dissertation is to study the modelling and control

of a high performance hydraulic system acquired not long ago by the laboratory (see figure 1.1).

FIGURE 1.1: High performance hydraulic test bench

1.2 High performance hydraulic test bench

This test bench (see figure 1.1) consists of a hydraulic actuator controlled by a complex system equipped with 2 high performance servovalves which have a wide bandwidth. This new technology provides new possibilities for applications in the aerospace and automotive industries where it can be used to test the wear and ageing effect of the components in real conditions. For example, it could be used to test some automotive components, such as silent block, with experimental signals corresponding to different real live situations (high/low speed, mission type, ...). Another advantage is that this bench allows different control methods and strategies to be applied in order to achieve targets as precise force or displacement trajectory tracking, energy efficiency, and high dynamic performances.

The test bench which will be studied along this dissertation was developed for very specific purposes:

- force/position control;

- high dynamic performances;
- high precision at low and high speed.

Figure 1.2 shows the schematic of the electro-hydraulic test bench under study. It consists of a hydraulic power unit with a powerful pump, an manifold that connects two accumulators, two high performance servovalves, and a double rod actuator with a symmetric piston which can be attached to an external load. The data acquisition and control system, and several sensors complete the test bench and enable model validation and implementation of different control laws. Its hydraulic schematic is presented on figure 1.3.

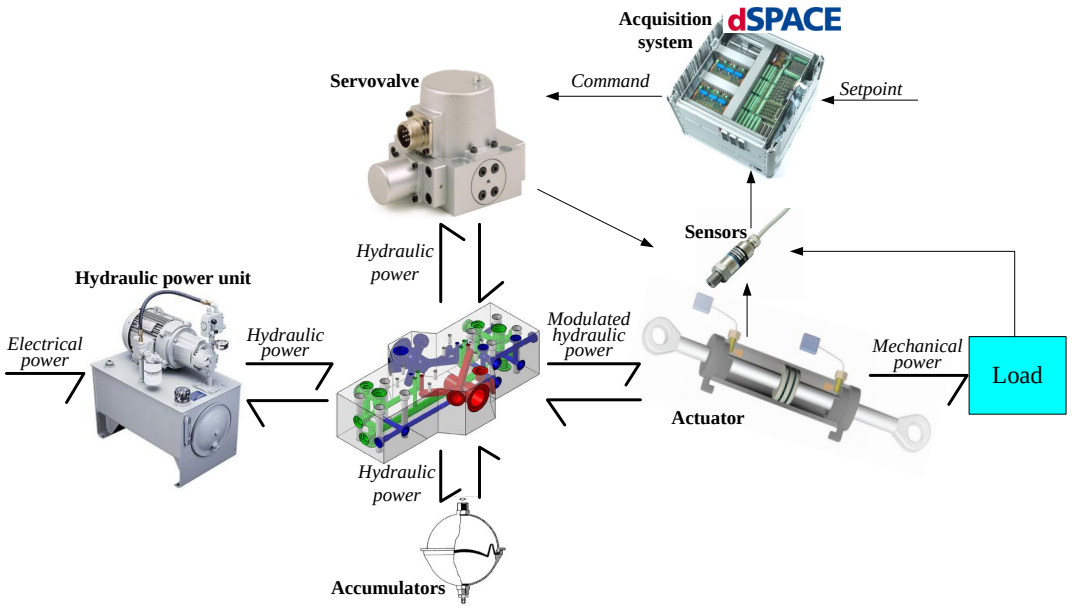

FIGURE 1.2: System overview

The two high performance servovalves MOOG D765 can work either in 3/2 or 5/2 mode. They control the hydraulic power supplied to the actuator by modulating the flow sections according to the control signal provided by the acquisition system (dSPACE).

These main subsystems are:

1. **Hydraulic power unit:**

It is an 18.5 kW hydraulic power unit consisting in variable displacement pump that supplies the compressed oil to the system at a maximum flow rate of 38 l/min

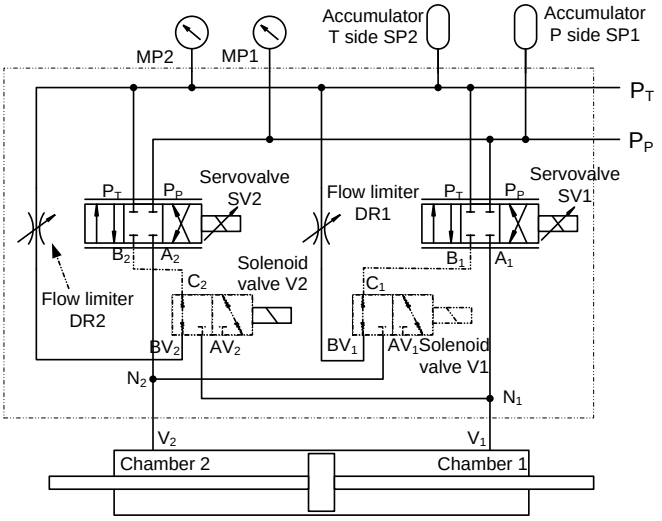

FIGURE 1.3: Scheme of the hydraulic test bench setup

@ 210 bar. A additional pump is used for the circulation of the oil in a cooling system equipped with a water/oil exchanger used at high temperature and an air exchanger for lower temperature. A pressure sensor indicates the supply pressure. The hydraulic power unit will not be modelled in this work.

2. **Hydraulic actuator:**

The Haenchen double rod jack (9.46 cm^2 active section) has a total stroke of 330 mm and is equipped with hydrodynamic bearings (low friction force). The piston has a guiding surface adjusted in the cylinder tube with an unattached seal, which allows the cylinder to have a particularly high efficiency coefficient with no stick-slip movement and a low friction, which is almost constant regardless of the pressure.

3. **MOOG high performance servovalves:**

The MOOG D765 servovalve used for the actuator command, is an industrial electro-hydraulic two-stage servovalve. The role of this servovalve is to modulate the flow rate in the jack. It has a nominal flow rate of 19 l/min @ 70 bar with a command of 10 V corresponding to the maximum spool displacement. Besides, the manufacturer indicates a theoretical bandwidth of 1 KHz (@ -3 dB) for 5% of maximum amplitude of the control input, but 160 Hz for 90% and 310 Hz for 40% (see figure 1.5).

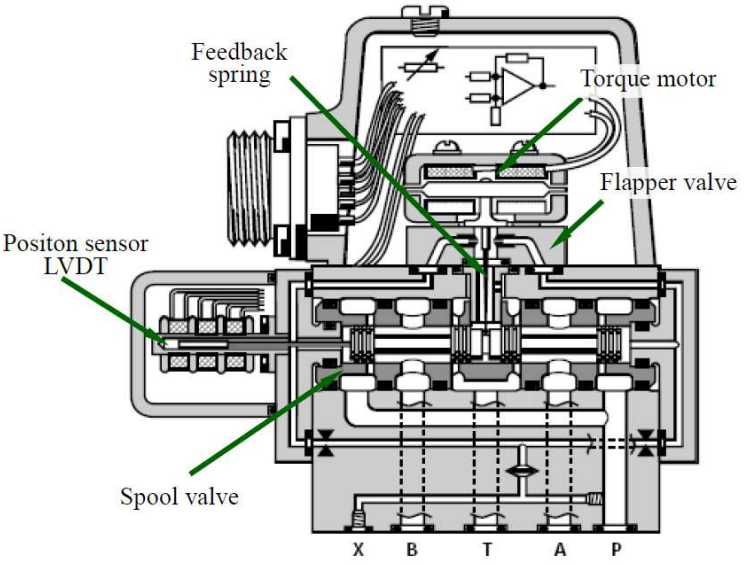

FIGURE 1.4: Architecture of the servovalve MOOG D765 [MOOG]

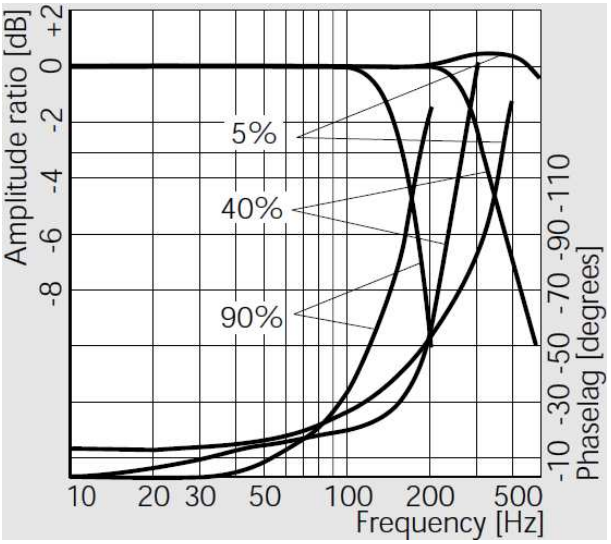

FIGURE 1.5: Frequency response of the servovalve MOOG D765 [MOOG]

4. **Manifold:**

The manifold manufactured specifically for this test bench allows the installation of two servovalves and enables the system to alternate between three different working modes:

1) using a single servovalve in 5/2 mode to control both chambers of the actuator,

2) applying two servovalves in 5/2 mode in parallel, or

3) using these two servovalves operated in 3/2 mode, i.e. each servovalve controlling individually one chamber.

In order to change the control mode, the manifold is equipped with two solenoid valves and two flow reducers. Two accumulators with a capacity of 1L are also mounted on the manifold and calibrated at a constant pressure, with 170 bar for the high pressure accumulator and 20 bar for the low pressure accumulator.

5. **Sensors and instrumentation:**

The experimental device is equipped with a set of instruments for measuring various physical signals according to the user's requirement:

1) A LVDT position sensor installed in the actuator to measure the piston displacement. It is an inductive transformer with a total stroke of 300 mm, having a linearity error less than 0.1% of the measuring range.

2) Four piezoresistive pressure sensors for measuring the supply line, tank line, and the two chamber pressures. The two sensors on the supply and tank lines have a measuring range of 0 to 250 bar, the precision is 0.15% of the maximum scale for the one on the supply line and 0.25% for the other on the tank line. The other two sensor in the cylinder chambers have an operating range of 0 to 206 bar, with an measuring error of $\pm 10\%$ involving the non-linearity, hysteresis and repeatability effects.

3) A force sensor used for the traction and compression tests with a measuring range of 0-2000 N and a precision equal to 0.05% of the measuring range.

4) An accelerometer fixed on the jack rod with a measuring range between ± 100g.
The parameters of the test bench are given in table 1.1.

Then, the electro-hydraulic test bench is able to work in a large bandwidth and stroke with a low friction force. Meanwhile, it is possible to implement different type of sophisticated control strategies on the bench which can realise high control performances. Our colleague, Lilia Sidhom [Sidhom 2011a], has already managed to implement a monovariable control based on the backstepping on this test bench, and obtained a good result on the position tracking. In this dissertation, we will take a further study on the control of this test bench.

TABLE 1.1: Test bench characteristics

Actuator	
Total stroke	300 mm
Mass of the moving part (rod+piston): M	5.8 Kg
Active section area: A	9.456 cm^2
Dead volume at each end	14.184 cm^3
Servovalve Moog D765	
Rated flow	19 L/min
Rated input signal	$\pm$10 V
Response time	2 ms
LVDT sensor installed on the rod of the actuator	
Measurement range (MR)	300 mm
Sensibility	4.4 mV/V/mm
Precision	$<$ 0.1% of the MR

In order to develop sophisticated control strategies, firstly, the main objective of this dissertation is to develop a virtual prototype based on a precise model which is derived from the physical principles and experimental works. This theoretical and experimental study allows the parameters to be identified and finally the validation of the virtual prototype. The difficulties which will be addressed in this work are mainly related to the establishment of a precise model valid over a large range of frequency and movement. It requires to take into account nonlinearities in the hydraulic system and energetic interactions, including effects which are generally neglected in classical modelling.

Then, this dissertation will focus on designing control strategies for the test bench to achieve high performances. Then, the controls should achieve the classic requirements, i.e. mono-objective specification such as precise position or force tracking in a large operating range with a good robustness to the perturbations, but also multi-objective control such as position/stiffness, position/energy efficiency.

1.3 Control

As described previously the test bench developed at the Ampere laboratory enables high performances in a large frequency range but also multi-objective control

thanks to the two power modulators (servovalves). Moreover, this equipment enables the implementation of the up-to-date control algorithms proposed by the control theory community. Usually, more than one control objective may be required with respect to application requirements. The multivariable control design aims at more than one objective simultaneously. In our case, the first one is naturally the position or the force control, and others can be defined according to the application requirements on the system performances such as the system stiffness, energy efficiency, and bandwidth [Ray 1983]. For example, [Wang 2011] investigated three control strategies which focused on realizing the output force control of a system equipped with two different types of actuators and minimizing the internal force fighting in order to improve the system energy efficiency and reliability. [Bai 2011] introduced two servovalves into an electro-hydraulic position servo system so that one servovalve was used to compensate the compressed oil volume for the sake of increasing the system dynamic stiffness.

In multivariable controls, more than one control loop exist, but each of these loops can not be designed individually for each specific control objective. When establishing a multivariable control strategy, the interaction between the different control loops must be taken into account in order to guarantee the system stability and achieve the expected objectives. Otherwise, each control loop may act against the interests of the other when trying to achieve these objectives. For example, [Zhou 1991] designed a multivariable sliding mode controller for linear and nonlinear systems, applying a Lyapunov approach to ensure the stability of the systems. Moreover, a large number of papers investigated multivariable control strategies based not only on linear controllers [Wang 2002, Cornieles 2006, Leena 2008], but also on nonlinear ones [Li 1987, Habibi 1994, Smaoui 2006, Liu 2012]. In this dissertation, we will be interested in designing multivariable control strategies based on the backstepping technique to realize the position and pressure control, but also in the implementation of a new control approach, called model-free control [Fliess 2008, Fliess 2009, Fliess 2011].

1.4 Outline of the dissertation

The dissertation is divided into two parts, corresponding to the two mains contributions of this work: the modelling of a virtual prototype and the control design of nonlinear control algorithms. They are organized as follows:

Part I: Modelling of the test bench

- **Chapter 2:** The dissertation investigates the static and dynamic analysis of the two-stage electro-hydraulic servovalve. We firstly study the static flows and hydrodynamic force of the servovalve. Then, a model is established according to the Bond Graph modelling methodology, and the results are validated in AMESim. Results show that this virtual prototype is valid up to 500 Hz.
- **Chapter 3:** The dynamic effect of the manifold of the test bench is here studied in details. Firstly, we introduce an analytical method to represent the energy losses in the manifold and we have analyzed the compressibility and inertial effects. Theoretically, these effects take a significant influence on the system dynamics.
- **Chapter 4:** The actuator model is studied and a virtual prototype of the test bench is developed in AMESim. Then, frequency responses obtained experimentally are compared to the results obtained with the virtual prototype in order to validate the proposed model.

Part II: Control of the test bench

- **Chapter 5:** Multivariable control strategies (pressure/position and position/weight on pressure controls, denoted by P-Y and Y-λ controls) for the test bench are presented. After introducing the control design, performances of the algorithms are studied according to simulations and experiments.
- **Chapter 6:** A model-free control and a control with restricted model are finally applied to the test bench for position tracking. Simulations and experiments are conducted to analyze the control performances. Both of them show good tracking accuracy and ease of implementation.

- **Chapter 7:** This final chapter is dedicated to the robustness analysis of the control strategies proposed in chapter 5 and 6. Payload perturbation and velocity/acceleration estimation precision are studied in simulation and experimentally. All proposed control laws show good robustness performances, except that the static error derived from one of the multivariable strategies, the Y-λ control, increases with the augmentation of the payload.

Finally, chapter 8 concludes the dissertation and gives an outlook onto future works.

1.5 Main contribution

In this dissertation, the research work concentrates on the problems and motivation presented above and the main contribution we will show, relies on the following aspects:

- Conducting static and dynamic analysis of the characteristics of the used high performance two-stage electro-hydraulic servovalve, and establishing a precise model of the servovalve by Bond Graph (see related publication [2]);
- Proposing a flow model for the second stage of the servovalve with respect to the physical phenomena, representing the transient phase between the underlap and overlap states of the spool valve (see related publication [2]);
- Studying the dynamic effect of the manifold installed between the servovalves and the actuator, i.e. compressibility effect, internal fluid inertia, and energy dissipation, and proposing a method to obtain the parameters corresponding to the losses for lumped-parameter model of this component based on the Bond Graph representation (see related publications [1, 3]);
- Validation of the virtual prototype of the test bench in AMESim based on the Bond Graph model of the system;

- Developing multivariable control strategies based on the backstepping technique in order to achieve precise position tracking and pressure control of the test bench, and analyzing the control performances and robustness of these methods (see related publications [4, 7]);
- Implementing the model-free control and the control with restricted model on the test bench, and analyzing the control performances and their robustness to the perturbation (see related publication [5, 6]).

1.6 List of related publications

Journal article

1. Y. Xu, E. Bideaux, S. Sesmat and J.-P. Simon. *Dynamic effect of the manifold in a hydraulic control system.* Journal of Mechanical Engineering and Automation, vol. 2, no. 6, pages 184 - 193, Nov. 2012.

International conference articles

2. Y. Xu, E. Bideaux, S. Sesmat, L. Sidhom and X. Brun. *Hydro-mechanical model of electro-hydraulic servovalve based on Bond Graph.* In Proc. of 6th FPNI-PhD Symp. West Lafayette, volume 1, pages 271 - 281, June 2010.
3. Y. Xu, E. Bideaux and S. Sesmat. *Bond Graph model of the manifold in a hydraulic control system.* In International Conference on Fluid Power and Mechatronics (FPM), Beijing, pages 492 - 497, Aug. 2011.
4. Y. Xu, L. Sidhom, Eric Bideaux and M. Smaoui. *Multivariable backstepping controls of a high bandwidth electro-hydraulic actuator.* In Proceeding of Bath/ASME Symposium on Fluid Power and Motion Control, Bath, pages 397 - 410, Sep. 2012.
5. Y. Xu, E. Bideaux and D. Thomasset. *Model-free control and control with restricted model of a high performance hydraulic system.* In Proceeding of International Conference on Fluid Power Transmission and Control (ICFP 2013), Hangzhou, April 2013.

6. Y. Xu, E. Bideaux and D. Thomasset. *Robustness study on the model-free control and the control with restricted model of a high performance electro-hydraulic system.* In Proceeding of the 13th Scandinavian International Conference on Fluid Power (SICFP2013), Linköping, June 2013.

7. L. Sidhom, Y. Xu, E. Bideaux and M. Smaoui. *A differentiator-controller design of an high bandwidth electro-hydraulic servoactuator.* In Proceeding of Recent Advances in Aerospace Actuation Systems and Components (R3ASC12), Toulouse, June 2012.

Part I

Modelling of the test bench

Context

Before the electro-hydraulic system control design, the analysis of the system dynamics is required, as well as system modelling. However, these tasks are troublesome due to the multidisciplinary nature of the electro-hydraulic system that requires electric, magnetic, mechanical and hydraulic knowledge. Meanwhile, the nonlinearities of this type of system, such as friction force, servovalve dynamic, flow rate characteristics, and fluid nonlinear properties mentioned in appendix A, increase the modelling complexity.

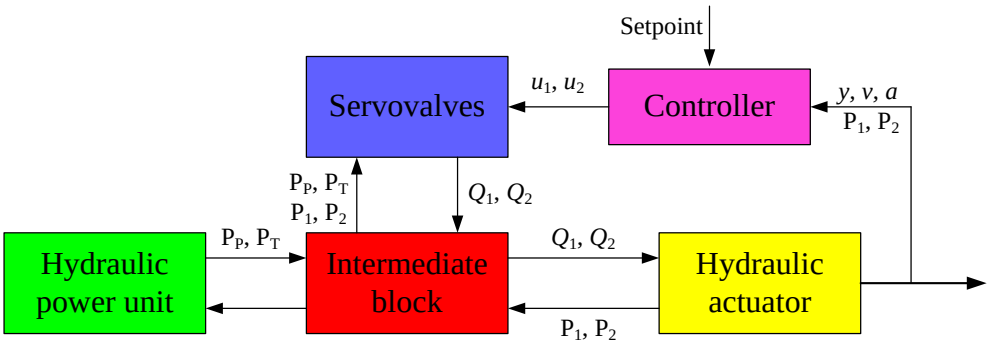

FIGURE I.1: Hydaulic system diagram

In a hydraulic system as shown in figure I.1, when the actuator piston displacements have small amplitude, the actuator is usually represented by a linear system of 2nd order, or 3rd order when considering the compressibility in each actuator chamber [Merritt 1967].

The other important hydraulic component is the servovalve (see figure I.1) which works as an interface between the actuator and the hydraulic pump. It plays a crucial role as a power modulator of the hydraulic system control. Therefore, the analysis of the servovalve dynamics becomes an essential point for the control design, as well as for servovalve design [Yuan 2002, Kang 2009]. A conventional two-stage servovalve consists of a flapper valve and a spool valve where the latter is driven by the former. Due to its complicated structure, the modelling of the servovalve becomes a more challenging problem than for the actuator.

In order to make simpler the modelling of a servovalve in practice, the conventional way to cope with this problem considers the system as a "black box", using a 2nd

order linear system, or a 3rd order one for more precise requirement [MOOG 1965] which takes into account the dynamics of the flapper/nozzle system. Besides, many researchers tend to analyze and design the control of servovalves by linearizing the nonlinear state equations to reformulate the problem with high-order linear models. Watton [Watton 1984, Watton 1987] engages most efforts into the modelling of the dynamics of the flapper/nozzle pilot valve and then proposes a 4th order model considering also the dynamics of the spool. Taking into account more details about the servovalve, some authors have developed more accurate but higher-order models, e.g., Kim [Kim 2000] has formulated a 5th order model considering the compressibility of the fluid in the pilot valve chambers. While taking into account the current dynamics due to the inductance of the torque motor, Nikiforuk [Nikiforuk 1969] developed a 6th order model.

Although all of the above linearized models are derived from the nonlinear state equations, and hence their coefficients can be partially expressed in terms of valve physical parameters and fluid properties, they are usually only valid for a specific frequency range at a given spool displacement. To solve this problem, their parameters have to be adjusted if the spool displacement changes. For example, Tafraouti [Tafraouti 2006] developed a model with adjustable parameters based on the conventional 2nd and 3rd order models, but it is still inaccurate for a large operating range due to the limitation of the linear approximation. These linear approaches are adequate for most of the conventional applications at low frequency, but if we want to fully exploit the high performances of servovalves such as the MOOG D765, it is necessary to develop a servovalve model which is accurate over a wide range of spool displacements and frequencies. Moreover, a careful study of the servovalve behavior at high frequency involves new phenomena that are highly influencing the servovalve performances, and therefore, the energy exchanges between the physical components have to be even more carefully represented [Rabie 1981, Maré 1993].

The modelling tool applied in the following chapter to develop a dynamic model for the hydraulic system is the Bond Graph [Karnopp 1975] which shows an excellent capacity to deal with this kind of problems. Because of its clear architecture and flexibility to approach different problems, this method is widely adopted in various domains, i.e. mechanics [Bryant 2011, Samantary 2010], hydraulics [Karnopp 1972, Dransfield 1979, Suzuki 1999, Alirand 2005], thermodynamics [Brown 2002, Brown 2010], robotics [Ghosh 1991, Zhang 2007, Pellicciari 2011], etc.. After establishing the main architecture of the system model, the Bond Graph enables engineers to refine the model by adding or removing graphically some phenomena without having to start again the whole modelling phase. It provides a useful and convenient method for analyzing complex systems which are concerned with multidiscipline and models that usually need to be modified. Maré [Maré 1993] has applied the Bond Graph on a specific hydraulic system and obtained good results. We will establish our Bond Graph model as J. C. Maré's previous work.

Chapter 2

Analysis and modelling of the high performance servovalve

Contents

2.1 Introduction

In a hydraulic system, the servovalve is a electro-hydraulic component which constitutes the main interface between the controller and the actuator. The hydraulic power unit supplies compressed oil at a constant pressure to this element. Then, it modulates the output flow rate according to the input command. It is employed in aerospace and automobile industry because of its high performance on amplification and very short response time.

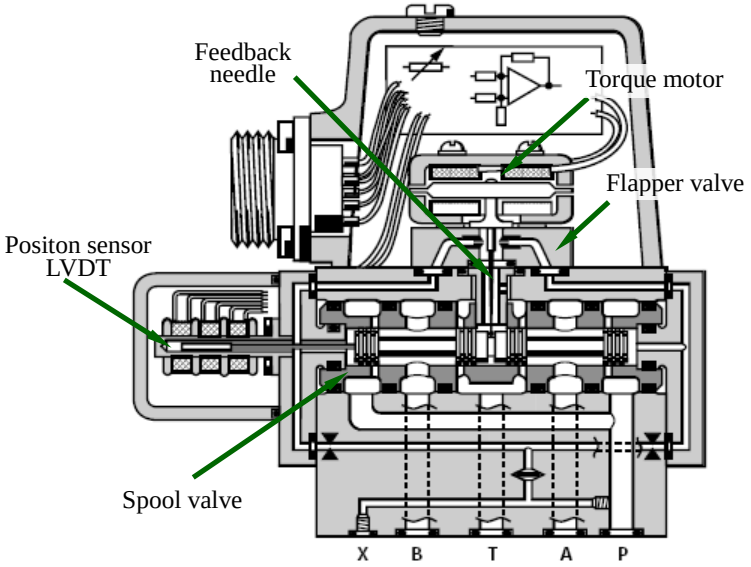

FIGURE 2.1: Architecture of the servovalve MOOG D765 [MOOG]

The servovalve under study is an industrial electro-hydraulic two-stage servovalve, the MOOG D765. This servovalve is a flow servovalve as it can modulate the output flow rate. It consists of an electro-mechanical part (torque motor), a hydro-mechanical part with two stages, and an electronic part (position sensor LVDT and PID controller). Figure 2.1 shows the architecture of the MOOG servovalve of type D765. The pilot stage (first stage) is a flapper/nozzle system which provides a force to the spool of the second stage valve, which derives from a pressure difference on the two sides of the spool. The pressure difference varies as a function of the flapper deflection driven by the torque motor which has a mechanical connection with the flapper. In the second stage, the spool valve modulates the output flow rate according to the spool displacement with respect to the command provided

by the servo system. The spool position is measured by a position sensor LVDT placed at one end of the spool, and this information is send to the servo system (see figure 2.2).

We can remark that this servovalve has two types of position feedback: one electronic related to the LVDT position sensor and one mechanical linked to the flapper deflection. The spool displacement causes the needle flexion, which leads to a mechanical spring feedback force acting on the spool. Meanwhile, the position information gathered by the LVDT position sensor is sent to the servo-system as a feedback signal.

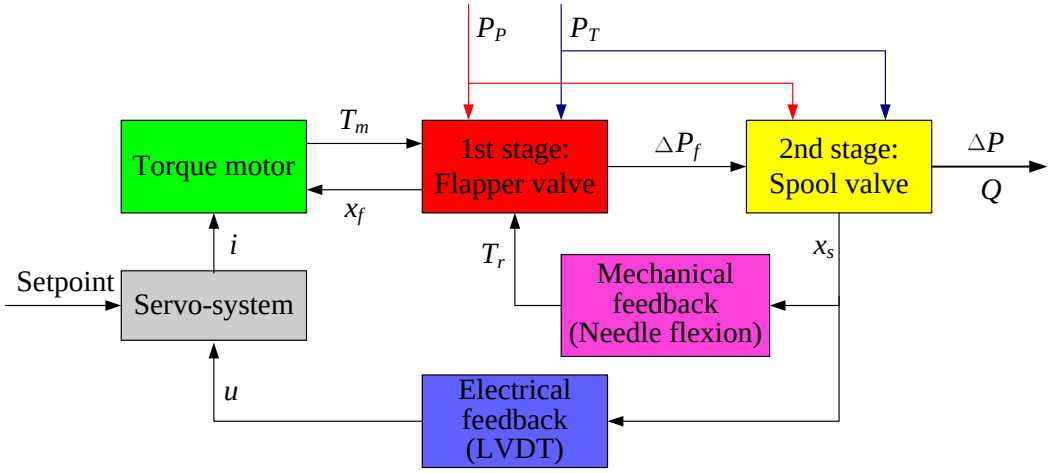

FIGURE 2.2: Servovalve overview

The servovalve MOOG D765-D128 has a nominal flow rate of 19 l/min at a pressure drop of 70 bar with a command of 10 V corresponding to the maximum spool displacement. Besides, it has a theoretical bandwidth of 1 kHz for 5% of maximum amplitude of the control input (see figure 2.3).

2.2 Analysis of the servovalve in stationary conditions

As an interface between the control system and the actuator, the servovalve takes a crucial place in the hydraulic control system. Its dynamic behaviour has a

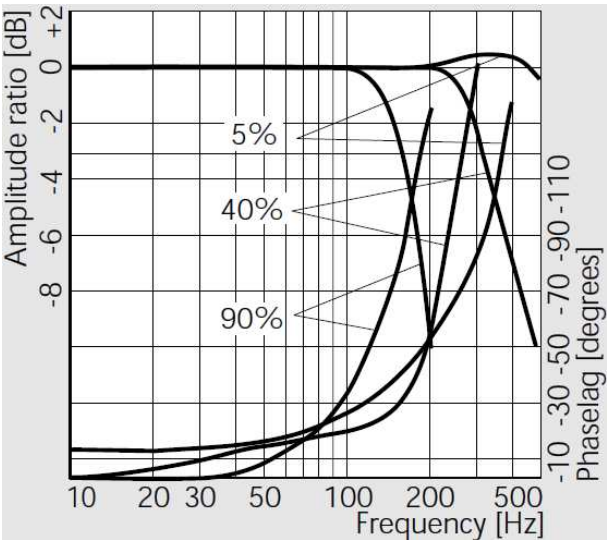

FIGURE 2.3: Frequency response of the servovalve MOOG D765 [MOOG]

significant effect on the control performances. We will first study its static characteristics to reveal its performances in steady state condition before considering the dynamics of this component in the following section.

The flows in the servovalve concerns two parts: one is involved in the pilot stage and the other in the second stage. For the flow in the spool valve, we propose a new flow model by considering the physical phenomena related to the manufacturing tolerances and leakage flows.

2.2.1 Structure of the servovalve

In figure 2.4, we present the simplified structure of the servovalve to highlight the critical parts of the structure to be studied.

According to the structure presented in figure 2.4,the flow circuits in the two hydraulic stages are given in figure 2.5.

In the first stage (figure 2.5(a)), the flapper deflects due to the torque generated by the torque motor. This force is the result of the current through the two coils fixed around the armature, which is connected to the flapper. As a result of this displacement, the cross sections of the orifices associated with the nozzles change. This leads to a variation of the pressures at both ends of the spool in the second

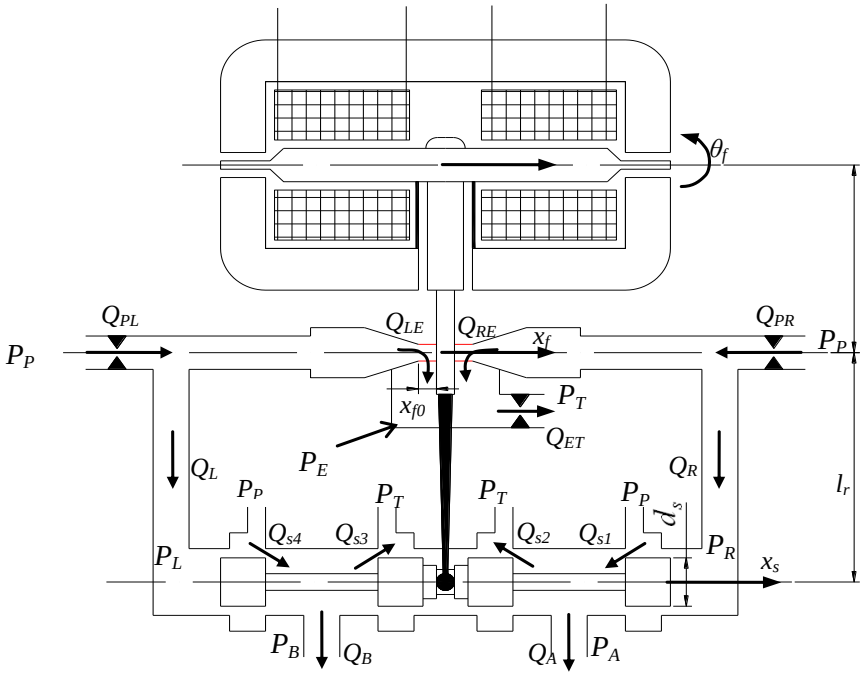

FIGURE 2.4: Simplified structure of the servovalve

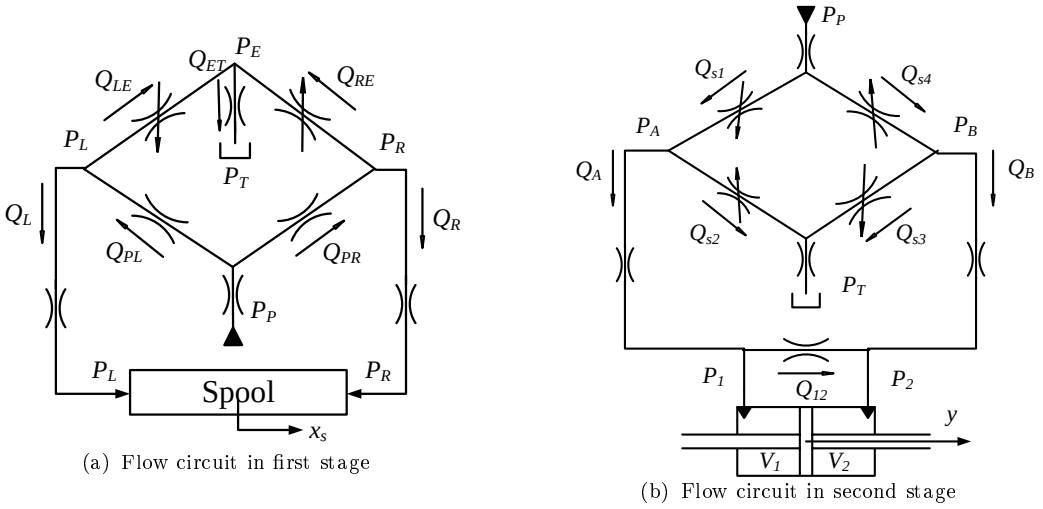

(a) Flow circuit in first stage

(b) Flow circuit in second stage

FIGURE 2.5: Schema of the flow circuits of the servovalve

stage. The drain orifice and those at the pressure entrance have fixed areas. We neglect the restrictions between the accumulators and the valve first stage and those between the two hydraulic stages as the pressure drops in these flow circuits have a negligible magnitude.

Figure 2.5(b) presents the flow circuit in the second stage valve. The spool moves due to the pressure difference $P_L - P_R$ on its ends. This movement induces a

variation of the cross section of the orifices associated with the ports A and B of the spool valve. This enables the output flow rates at ports A and B to be modulated. We neglect the restrictions between the accumulators and the second stage valve as done for the first stage. The fluid flow between the spool valve and the actuator will be taken into consideration in chapter 3 where the energy losses induced by the manifold are studied.

2.2.2 Study of the flows in the first stage

According to the conventional point of view, the orifices in the first stage are considered as sudden restrictions of short length and may have a fixed or variable area. We assume also that the flows in these orifices are turbulent flows and the discharge coefficients are considered as constants in the first stage. For these orifices, the flow equations [Merritt 1967] are given as follows:

$$Q_{PL} = A_0 C_{d0}\sqrt{\frac{2}{\rho}(P_P - P_L)} = \frac{\pi}{4} d_0^2 C_{d0}\sqrt{\frac{2}{\rho}(P_P - P_L)} \tag{2.1}$$

$$Q_{PR} = A_0 C_{d0}\sqrt{\frac{2}{\rho}(P_P - P_R)} = \frac{\pi}{4} d_0^2 C_{d0}\sqrt{\frac{2}{\rho}(P_P - P_R)} \tag{2.2}$$

$$Q_{LE} = A_{fL} C_{df}\sqrt{\frac{2}{\rho}(P_L - P_E)} = \pi d_n (x_{f0} + x_f)\cdot C_{d0}\sqrt{\frac{2}{\rho}(P_L - P_E)} \tag{2.3}$$

$$Q_{RE} = A_{fR} C_{df}\sqrt{\frac{2}{\rho}(P_R - P_E)} = \pi d_n (x_{f0} - x_f)\cdot C_{d0}\sqrt{\frac{2}{\rho}(P_R - P_E)} \tag{2.4}$$

$$Q_{ET} = Q_{LE} + Q_{RE} = A_d C_{dd}\sqrt{\frac{2}{\rho}(P_E - P_T)} = \frac{\pi}{4} d_d^2 C_{d0}\sqrt{\frac{2}{\rho}(P_E - P_T)} \tag{2.5}$$

The upstream cross sections for Q_{PL} and Q_{PR}, as well as those of the drain orifice, are considered as circular section with diameters d_0 and d_d. The controlling restrictions A_{fL} and A_{fR} are considered as cylinder surfaces. Their cross-section diameter is equal to the nozzle diameter d_n and the length of the cylinder is the distance between the flapper and nuzzle.

According to the fluid compressibility in the volumes of each end of the second stage spool, we can obtain the following expressions:

$$Q_L = Q_{PL} - Q_{LE} = \frac{1}{\beta} V_L \frac{dP_L}{dt} + A_s \frac{dx_s}{dt} \tag{2.6}$$

$$Q_R = Q_{PR} - Q_{RE} = \frac{1}{\beta} V_R \frac{dP_R}{dt} - A_s \frac{dx_s}{dt} \tag{2.7}$$

We assume that the sections of the two nozzles are symmetric and have an identical geometry. Besides, we consider also the following assumptions:

$$\begin{cases} C_{d0} = C_{df} = C_{dd} = C_f \\ A_{fL} = \pi d_n x_{f0}(1 + \delta_f) \text{ with } \delta_f = \dfrac{x_f}{x_{f0}} \\ A_{fR} = \pi d_n x_{f0}(1 - \delta_f) \end{cases} \tag{2.8}$$

where δ_f is the relative opening parameter, x_f and x_{f0} are defined on figure 2.4.

The flow rates Q_L and Q_R are null at equilibrium and negligible at very low spool speed. From (2.6) and (2.7), we then deduce

$$\begin{cases} Q_{PL} = Q_{LE} \\ Q_{PR} = Q_{RE} \end{cases} \tag{2.9}$$

According to equations (2.1)-(2.4), (2.8), and (2.9), the expressions of the pilot pressure difference (2.10) and the total leakage flow rates (2.11) can be obtained in steady state assuming that $P_E = P_T$.

$$\frac{P_L - P_R}{P_P - P_T} = \frac{\alpha_f^2(1+\delta_f)^2 \dfrac{P_T}{P_P - P_T} + \dfrac{P_P}{P_P - P_T}}{\alpha_f^2(1+\delta_f)^2 + 1} - \frac{\alpha_f^2(1-\delta_f)^2 \dfrac{P_T}{P_P - P_T} + \dfrac{P_P}{P_P - P_T}}{\alpha_f^2(1-\delta_f)^2 + 1} \tag{2.10}$$

where α_f is the ratio of initial section areas A_{fL} or A_{fR} to A_0, $\alpha_f = \dfrac{\pi d_n x_{f0}}{A_0} = \dfrac{4 d_n x_{f0}}{d_0^2}$.

$$\begin{cases} \dfrac{Q_{LE}}{C_f \pi d_n x_{f0} \sqrt{\dfrac{2}{\rho}(P_P - P_T)}} = \dfrac{1+\delta_f}{\sqrt{\alpha_f^2 (1+\delta_f)^2 + 1}} \\ \dfrac{Q_{RE}}{C_f \pi d_n x_{f0} \sqrt{\dfrac{2}{\rho}(P_P - P_T)}} = \dfrac{1-\delta_f}{\sqrt{\alpha_f^2 (1-\delta_f)^2 + 1}} \end{cases} \tag{2.11}$$

where $C_f \pi d_n x_{f0} \sqrt{\dfrac{2}{\rho}(P_P - P_T)}$ represents the flow rate through the nozzle at equilibrium, noted Q_{f0}.

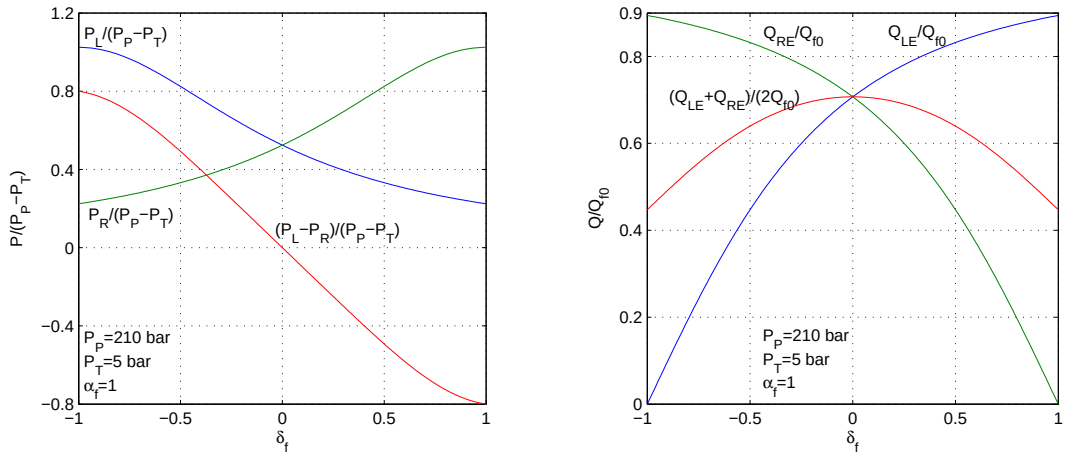

(a) Pressure evolution (b) Flow rate evolution

FIGURE 2.6: Pressure and flow rate evolution of the first stage in function of δ_f

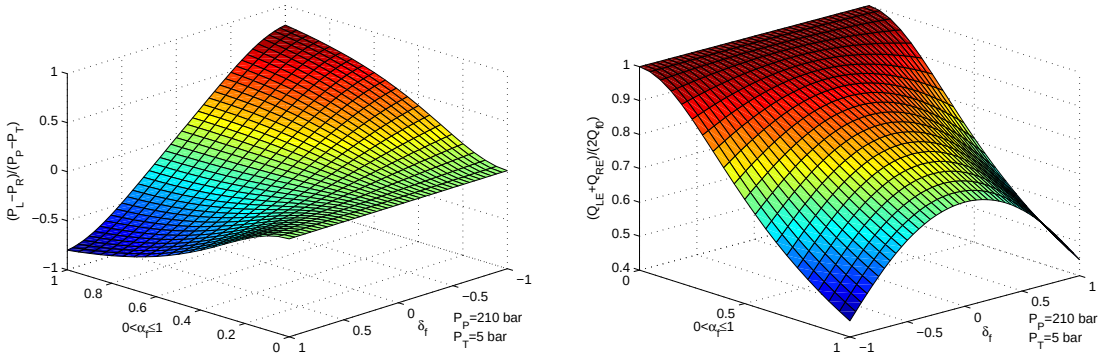

(a) Pressure evolution (b) Flow rate evolution

FIGURE 2.7: Pressure and flow rate evolution of the first stage in function of δ_f and α_f

Figure 2.6 presents the pressure and flow rate evolution in the first stage as functions of the relative opening δ_f with $\alpha_f = 1$. Figure 2.7 shows the pressure and flow rate evolution in the first stage as functions of δ_f and α_f.

According to figure 2.6(a), it is obvious that the relation between the pilot pressure difference and flapper deflection is nonlinear, particularly at the extreme position. The maximum of the total leakage flows (figure 2.6(b)) is achieved at flapper neutral position. Besides, in figure 2.7(a), we can notice that the ratio of $P_L - P_R$ to the total pressure difference achieves a better linearity when α_f decreases. This property will improve the control performance when applying a control designed from a linearized model. However, the operating range of the pilot pressure difference decreases while α_f is reduced. Figure 2.7(b) shows that the leakage flow rate goes up as α_f decreases, and this leakage become less sensible to the flapper displacement.

2.2.3 Study of the flows in the second stage

2.2.3.1 Overview of the flow model of the spool valve

In order to improve the flow model in the second stage, we focus our study mainly on the leakage flow model at overlap position and on the flow continuity between overlap and underlap position. There are several models, which investigate the flow at overlap and provide flow equations valid in the whole range of the spool displacement.

[Ellman 1995, Ellman 1998] proposed a nonlinear leakage model by considering the asymmetry of the spool valve. In this model, the leakage at overlap is considered as a short annular passage with a small clearance. For the flow at underlap position, the classic turbulent flow equation is used. Thus, this model has the following

form with $k_i,\ i = 1$ to 4 constant parameters.

$$\begin{cases} Q_{\text{underlap}} = (k_1 + k_2 \cdot x)\sqrt{\Delta P}, & x \geq 0 \\ Q_{\text{overlap}} = \dfrac{k_3}{2}\sqrt{\left(\dfrac{k_3}{k_4}\right)x^2 + 4 \cdot \Delta P} - \dfrac{k_3^2}{2 \cdot k_4}|x|, & x < 0 \end{cases} \tag{2.12}$$

This model shows good performances with smooth flow curve between overlap and underlap. However, the parameters of this model, i.e. k_3 and k_4, depend on the servovalve geometry and fluid properties and can not be easily estimated from the technical data provided by the manufacturer.

Considering that the leakage flow rates are turbulent at overlap and inversely proportional to the overlap length, [Eryilmaz 2000a, Eryilmaz 2000b] proposed a simplified flow model of the spool valve defined as follows:

$$\begin{cases} Q_{\text{underlap}} = K(x_0 + x)\sqrt{\Delta P}, & x \geq 0 \\ Q_{\text{overlap}} = \dfrac{K \cdot x_0^2\sqrt{\Delta P}}{x_0 + k \cdot |x|}, & x < 0 \end{cases} \tag{2.13}$$

The model parameters, K, k, and x_0, are easily estimated from the data given by the manufacturer. Besides, this model has a good continuity between overlap and underlap. It has been validated using measurements of a MOOG 760-723A servovalve. However, the model is not accurate enough around $x = 0$.

The flow model widely employed is the one proposed by Lebrun which is written as follows [Lebrun 1978, Maré 1993, Maré 1996]:

$$\begin{cases} Q_{\text{underlap}} = C_d(\text{Re}) \cdot A(x) \cdot \sqrt{\dfrac{2}{\rho}\Delta P}, & x \geq 0 \\ Q_{\text{overlap}} = \dfrac{\pi D_h \cdot c^3}{12(|x| + k)}\Delta P, & x < 0 \end{cases} \tag{2.14}$$

where c is the diameter of the annular clearance between the spool and sleeve; C_d is the discharge coefficient as a function of the Reynolds number; and D_h is the hydraulic diameter defined as the ratio of four times of the cross sectional area to the wetted perimeter of the cross-section.

In this model, the parameter k is a constant that ensures the flow continuity. Although this parameter can be easily estimated from the manufacturer's data, the continuity of the flow derivative is not guaranteed and this results in a sharp change in flow rates between overlap and underlap states.

[Feki 2005] proposed a servovalve static flow model by considering the small radial clearance and the leakage flow. This model applied a simple formula to guarantee the transition between the laminar and turbulent phases at large opening. The model is given as follows:

$$\begin{cases} Q_{\text{underlap}} = k|i|\sqrt{\Delta P} + \dfrac{\alpha}{1+\gamma|i|}\Delta P \\ Q_{\text{overlap}} = \dfrac{\alpha}{1+\gamma|i|}\Delta P \end{cases} \tag{2.15}$$

where i is the input current; k is the servovalve sizing factor; α and γ are the model coefficient in function of the radial clearance, sleeve radius, and fluid viscosity.

This model can be easily applied in the hydraulic design. However, if more details (initial overlap, rounded edge, $\cdots$) at the orifice are considered, this model is inapplicable. Besides, there exists a flow underestimation for high input current, and its connection between overlap and underlap flows is not smooth.

The most recent model is the one proposed by Attar, which consists of a uniform equation for overlap and underlap flow [Attar 2008]. This model is written as

$$Q_{i(\forall x_i)} = C_{q\infty} \tanh\left(\frac{\lambda_i}{\lambda_t}\frac{1}{1+\dfrac{1}{2}K_{\text{rec}}(|x_i|-x_i)}\right) A_i \cdot \sqrt{\frac{2}{\rho}|\Delta P_i|}\text{sgn}(\Delta P_i) \tag{2.16}$$

where

- $K_{\text{rec}} = \dfrac{64 C_{q\infty}}{D_h \lambda_t}$ is the overlap discharge coefficient;
- λ_i is the flow number at port i defined as $\lambda_i = \dfrac{D_h}{\nu}\sqrt{\dfrac{2}{\rho}|\Delta P_i|}$;
- λ_t is the transition flow number.

In this model, it is considered that the change between overlap and underlap flow is only involved with the variation of the discharge coefficient C_q, which can be

estimated according to a function of the flow number λ. According to this model, we obtain a smooth flow curve between laminar and turbulent flows in the spool valve. Nevertheless, there still exists errors at small opening. It can not obtain a compromised estimation precision between the leakages and the pressures. The relative error of the pressure gain reaches to 30%, while the one of the maximum leakage is 1.8%.

2.2.3.2 Local geometric defects in the spool valve

Through the process of manufacturing and assembly, the edges of the spool and sleeve show inevitably irregular geometries and ideal sharp edges are impossible in practice. For flow calculation in the spool valve, these local geometric defects influence significantly the flow evolution. In order to take into account these effects, we propose to introduce some additional geometric parameters for the representation of the flow in the spool valve, i.e. the diameter of rounded edges d_r and the radius of radial clearance of the spool valve e_s (see figure 2.8). Besides, we believe that these parameters will increase along with the use of the valve due to wear and abrasion.

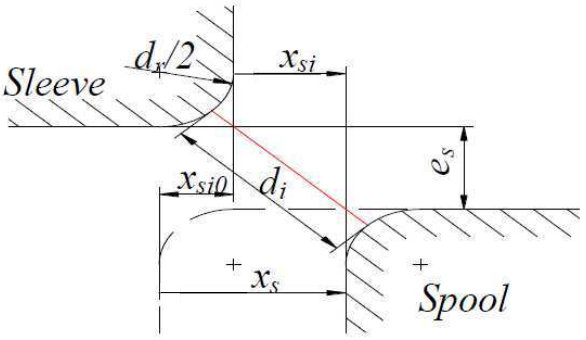

FIGURE 2.8: Local geometric configuration around spool and valve control port

According to figure 2.8, the opening diameter is given by

$$d_i = \begin{cases} \sqrt{(e_s + d_r)^2 + (d_r + x_{si})^2} - d_r & \text{if } x_{si} \geq -d_r \\ e_s & \text{if } x_{si} < -d_r \end{cases} \tag{2.17}$$

where

$$x_{si} = \begin{cases} x_s - x_{si0} & i = 1,3 \\ -x_s - x_{si0} & i = 2,4 \end{cases} \tag{2.18}$$

Let us define the opening diameter at neutral position (for $x_{si} = 0$) as

$$d_0 = d_i(0) = \sqrt{(e_s + d_r)^2 + d_r^2} - d_r \tag{2.19}$$

2.2.3.3 Study of the underlap flows in the spool valve

The flows in the spool valve can be defined as two types: (1) orifice flow when $x_{si} \geq 0$ and (2) leakage flow when $x_{si} < 0$. The orifice flow at underlap position ($x_{si} \geq 0$) is evaluated by [Merritt 1967]

$$Q_{si,\text{underlap}} = C_{di} A_{si} \sqrt{\frac{2}{\rho}|\Delta P|} = C_{di} \cdot n \cdot w_s d_i \sqrt{\frac{2}{\rho}|\Delta P|} \quad \text{if } x_{si} \geq 0 \tag{2.20}$$

where

- ΔP is the pressure drop corresponding to the valve control port;
- C_{di} is the discharge coefficient;
- A_{si} is the section area at valve control port.
- n is the number of slit orifices on the sleeve;
- w_s is the width of the slits.

In this case, the Reynolds number that characterizes the flow regime is given by

$$\text{Re} = \frac{\rho D_h Q}{\mu A} \tag{2.21}$$

where D_h is the hydraulic diameter, defined as $D_h = \dfrac{4A}{P}$ with A the cross section area and P the wetted perimeter of the cross section. For the spool valve, the hydraulic diameter is then:

$$D_h = \frac{4 \cdot n \cdot w_s d_i}{n \cdot 2(w + d_i)} = \frac{2 w d_i}{w + d_i} \approx 2 d_i \quad \text{for } w \gg d_i \tag{2.22}$$

According to experiments, the discharge coefficient curve as a function of the Reynolds number is illustrated in figure 2.9.

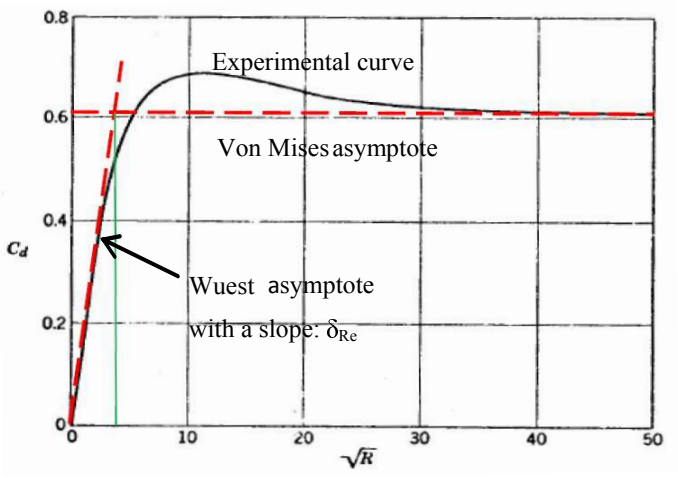

FIGURE 2.9: Experimental curve of the discharge coefficient as a function of the Reynolds number [Merritt 1967]

According to figure 2.9, it is acceptable to make an approximation of the experimental curve by two linear asymptotes, which take the following forms:

$$C_{di} = \begin{cases} \delta_{\mathrm{Re}}\sqrt{\mathrm{Re}_i}, & \mathrm{Re}_i \leq \mathrm{Re}_t \\ C_{d\infty}, & \mathrm{Re}_i > \mathrm{Re}_t \end{cases} \tag{2.23}$$

where

- $C_{d\infty}$ is the discharge coefficient in turbulent regime;
- δ_{Re} is a parameter depending on geometry and called the laminar flow coefficient;
- Re_t is the transition Reynolds number, defined by the intersection point of the two asymptotes, that is

$$\mathrm{Re}_t = \left(\frac{C_{d\infty}}{\delta_{\mathrm{Re}}}\right)^2 \tag{2.24}$$

By substituting (2.21) and (**??**) into (2.20), we obtain the flow rate expression at underlap position 2.25:

$$Q_{si,\text{underlap}} = \begin{cases} 4\frac{\delta_{\text{Re}}^2}{\mu} \cdot n \cdot w_s d_i^2(x_{si}) \cdot |\Delta P|, & \text{Re}_i \leq \text{Re}_t \\ C_{d\infty} \cdot n \cdot w_s d_i \sqrt{\frac{2}{\rho}|\Delta P|}, & \text{Re}_i > \text{Re}_t \end{cases} \tag{2.25}$$

2.2.3.4 Study of the overlap flows in the spool valve

At overlap position ($x_{si} < 0$), and when $|x_{si}| \gg e_s$, we can assume that the flow complies with the Hagen-Poiseuille law. Namely, in this case, the flow is inversely proportional to the overlap length. In practice, there exists a transitional region along with the spool displacement. In this region, the additional kinetic energy losses consist of those due to fluid inertia due to the acceleration in the transition length at inlet and outlet. Inspired by Lebrun's model [Lebrun 1978], we introduce a new leakage model based on the Hagen-Poiseuille law for representing the flows between the spool and the sleeve. In order to guarantee the continuity of the flow curve and with respect to the physical phenomena, the proposed model is formulated by substituting the overlap length by an equivalent one, which leads finally to:

$$Q_{si,\text{overlap}} = \frac{n \cdot w_s \cdot e_s^3}{12\mu \left(k_s + |x_{si}| + k_I \tanh\left(\frac{|x_{si}|}{L_t} \right) \right)} |\Delta P| \quad \text{if } x_{si} < 0 \tag{2.26}$$

where

- k_s is the energy losses parameter for inlet and outlet flows;
- k_I is the energy losses coefficient related to fluid inertia;
- L_t is the transition length.

In the expression of equivalent overlap length, the first term k_s represents the inlet and outlet losses, and the losses due to fluid inertia are taken into account in the third term. The term $\tanh\left(\frac{|x_{si}|}{L_t}\right)$ is applied here to demonstrate the fact that the

fluid velocity takes a certain length in a circuit to achieve the evolution caused by the change of the cross section.

Assuming that the flow is laminar at overlap positions or small spool stroke, i.e. $\mathrm{Re}_i < \mathrm{Re}_t$ for $x_{si} < 0$ or $x_{si} \to 0$, the boundary conditions can be used to define smooth flow curves, that is

$$\begin{cases} \lim_{x_{si}\to 0} Q_{si,\mathrm{underlap}} = \lim_{x_{si}\to 0} Q_{si,\mathrm{overlap}} \\ \lim_{x_{si}\to 0} \dfrac{\partial Q_{si,\mathrm{underlap}}}{\partial x_{si}} = \lim_{x_{si}\to 0} \dfrac{\partial Q_{si,\mathrm{overlap}}}{\partial x_{si}} \end{cases} \tag{2.27}$$

Then we can define the flow model around the neutral position as

$$\begin{cases} Q_{si,\mathrm{underlap}} = 4\dfrac{\delta_{\mathrm{Re}}^2}{\mu} \cdot n \cdot w_s d_i^2(x_{si}) \cdot |\Delta P|, & x_{si} \geq 0 \\ Q_{si,\mathrm{overlap}} = \dfrac{n \cdot w_s \cdot e_s^3}{12\mu \cdot f_L(x_{si})} |\Delta P|, & x_{si} < 0 \end{cases} \tag{2.28}$$

with

$$f_L(x_{si}) = \left(k_s - x_{si} + k_I \tanh\left(-\frac{x_{si}}{L_t} \right) \right)$$

The derivative of the flow with respect to x_{si} is finally given by

$$\begin{cases} \dfrac{\partial Q_{si,\mathrm{underlap}}}{\partial x_{si}} = 8\dfrac{\delta_{\mathrm{Re}}^2}{\mu} \cdot n \cdot w_s d_i^2(x_{si}) \cdot \dfrac{\partial d_i(x_{si})}{\partial x_{si}} \cdot |\Delta P|, & x_{si} \geq 0 \\ \dfrac{\partial Q_{si,\mathrm{overlap}}}{\partial x_{si}} = -\dfrac{n \cdot w_s \cdot e_s^3}{12\mu \cdot f_L^2(x_{si})} \cdot \dfrac{\partial f_L(x_{si})}{\partial x_{si}} \cdot |\Delta P|, & x_{si} < 0 \end{cases} \tag{2.29}$$

Defining that $L_t = k_t d_0$, where k_t is a constant depending on the geometry of the spool valve, the unknown parameters is then given by:

$$k_s = \frac{e_s^3}{48\delta_{\mathrm{Re}}^2 \cdot d_0^2} \tag{2.30}$$

$$k_I = k_t(2k_s d_i'(0) - d_0) = k_t \left(\frac{e_s^3 \cdot d_r}{24\delta_{\mathrm{Re}}^2 \cdot d_0^2(d_0 + d_r)} - d_0 \right) \tag{2.31}$$

2.2.3.5 Identification and validation of the model parameters

According to the proposed flow model (2.28), an unknown parameter vector of eight elements was to be determined, namely, $\gamma =$

$[x_{s10},\ x_{s20},\ x_{s30},\ x_{s40},\ d_r,\ e_s,\ k_t,\ \delta_{\mathrm{Re}}]$. Six of them are related to diameters of geometric defects, one is introduced by the proposed model, and the last one is depending on the flow condition.

To estimate this parameter vector, experimental results are used, namely the leakage and the pressure gain. In our case, the experimental data are obtained with the experiments, the output ports A and B closed at a supply pressure of 215 bar and tank pressure of 2 bar. By applying the Levenberg-Marquardt estimation method in Matlab, we minimized the difference between the experimental and simulation results. Due to the non-convexity of the optimal function, there exist a number of local minimums. By setting the initial values to [0, 0, 0, 0, 2 μm, 2 μm, 10, 0.1] because of the small defects, the parameters are finally obtained as presented in table 2.1.

TABLE 2.1: Estimated values of the unknown parameters

$x_{s10}(\mu\mathrm{m})$	$x_{s20}(\mu\mathrm{m})$	$x_{s30}(\mu\mathrm{m})$	$x_{s40}(\mu\mathrm{m})$	$d_r(\mu\mathrm{m})$	$e_s(\mu\mathrm{m})$	k_t	δ_{Re}
7.6	7.1	18.7	25.2	18.7	2.4	10	0.151

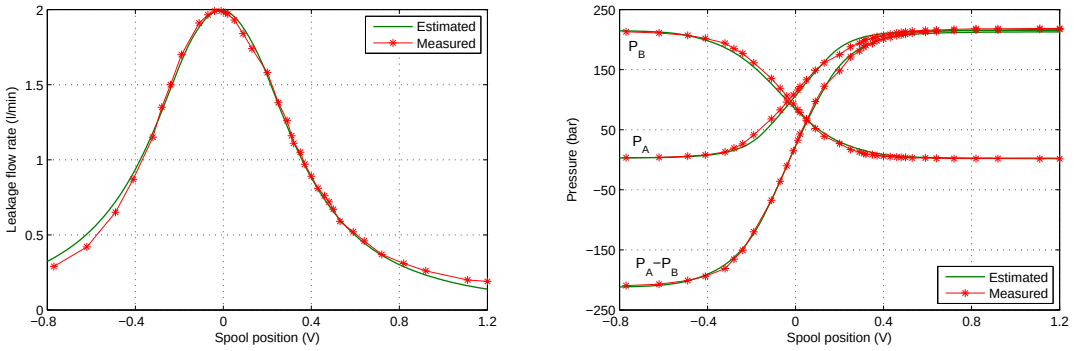

(a) Leakage flow rates (b) Pressure gain

FIGURE 2.10: Comparison of experimental and simulation results for the leakage characteristic and the pressure gain in the spool valve

Figure 2.10 presents the comparison between the proposed model and measurements. In figure 2.10(a), the error between the experimental and simulation leakage characteristic at peak is about 0.005 l/min that is less than 2.5%. The maximum leakage error located at wide opening where the leakage is small, reaches nearly 0.08 l/min. On the other side, the experimental pressure gain is 850 bar/V and the simulated is 827 bar/V in figure 2.10(b). The difference between the two

values is 23 bar/V, i.e. 2.7% relative error. The errors of the estimated pressures P_A and P_B are less than 10 bar. To conclude, the proposed flow model enables a good agreement with experimental or manufacturer data sheets and can be directly related to the physical characteristics of the spool valve.

2.3 CFD analysis of the flow force in the spool valve

When the fluid flows into or out of the valve chambers, a jet force occurs and acts on the fluid. Thus, there is a reaction force acting on the spool. This force is referred to as the flow force and tends to close the valve port. According to [Merritt 1967], the static flow force is given by:

$$F_f = \frac{\rho Q^2}{A} \tag{2.32}$$

While the radial component of this force is always compensated in practice by symmetrical arrangement of the valve ports, only the axial component has to be considered in the valve design. This component is given by:

$$F_x = F_f \cos\theta = \frac{\rho Q^2}{A} \cos\theta \tag{2.33}$$

where θ is the jet angle, which depends on the port opening. This parameter can be evaluated by the following formula [Merritt 1967]:

$$\frac{x_v}{C_r} = \frac{1 + \frac{\pi}{2}\sin\theta - \ln\left(\tan\frac{1}{2}(\pi - \theta)\right) \cdot \cos\theta}{1 + \frac{\pi}{2}\cos\theta - \ln\left(\tan\frac{1}{2}(\pi - \theta)\right) \cdot \sin\theta} \tag{2.34}$$

where C_r is the radial clearance. Figure 2.11 illustrates the relation between the jet angle and the valve opening.

The study of the flow force takes a crucial role in the structure analysis or the control design of a high performance servovalve which has a very small inertia. In this section, we apply CFD approach (using the software Fluent) to conduct

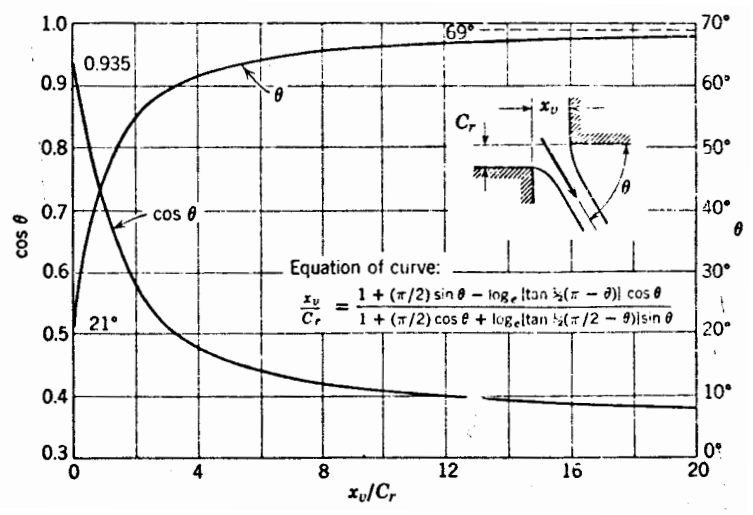

FIGURE 2.11: Jet angle in function of the opening [Merritt 1967]

a brief study on the flow force effect of the studied servovalve. The purpose of our study will only focus on the flow force effect in the spool valve. Due to the symmetry of the valve, a 2D mesh of the inner volume of the valve is considered and can be sufficient to analyze the phenomena (see figure 2.12). The annular clearance between the spool and sleeve has been taken into account and set to 2.5 μm. The turbulence model applied here is the $\kappa - \epsilon$ turbulent model with its default settings. This model is a semi-empirical model proposed by [Launder 1972] and the most widely applied in industry because of its robustness, economy and reasonable accuracy for a wide range of turbulent flows.

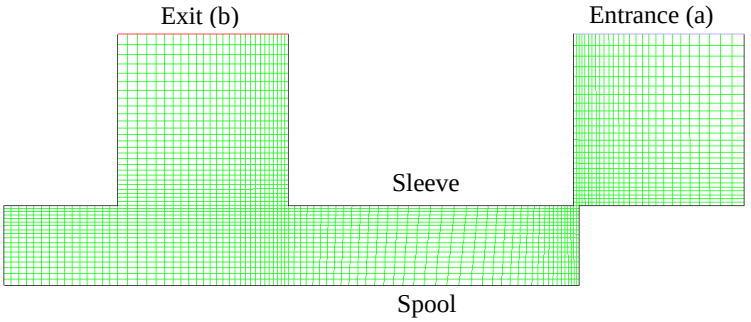

FIGURE 2.12: Mesh model of the spool valve

As boundary condition, a speed input with a uniform flow velocity profile on face (a) and a pressure output on face (b) are applied for the calculations. In this study, we consider changes of the input flow rates at different orifice openings.

Figure 2.13 presents the velocity distribution in the spool valve for an opening of 0.1 mm, and flow rate of 5 l/min. It can be observed that the flow, after passing through the orifice, is divided into two main parts, one attached to the spool surface, and the other attached to the sleeve surface. The jet attachment results in a reduction of the jet angle which leads to increase the flow force.

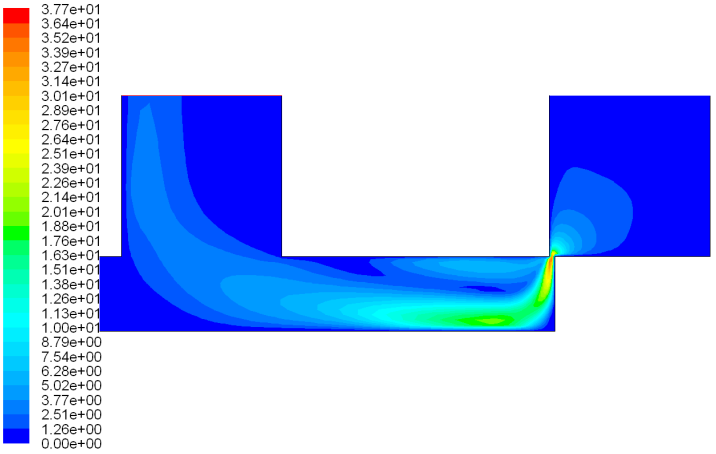

FIGURE 2.13: Velocity distribution in the spool valve

Figure 2.14 presents the pressure drop and flow force evolution as a function of the input flow rates. The pressure drop is the pressure difference between the inlet and outlet total pressure. In real applications, the pressure drop is derived from the pressures measured according to physical pressure sensors which acquire indeed the static pressure of the fluid. In this case, the dynamic pressure is neglected due to the small fluid velocity. In figure 2.14(a), the relation between the pressure drop and the flow rate complies with the conventional form $Q \propto \sqrt{\Delta P}$ at wide

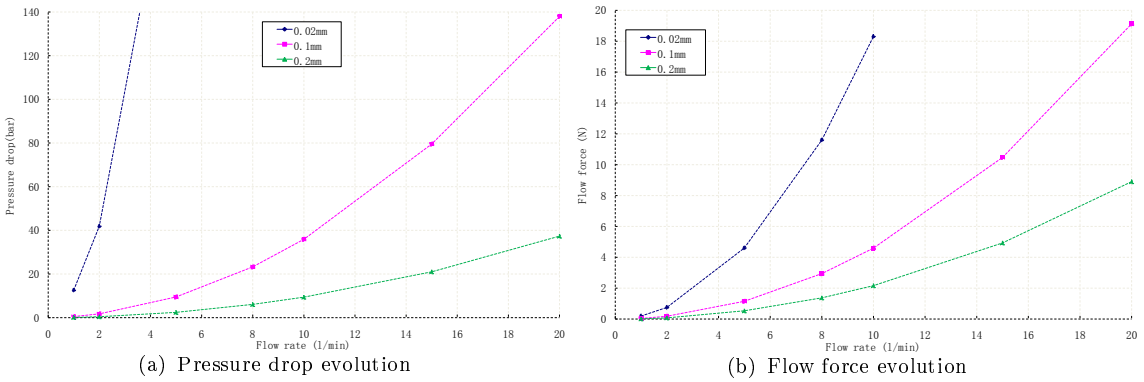

(a) Pressure drop evolution

(b) Flow force evolution

FIGURE 2.14: Pressure drop and flow force evolution as a function of flow rate

opening. According to figure 2.14(b), the flow force is proportional to the square of the flow rates. When the opening decreases, the flow force increases with a more significant gain due to the reduction of the jet angle.

This CFD study confirms the applicability of equation (2.33) for the servovalve modelling. A more precise evaluation of the flow angle will require the exact definition of the spool and sleeve geometries.

2.4 Modelling of the servovalve

Bond Graph, as a graphical modelling language, can represent various physical domains in a unified form. This section deals with the establishment of a Bond Graph model of the electro-hydraulic servovalve, which consists in a torque motor, a cantilever feedback needle, and two hydraulic stages, one with a flapper/nozzle system and the other with a spool valve. The entire model can be divided into hydraulic, mechanical and electromagnetic subsystems, which are connected by 2-port modulated R-elements representing orifice pressure drop and jet force phenomena, and TF-elements coupling the mechanical and hydraulic domains. The Bond Graph model of the whole system is finally presented, before introducing the AMESim model based on the established Bond Graph. Simulation results compared with the experimental measurements will conclude this section.

2.4.1 Modelling of the flapper/nozzle system

As the modelling of a servovalve concerns hydraulic, mechanic, and electromagnetic domains, the application of the Bond Graph here is quite convenient. Firstly, we will cope with the modelling of the first hydraulic stage, i.e. the flapper/nozzle system.

2.4.1.1 Bond Graph of the hydraulic part of the flapper/nozzle subsystem

In section 2.2.2, we discussed the flows in the flapper/nozzle system (equations (2.1)-(2.5)). Taking into account the compressibility of the fluid in each chamber of the flapper/nozzle system, the pilot flows injected into the main spool valve for driving its movement are expressed by equations (2.6) and (2.7). To represent this compressibility effect in Bond Graph, a convenient means is the use of a 2-port capacitive phenomenon which couples hydraulic and mechanical domains [Maré 1993]. Besides, all of the orifice flows can be expressed by resistive phenomena in Bond Graph due to power dissipation associated with pressure drops. The Bond Graph of the hydraulic part of the flapper/nozzle system is shown in figure 2.15.

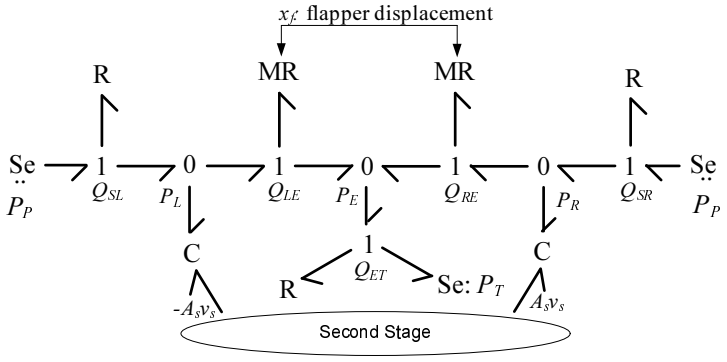

FIGURE 2.15: Bond Graph of the hydraulic part of the flapper/nozzle system

2.4.1.2 Bond Graph of mechanical part of the flapper/armature

The first-stage flapper is influenced by the following forces [Morse 1963] (figure 2.16):

1) Control torque T_m, which is derived from the torque motor and related to the input electrical current;
2) Spring forces F_r and torque T_r proportional to the deflection of the cantilever feedback needle;
3) Flexible tube force F_t and torque T_t induced by the deflection of the flexible tube;

4) Hydrostatic force F_{fhs} produced by the pressure difference applied on the two sides of the flapper;

5) Flow force F_{fhd} due to the non uniform pressure distribution caused by the fluid flow across the areas between nozzles and flapper;

6) Viscous damping force T_v due to mechanical armature mounting and load.

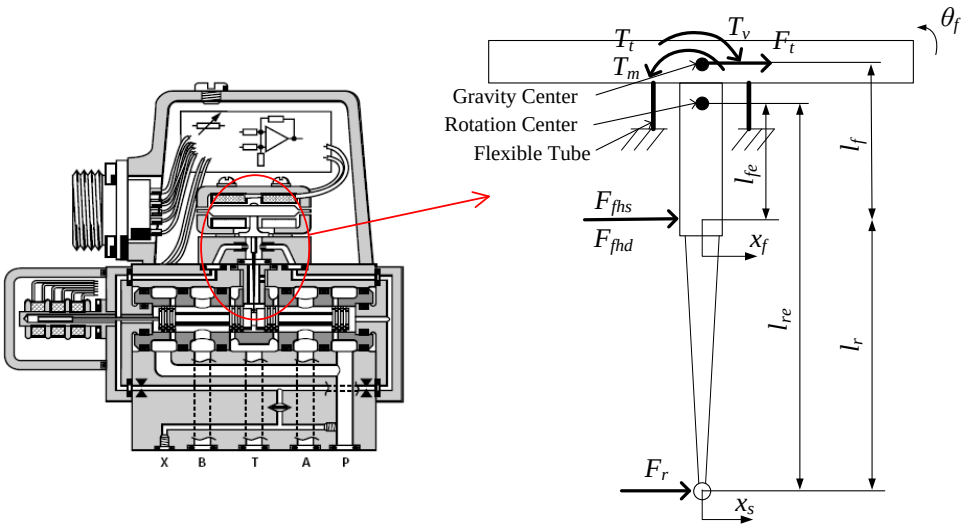

FIGURE 2.16: Forces applied to the flapper/armature

Models for the reaction of the feedback needle and flexible tube can be developed from the material mechanics. Consider a cantilever beam, i.e. a beam fixed at one end, with a force and a moment acting at the free end as shown in figure 2.17.

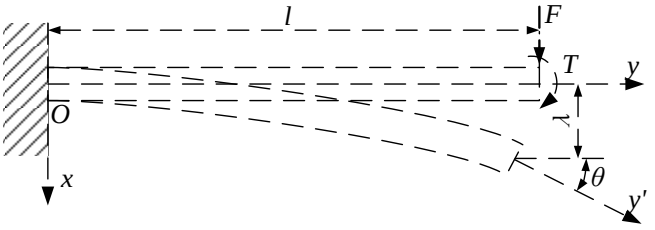

FIGURE 2.17: Cantilever beam model

From material mechanics [Hibbeler 1997], the slope θ and deflection λ of the free end are functions of the force and moment acting on the beam which are given as

$$\begin{cases} \theta = \dfrac{T \cdot l}{E \cdot I_Z} - \dfrac{F \cdot l^2}{2E \cdot I_Z} \\ \lambda = -\dfrac{M \cdot l^2}{2E \cdot I_z} + \dfrac{F \cdot l^3}{3E \cdot I_Z} \end{cases} \tag{2.35}$$

where

- E is the material elasticity modulus;
- I_Z is the beam's moment of inertia computed about the neutral axis.

Then, we can deduce

$$\begin{cases} T = \dfrac{4E \cdot I_Z}{l} \cdot \theta + \dfrac{6E \cdot I_Z}{l^2} \cdot \lambda \\ F = \dfrac{6E \cdot I_Z}{l^2} \cdot \theta + \dfrac{12E \cdot I_Z}{l^3} \cdot \lambda \end{cases} \tag{2.36}$$

In our case, θ represents the flapper's deflection, and λ is related to the displacement of the cantilever feedback needle and the flexible tube at their free end.

The resultants of forces and torques that act on the gravity center of the entire flapper/armature are given by:

$$\begin{aligned} m_f \frac{d^2 x_{fG}}{dt^2} &= F_r - F_t + F_{\text{fhs}} + F_{\text{fhd}} \\ \Rightarrow m_f \frac{d^2 x_{fG}}{dt^2} &= 3K_r \cdot x_r - (6l_t \cdot K_t \cdot \theta_f + 12K_t \cdot x_{fG}) + F_{\text{fhs}} + F_{\text{fhd}} \end{aligned} \tag{2.37}$$

$$\begin{aligned} J_f \frac{d^2 \theta_f}{dt^2} &= Tm + T_r - T_t + (F_{\text{fhs}} + F_{\text{fhd}}) l_f - T_v \\ \Rightarrow J_f \frac{d^2 \theta_f}{dt^2} &= Tm + 3K_r \cdot x_r \cdot (l_f + l_r) - (4l^2 \cdot K_t \cdot \theta_f + 6l_t \cdot K_t \cdot x_{fG}) \\ &\quad + (F_{\text{fhs}} + F_{\text{fhd}}) l_f - B_f \frac{d\theta_f}{dt} \end{aligned} \tag{2.38}$$

where

- m_f is the mass of the flapper/armature;
- J_f is the rotary inertia of the flapper/armature;
- B_f is the flapper viscous damping coefficient;
- $K_t = \dfrac{E_t I_t}{l_t^3}$ and $K_r = \dfrac{E_r I_r}{l_r^3}$ are the flexible tube and feedback needle constants;
- $F_{\text{fhs}} = (P_L - P_R) \cdot \dfrac{\pi d_n^2}{4}$ is the hydrostatic force with d_n the diameter of the nozzle.
- $F_{\text{fhd}} = \dfrac{4\rho}{\pi d_n^2}(Q_{LE}^2 - Q_{RE}^2)$ is the flow force discussed in section 2.3.

Note that the modal frequencies of translational vibration are quite higher than the rotational ones [Maré 1993]. The mass of the flapper/armature then can be neglected. Equations (2.37) and (2.38) are reduced to one equation concerning the rotational dynamics of the system:

$$J_f \frac{d^2\theta_f}{dt^2} = Tm + 3K_r \cdot x_r \cdot l_{re} - l^2 \cdot K_t \cdot \theta_f + (F_{\text{fhs}} + F_{\text{fhd}}) l_f e - B_f \frac{d\theta_f}{dt} \qquad (2.39)$$

where

- $l_{re} = l_f + l_r - \frac{l_t}{2}$ is the equivalent needle length;
- $l_{fe} = l_f - \frac{l_t}{2}$ is the equivalent flapper length;
- $x_r = x_s - l_{re} \cdot \theta_f$ is the relative displacement of the feedback needle at its free end.

According to (2.39), the Bond Graph of the mechanical part of the flapper/armature is given by figure 2.18.

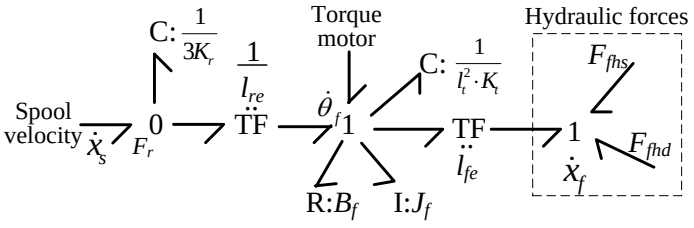

FIGURE 2.18: Bond Graph of the mechanical part of the flapper/armature

2.4.2 Modelling of the spool valve

2.4.2.1 Bond Graph of the hydraulic part of the spool valve

In section 2.2.3, we have carefully studied the flows in the spool valve and proposed a flow model (2.25) and (2.28). The flow rates at the control ports A and B are expressed as

$$\begin{cases} Q_A = Q_{s1} - Q_{s2} \\ Q_B = Q_{s4} - Q_{s3} \end{cases} \qquad (2.40)$$

While applying modulated R-elements to represent the valve resistances to the flow, the Bond Graph of the hydraulic part of the spool valve is represented in figure 2.19.

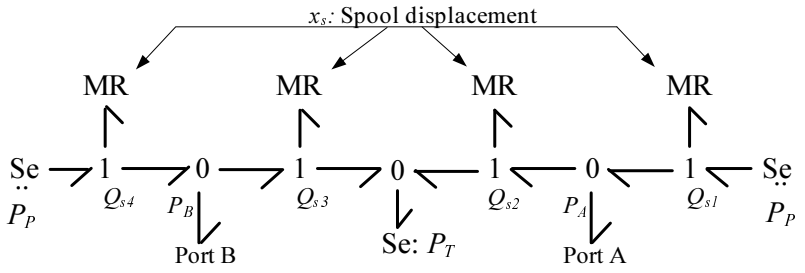

FIGURE 2.19: Bond Graph of the hydraulic part of the spool valve

2.4.2.2 Bond Graph of mechanical part of the spool valve

The forces acting upon the second-stage spool include the following types (figure 2.20):

1) Pilot force F_{shs} due to a pressure difference across the spool produced by the pilot stage;
2) Spring force F_r proportional to the deflection of the feedback needle;
3) Flow force F_{shd} due to the non uniform pressure distribution caused by the flow across the valve control ports;
4) Frictional force F_v between spool/sleeve with a viscous friction coefficient. This coefficient is assumed to be a linear function of x_{si} as the contact surface varies in function of x_{si}:

$$B_s = a_s + b_s \cdot |x_{si}| \tag{2.41}$$

where
- B_s is the spool viscous damping coefficient;
- a_s, b_s are the coefficients of the spool viscous damping model;

The resultants of forces applied to the spool are given by:

$$m_s \frac{d^2 x_s}{dt^2} = F_{\text{shs}} - F_r - F_v + F_{\text{shd}} = \frac{\pi d_s^2}{4}(P_L - P_R) - 3K_r \cdot x_r - B_s \frac{dx_s}{dt} + F_{\text{shd}} \tag{2.42}$$

where

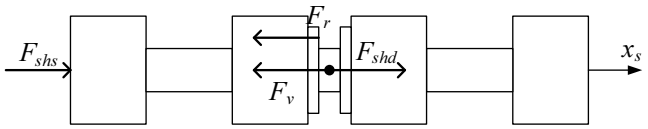

FIGURE 2.20: Forces applied to the spool

- m_s is the spool mass;
- d_s is the piston diameter of the spool valve.

The spool flow force F_{shd} is calculated from (2.33) using the following formula:

$$F_{\text{shd}} = \rho \cdot \left(\frac{\cos\theta_2}{A_{s2}} Q_{s2}^2 - \frac{\cos\theta_1}{A_{s1}} Q_{s1}^2 + \frac{\cos\theta_4}{A_{s4}} Q_{s4}^2 - \frac{\cos\theta_3}{A_{s3}} Q_{s3}^2 \right) \tag{2.43}$$

where $A_{si},\ i = 1, 2, 3, 4$ are the cross section areas of the valve ports, and θ_i is the jet angle estimated by equation (2.34).

Finally, figure 2.21 represents the Bond Graph of the mechanical part of the spool by simply applying all these forces on a 1-junction representing the spool motion.

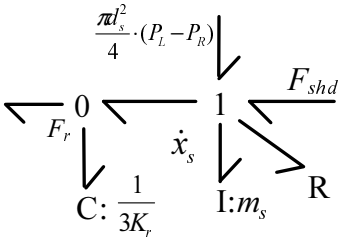

FIGURE 2.21: Bond Graph of the mechanical part of the spool valve

2.4.3 Modelling of the torque motor

The torque motor is an electromechanical device which provides a torque to the flapper/nozzle system and induces the deflection of the flapper. It consists of a permanent magnet and an armature enclosed by coils. Due to the magnetic flux in the air gaps between the armature and the permanent magnet, it generates a force which is approximately proportional to the current. The motor configuration is symmetrical as shown in figure 2.22.

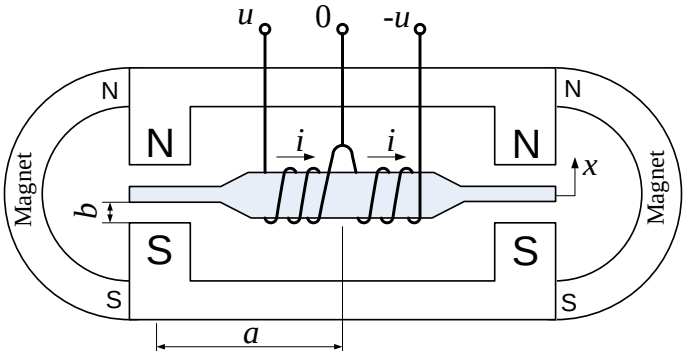

FIGURE 2.22: Torque motor configuration

2.4.3.1 Magnetic circuit

As the reluctance of the air gaps are larger than those of the armature material, the magnetic circuit can be approximated as presented in figure 2.23.

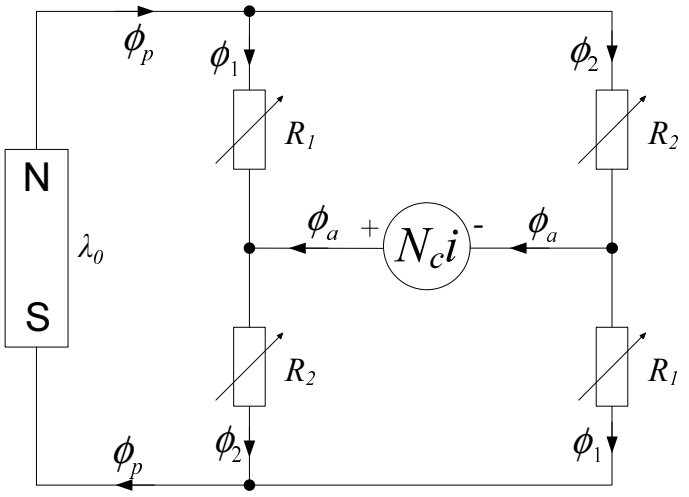

FIGURE 2.23: Magnetic circuit

The magnetic flux is given [Merritt 1967] as

$$\phi_i = \begin{cases} \dfrac{\lambda_0 - 2N_c i}{2R_0(1 + x/b)}, & i = 1 \\ \dfrac{\lambda_0 + 2N_c i}{2R_0(1 - x/b)}, & i = 2 \end{cases} \tag{2.44}$$

$$\phi_a = \phi_2 - \phi_1 = \frac{\lambda_0(x/b) + 2N_c i}{R_0(1 - x^2/b^2)} \tag{2.45}$$

where

- $R_0 = \dfrac{b}{\mu_0 A}$ is the reluctance of the air gaps at neutral position with μ_0 the air permeability;
- λ_0 is the magnetomotive force of the permanent magnet, in A·turns.
- N_c is the number of turns in each coil;

Considering the geometrical approximation that $\tan\theta_f = x/a \approx \theta_f$ and assumption that $x \ll b$, i.e. $x/b \ll 1$, (2.45) can be rewritten as

$$\phi_a = \frac{\lambda_0 \cdot \theta_f}{R_0} \cdot \frac{a}{b} + \frac{2N_c i}{R_0} \tag{2.46}$$

The expression for the electrical circuit is written as

$$u = R \cdot i + N_c \frac{d\phi_a}{dt} \tag{2.47}$$

where R is the resistance of each coil.

Substituting (2.46) into (2.47), yields

$$u = R \cdot i + N_c \frac{\lambda_0}{R_0} \cdot \frac{a}{b} \cdot \frac{d\theta_f}{dt} + \frac{2N_c^2}{R_0} \cdot \frac{di}{dt} = R \cdot i + K_b \frac{d\theta_f}{dt} + L_c \frac{di}{dt} \tag{2.48}$$

From equation (2.48), it can be found that the voltage is not only related to the coil resistance and the self-inductance, but also to the reaction of the armature rotational velocity.

Besides, the force caused by the magnetic flux in the air gaps is then given by

$$F_i = \frac{B_i^2 A}{2\mu_0} = \frac{\phi_i^2}{2\mu_0 A} \tag{2.49}$$

where $B_i,\ i = 1, 2, 3, 4$ are the flux density in the air gap.

Thus, the torque generated by the motor can be expressed as

$$\begin{aligned} T_m &= 2a \cdot (F_2 - F_1) = \frac{a \cdot (\phi_2^2 - \phi_1^2)}{\mu_0 A} \\ &= \frac{a}{\mu_0 A} \frac{4\frac{x}{b}\left(\frac{\lambda_0}{2R_0}\right)^2 \left(1 + \left(\frac{2N_c i}{\lambda_0}\right)^2\right) + 2\left(1 + \left(\frac{x}{b}\right)^2\right)\frac{\lambda_0 N_c i}{R_0^2}}{\left(1 - \left(\frac{x}{b}\right)^2\right)^2} \end{aligned} \tag{2.50}$$

In order to simplify this formulation, it can be assumed that $x \ll b$ and $2N_c i \ll \lambda_0$. Then, equation (2.50) can be rewritten as

$$\begin{aligned} T_m &= \frac{a}{\mu_0 A}\left(4\frac{a}{b}\left(\frac{\lambda_0}{2R_0}\right)^2 \cdot \theta + 2\frac{\lambda_0 N_c}{R_0^2} \cdot i\right) \\ &= 4\left(\frac{a}{b}\right)^2\left(\frac{\lambda_0}{2R_0}\right)^2 \cdot \theta + 4\frac{a}{b}\frac{\lambda_0}{2R_0} \cdot N_c \cdot i = K_{mr} \cdot \theta_f + K_m \cdot i \end{aligned} \tag{2.51}$$

According to equation (2.51), the output torque of the motor is proportional to the input current. Besides, there is an interaction between the output torque and the armature deflection θ_f, which tends to close the gap.

2.4.3.2 Bond Graph model of the torque motor

In the magnetic circuit of the torque motor, the most important phenomena are the air gaps coupling magnetics and mechanics. In the magnetic domain, the effort

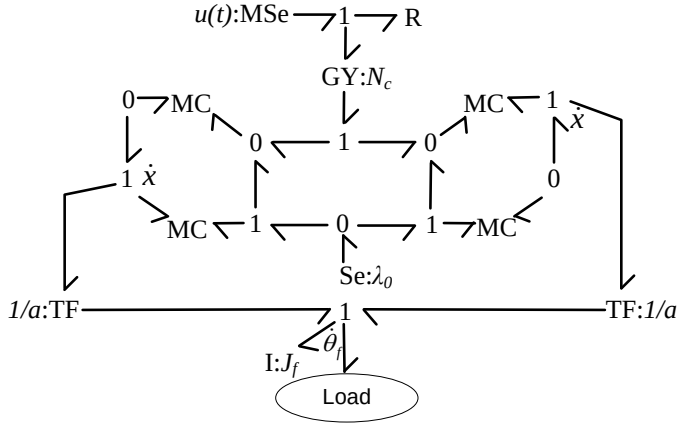

FIGURE 2.24: Bond Graph model of the torque motor

in a Bond Graph model is related to the magnetomotive force λ, while the flow is corresponding to the derivative of the magnetic flux $\dot{\phi}$. From equation (2.44), we can notice that the constitutive law complies with that of the capacitive element in which the magnetic effort $\lambda_0 \pm 2N_c i$ can be expressed as a function of the generalized displacement ϕ. On mechanical side, equation (2.49) is taken into account; it implies that the mechanical effort F_i is a function of the magnetic flux related to the mechanical displacement x. Thus, 2-port capacitive elements are used for coupling the magnetic and mechanical domains. Figure 2.24 illustrates the Bond Graph model of the torque motor.

2.4.4 Entire model of the servovalve

Having developed the Bond Graph models of each part of the servovalve, we can now establish connections between these models. To properly model the coupling between the hydraulic and mechanical domains, 2-port R-elements modulated by the spool or flapper displacement are used for representing the pressure drop at one port and the hydraulic jet force at the other (figure 2.25). Besides, TF-elements are used for modelling the conversion between hydraulic and mechanical power. In addition, the system contains an electric feedback corresponding to the spool position measurement. The Bond Graph of the entire system including the power exchanges between the different subsystems is finally shown in figure 2.26.

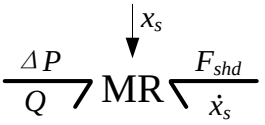

FIGURE 2.25: 2-port MR-element

2.4.5 Simulation results and validation

According to the Bond Graph approach, we have defined a simulation model of the servovalve using the AMESim software where all the phenomena are represented with respect to the former Bond Graph model (see figures 2.27 and 2.28).

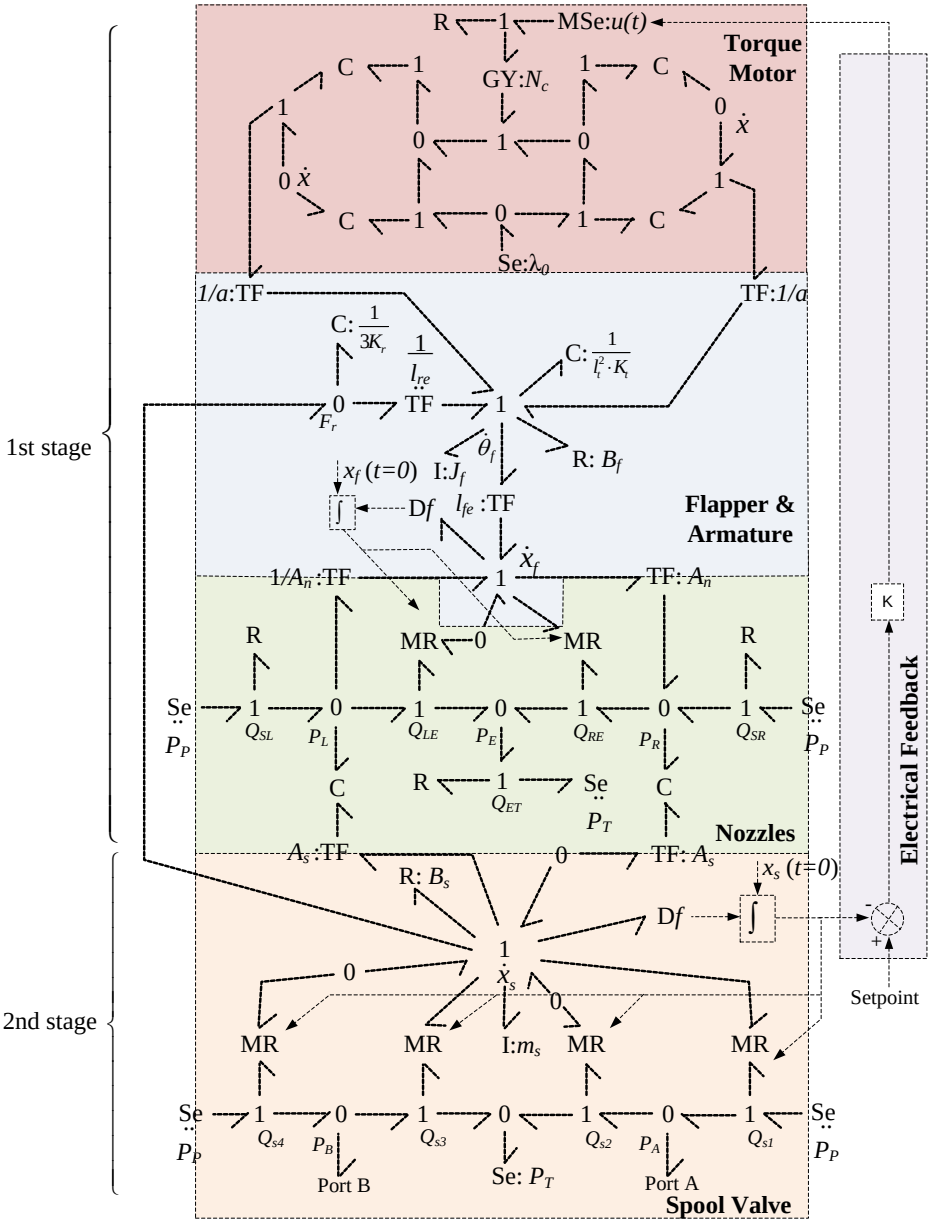

FIGURE 2.26: Bond Graph model of the servovalve

The parameters used in the AMESim model are:

1) Values provided by the manufacturer, e.g. spool drive area A_s;
2) Values derived from the calculation, e.g. feedback needle and flexible tube constant K_r, K_t;
3) Estimated values from the experimental data about the static characteristics, e.g. parameter values of the flow model (2.28);
4) Empirical values, e.g. viscosity is the spool valve B_s.

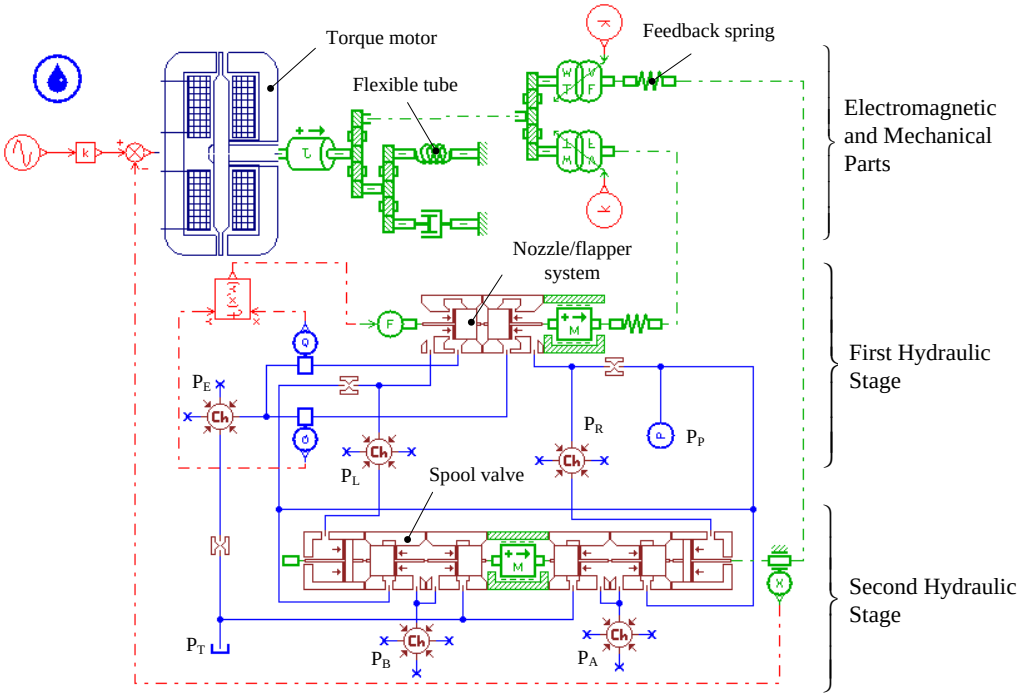

FIGURE 2.27: AMESim model of the servovalve

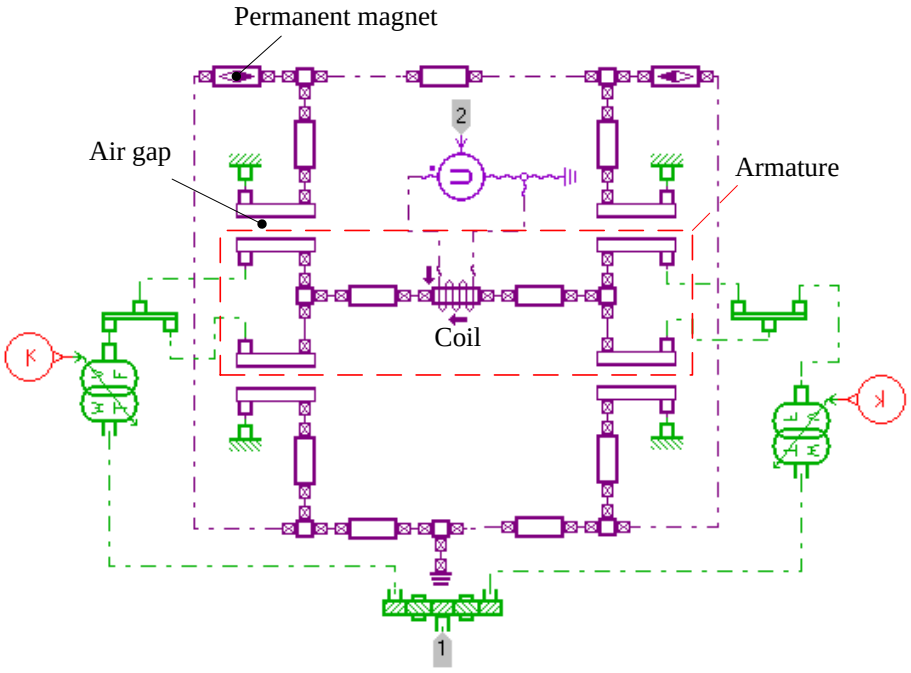

FIGURE 2.28: AMESim model of the torque motor

The simulation is conducted with zero output flow rates Q_A and Q_B, i.e. the ports A and B closed. The input signal applied is 40% and 100% of the nominal command (equals to 10 V) in a frequency range between 1 and 500 Hz. Finally,

the simulations are compared with experimental results obtained from the manufacturer as presented in figure 2.29.

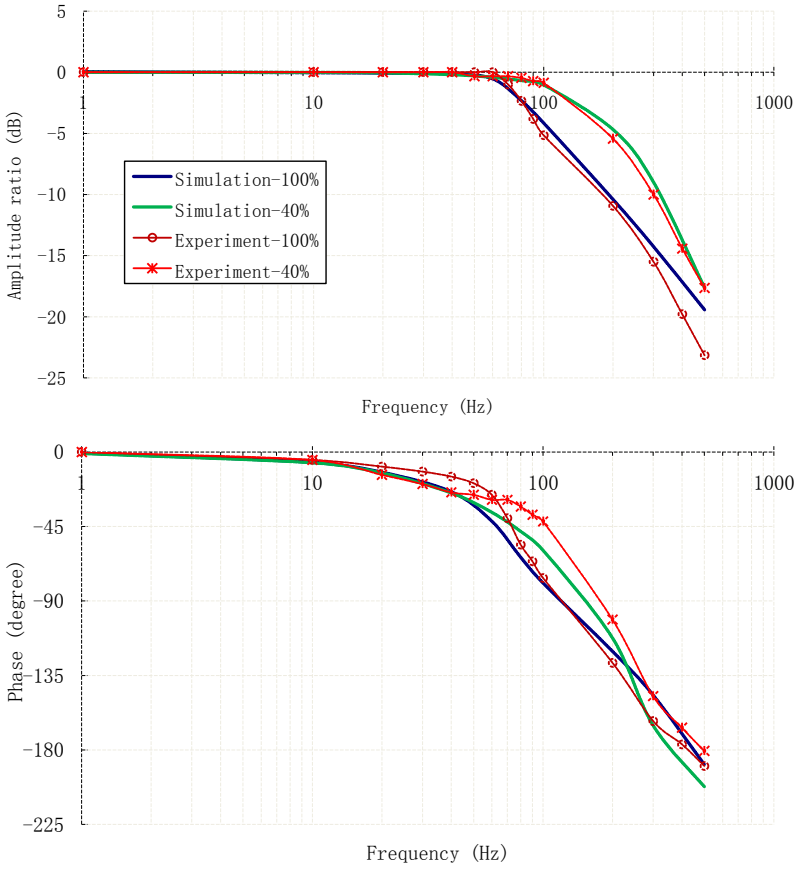

FIGURE 2.29: Frequency response: experiment and simulation

For the dynamic characteristics, we can remark that the simulated magnitude and phase (see figure 2.29) show a good agreement with the experimental result at low frequency. However, a larger error is observed at about 100 Hz, especially for the phase. The maximum amplitude error is less than 5 dB, whereas the maximum phase error reaches nearly 20°. This could be explained in several aspects:

1) influence of the transverse vibration mode of the flapper at high frequencies,

2) no information about the internal control law of the servovalve,

3) phase shift raised by the LVDT position sensor.

However, the dynamic model illustrates accurately the dynamic behaviours of the servovalve on a range from 0 to 100 Hz. Despite a certain phase error, it is still valid up to 500 Hz, in particular for 100% of the control input.

2.5 Conclusion

In this chapter, we firstly have analyzed the static characteristics of the two-stage servovalve. The flows both in the flapper valve and in spool valve were carefully studied. More specifically, we proposed a flow model of the spool valve by considering in details the flows in transitional region. This model increases the flow estimation accuracy compared with previous models. After identifying the parameters of the proposed model, the simulation results of the pressure gain and leakage characteristic presented a good agreement with measurements.

To characterize the dynamic behaviours of the servovalve, we then studied and modelled the flapper/nozzle system, the spool valve, and the torque motor using the Bond Graph approach. We showed that an accurate model for a wide range of frequency and spool displacements can be obtained with a fully physical approach, that is to say the knowledge of all relevant constitutive equations and physical parameters. Finally, we have implemented a simulation model of the servovalve in AMESim based on the Bond Graph analysis and the defined structure of the energy exchanges in and between the different subsystems. The comparison of the frequency responses obtained in simulation and experiments shows a good reliability of the proposed Bond Graph model. This model is fully validated at low frequencies, meanwhile, it is still applicable at high frequency application as the modelling errors are acceptable. To conclude, in this chapter we achieve the first goal of the modelling part, that is the development of a virtual model of the servovalve valid in a wide range of frequency and spool displacement.

Chapter 3

Dynamic effect of the manifold

Contents

3.1 Introduction

In a typical hydraulic control system, the displacement of the actuator is piloted via a control element, such as a servovalve, which is connected to the actuator by an manifold. Moreover, most of the other hydraulic components required by the application are also installed on this manifold, for example accumulators, pressure

sensors, solenoid valves, flow reducers, etc.. This can lead to complex manifolds, which may influence the whole system dynamics. Figure 3.1 shows the configuration of the inner circuit of the manifold in our test rig. The oil from the hydraulic pump is guided into the manifold after a filter, and then redirected towards the servovalve. Controlled by the servovalve, the flow is supplied to the actuator through the manifold. Besides, the manifold enables the system to alternate between three different working modes via the commutation of two solenoid valves (V1 and V2):

- Mode 1: a single 4-way servovalve to control the actuator;
- Mode 2: two 4-way servovalves in parallel to control the actuator;
- Mode 3: two 4-way servovalves with each servovalve used as a 3-way component to control the flow in one actuator chamber each.

According to the working mode, the oil flows in different passages and crosses several inner tubes.

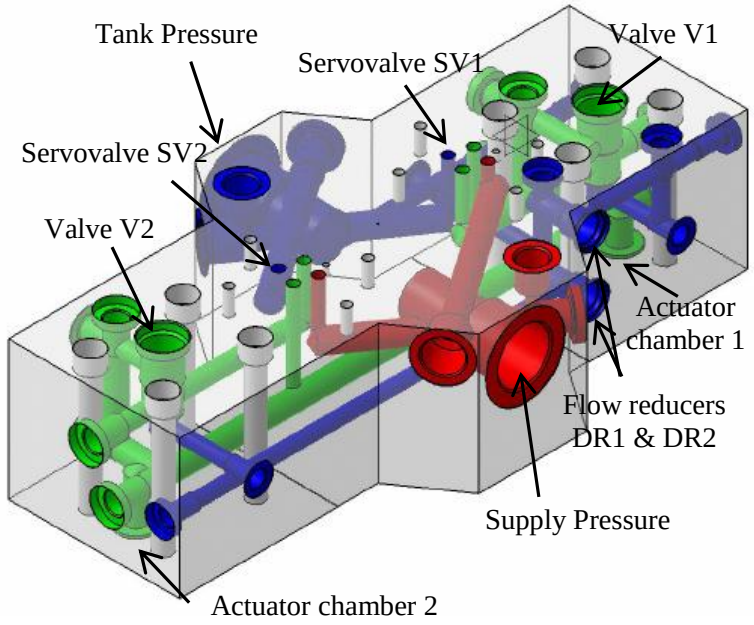

FIGURE 3.1: Configuration of the inner tubes of the manifold

Most of previous studies dealing with the dynamics analysis of hydraulic servovalves and actuators make the assumption that the effect of the manifold could be neglected [Merritt 1967, Sohl 1999, Sekhavat 2004, Zeng 2008, Choux 2010].

This assumption is reasonable for most of the conventional applications at low frequency. But for high frequency systems, this assumption becomes invalid and leads to inaccurate results. The total inner volume of the manifold under consideration reaches 0.2 liter. Compared to the total actuator volume of 0.3 liter, it would influence the dynamics behaviour of the hydraulic system at high frequencies. Therefore, it makes sense to establish a dynamic model of the manifold in the aim to integrate it into the whole system model. This would be helpful to study the performances of the hydraulic control system at high frequencies. The main contribution of this chapter is to focus on the modelling of the manifold and to show how it may influence the hydraulic performances due to induced losses, compressibility and inertial effects. According to this study, the virtual model performance will be finally improved, especially at high frequencies where the effect of the manifold volume and that of the fluid inertia in the manifold are involved and have a significant effect.

The model of the manifold should deal with the flow energy losses which are very complex. In the field of the fluid dynamics, most problems yield to nonlinear and differential representations to get an accurate result. A first way to calculate these losses is to use the Computational Fluid Dynamics (CFD) analysis. This numerical approach is based on the discretization of space and time, the continuous variables being turned to a finite set of nodal values and interpolating functions. Then, the original problem becomes an algebraic one that can be solved numerically. This method has been applied here for calculating the pressure drop in the different flow passages in the manifold. However, the CFD simulation is still not usable for the simulation of the dynamics of such a system [Ferziger 1996, Sorensen 1999].

This chapter proposes then a method to obtain the losses parameters of the lumped-parameter model of the manifold based on the Bond Graph representation. It consists in considering that the inner circuits of the manifold are made up of associations of basic hydraulic resistance elements such as tubes, bends and bifurcations. The energy losses are then calculated using formulae and abacuses from literature for determining the pressure loss coefficients for each basic element

[Idelchik 1994, Filonenko 1948]. In the following, this method is called "abacus-based method" (ABM). The CFD method is then used to bring a comparison and validate the results of the proposed method.

In order to take the dynamic effect of the manifold into consideration, Section 2 of this chapter will describe the modelling approach applied to represent accurately the manifold. Section 3 will introduce CFD and abacus-based methods to find the function of the energy dissipation due to the fluid flow in the manifold, and their results will be compared. Section 4 and 5 will study respectively the compressibility and inertial effects of the manifold. Finally, section 6 will give some conclusions.

3.2 Modelling of the manifold

All components are connected on the manifold which guides the fluid flow according to the selected mode. The control of the solenoid valves V1 and V2 allows the system to switch between the three working modes as described in the introduction.

As shown on its hydraulic schematic (see figure 1.3), when both solenoid valves are in ON-position and the control input of one servovalve is set to 0, the control of the actuator corresponds to conventional hydraulic applications: control by a 4-way servovalve (mode 1). However, in this configuration, both servovalves can be simultaneously controlled, this lead to a parallel 4-way mode which can provide a greater flow rate to the actuator (mode 2). Finally, when both solenoid valves are in OFF-position, the servovalves are used in 3-way mode, i.e., only one outlet port of each servovalve is connected to a chamber of the actuator (mode 3). These two last modes enable the use of multivariable control strategy.

The analysis done in this chapter focuses on the study of this manifold circuit connecting the outlet ports A and B of the servovalves and the ports V_1 and V_2

of the actuator. Two bifurcations N_1 and N_2 are involved. Five passages are then taken into consideration:

1) Passage A_i-N_i: from the port A_i of servovalve SVi to the bifurcation N_i;
2) Passage N_i-V_i: from the bifurcation N_i to the port V_i of the chamber of the actuator;
3) Passage B_i-C_i: from the port B_i of the servovalve SVi to port C_i of the solenoid valve Vi;
4) Passage C_i-N_j: from the port C_i of the solenoid valve Vi (when the valve is ON) to the bifurcation N_j;
5) Passage C_i-P_T: from the port C_i of the solenoid valve Vi (when the valve is OFF) to the tank (passing through the flow reducer).

The diagram of the distribution of passages is presented in figure 3.2.

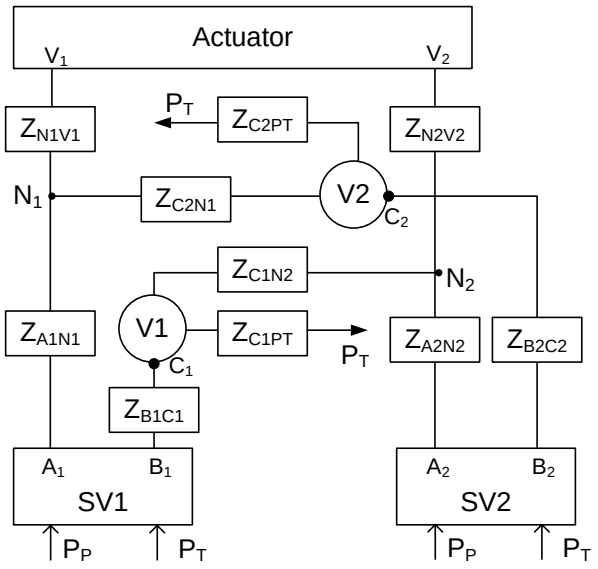

FIGURE 3.2: Diagram of the different passages of the manifold

While considering only the effect of the manifold, the influence of the losses in solenoid valves and flow reducers are neglected as the flow passes through these components without bend or section change.

Each passage (noted Z in figure 3.2) is modelled considering three effects: the energy dissipation (pressure drop), the compressibility, and the fluid inertia. They

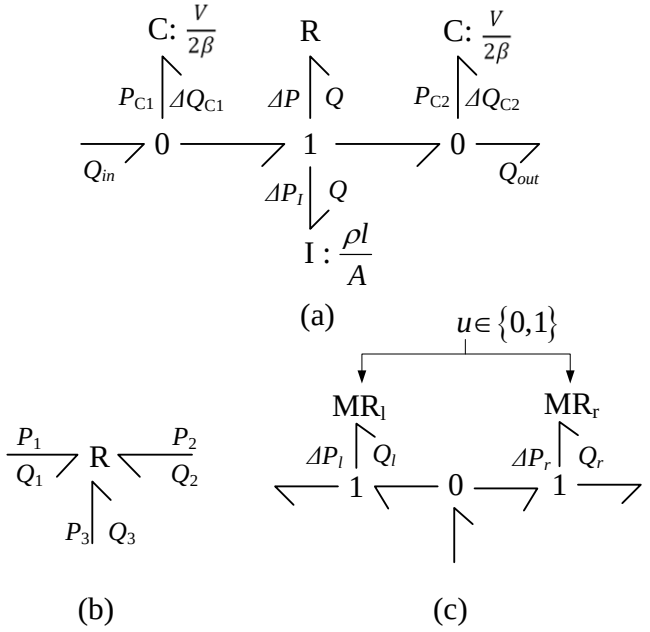

FIGURE 3.3: Bond Graph model of (a) a passage, (b) a bifurcation and (c) a valve

can be considered as non linear impedances that enable the representation of the first frequency mode for each passage.

Figure 3.3(a) shows the corresponding Bond Graph representation of a passage. The energy dissipation effect is represented by R-elements, all energy losses throughout each part of the passage being considered as a single equivalent pressure drop. These losses include the singular losses due to the local geometry (change of direction or flow area), and the frictional losses caused by the fluid viscosity. The total energy loss can be expressed as a function of the flow rate (3.1):

$$\Delta P = f(Q) \tag{3.1}$$

This relation will be fully developed in the following section by the means of CFD analysis and ABM (Abacus-Based Method).

The fluid compressibility effect is represented by capacitive elements (C-elements) placed on both sides of the R-element, splitting the fluid volume of the passage into two identical volumes for model causality reasons. The constitutive equation

of these C-elements can be written as

$$\frac{dP_{Ci}}{dt} = \frac{2\beta}{V} \cdot \Delta Q_{Ci} \tag{3.2}$$

where β is the bulk modulus, and V is the whole passage volume.

The fluid inertia effect (I-element) is related to the kinetic energy of the fluid in the passage under consideration. The corresponding constitutive relationship is given by

$$\frac{dQ}{dt} = \frac{A}{\rho l} \cdot \Delta P_I \tag{3.3}$$

where l is the passage length, and A is the equivalent section area derived from the ratio of the passage total volume and length.

A bifurcation N combines two passages together. This component can be represented by a 3-port R-element as shown in figure 3.3(b). No matter which two flow rates among the three are given, the pressure drop can be calculated according to abacus-based method according to the geometric dimensions of the bifurcation. Details will be given in the next section.

Due to the choice made for the solenoid valves, the pressure losses in these components can be neglected, and they are considered to have ideal properties. As shown in figure 3.3(c), each valve is modelled by a modulated resistor (MR-element) which is controlled by a two-state command ($u \in \{0, 1\}$). The constitutive equations of the MR-elements (see figure 3.3(c)) are as follows:

$$\begin{cases} Q_l = 0, & u = 0 \\ \Delta P_l = 0, & u = 1 \end{cases} \quad \text{and} \quad \begin{cases} \Delta P_r = 0, & u = 0 \\ Q_r = 0, & u = 1 \end{cases} \tag{3.4}$$

Equation (3.4) implies that the flow passes through the left-side MR-element with no energy loss for $u = 1$, whereas the losses become infinite, namely there is no fluid flowing through this element, for $u = 0$. The equation of MR-element on the right side takes the same values but for the opposite command values in (3.4).

Finally, the Bond Graph model (figure 3.4) of the manifold is established by integrating all passages and bifurcations models. In this model, the compressibility and inertia effects of the passage Z_{A1N1} are neglected due to its small volume (nearly $2 \cdot 10^{-6}$ m^3).

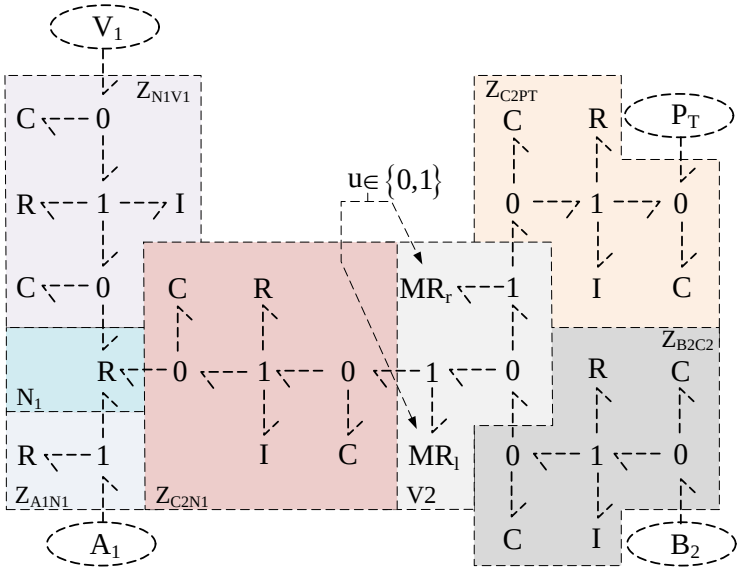

FIGURE 3.4: Bond Graph model of the manifold for controlling chamber 1 of the actuator

3.3 Energy dissipation calculation by abacus-based and CFD methods

The relationship between the flow rate and the pressure drop is complex in hydraulic systems. The energy dissipation depends not only on the local geometry and the fluid properties, but also on the Reynolds number, which is a function of the flow velocity. It does not exist a unified formula valid for all cases. The CFD analysis enables to obtain the energy dissipation in the manifold but this method is difficult to apply for a lumped parameter approach. Indeed, boundary conditions to be set in the numerical model are not straightforward for the inner passages as these conditions change according to what happens in all the other passages. CFD is used here only to validate the results of the abacus-based method. This is

done by comparing flow rates and pressure drops characteristics for each passage and their combinations.

The CFD approach is used to determine the relationship of the flow rates and pressure drops with 3D geometric models. All passages mentioned in the previous section are exactly modelled and meshed.

3.3.1 Energy dissipation calculation by abacus-based method (ABM)

For the abacus-based approach, each passage under study is divided into basic hydraulic resistances, such as tubes, bends and bifurcations. The pressure drop of each basic element is calculated from the following equation:

$$\Delta P_{\text{total}} = \zeta_{\text{total}} \cdot \frac{\rho w_e^2}{2} = \zeta_{\text{total}} \cdot \frac{\rho}{2} \cdot \left(\frac{Q}{A_e}\right)^2 \tag{3.5}$$

where

- ζ_{total} is the global pressure loss coefficient of a resistance element;
- w_e is the flow velocity in the element;
- A_e is the section area of the element.

The global pressure loss coefficient depends on the flow conditions defined by the Reynolds number, and on the shape of the resistance element. For the calculation of the pressure drop, it is just necessary to determine the global pressure loss coefficient by applying the empirical formulae or abacuses given in the literature [Idelchik 1994, Filonenko 1948].

For example, [Idelchik 1994] gives the following empirical formula for an element formed by two bends of same section area A_e assembled at an angle of 90° (figure 3.5):

$$\zeta_{\text{total}} = C_l \zeta_M + \zeta_f \tag{3.6}$$

where

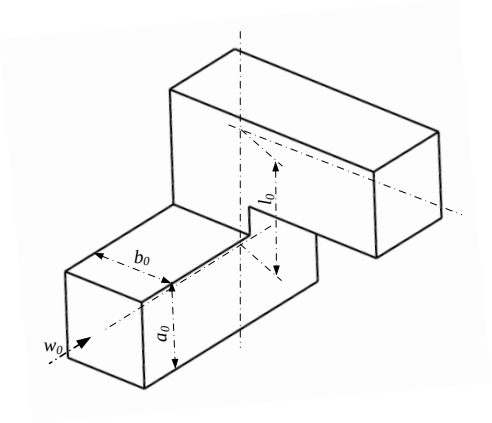

FIGURE 3.5: Element formed by two bends assembled at an angle of 90°

- C_l is a constant depending on the form of the tube;
- ζ_M is the frictional loss coefficient due to the fluid viscosity;
- ζ_f is the singular loss coefficient in the local resistance place.

C_l and ζ_M are obtained according to the abacuses in [Idelchik 1994], whereas ζ_f is given by the Hagen-Poiseuille law:

$$\zeta_f = \frac{64}{\mathrm{Re}} \cdot \frac{l_0}{D_h} \tag{3.7}$$

where l_0 is the distance between the axes of two consecutive bends, and D_h is the hydraulic diameter of the tube. Finally, the pressure drop for this element can be calculated by (3.5).

The total pressure drop in a passage is the sum of all the pressure drops coming from the serial association of elementary hydraulic resistances. This calculation is illustrated for the passage Z_{C1N2} in figure 3.6 and tables 3.1 and 3.2.
Figure 3.6(a) shows the geometry of the passage Z_{C1N2} which can be divided into five elementary hydraulic resistances, i.e. three straight tubes, two junctions. The characteristic parameters are calculated based on geometry, as well as the total loss coefficients using the abacuses carefully chosen according to the Reynolds number (see table 3.1). Finally, a set of pressure drop values is given as a function of flow (table 3.2) which is plotted in figure 3.6(b).

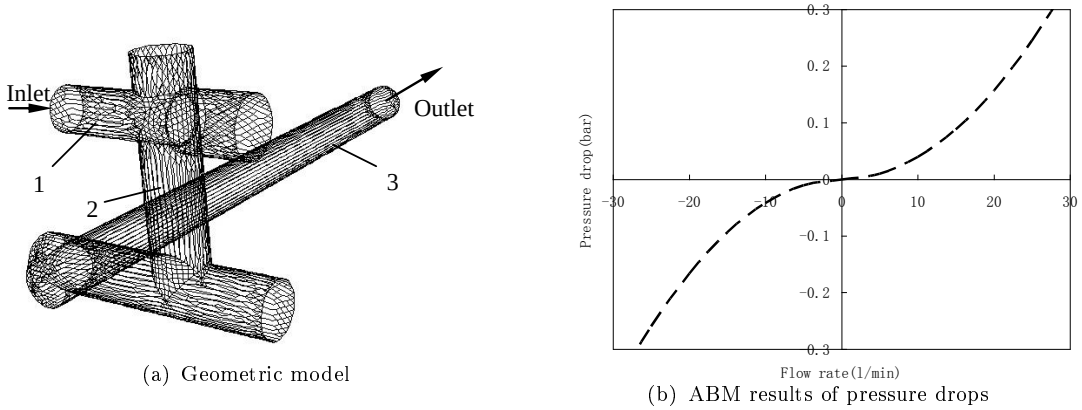

(a) Geometric model

(b) ABM results of pressure drops

FIGURE 3.6: Energy dissipation calculation for the passage Z_{C1N2}

TABLE 3.1: Calculation of the pressure loss coefficient according to ABM

No.	**Resistance composition**	**Type of resistance**	**Principal dimensions**	**Characteristic parameter**	ζ_{total}
1	tube 1	straight tube	len.:$l_1 = 28$mm dia.:$D_1 = 12$mm	$\frac{l_1}{D_1} = 2.33$	$\frac{64}{\text{Re}}\frac{l_1}{D_1} = \frac{149.1}{\text{Re}}$
2	tube 2	straight tube	len.:$l_2 = 46$mm dia.:$D_2 = 15.2$mm	$\frac{l_2}{D_2} = 3.03$	$\frac{64}{\text{Re}}\frac{l_2}{D_2} = \frac{193.9}{\text{Re}}$
3	tube 3	straight tube	len.:$l_3 = 212$mm dia.:$D_3 = 15$mm	$\frac{l_3}{D_3} = 14.13$	$\frac{64}{\text{Re}}\frac{l_3}{D_3} = \frac{904.3}{\text{Re}}$
4	junction of tube 1 & 2	resistance with 2 bends at 90°	tube 1 dia.:D_1 tube 2 dia.:D_2 axis dist.:$l_4 = 5$mm	$\frac{l_4}{D_1} = 0.42$ [b]	$2.44 \times 1.2 + \frac{64}{\text{Re}}\frac{l_4}{D_1}$
5	junction of tube 2 & 3 [a]	resistance with 2 bends at 90°	tube 2 dia.:D_2 tube 3 dia.:D_3 axis dist.:$l_5 = 45$mm	$\frac{l_5}{D_3} = 3$ [b]	Q from 2 to 3: $3.17 + \frac{64}{\text{Re}}\frac{l_5}{D_3}$ Q from 3 to 2 [c]: $3.17 \times 1.2 + \frac{64}{\text{Re}}\frac{l_5}{D_3}$

a. The losses of the tube between 2 and 3 are considered in those of the junction.

b. As an approximation, the smallest value of both diameters is taken for calculation.

c. Bend with recess.

TABLE 3.2: Calculation of the pressure drop

Q (L/min)	**Pressure drop** (bar): $\Delta P = \zeta_{\text{total}} \cdot \rho/2 \cdot (Q/A_e)^2$					
	Elem. 1 A_e:113.1mm^2	**Elem. 2** A_e:181.5mm^2	**Elem. 3** A_e:176.7mm^2	**Elem. 4** A_e:113.1mm^2	**Elem. 5** A_e:176.7mm^2	ΔP_{total}
30	0.00748	0.00478	0.02320	0.24455	0.11236	0.39237
20	0.00499	0.00318	0.01547	0.10899	0.05097	0.18360
10	0.00249	0.00159	0.00774	0.02747	0.01352	0.05281
0	0	0	0	0	0	0
-10	-0.00249	-0.00159	-0.00774	-0.02747	-0.01592	-0.05521
-20	-0.00499	-0.00318	-0.01547	-0.10899	-0.06055	-0.19318
-30	-0.00748	-0.00478	-0.02320	-0.24455	-0.13389	-0.41391

3.3.2 Comparison with the CFD results

The CFD approach is used here to determine the relation between flow rates and pressure drops with 3D mesh models. The passages mentioned in the previous section were modelled and meshed in the CFD software Fluent. For a single-input and single-output passage, the constant pressure input and output were chosen as the boundary conditions in order to reach a given pressure drop. For those with multiple inputs or multiple outputs, such as bifurcations and passages containing a bifurcation, constant speed inputs and pressure outputs have been set as boundary conditions so that the flow rate distribution in each circuit of the passage can be easily controlled. As the Reynolds number in the manifold is normally less than 5000, the flow was considered as a laminar flow to improve the calculation efficiency.

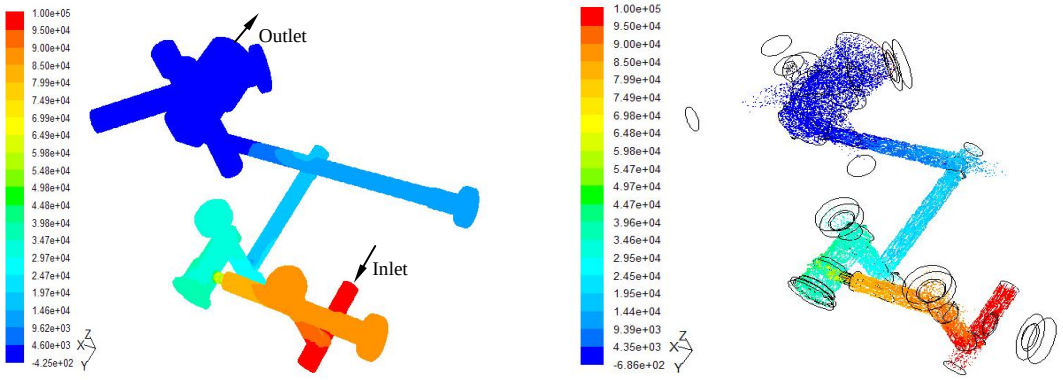

(a) Total pressures profile (b) Velocity evolution

FIGURE 3.7: Total pressures profile and velocity evolution of the passage Z_{C1PT} in CFD analysis

Figure 3.7 presents the distribution of total pressures and velocities in the passage Z_{C1PT} obtained from the CFD. The figure shows that the singular losses are predominant, as the flow twists violently at those places. Compared to the singular losses, the friction (regular losses) in tubes can be nearly neglected. The magnitude of the total losses in a passage is in this case mainly equivalent to the sum of the singular losses.

Figure 3.8 presents several comparisons of the CFD and ABM results for the four main passages in the manifold. Both methods introduce approximately the same

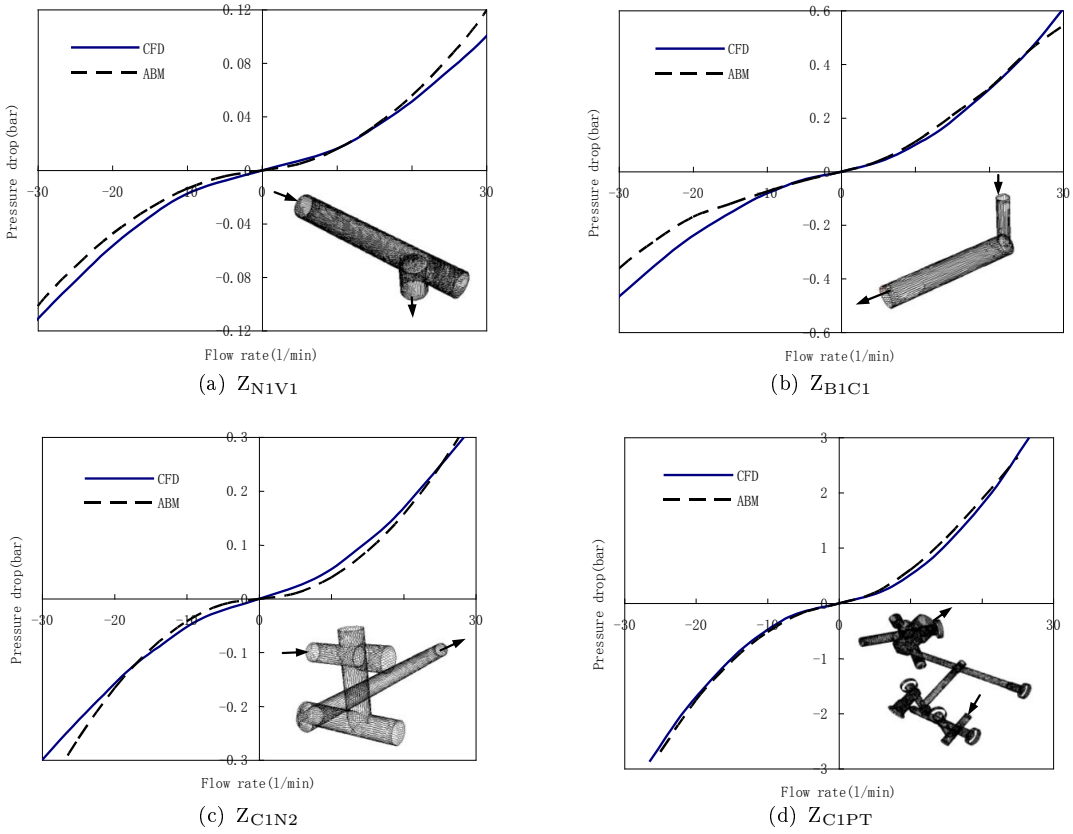

(a) Z_{N1V1} (b) Z_{B1C1}

(c) Z_{C1N2} (d) Z_{C1PT}

FIGURE 3.8: CFD and ABM results of pressure drops in each passage

evolution of the pressure drop as a function of the flow rate. At low Reynolds numbers, the results of the two methods are in very good agreement. However, non negligible differences between the two methods appear when the Reynolds number increases. It is especially the case for the models made up of a small number of resistance elements, as in figures 3.8(a) and 3.8(b). These differences arise due to the following reasons:

1. The outlet flow port of the geometry is close to bend or some section change that may have effect on the flow behaviour as shown in figure 3.8(a). As a result, the flow is not fully developed when it passed through these places. The pressure drop obtained from CFD analysis is thus less than the one calculated from the ABM which assumes decoupled conditions.
2. The distribution of the velocity field at inlet port is not properly set. The evolution of the velocity field in the tube causes additional energy losses.
3. The cases described in the literature (abacus) do not exactly fit ours. They are used as approximation, which could lead to errors.

4. The accuracy of the CFD analysis depends on the refinement of the model, the calculation method, and the flow regime. To get more accurate results, we could refine the mesh of the model or implement a turbulent method when the Reynolds number gets higher. But the computational time is significantly increased.

The two first effects become negligible when the energy dissipation is more important in the middle of the considered passage than at the ends as in Figure 3.8(d).

The global pressure drop can also be studied by summing all the elementary passages. A set of results of this total energy dissipation in the manifold including all the passages between servovalves (A_2, B_1) towards the actuator chamber volume V_2 in 4-way mode is also shown in figure 3.9. In this figure, the pressure drop is calculated between the port B_1 and V_2 according to the flow rate at port A_2. The analytic results coming from ABM involve losses of all related passages and bifurcations. They are in good agreement with the CFD results at low flow rates imposed at port A_2 of servovalve SV2 (see figure 1.3). As previously, larger differences are observed at high flow rates and can be explained by the stronger influence of the turbulent effects.

3.4 Compressibility effect in the manifold

The volume of fluid in the manifold between the servovalve and the actuator induces a compressibility effect. This effect will influence the dynamics of the whole system and decrease the hydraulic pulsation.

If the pressures in each passage are assumed to be identical, the volume effect of the manifold can be considered as an additional equivalent volume to each actuator chamber. The additional volume is the sum of the manifold volumes joint together. Therefore, although there is no flow in certain passages (Z_{C2N1} and Z_{B2C2}) in mode 1, the additional volumes in modes 1 and 2 are the same as they have the same

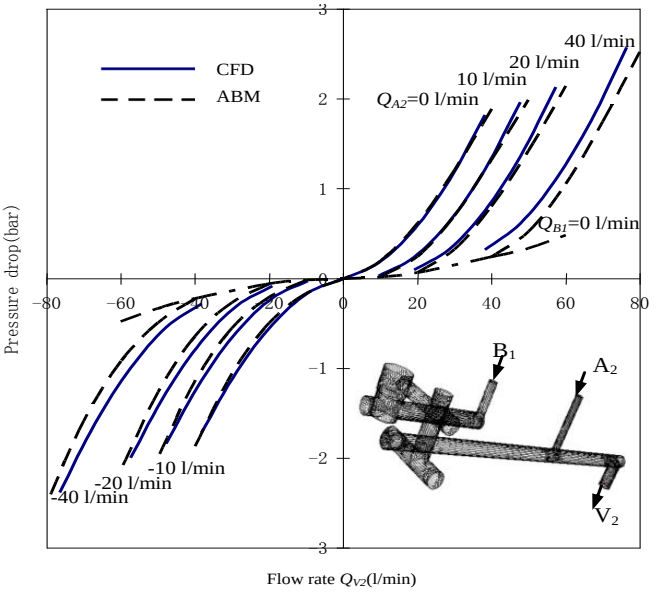

FIGURE 3.9: CFD and ABM results of pressure drop between B_1 and V_2 versus flow rates to or from V_2 in a passage from the servovalves to the actuator chamber volume V_2 (4-way mode) with various flow rates at port A_2

condition concerning the passage connection, i.e. the solenoid valves V1 and V2 in ON-position. Table 3.3 gives the calculated additional volumes for each of the three working modes.

TABLE 3.3: Additional volume of each flow circuit

Working mode	Mode 1	Mode 2	Mode 3
Additional volume 1 (m^3)	1.0041×10^{-4}	1.0041×10^{-4}	7.9754×10^{-5}
Additional volume 2 (m^3)	1.0041×10^{-4}	1.0041×10^{-4}	7.9754×10^{-5}

The additional volumes 1 and 2 correspond to the flow circuits from servovalve to the chamber V_1 and for servovalve to V_2 respectively.

Compared to the midstroke actuator volume of $1.56 \cdot 10^{-4}$ m^3, the volume in the manifold is more than half of it, and hence can not be neglected. This implies that the volume of fluid in the flow circuit has a significant influence on the system dynamics.

As illustrated in [Morse 1963], the hydraulic natural frequency of a linear-motion hydraulic actuator can be calculated as follows:

$$f_H = \frac{1}{2\pi}\sqrt{\frac{2\beta \cdot A^2}{V} \cdot \frac{2}{M}} = \frac{A}{\pi}\sqrt{\frac{\beta}{MV}} \tag{3.8}$$

with the hydraulic stiffness

$$k_H = \frac{2\beta \cdot A^2}{V} \tag{3.9}$$

where

- A is the active section area of the actuator;
- M is the mass of the moving part;
- V is the actuator total volume.

Equations (3.8) and (3.9) stand for the case where the actuator is at its mid-stroke position. For piston at an arbitrary position, the equations should be extended to be

$$f_H = \frac{1}{2\pi}\sqrt{\frac{k_{H1} + k_{H2}}{M}} \tag{3.10}$$

where

$$k_{Hi} = \frac{2\beta \cdot A^2}{V_{Ti}}, \quad i = 1,\ 2 \tag{3.11}$$

- V_{Ti} is the total equivalent volume of the actuator chamber i.

Figure 3.10 presents the evolution of the hydraulic natural frequency of the actuator with respect to the piston position. The results show that the additional volumes, introduced by the connection with the manifold, have an important effect on the evolution of the hydraulic natural frequency. The natural frequency decreases significantly. This frequency at the end of the actuator stroke falls sharply from 700 Hz to 273 Hz for modes 1&2, and to 297 Hz for mode 3. At mid-stroke, the natural frequency falls from 292 Hz to 228 Hz (modes 1&2) and to 238 Hz (mode 3).

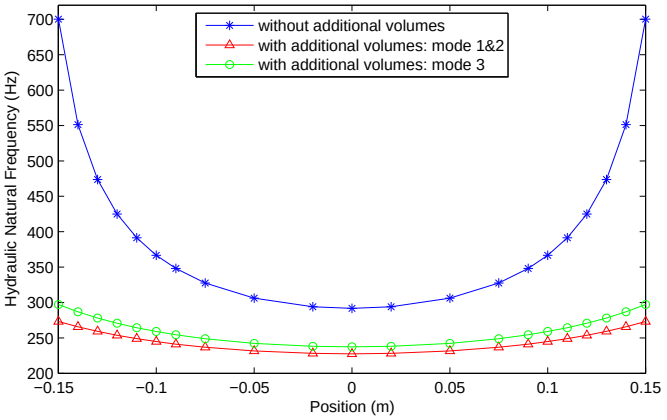

FIGURE 3.10: Evolution of the hydraulic natural frequency of the actuator according to piston position with the effect of the manifold volumes

3.5 Inertia effect study of the manifold

Although the mass of fluid in the manifold is not important, the inertia effect can not be ignored, especially for a high performance system with a large bandwidth. This is mainly due to the small tube section in the manifold. The smaller the section is, the larger the velocity of the flow is, and then kinetic energy has to be taken into account.

For ease of implementation of the manifold inertial effect into the dynamic model, and to demonstrate its importance, an equivalent mass of fluid in the manifold is added to the mass of the moving part of the actuator.

The kinematic energy of the hydraulic system is given by

$$E = \frac{1}{2}Mw^2 + \frac{1}{2}\rho V_{t1} w_{t1}^2 + \frac{1}{2}\rho V_{t2} w_{t2}^2 + \cdots \tag{3.12}$$

where

- w is the piston velocity of the actuator;
- V_{t1}, $V_{t2}, \cdots$ are the oil volume in tube 1, 2,$\cdots$;
- w_{t1}, $w_{t2}, \cdots$ are the oil velocity in tube 1, 2,$\cdots$.

Considering stationary conditions, the fluid velocity in the tube i can be calculated as follows:

$$w_{ti} = \lambda_{ti} \cdot \frac{A}{A_{ti}} \cdot w \tag{3.13}$$

with

$$\lambda_{ti} = \frac{Q_{ti}}{Q_{\text{total}}} \tag{3.14}$$

where

- λ_{ti} is the ratio of the branch flow rate to the total flow rate;
- Q_{ti} is the flow rate in the tube i;
- Q_{total} is the total flow rate entering into the actuator;
- A_{ti} is the tube i section area.

Then, equation (3.12) can be rewritten as

$$E = \frac{1}{2}\left(M + \rho V_{t1}\left(\lambda_{t1} \cdot \frac{A}{A_{t1}}\right)^2 + \rho V_{t2}\left(\lambda_{t2} \cdot \frac{A}{A_{t2}}\right)^2 + \cdots\right) \cdot w^2 \tag{3.15}$$

The equivalent mass of the fluid in the tube i is finally obtained from:

$$m_{ei} = \rho V_{t1}\left(\lambda_{t1} \cdot \frac{A}{A_{t1}}\right)^2 \tag{3.16}$$

Table 3.4 gives the calculated values of the total equivalent mass in each working mode. Here, all the calculations are made under the assumption that in mode 2 where two servovalves are used in parallel, the output flow rates of the servovalves are identical, i.e. λ_{ti} equals 0.5 in each branch passage.

TABLE 3.4: Fluid total equivalent mass in each working mode

Working mode	Mode 1	Mode 2	Mode 3
Total equivalent mass of fluid (Kg)	4.70	2.80	3.42

The moving part of the actuator has a mass M of 5.8 kg. Therefore, it can be noted that the fluid equivalent mass presented in table 3.4 is not negligible at all. This obviously leads to decrease the hydraulic natural pulsation, similarly to what we observed for the effect of volume in section 3.4. According to (3.10) and

(3.11), Figure 3.11 shows the evolution of the hydraulic natural frequency with consideration both of the volume and inertial effects in the manifold. The natural frequency values at the middle and end of stroke are listed in table 3.5.

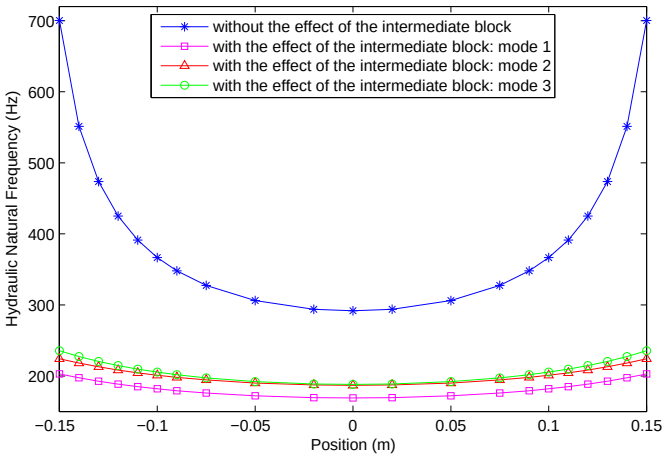

FIGURE 3.11: Evolution of the hydraulic natural frequency of the actuator with the effect of the manifold

TABLE 3.5: The natural frequency values (Hz)

Working mode	Mode 1		Mode 2		Mode 3	
	Middle	End	Middle	End	Middle	End
With only volume effect	227.5	273.1	227.5	273.1	237.3	297.1
With only inertia effect	216.8	520.5	239.6	575.1	231.4	555.5
With combined effect of the manifold	169.1	203.0	186.7	224.3	188.2	235.6
Without the manifold	291.7	700.3	291.7	700.3	291.7	700.3

Both volume and inertia effect influence significantly the dynamics of the actuator by decreasing the hydraulic natural frequency. The results show that the volume effect has a more important impact on the natural frequency at the end of the stroke, while the inertia effect gives a proportional decrease all along the stroke. When taking into account these phenomena in mode 2, the natural frequency drops from 292 Hz to 187 Hz at mid-stroke, and from 700 Hz to 224 Hz at stroke end.

3.6 Conclusion

This chapter has investigated the modelling of the manifold installed on our test bench. We show here that it will probably influence the performance of the hydraulic control system at high frequencies. A model including the compressibility effects, the fluid inertia, and the energy dissipation has been developed using the Bond Graph approach. Besides, an approach based on abacuses has been applied to determine the energy dissipation in each passage. The results have been validated by comparison with CFD analysis. The characteristics of the pressure drops versus flow rates were built, and gave the necessary parameters for the lumped parameter model of the manifold. Moreover, the compressibility and inertia effects of the manifold have been studied and the calculation illustrates that they can cause an obvious decrease of the hydraulic natural frequency, which means that the effects of the manifold take a significant influence on the system dynamics, particularly at high frequencies. This study constitutes original contribution of our PhD work and it justifies the hypotheses that will be assumed for the control model as the actuator natural frequency is highly reduced by the presence of the manifold.

Though this analysis and modelling of the manifold, we have achieved an essential step towards an accurate virtual prototype of our test bench. The modelling of the actuator being more conventional, the next chapter will focus on the experimental validation of the whole model of our test bench.

Chapter 4

Modelling and validation of the whole system

Contents

4.1 Modelling of the actuator

The actuator is a cylinder with hydrostatic bearing. It has a double rod and a circular front flange in order to connect to the mechanical chassis. The rod is equipped with two guide bearings, each with a floating seal (durable elements within the permissible radial forces). The oil leakages in these two bearings are

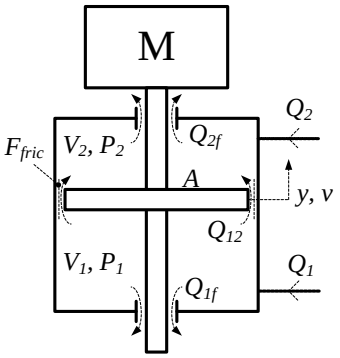

FIGURE 4.1: Schema of the actuator

channelled outwards and directed into the tank of the hydraulic power unit. The rod and piston are machined from a single piece. This piston consists of a bronze guiding surface adjusted to the cylinder tube and with a seal. As a result of this configuration, this type of cylinder provides a high system efficiency with no stick-slip phenomenon and low frictional forces.

To complete the virtual model of the test bench, we will finally consider the actuator, a double rod jack. The actuator is composed of two compressible volumes, and a movable mass (rod+piston) that separates the two volumes (figure 4.1). The inlet and outlet flows in the compressible volumes are related to the flow rates controlled by the two servovalves and the internal/external leakages. Due to these inlet and outlet flows, the fluid volume and mass in the actuator chamber vary, which causes a variation of the chamber pressure and leads to a linear displacement of the piston. Considering that the temperature and the bulk modulus β are constant, the flow balance can be written as

$$\begin{cases} \dfrac{V_1(y)}{\beta}\dfrac{dP_1}{dt} = Q_1 - Q_{12} - Q_{1f} - A\dfrac{dy}{dt} \\ \dfrac{V_2(y)}{\beta}\dfrac{dP_2}{dt} = Q_2 + Q_{12} - Q_{2f} + A\dfrac{dy}{dt} \end{cases} \tag{4.1}$$

where

- Q_1, Q_2 are the modulated flows from the servovalves;
- Q_{1f}, Q_{2f} are the external leakages from the actuator chamber 1 & 2 respectively;
- Q_{12} is the internal leakage from the chamber 1 to the chamber 2;

- $V_1(y)$, $V_2(y)$ are the volume of the chambers 1 & 2, defined by:

$$\begin{cases} V_1(y) = V_0 + A \cdot y \\ V_2(y) = V_0 - A \cdot y \end{cases} \text{ with } V_0 \text{ the initial volume;} \tag{4.2}$$

- y is the piston displacement;
- P_i is the pressure in chamber i.

According to the technical specification provided by manufacturer, the internal leakage Q_{12} is about 10^{-4} L/min, and the external leakages are negligible thanks to the hydrostatic bearings. Compared to the flow rates from the servovalves, which reach several litres per minute, the internal and external leakages can be ignored in order to simplify the control model in the control design. Then, for the control model, (4.1) is rewritten as

$$\begin{cases} \frac{V_1(y)}{\beta}\frac{dP_1}{dt} = Q_1 - A\frac{dy}{dt} \\ \frac{V_2(y)}{\beta}\frac{dP_2}{dt} = Q_2 + A\frac{dy}{dt} \end{cases} \tag{4.3}$$

The moving part is submitted to: 1) a driving force due to the static pressure difference between the two chambers, 2) the gravity caused by its vertical installation, 3) some friction forces, 4) an external force caused by the system load, and 5) the fluid inertia and gravity in each chamber. The dynamic of the mechanical part is then expressed by the following equation:

$$M\frac{d^2y}{dt^2} = A(P_1 - P_2) - Mg - F_{fric}(y, \dot{y}, P_1, P_2) - F_{ext} + F_{\text{fluid}} \tag{4.4}$$

where F_{fric} is the frictional force, which will be discussed in the following section; F_{ext} is the external force; F_{fluid} is the force caused by the fluid inertia and gravity in the actuator chambers.

According to (4.1) and (4.4), we can represent the Bond Graph model of the actuator as shown in figure 4.2. In this model, each actuator chamber is modelled by a

capacitive element with a constitutive parameter $V_{1\,or\,2}(y)/\beta$ modulated by the piston position, two transformers (TF-elements) representing the energy conversion between hydraulic and mechanical domains.

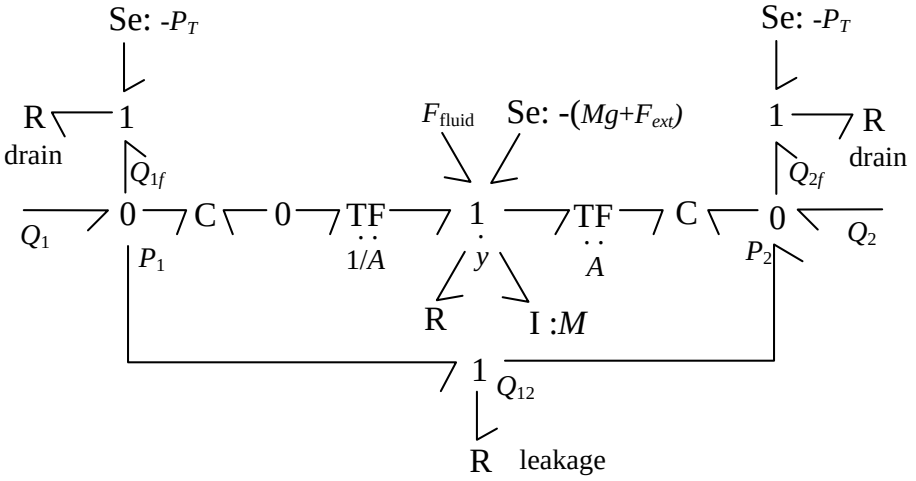

FIGURE 4.2: Bond Graph model of the actuator

4.2 Modelling of the friction force

A very critical aspect in the modelling of the actuator is related to the friction phenomena between the piston and the cylinder barrel. Actually, the actuator friction depends on several physical parameters, such as the roughness of the contact surfaces, the fluid viscosity, the chamber temperature, the relative velocity of the contact surfaces, the pressure difference between the two chambers, ... [Kühnlein 2012]. Thus, the friction phenomenon is difficult to identify and to analyze.

When analysing the friction phenomena, it has been shown that it can be defined by eight different regimes with respect to the relative velocity of the two contact surfaces [Sidhom 2011a]. Figure 4.3 illustrates the different friction types as a function of the relative velocity of the rubbing surfaces.

When the velocity increases, the different friction regimes are described below:
(1) The adhering regime is located in the interval [0, $v_{\min}^{+}$]. The contact between

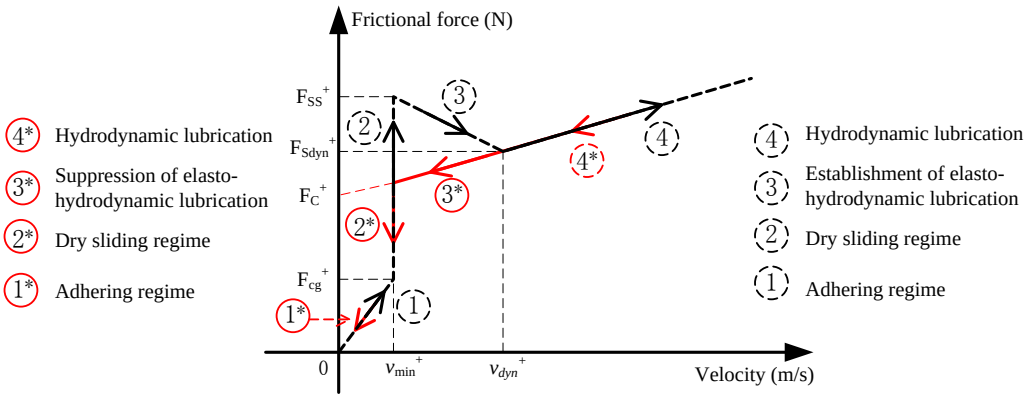

FIGURE 4.3: Different regimes in a cycle of the friction evolution [Sidhom 2011a]

the actuator piston and barrel surfaces remains a solid contact.

(2) The dry sliding regime is located at a given velocity v_{min}^+. In this regime, the friction force is the resultant force applied to the system until it reaches the dry static friction force limit F_{SS}^+, whereas the relative velocity remains unchanged.

(3) The establishment of elasto-hydrodynamic lubrication occurs in the interval $[v_{\text{min}}^+,\ v_{\text{dyn}}^+]$. When the forces applied to the system is greater than the static friction force F_{SS}^+, the coefficient of friction decreases with the increase of the relative velocity and the oil film thickness between the contact surfaces. This regime is also called Stribeck effect.

(4) The hydrodynamic lubrication, or the viscous friction regime, takes place when the speed exceeds v_{dyn}^+. In this regime, the sliding surfaces are separated by a thick oil film, and the friction force is then proportional to the relative velocity as a result of the fluid viscosity.

When the velocity decreases, (4^*) the hydrodynamic lubrication decreases with the relative velocity. In the interval $[v_{\text{min}}^+,\ v_{\text{dyn}}^+]$, ($3^*$) the elasto-hydrodynamic lubrication disappears, and the dry sliding regime appears directly (2^*). When the force resultant applied on the system is less than the limit force F_{cg}^+, the adhering regime (1^*) arises.

There exists a large number of friction model [Karnopp 1985, Tustin 1947, Bo 1982, Sidhom 2011a] to describe the above phenomenon. For our test bench, previous works have already studied these phenomena [Sidhom 2011a] and we will use the friction model proposed by Sidhom, which represents quite well the

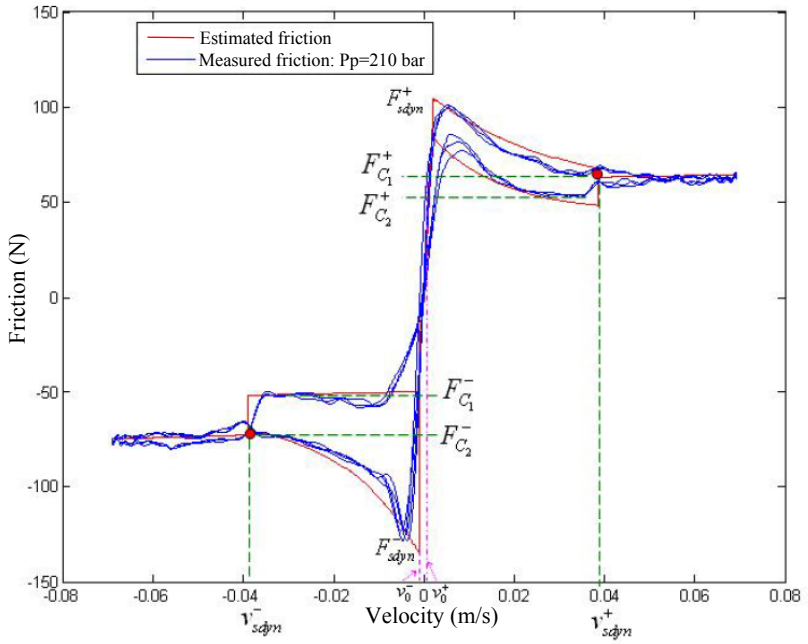

FIGURE 4.4: The estimated and measured friction in function of the velocity [Sidhom 2011a]

Stribeck effect and the viscous friction. This model is based on the Tustin model [Tustin 1947] which introduces an approximation of the transition between the elasto-hydrodynamic/hydrodynamic regimes by using an exponential form of the relative velocity (see equations (4.6) and (4.10)). An example of the friction estimation obtained with the model proposed by Sidhom is presented in figure 4.4. We can remark that the static dry friction regime is absent because the hydrodynamic bearing can establish an oil film even for very low velocity. This model is consequently given by:

For $v \in [v_0^-, 0[$:

$$F_{fric}(v) = K^- v \tag{4.5}$$

For $v \in [v_{sdyn}^-, v_0^-[$:

$$F_{fric}(v) = \begin{cases} F_{C1}^- + (F_{sdyn}^- - F_{C1}^-)e^{C_1^-(v-v_0^-)}, & a > 0 \\ F_{C2}^- + (F_{sdyn}^- - F_{C2}^-)e^{C_1^-(v-v_0^-)}, & a < 0 \end{cases} \tag{4.6}$$

For $v \in [v_{min}^e, v_{sdyn}^-[$:

$$F_{fric}(v) = F_{C2}^- + d^-(v - v_{sdyn}^-) \tag{4.7}$$

For $v \leq v^e_{min}$:

$$F_{fric}(v) = b^-(v - v^e_{min}) \tag{4.8}$$

For $v \in [0, v^+_0[$:

$$F_{fric}(v) = K^+ v \tag{4.9}$$

For $v \in [v^+_0, v^+_{sdyn}[$:

$$F_{fric}(v) = \begin{cases} F^+_{C1} + (F^+_{sdyn} - F^+_{C1})e^{C^+_1(v-v^+_0)}, & a > 0 \\ F^+_{C2} + (F^+_{sdyn} - F^+_{C2})e^{C^+_1(v-v^+_0)}, & a < 0 \end{cases} \tag{4.10}$$

For $v \in [v^+_{sdyn}, v^e_{max}[$:

$$F_{fric}(v) = F^+_{C2} + d^+(v - v^+_{sdyn}) \tag{4.11}$$

For $v \geq v^e_{max}$:

$$F_{fric}(v) = b^+(v - v^e_{max}) \tag{4.12}$$

where

- b is the viscous friction coefficient;
- a is the relative acceleration of the contact surfaces;
- F_C is the Coulomb friction;
- F_{sdyn} is the dry dynamic friction as a function of the chamber pressure;
- $[v^e_{min}, v^e_{max}]$ is the speed range during the experiments for which the low speeds (nearly ± 0.07m/s) lead to an important error in the viscous friction coefficient estimation;
- The other constants are introduced in figure 4.4.

The friction model described above is quite complex for the conception of control strategies. Thus, some assumptions were taken into consideration in [Sidhom 2011a]. For the control model, the hysteresis effect is neglected and it is assumed that the friction is symmetric with respect to the displacement direction. While conducting control strategy design, the dry friction force can be

simplified in using the following approximation:

$$F_{fs}(v) = \left(F_C + (F_{sdyn} - F_C)\, e^{-C\left|\frac{v}{v_0}\right|} \right) tanh\left(\frac{v}{v_0}\right) \tag{4.13}$$

4.3 Theoretic analysis of the frequency response of the actuator

According to the previous discussion, the dynamic of the actuator can be represented by

$$\begin{cases} \dfrac{dy}{dt} = v \\ \dfrac{dv}{dt} = \dfrac{A}{M}(P_1 - P_2) - g - \dfrac{F_{fric}(y, \dot{y}, P_1, P_2)}{M} - \dfrac{F_{ext}}{M} \\ \dfrac{dP_1}{dt} = \dfrac{\beta}{V_1(y)} \cdot (Q_1 - Q_{12} - Q_{1f} - A \cdot v) \\ \dfrac{dP_2}{dt} = \dfrac{\beta}{V_2(y)} \cdot (Q_2 + Q_{12} - Q_{2f} + A \cdot v) \end{cases} \tag{4.14}$$

To study the dynamics of the actuator, we propose here to discuss this problem by approximating the nonlinear equations by linear ones around an equilibrium point. To facilitate the dynamic study, we first take the following assumptions:

1) The external leakage is neglected, i.e. $Q_{1f}, Q_{2f} = 0$;
2) The actuator has same input and output flow rates, i.e. $Q_1 = -Q_2 = Q_v$, which ensure a single-input system;
3) The friction force is simplified by a sum of the viscous force $F_{viscous} = b \cdot v$ and the dry friction force F_{fs} defined by (4.13);
4) The internal leakage is assume proportional to the pressure difference between the chambers, i.e. $Q_{12} = K_{lk}(P_1 - P_2)$.

The previous assumption enable to reduce the number of system variables. The system variables are changed to $[y, v, \Delta P]$, where $\Delta P = P_1 - P_2$ replaces the

variables P_1 and P_2. Then, the system dynamic equations (4.14) are rewritten as

$$\begin{cases} \dfrac{dy}{dt} = v \\ \dfrac{dv}{dt} = \dfrac{A}{M} \cdot \Delta P - g - \dfrac{b}{M} v - \dfrac{F_{fs}(v)}{M} - \dfrac{F_{ext}}{M} \\ \dfrac{d\Delta P}{dt} = \left(\dfrac{\beta}{V_1(y)} + \dfrac{\beta}{V_2(y)} \right) \cdot (Q_v - K_{lk} \cdot \Delta P - A \cdot v) \end{cases} \tag{4.15}$$

At equilibrium, we have

$$\begin{cases} v_{eq} = 0 \\ \dfrac{A}{M} \cdot \Delta P_{eq} - g - \dfrac{b}{M} v_{eq} - \dfrac{F_{fs}(v_{eq})}{M} - \dfrac{F_{ext}}{M} = 0 \\ \left(\dfrac{\beta}{V_1(y_{eq})} + \dfrac{\beta}{V_2(y_{eq})} \right) \cdot (Q_{v,eq} - K_{lk} \cdot \Delta P_{eq} - A \cdot v_{eq}) = 0 \end{cases} \tag{4.16}$$

By solving the system (4.16), we obtain an equilibrium point with input $Q_{v,eq} = K_{lk} \cdot \Delta P_{eq}$ and state variables (y_{eq}, 0, $\frac{Mg+F_{ext}}{A}$), where y_{eq} can take any value within its definition field.

Linearizing the system (4.15) around the cylinder central position ($y_{eq} = 0$), that means around the equilibrium point (0, 0, ΔP_{eq}), yields

$$\begin{cases} \dfrac{dy}{dt} = v \\ \dfrac{dv}{dt} = \dfrac{A}{M} \cdot (\Delta P - \Delta P_{ep}) - \left(\dfrac{b}{M} + F_{sdyn} \right) v \\ \dfrac{d(\Delta P - \Delta P_{eq})}{dt} = \dfrac{2\beta}{V_0} (Q_v - Q_{v,eq}) - \dfrac{2\beta K_{lk}}{V_0} (\Delta P - \Delta P_{eq}) - \dfrac{2\beta A}{V_0} v \end{cases} \tag{4.17}$$

Let us define $p = \Delta P - \Delta P_{eq}$ and $q = Q_v - Q_{v,eq}$. Then, (4.17) is rewritten as

$$\begin{cases} \dfrac{dy}{dt} = v \\ \dfrac{dv}{dt} = \dfrac{A}{M} \cdot p - \left(\dfrac{b}{M} + F_{sdyn} \right) v \\ \dfrac{dp}{dt} = \dfrac{2\beta}{V_0} q - \dfrac{2\beta K_{lk}}{V_0} p - \dfrac{2\beta A}{V_0} v \end{cases} \tag{4.18}$$

Taking the Laplace transforms of (4.18),

$$\begin{cases} sY(s) = V(s) \\ sV(s) = \dfrac{A}{M} \cdot P(s) - K_{fr}V(s) \\ sP(s) = K_{hyd} \cdot (Q(s) - K_{lk} \cdot P(s) - A \cdot V(s)) \end{cases} \tag{4.19}$$

where $K_{fr} = \dfrac{b}{M} + F_{sdyn}$ is the friction gain, and $K_{hyd} = \dfrac{2\beta}{V_0}$ the hydraulic stiffness gain. Hence, the transfer function of the actuator around the equilibrium point is given by

$$\frac{Y(s)}{Q(s)} = \frac{\dfrac{A}{A^2 + M \cdot K_{lk}K_{fr}}}{s\left(\dfrac{1}{\frac{A^2K_{hyd}}{M} + K_{hyd}K_{lk}K_{fr}}s^2 + \dfrac{K_{hyd}K_{lk} + K_{fr}}{\frac{A^2K_{hyd}}{M} + K_{hyd}K_{lk}K_{fr}}s + 1\right)} \tag{4.20}$$

The transfer function (4.20) implies that, considering the position as output, the actuator is a third-order system. The transfer function of the velocity to the flow rate is then given by

$$\frac{V(s)}{Q(s)} = \frac{\dfrac{A}{A^2 + M \cdot K_{lk}K_{fr}}}{\dfrac{1}{\frac{A^2K_{hyd}}{M} + K_{hyd}K_{lk}K_{fr}}s^2 + \dfrac{K_{hyd}K_{lk} + K_{fr}}{\frac{A^2K_{hyd}}{M} + K_{hyd}K_{lk}K_{fr}}s + 1} \tag{4.21}$$

The static gain $G_{DC} = \dfrac{A}{A^2 + M \cdot K_{lk}K_{fr}}$ that determines the steady state response is associated with the piston active area, the mass of the moving part, and the damping effects. As the actuator has a low friction and small leakage, the static gain increases when the piston active area is reduced. The undamped natural frequency is $\omega_n = \sqrt{\frac{A^2K_{hyd}}{M} + K_{hyd}K_{lk}K_{fr}}$ which has a slight difference with the discussion in section 3.4 3.10 by considering the leakage effect and the friction force (K_{lk} and K_{fr}). These damping effects induce a slight increase of the natural frequency. The damping ratio is then defined by $\xi_v = \dfrac{K_{hyd}K_{lk} + K_{fr}}{2\omega_n}$.

Given the physical parameters, $G_{DC} = 1058$, $\omega_n = 1833$ rad/s, $\xi_v = 0.04$. The transfer function $\frac{V(s)}{Q(s)}$ have two poles, i.e. $s = -62 \pm 1181i$, which means that the

system is stable. The bode diagram of the actuator transfer function $\frac{V(s)}{Q(s)}$, as well as those with the effect of the manifold working in each of the three modes, are presented in figure 4.5.

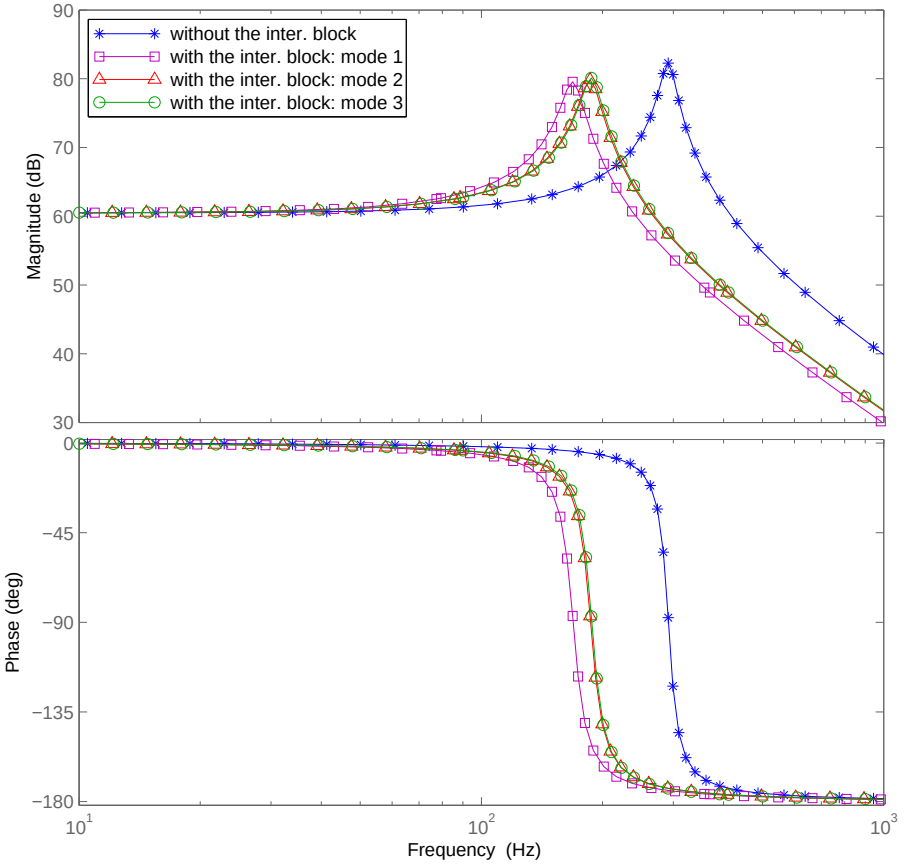

FIGURE 4.5: Bode diagram of the actuator

Due to the small friction of the hydraulic bearing, the frequency response of the actuator presents a notable resonance around its natural frequency. As demonstrated in the previous chapter, the dynamics of the manifold influences obviously on the actuator dynamic behaviour in high frequencies, which results in a decrease of the system bandwidth.

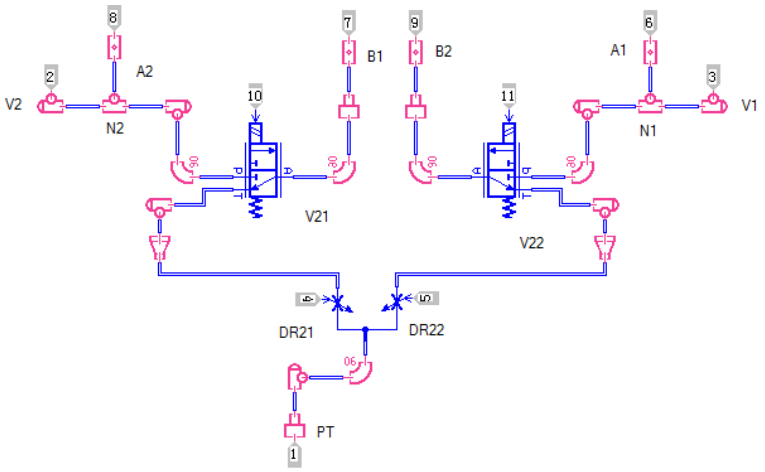

FIGURE 4.6: AMESim model of the manifold

4.4 Experimental results and validation

On the test bench, all the measured signals are collected on an analog conditioning unit, and then digitalized at a sampling rate of 1 kHz with 16 bits precision on a dSPACE acquisition board (model DS1104).

Besides, the effect of the manifold is also studied in simulation (AMESim). The actuator simulation model takes into account the leakage between the two chambers with a coefficient of 1×10^{-4} l/min/bar and the viscous friction with a coefficient of 400 N/(m/s). The AMESim model of the servovalves is the one introduced in section 2.4.5 and the AMESim model of the manifold is illustrated in figure 4.6. It is established by involving the passage arrangement with respect to the Bond Graph representation (figure 3.4). The virtual prototype of the whole test bench developed in AMESim is presented in figure 4.7. It integrates supercomponents for the manifold and the servovalves. The temperature of the system and the bulk modulus are assumed constant during the simulation.

4.4.1 Results in time domain

Simulations and experiments are conducted with a step signal in time domain. This step signal has an amplitude of ± 10 mm. The controller is a classic proportional regulator (4.22) with a proportional gain of 1169 V/m. The simulation and

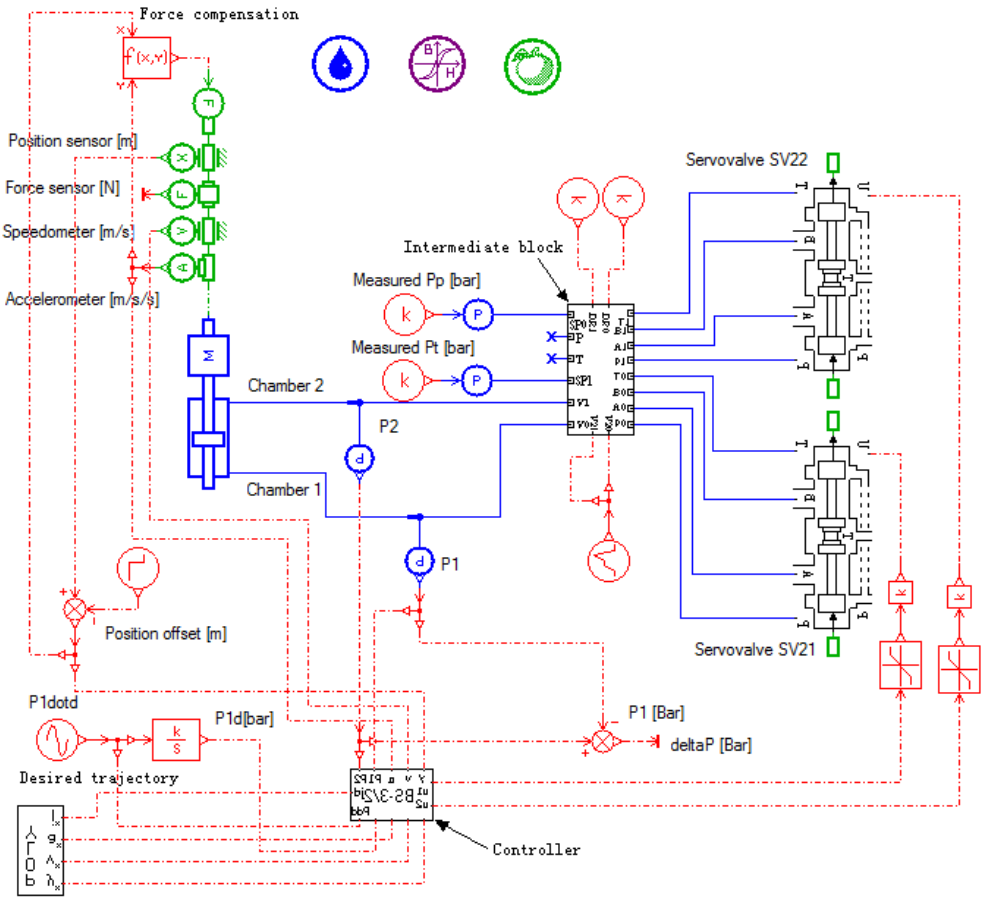

FIGURE 4.7: Virtual prototype of the test bench in AMESim

experimental results for the three working modes are presented in figure 4.8.

$$u_1 = -u_2 = K_P \cdot (y^d - y) \tag{4.22}$$

According to figure 4.8, it can be observed that during much of the transient step response, the control signals are saturated and two simulation commands are nearly overlapped. Besides, position tracking results show that the virtual prototype has the same step response with the real equipment, except that the system responds faster to the step signal in simulation than in experiment. This is probably caused by the hysteresis of the torque motor and gaps between mechanical junctions. Moreover, it can be observed that the response speed in mode 2 is fastest compared with the other working modes due to its ability to provide a larger flow rate. The response time at 95% of the step amplitude obtained by

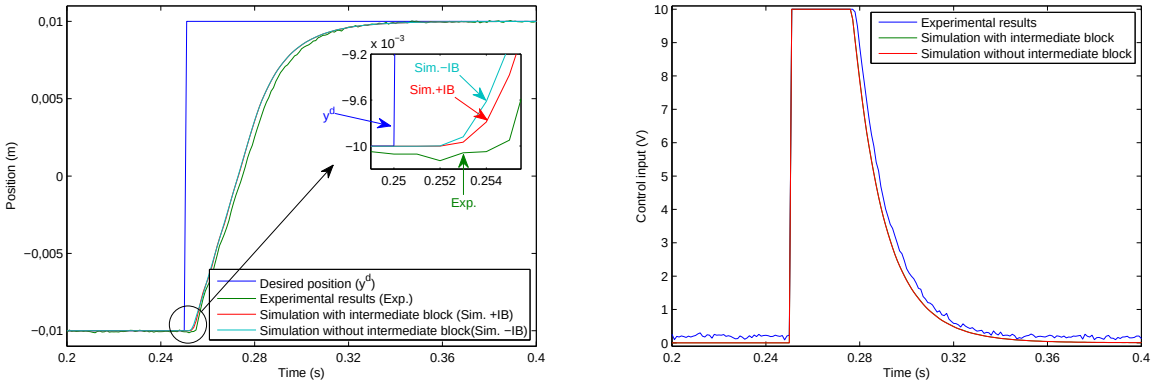

(a) Mode 1

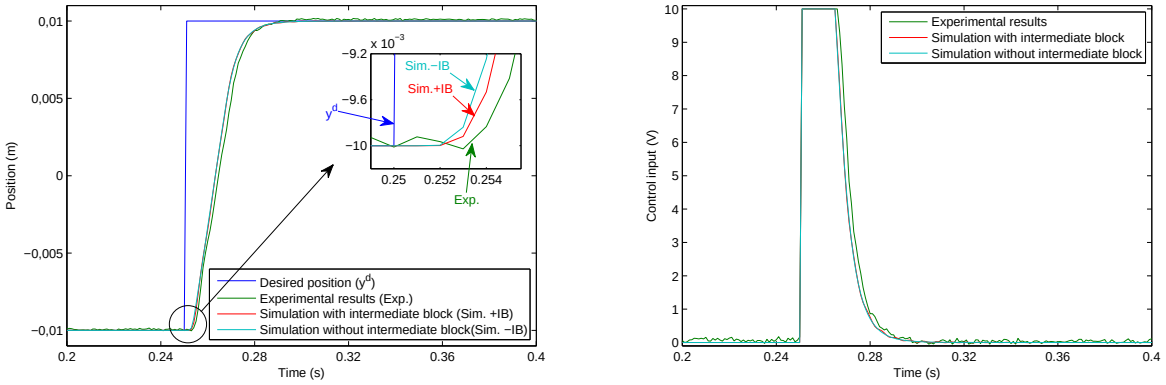

(b) Mode 2

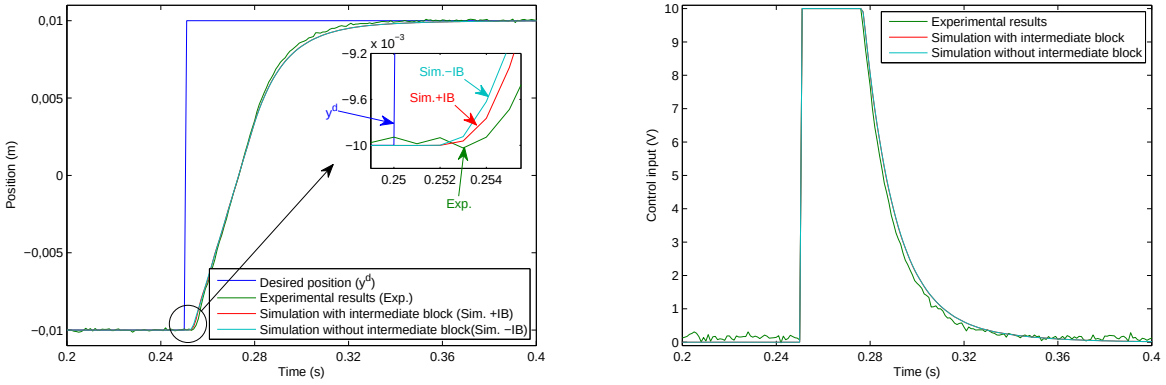

(c) Mode 3

FIGURE 4.8: Step response results

experiments is 0.028 s in mode 2 and nearly half of those in mode 1 & 3 (0.058 s and 0.055 s respectively).

4.4.2 Results in frequency domain

Both experimental work and simulation are implemented with a sinusoidal position input of 3.4 mm amplitude to keep the command signal near its mid-stroke. The system is tested in the three working modes. The control law applied here is a conventional proportional controller with a position feedback as defined in section 4.4.1. The frequency response results of the closed-loop system from the simulation and experiments are compared in figures 4.9, 4.10, and 4.11. During the simulation and experiments, the frequency response of the open-loop system can also be presented, see figures 4.12, 4.13, and 4.14. For the open-loop system, the input is the command of the servovalves and the output is the actuator position.

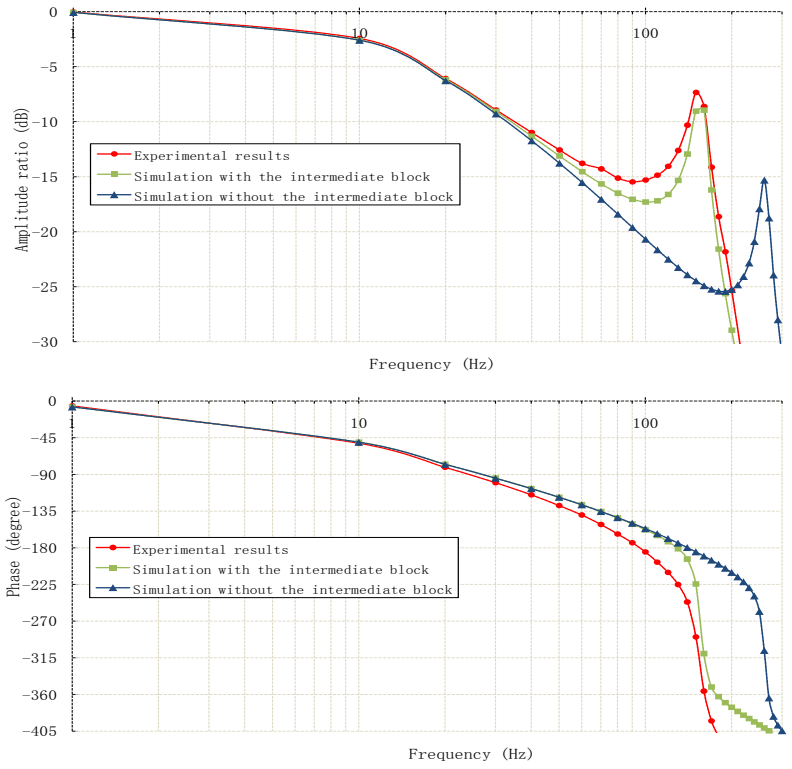

FIGURE 4.9: Frequency responses of the closed-loop system from simulations and experiments in mode 1

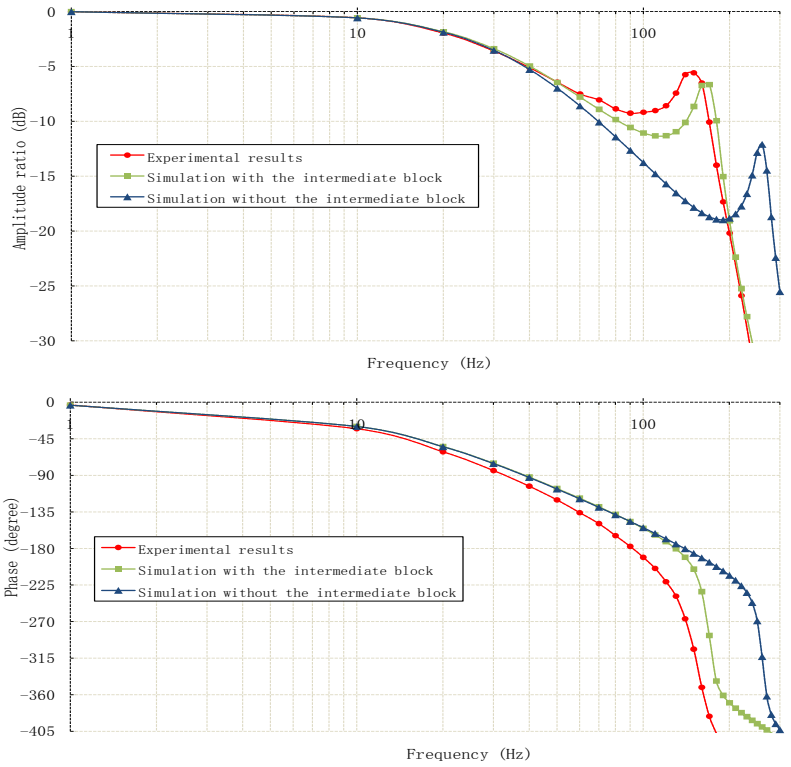

FIGURE 4.10: Frequency responses of the closed-loop system from simulations and experiments in mode 2

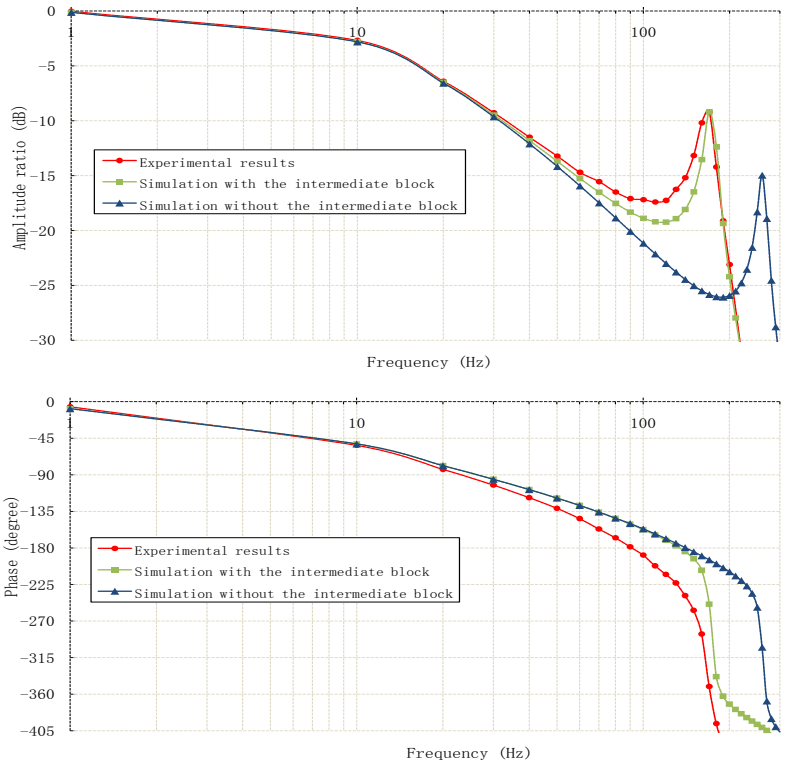

FIGURE 4.11: Frequency responses of the closed-loop system from simulations and experiments in mode 3

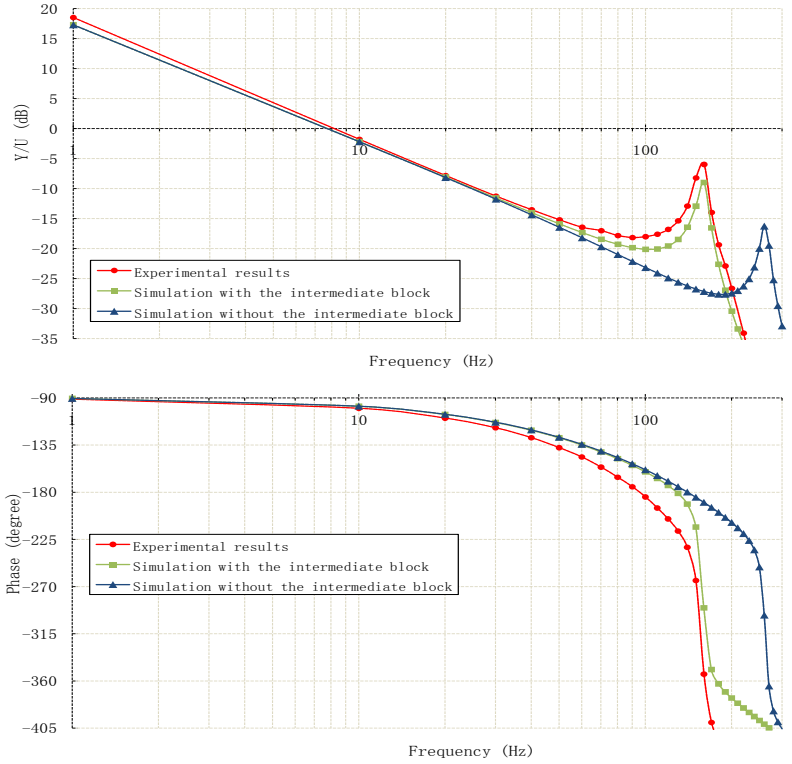

FIGURE 4.12: Frequency responses of the open-loop system from simulations and experiments in mode 1

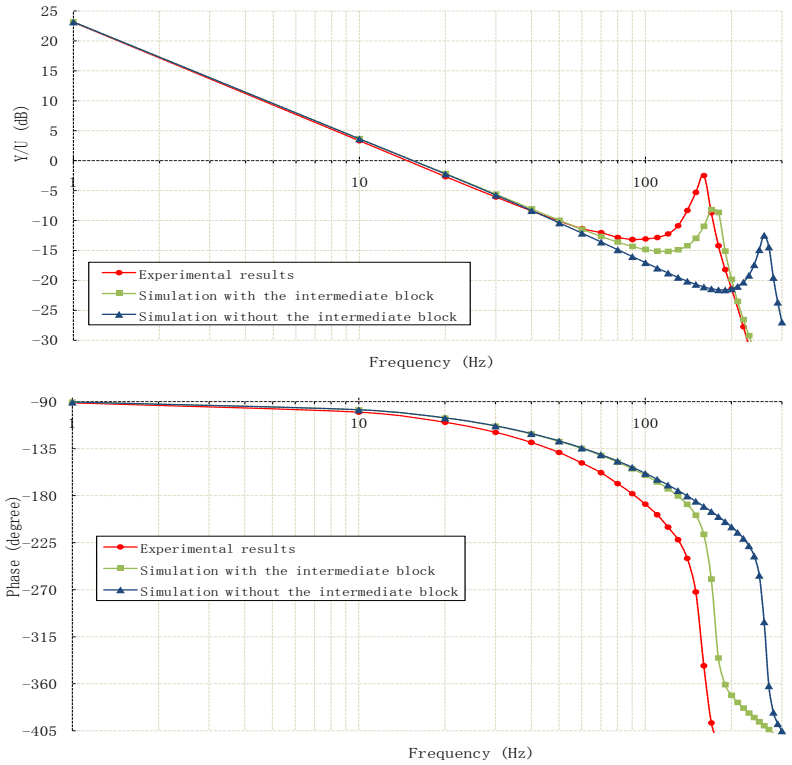

FIGURE 4.13: Frequency responses of the open-loop system from simulations and experiments in mode 2

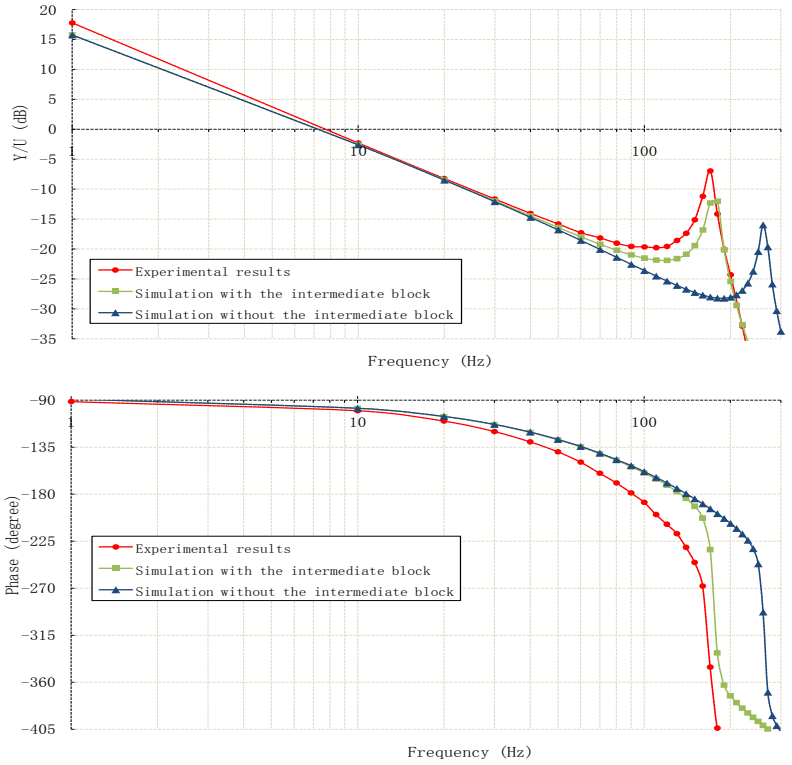

FIGURE 4.14: Frequency responses of the open-loop system from simulations and experiments in mode 3

The simulation and experimental results of the system show a good agreement at low frequencies. However, differences between the simulation and experiment for the closed-loop become more significant as the frequency grows until 100 Hz. At low frequencies, the open-loop system presents a behaviour similar to that of an integrator; the amplitude results in simulation are more coherent with the experimental ones than those of the closed-loop system. This is probably caused by the modelling error of the feedback loop where the LVDT position sensor induces a phase shift and a gain difficult to estimate accurately. At the very low frequency (1 Hz for example) or even in steady state, the maximum amplitude error (nearly 2 dB) appears in mode 3 because the two operating servovalves are not symmetric. While applying a same command to these two servovalves, two different flow rates are introduced into the two actuator chambers, which leads to an inequilibrium. Besides, it can be observed that the working mode 2 enables the highest gain of the amplitude ratio because of its ability to provide a high hydraulic power with parallel servovalves.

The resonance frequencies of our system operating in the three working modes are around 150 Hz. Compared to the simulation results without considering the manifold, the results obtained with the full model achieve a better coherence with experiments, particularly when considering the resonance frequency. This confirms that the effect of the manifold takes great importance in the modelling of the hydraulic system, especially at high frequencies. The differences between the simulation and experiment can be explained by the following reasons:

a) Several parameters of the hydraulic system are difficult to obtain, e.g. the bulk modulus, friction coefficient, etc. This may induce some differences between simulation and experimental results;

b) The models used to represent some phenomena may be inefficient in some conditions, for example according to the frequency range. Indeed, dry friction and small servovalve opening can introduce behaviours that change according to the frequency (turbulence, hysteresis);

c) In the calculation of the fluid equivalent mass in the manifold, the flow rate ratio λ_{ti} is not strictly constant. It varies with respect to time;

d) The measurement of the sensors contains noise and different types of errors, such as the LVDT phase shift. e) Because of the sampling frequency of 1 kHz, there is a time deley of 0.5ms in the digital control. This will introduce nearly 18° at 100 Hz.

4.5 Conclusion

In this chapter, following a brief study on the actuator, the analysis fo its dynamic behaviour has been achieved through linearization. The results show that the actuator can be approximated to be a 3rd-order system including an integrator which results in the system instability. Besides, a comparison in time and frequency domains has been made between experimental measurements and the virtual prototype of the whole test bench using the models developed in the previous chapters. The model developed in AMESim was validated experimentally and it has been shown that the validity domain of this model allows its use as a virtual

prototype for testing and evaluating the performances of the control strategies that will be introduced in the next part. It is important to note that it really makes sense to consider the effect of the manifold while modelling a hydraulic system with high performance and large bandwidth.

Conclusion on Part I

To conclude, this part dedicated to the modelling aspects of a high performance electro-hydraulic test bench, our original contribution can be summarized by:

- Conducting static and dynamic analysis of the characteristics of the used high performance two-stage electro-hydraulic servovalve, and establishing a precise model of the servovalve by Bond Graph;
- Proposing a flow model for the second stage of the servovalve with respect to the physical phenomena, representing the transient phase between the underlap and overlap states of the spool valve;
- Studying the dynamic effect of the manifold installed between the servovalves and the actuator, i.e. compressibility effect, internal fluid inertia, and energy dissipation, and proposing a method to obtain the parameters corresponding to the losses for lumped-parameter model of this component based on the Bond Graph representation;
- Validation of the virtual prototype of the test bench in AMESim based on the Bond Graph model of the system.

However, there are still limitations, and further studies to this work can be

- Taking into account thermal effects while more precise results are expected, e.g. considering the temperature-dependent function for the viscosity, pressure, flow coefficient,$\cdots$;
- Variable bulk modulus with respect to the temperature, pressure, ratio of entrained air, and etc. (e.g. the effect of entrained air in appendix A);

- Dynamic friction force model which is related to ,for example, pressure dependency, tribology,$\cdots$;
- Supply and tank line modelling;
- Different external loads could be taken into account.

Part II

Controls of the test bench

Context

This dissertation began with the description and modelling of the electro-hydraulic test bench in part I. The model of the bench has been validated in the previous discussion, which allows to conduct the next step of this dissertation, the control of the bench. As described in figure II.1, the proposed controls will first be implemented on the virtual prototype developed in part I. After the validation by simulation, the experimental analysis will be conducted on the physical equipments to study the control performances of the proposed methods.

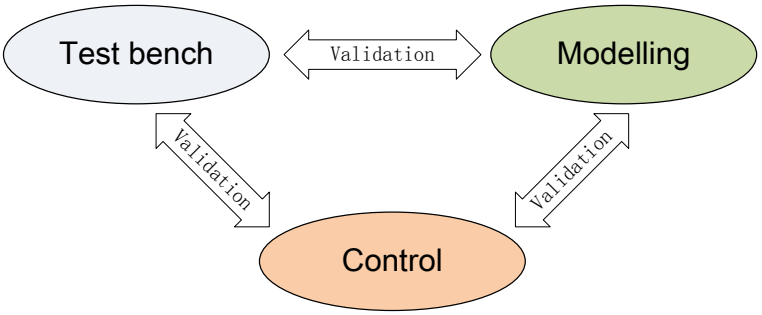

FIGURE II.1: The dissertation flow chart

The control laws will be developed with the test bench operating in mode 3, namely, two servovalves working as 3-way components to control each actuator chamber. In this mode, multivariable controls could be easily applied. The hydraulic diagram can be simplified as shown in figure II.2.

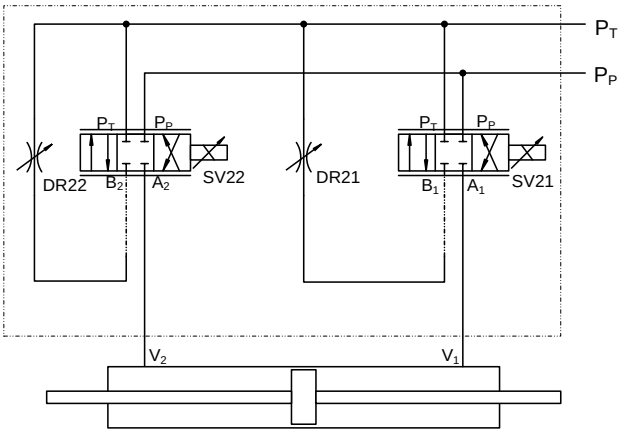

FIGURE II.2: Simplified diagram of the test bench (Mode 3)

Integrated with the effect of the manifold, the hydraulic natural frequency of the actuator is less than 200 Hz with the piston at mid-stroke, whereas the servovalves

MOOG D765 has a large bandwidth of 310 Hz at 40% maximum input, which is quite large compared to this natural frequency. Thus, to simplify the control model, the dynamics of the servovalve can be neglected while considering the dynamic model for the control design. Therefore, the servovalve model consists only in a static characteristic described by (II.2). This formulation is proposed by [MOOG] for simplifying the flow rate calculation. It is related to the supply pressure P_P, tank pressure P_T, actuator chamber pressure P_1 or P_2, and input command u_1 or u_2. In order to get a unified control model, we use an operator $sign(.)$ to couple the inlet and outlet flow in (II.2). While handling the control of this system, the focus is given on the dynamic of the actuator.

As illustrated in section 4.1, the compressibility of the fluid gives the pressure dynamics in each actuator chamber according to the piston velocity and the flow provided by each servovalve ($\phi_1 u_1$ and $\phi_2 u_2$), internal and external leakages being here neglected. The Newton's law gives the dynamics of the moving load. The fluid inertia and gravity in each chamber are neglected. Dry friction F_{fs} calculated by (4.13), as well as the viscous friction term and gravity, are taken into account. The dynamic model of the actuator is then as follows:

$$\begin{cases} \frac{dy}{dt} = v \\ \frac{dv}{dt} = \frac{A}{M}\left(P_1 - P_2\right) - g - \frac{b}{M}v - \frac{F_{fs}(v)}{M} - \frac{F_{ext}}{M} \\ \frac{dP_1}{dt} = -\frac{\beta}{V_1(y)} \cdot A \cdot v + \frac{\beta}{V_1(y)} \cdot \phi_1\left(P_1, P_P, P_T, sign(u_1)\right) \cdot u_1 \\ \frac{dP_2}{dt} = \frac{\beta}{V_2(y)} \cdot A \cdot v + \frac{\beta}{V_2(y)} \cdot \phi_2\left(P_2, P_P, P_T, sign(u_2)\right) \cdot u_2 \end{cases} \tag{II.1}$$

$$\text{where } \phi_i = \frac{Q_n}{u_n} \cdot \sqrt{\frac{|P_P - P_i|}{\Delta P_n}} \cdot \frac{sign(u_i) + 1}{2} + \frac{Q_n}{u_n} \cdot \sqrt{\frac{|P_i - P_T|}{\Delta P_n}} \cdot \frac{1 - sign(u_i)}{2} \tag{II.2}$$

with Q_n, u_n, and ΔP_n : the nominal flow rate, command, and pressure drop given by the manufacturer.

In this part, we will develop two multivariable control strategies based on the backstepping to realise the position and pressure tracking. Besides, two model-free based control strategies will also be applied on the test bench. These control

methods are recently developed by Fliess and Join in [Fliess 2008, Fliess 2009, Fliess 2011] with ease of implementation and good control performances. Finally, the robustness performance of the proposed control strategies will be taken into account. The study will finally focus on the robustness analysis with the perturbation of the payload and the velocity estimation precision which are two important factors related to the control performances.

Chapter 5

Multivariable controls of the test bench based on the backstepping

Contents

5.1 Introduction

For some operating ranges, position control of electro-hydraulic actuators is widely used without any problem. However, the accurate position tracking on a large frequency domain can be a difficult target to achieve with only a linear control strategy. This is due to the nonlinearities of this system, such as friction force, servovalve dynamics and flow rate characteristics as mentioned in the previous chapters. Some previous research works [Kim 2000, Watton 1987] have used high-order linear models for control system design by reformulating the problem from its nonlinear state equations. Nevertheless, this kind of linear model is valid only on the neighbourhood of an operating point and not suitable for certain applications where high performance and large frequency response ranges are required.

In this chapter, we focus on the implementation of a multivariable nonlinear control, which is based on backstepping theory. The electro-hydraulic system under study is equipped with two servovalves and has therefore two control inputs. This enables multivariable control laws to be developed. Therefore, the control could aim at tracking two trajectories simultaneously: the first one is naturally the position and the second one can be defined according to other requirements on the system performance such as actuator stiffness, energy, bandwidth, etc.. We propose here two types of control laws based on the backstepping method. For the first one, called P-Y control, the tracking trajectories are the piston displacement and the pressure in one chamber of the cylinder. For the second one, called Y-λ control, the tracking trajectories are the piston displacement and a dynamic weight on the pressure in each cylinder chamber. This last control law enables the accuracy of the piston position tracking to be improved. In both cases, the backstepping based control design enables the asymptotical stability of the system to be guaranteed except in some singular points [Khalil 2001].

Following this introduction, we will review the backstepping algorithm in section 5.2. The P-Y and Y-λ control design are presented in section 5.3. According to properly chosen Lyapunov functions, it is demonstrated that the proposed control laws are theoretically asymptotically stable. Simulations are conducted in section

5.5 to validate the proposed control laws. Experimental validation and results are given in section 5.6 for different values of the control law parameters. Finally, section 5.7 will give some conclusion on the control performance and possible uses of such approaches.

5.2 Review of the backstepping control algorithm

During the last decades, numbers of researchers in the control theory community tended to ensure the global stability of nonlinear systems for the whole operating domain and to guarantee high control performances. Nonlinear robust control methods have been extensively studied, such as sliding mode control [Bartolini 2003], backstepping control [Smaoui 2006], fuzzy control [Precup 2011], and adaptive control [dos Santos Coelho 2011]. Among the mentioned methods, backstepping is one of the most interesting techniques. This approach gives a powerful design methodology for stabilizing controls applied to nonlinear systems. It provides a recursive control design, which begins with the simplest known-stable subsystem to build a series of virtual feedback controllers to stabilize progressively each subsystem until it reaches the ultimate external control [Kristic 1995, Khalil 2001]. While dealing with the stability of the subsystems, the backstepping approach constructs systematically a number of Lyapunov functions to guarantee the asymptotical stability of the controlled system.

The backstepping design technique was developed around 1990 by P. V. Kokotovic and others [Kokotovic 1989, Kokotovic 1992, Lozano 1992]. This technique was originated in [Sontag 1989] where the use of a virtual command provided a great idea to the ultimate contribution in [Kokotovic 1989]. In [Kokotovic 1989], a nonlinear system was split into two subsystems, where the first subsystem was controlled by a virtual command which is a state variable of the second subsystem.

Since the emergence of the backstepping design approach, researchers gave great efforts and interests to exploit this technique, for example, [Kanellakopoulos 1991, Freeman 1993, Arcak 2000, Ezal 2000] revealed the robustness of the backstepping

approach. Because of its robustness and ease of implementation, the backstepping-based design has been quickly and successfully applied to accurate position tracking or regulation purpose in many domains, including hydraulics [Alleyne 2000], pneumatics [Smaoui 2006], electrics [Dawson 1994, Lin 2000, Xu 1998], magnetics [de Queiroz 1996, Yang 2001], and robotics [Jiang 1997, Jiang 2001, Lee 2001].

To illustrate one step of the backstepping design process [Khalil 2001], we consider the following nonlinear system (5.1) as shown in figure 5.1(a) which can be obtained from the previous application of the backstepping method procedure.

$$\begin{cases} \dot{x} = f(x) + g(x) \cdot \xi \\ \dot{\xi} = u \end{cases} \tag{5.1}$$

where $[x^T, \xi]^T \in \mathbb{R}^{n+1}$ is the system state and $u \in \mathbb{R}$ is the control input. The functions $f : \mathcal{D} \to \mathbb{R}^n$ and $g : \mathcal{D} \to \mathbb{R}^n$ are assumed known and smooth in a domain $\mathcal{D} \subset \mathbb{R}^n$ with $f(0) = 0$.

We assume that there exists a smooth state feedback control law $\xi = \alpha(x)$ with $\alpha(0) = 0$, which can stabilize the first term of the system (5.1). Namely, the system (5.2) is asymptotically stable.

$$\dot{x} = f(x) + g(x) \cdot \alpha(x) \tag{5.2}$$

We suppose that there is a Lyapunov function $V(x) : \mathbb{R}^n \to \mathbb{R}^n$ which is smooth, positive definite and can satisfy the following assumptions:

$$\begin{cases} \lim_{\|x\| \to +\infty} V(x) = +\infty \\ \frac{\partial V(x)}{\partial x} \left(f(x) + g(x)\alpha(x) \right) \leq -W(x) \leq 0, \quad \forall x \in \mathbb{R}^n \end{cases} \tag{5.3}$$

where $W(x)$ is a positive definite function.

Note: Here, we use the common notation for the Lyapunov stability condition: $-W(x) \leq 0$ means the two following conditions

$$\begin{cases} -W(x) < 0, \quad \forall x \in \mathbb{R}^{n*} \\ W(0) = 0 \end{cases} \tag{5.4}$$

Adding and subtracting $g(x)\alpha(x)$ in (5.1), yields

$$\begin{cases} \dot{x} = (f(x) + g(x)\alpha(x)) + g(x) \cdot (\xi - \alpha(x)) \\ \dot{\xi} = u \end{cases} \tag{5.5}$$

The new system (5.5) is presented by the block diagram in figure 5.1(b).

We notice that it would be simple to choose $\xi = \alpha(x)$ to stabilize the system if ξ was the actual control input. However, ξ is only the system state, but not the actual input. In this case, ξ is called as the virtual command and $\alpha(x)$ is called as the stabilizing function.

Then, a error variable e is defined to represent the difference between the actual state value ξ and the stabilizing function:

$$e = \xi - \alpha(x) \tag{5.6}$$

$$\Rightarrow \dot{\xi} = \dot{e} + \frac{\partial \alpha(x)}{\partial x} \left(f(x) + g(x) \left(\alpha(x) + e\right)\right) \tag{5.7}$$

Hence, by substituting (5.6) and (5.7) into (5.5), we obtain

$$\begin{cases} \dot{x} = f(x) + g(x) \cdot (\alpha(x) + e) \\ \dot{e} = u - \frac{\partial \alpha(x)}{\partial x} \left(f(x) + g(x) \left(\alpha(x) + e\right)\right) \end{cases} \tag{5.8}$$

which is shown in figure 5.1(c).

By defining a Lyapunov function candidate as

$$V_\alpha(x, e) = V(x) + \frac{1}{2} e^2 \tag{5.9}$$

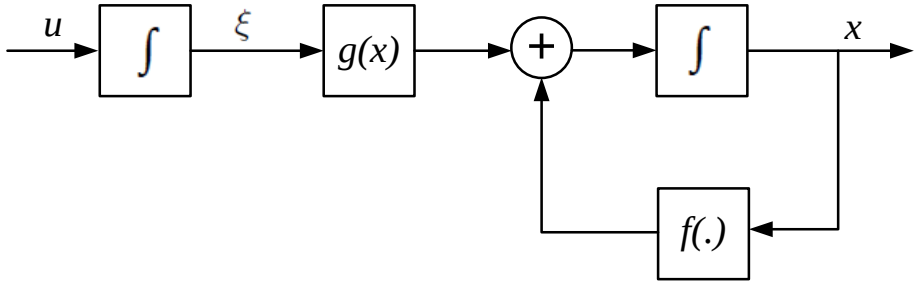

(a) The block diagram of system (5.1)

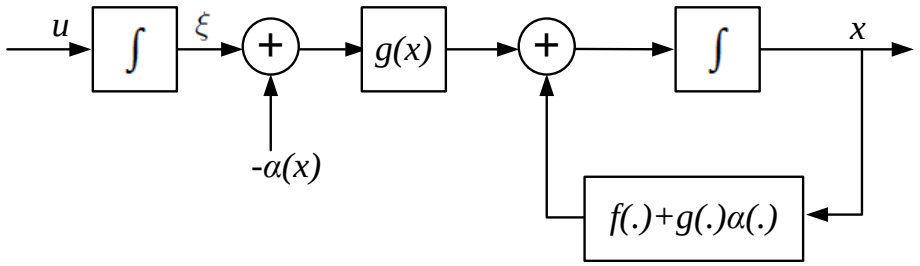

(b) The block diagram for introducing $\alpha(x)$

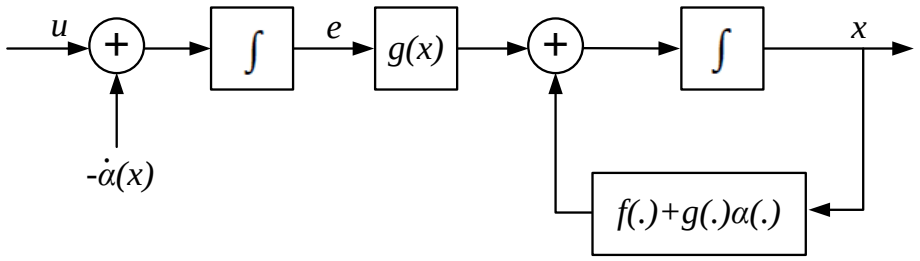

(c) "backstepping"

FIGURE 5.1: Principle of the backstepping technique [Khalil 2001]

We can show that the derivative of the Lyapunov function (5.9) is given by

$$\begin{aligned}\dot{V}_\alpha(\cdot) &= \frac{\partial V(x)}{\partial x}(f(x)+g(x)(\alpha(x)+e)) + e\left(u - \frac{\partial \alpha(x)}{\partial x}\left(f(x)+g(x)\left(\alpha(x)+e\right)\right)\right) \\ &= \frac{\partial V(x)}{\partial x}\left(f(x)+g(x)\alpha(x)\right) + e\Big(u - \frac{\partial \alpha(x)}{\partial x}\left(f(x)+g(x)\left(\alpha(x)+e\right)\right) \\ &\qquad + \frac{\partial V(x)}{\partial x}g(x)\Big) \\ &\leq -W(x) + e\Big(u - \frac{\partial \alpha(x)}{\partial x}(f(x)+g(x)(\alpha(x)+e)) + \frac{\partial V(x)}{\partial x}g(x)\Big)\end{aligned} \tag{5.10}$$

If the control law is chosen as

$$u = \frac{\partial \alpha(x)}{\partial x}(f(x)+g(x)(\alpha(x)+e)) - \frac{\partial V(x)}{\partial x}g(x) - ce \tag{5.11}$$

where c is a positive constant, (5.10) becomes

$$\dot{V}_\alpha(x,e) \leq -W(x) - ce^2 = -W_\alpha(x,e) \tag{5.12}$$

$W_\alpha(x,e)$ is then positive definite. Hence, the system (5.8) is globally asymptotically stable if all the assumptions are hold globally.

According to the design procedure, it should be noticed that the ultimate choice of the control law u is to eliminate terms involving the function $f(x)$ and $g(x)$ which are assumed known exactly. However, due to the unexpected perturbations that may degrade the control performances or stability, in practice, it is better to choose the control law in which terms are able to dominate any uncertainties in $f(x)$ and $g(x)$, if possible. The asymptotic system stability can be guaranteed only if the $W_\alpha(x,e)$ is positive definite.

5.3 Design of the P-Y and Y-λ control laws

As explained in introduction to Part II, the proposed control laws will work in mode 3 where two servovalves control each actuator chamber separately. The control model is given by equation (II.1) recalled here in equation (5.13) obtained with the assumption of neglecting the servovalve dynamics.

$$\begin{cases} \frac{dy}{dt} = v \\ \frac{dv}{dt} = \frac{A}{M}(P_1 - P_2) - g - \frac{b}{M}v - \frac{F_{fs}(v)}{M} - \frac{F_{ext}}{M} \\ \frac{dP_1}{dt} = -\frac{\beta}{V_1(y)} \cdot A \cdot v + \frac{\beta}{V_1(y)} \cdot \phi_1(P_1, P_P, P_T, sign(u_1)) \cdot u_1 \\ \frac{dP_2}{dt} = \frac{\beta}{V_2(y)} \cdot A \cdot v + \frac{\beta}{V_2(y)} \cdot \phi_2(P_2, P_P, P_T, sign(u_2)) \cdot u_2 \end{cases} \tag{5.13}$$

$$\text{where } \phi_i = \frac{Q_n}{u_n} \cdot \sqrt{\frac{|P_P - P_i|}{\Delta P_n}} \cdot \frac{sign(u_i)+1}{2} + \frac{Q_n}{u_n} \cdot \sqrt{\frac{|P_i - P_T|}{\Delta P_n}} \cdot \frac{1 - sign(u_i)}{2} \tag{5.14}$$

It can be noticed that the two system inputs (u_1 and u_2) enable a multiple-objective control to be implemented. Namely, we can develop a control strategy to track

different trajectories corresponding to different requirements. The following control designs mainly focus on tracking the piston position and chamber pressures. These control strategies, based on the backstepping method, follow the general control scheme given in figure 5.2.

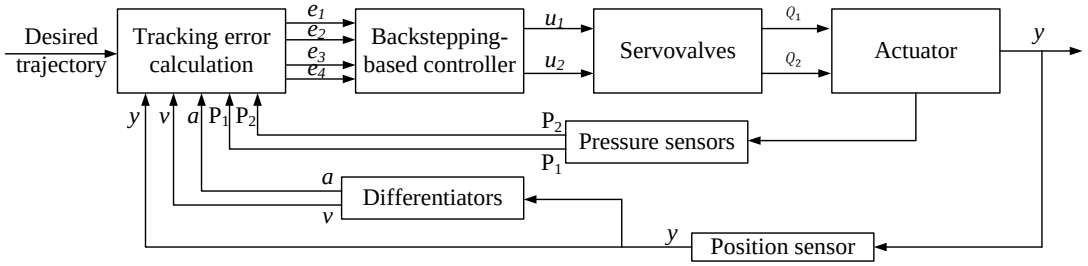

FIGURE 5.2: General control scheme based on backstepping technique

As shown on figure 5.2, to apply the backstepping technique, several state variables have to be determined. Here position and chamber pressures are obtained from sensors, but for cost reasons, numeric differentiators, instead of the physical sensors, have been implemented to obtain velocity and acceleration from the position measurement. In addition, due to the reduction of the physical sensors, the system reliability has been improved. The differentiators applied in control strategies are second-order sliding modes differentiators developed at AMPERE by L. Sidhom [Sidhom 2011b, Sidhom 2011a].

The two control strategies are denoted by P-Y and Y-λ controls. The control objectives of the first control law are to track the actuator position $y^d(t)$ and the pressure $P_1^d(t)$ in chamber 1 of the actuator. The second one focuses on the actuator position $y^d(t)$ tracking and the control of a dynamic weight $\lambda(t)$ which determines the distribution of the pressures in the actuator chambers according to the following expression:

$$\begin{cases} P_1(t) = P_0(t) + \lambda(t) \cdot \Delta P(t) \\ P_2(t) = P_0(t) + (\lambda(t) - 1) \cdot \Delta P(t) \end{cases} \tag{5.15}$$

where P_0 is the reference pressure.

5.3.1 Y-λ control strategy

Firstly, the backstepping-based method is applied to synthesize the Y-λ control. It can be decomposed in 3 steps:

Step 1: The position tracking error e_1 is defined by (5.16) as the difference between the measured y and the desired y^d piston position.

$$e_1 = y - y^d \tag{5.16}$$

$$\Rightarrow \dot{e}_1 = \dot{y} - \dot{y}^d = v - v^d \tag{5.17}$$

The piston velocity is considered as a virtual command for the above subsystem and a first Lyapunov function candidate is chosen as follows:

$$V_1(e_1) = \frac{1}{2}e_1^2 \tag{5.18}$$

To ensure stability, its derivative (5.18) has to be negative. A first feedback function $v = \alpha_0(e_1, v^d)$ is therefore defined by (5.20) with c_1 a positive constant, which is satisfying the asymptotical stability condition from $e_1 = 0$.

$$\dot{V}_1(e_1) = e_1\dot{e}_1 \tag{5.19}$$

$$v = \alpha_0(e_1, v^d) = v^d - c_1e_1 \tag{5.20}$$

$$\Rightarrow \dot{V}_1 = -c_1e_1^2 \leq 0 \tag{5.21}$$

Step 2: The velocity v is not an actual command input, but a system state. Thus, a new error variable e_2 between the measured value v and the defined function $\alpha_0(e_1, v^d)$ is now defined by

$$e_2 = v - \alpha_0(e_1, v^d) = v - v^d + c_1e_1 = \dot{e_1} + c_1e_1 \tag{5.22}$$

$$\Rightarrow \begin{cases} \dot{e}_1 = e_2 - c_1e_1 \\ \dot{e}_2 = a - \dot{\alpha}_0(e_1, v^d) \end{cases} \tag{5.23}$$

A new Lyapunov function is defined for this new subsystem as

$$V_2(e_1, e_2) = V_1(e_1) + \frac{1}{2}e_2^2 = \frac{1}{2}e_1^2 + \frac{1}{2}e_2^2 \tag{5.24}$$

$$\begin{aligned}\dot{V}_2(e_1, e_2) = e_1\dot{e}_1 + e_2\dot{e}_2 = -c_1e_1^2 + e_2\Big(e_1 + \frac{A}{M}(P_1 - P_2) - g - \frac{b}{M}v \\ - \frac{F_{fs}(v)}{M} - \frac{F_{ext}}{M} - \dot{\alpha}_0(e_1, v^d)\Big)\end{aligned} \tag{5.25}$$

To verify the stability condition, $\dot{V}_2(e_1, e_2)$has to be negative and the pressure difference $\Delta P = P_1 - P_2$ is chosen as a new virtual control defined by (5.26). This ensures the subsystem asymptotical stability from $e_1 = e_2 = 0$ with c_2 a positive constant (5.27).

$$\begin{aligned}\Delta P = P_1 - P_2 = \alpha_1(e_1, e_2, y^d, v^d, a^d) \\ = \frac{M}{A}\left(a^d + \frac{b}{M}v + \frac{F_{fs}(v)}{M} + \frac{F_{ext}}{M} + g + (c_1^2 - 1)e_1 - (c_1 + c_2)e_2\right)\end{aligned} \tag{5.26}$$

$$\Rightarrow \dot{V}_2(e_1, e_2) = -c_1e_1^2 - c_2e_2^2 \leq 0 \tag{5.27}$$

Step 3: This step has a slight difference from the traditional backstepping method since the last virtual command does not directly appear in the residual equations. Thus, we propose here two virtual functions by using a new parameter λ which is called the dynamic weight of the pressures. This parameter will determine the distribution of the two pressures P_1 and P_2 in the two chamber. The two estimated pressures values in the cylinder chambers are then assumed given by (5.28) where P_0 is a reference pressure.

$$\begin{cases} P_1 = \alpha_2(e_1, e_2, y^d, v^d, a^d) = P_0 + \lambda{\cdot}\alpha_1(e_1, e_2, y^d, v^d, a^d) \\ P_2 = \alpha_3(e_1, e_2, y^d, v^d, a^d) = P_0 + (\lambda - 1){\cdot}\alpha_1(e_1, e_2, y^d, v^d, a^d) \end{cases} \tag{5.28}$$

As P_1 and P_2 are not actual commands, the differences between the measured pressures and estimated ones exist and are given by equation (5.29). This leads

to a formulation which differs from the conventional backstepping technique.

$$\begin{cases} e_3 = P_1 - \alpha_2(e_1, e_2, y^d, v^d, a^d) = P_1 - P_0 - \lambda{\cdot}\alpha_1(e_1, e_2, y^d, v^d, a^d) \\ e_4 = P_2 - \alpha_3(e_1, e_2, y^d, v^d, a^d) = P_2 - P_0 - (\lambda - 1){\cdot}\alpha_1(e_1, e_2, y^d, v^d, a^d) \end{cases} \tag{5.29}$$

Then, we establish a new system with coordinates derived from equations (5.16), (5.22), and (5.29). In the new coordinates, the system is written as

$$\begin{cases} \dot{e}_1 = e_2 - c_1 e_1 \\ \dot{e}_2 = \frac{A}{M}(e_3 - e_4) - c_2 e_2 - e_1 \\ \dot{e}_3 = \dot{P}_1 - \dot{\alpha}_2(\cdot) = f_1 + g_1{\cdot}u_1 - \dot{P}_0 - \lambda{\cdot}\dot{\alpha}_1(\cdot) - \dot{\lambda}{\cdot}\alpha_1(\cdot) \\ \dot{e}_4 = \dot{P}_2 - \dot{\alpha}_3(\cdot) = f_2 + g_2{\cdot}u_2 - \dot{P}_0 - (\lambda - 1){\cdot}\dot{\alpha}_1(\cdot) - \dot{\lambda}{\cdot}\alpha_1(\cdot) \end{cases} \tag{5.30}$$

$$\text{with} \begin{cases} f_1 = -\frac{\beta}{V_1(y)}{\cdot}A{\cdot}v \\ f_2 = \frac{\beta}{V_2(y)}{\cdot}A{\cdot}v \\ g_1 = \frac{\beta}{V_1(y)}{\cdot}\phi_1(\cdot) \\ g_2 = \frac{\beta}{V_2(y)}{\cdot}\phi_2(\cdot) \end{cases}$$

$$\text{and } \dot{\alpha}_1(\cdot) = \frac{M}{A}\Big(\dot{a}^d + \frac{b}{M}\cdot a + \frac{\partial F_{fs}(v)}{\partial v}{\cdot}\frac{a}{M} \quad -(c_1^3 - 2c_1 - c_2)e_1 + (c_1^2 + c_1c_2 + c_2^2 - 1)e_2 - \frac{A}{M}(c_1 + c_2)(e_3 - e_4)\Big).$$

A final Lyapunov function candidate is defined as follows:

$$V_3(e_1, e_2, e_3, e_4) = V_2(e_1, e_2) + \frac{1}{2}e_3^2 + \frac{1}{2}e_4^2 = \frac{1}{2}e_1^2 + \frac{1}{2}e_2^2 + \frac{1}{2}e_3^2 + \frac{1}{2}e_4^2 \tag{5.31}$$

$$\begin{aligned} \Rightarrow \dot{V}_3(e_1, e_2, e_3, e_4) &= e_1\dot{e}_1 + e_2\dot{e}_2 + e_3\dot{e}_3 + e_4\dot{e}_4 \\ &= -c_1e_1^2 - c_2e_2^2 + e_3\left(\frac{A}{M}e_2 + \dot{e}_3\right) + e_4\left(-\frac{A}{M}e_2 + \dot{e}_4\right) \end{aligned} \tag{5.32}$$

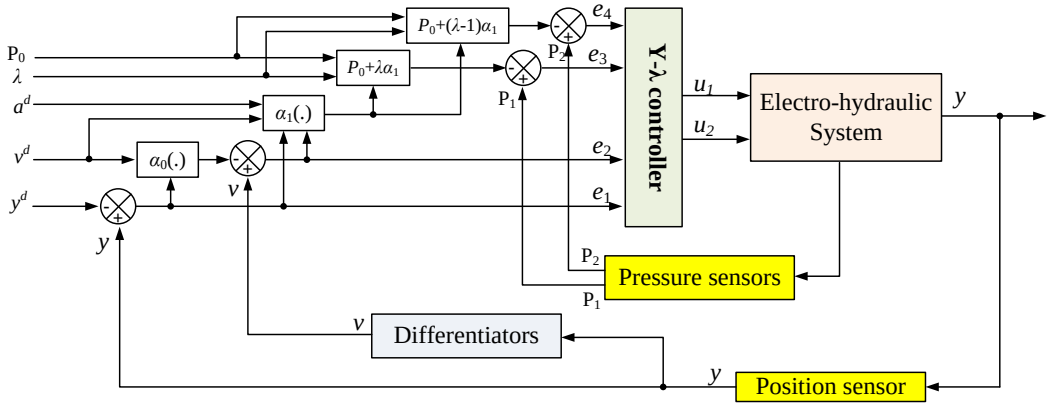

FIGURE 5.3: Schema of the Y-λ control law

In order to guarantee the stability of the system, a series of command combinations which solve the following system of equations (5.33) are required.

$$\begin{cases} f_1 + g_1 \cdot u_1 - \dot{P}_0 - \lambda \cdot \dot{\alpha}_1(\cdot) - \dot{\lambda} \cdot \alpha_1(\cdot) + \frac{A}{M} e_2 = -c_3 e_3 \\ f_2 + g_2 \cdot u_2 - \dot{P}_0 - (\lambda - 1) \cdot \dot{\alpha}_1(\cdot) - \dot{\lambda} \cdot \alpha_1(\cdot) - \frac{A}{M} e_2 = -c_4 e_4 \end{cases} \tag{5.33}$$

$$\begin{cases} u_1 = \frac{1}{g_1} \left(-f_1 + \dot{P}_0 + \lambda \cdot \dot{\alpha}_1(\cdot) + \dot{\lambda} \cdot \alpha_1(\cdot) - \frac{A}{M} e_2 - c_3 e_3 \right) \\ u_2 = \frac{1}{g_2} \left(-f_2 + \dot{P}_0 + (\lambda - 1) \cdot \dot{\alpha}_1(\cdot) + \dot{\lambda} \cdot \alpha_1(\cdot) + \frac{A}{M} e_2 - c_4 e_4 \right) \end{cases} \tag{5.34}$$

Note: To calculate the flow gain in terms g_1 and g_2, the signs of u_1 and u_2 are determined by the terms in the brackets of (5.34) as $\frac{1}{g_1}$ and $\frac{1}{g_2}$ are always positive.

According to the above commands, the whole system has an asymptotical stability from $e_1 = e_2 = e_3 = e_4 = 0$ with c_3 and c_4 two positive constants.

$$\dot{V}_3(e_1, e_2, e_3, e_4) = -c_1 e_1^2 - c_2 e_2^2 - c_3 e_3^2 - c_4 e_4^2 \leq 0 \tag{5.35}$$

Finally, according to the control design process, figure 5.3 presents the block diagram of the Y-λ control law.

In the case of Y-λ control, the two pressures P_1 and P_2 can be controlled simultaneously according to the reference pressure P_0 and the dynamic weight λ.

5.3.2 P-Y control strategy

For the design of the P-Y control strategy, a diffeomorphism is firstly required from the initial system coordinates (II.1) (y, v, P_1, P_2) to the new coordinates defined as (y, v, a, P_1). The new system equations are written straightforwardly as

$$\begin{cases} \frac{dy}{dt} = & v \\ \frac{dv}{dt} = & a \\ \frac{da}{dt} = & \frac{1}{M}\Bigg(- b \cdot a - \frac{\partial F_{fs}(v)}{\partial v} \cdot a - A^2\beta\left(\frac{1}{V_1(y)} + \frac{1}{V_2(y)}\right) \cdot v \\ & + A\beta\left(\frac{\phi_1(\cdot)}{V_1(y)} \cdot u_1 - \frac{\phi_2(\cdot)}{V_2(y)} \cdot u_2\right)\Bigg) \\ \frac{dP_1}{dt} = & -\frac{\beta}{V_1(y)} \cdot A \cdot v + \frac{\beta}{V_1(y)} \cdot \phi_1\left(P_1, P_P, P_T, sign(u_1)\right) \cdot u_1 \end{cases} \tag{5.36}$$

It makes appear two subsystems, the first one is composed of the three first equations showing a strict feedback form which can directly apply the backstepping method. The second one composed of the last equation associates to the direct pressure control.

The backstepping method is now applied to the subsystems mentioned above to synthesize the P-Y control.

Step 1: First, treating the second subsystem corresponding to the P_1 differential equation of (5.36), consider a pressure control in chamber V_1 using an error e_4 between the measured and the desired pressure P_1.

$$e_4 = P_1 - P_1^d \tag{5.37}$$

$$\Rightarrow \dot{e}_4 = \dot{P}_1 - \dot{P}_1^d \tag{5.38}$$

The Lyapunov function selected for this subsystem is written as

$$V_4(e_4) = \frac{1}{2}e_4^2 \tag{5.39}$$

$$\Rightarrow \dot{V}_4(e_4) = e_4\dot{e}_4 = e_4\left(-\frac{\beta}{V_1(y)}\cdot A\cdot v + \frac{\beta}{V_1(y)}\cdot\phi_1(\cdot)\cdot u_1 - \dot{P}_1^d\right) \tag{5.40}$$

$$u_1 = \frac{1}{g_1}\left(\frac{\beta}{V_1(y)}\cdot A\cdot v + \dot{P}_1^d - c_4e_4\right) \text{ where } g_1 = \frac{\beta}{V_1(y)}\cdot\phi_1(\cdot) \tag{5.41}$$

Note: To calculate the flow gain in the term g_1, the signs of u_1 is determined by the terms in the brackets of (5.41) as $\frac{1}{g_1}$ is always positive.

In order to make sure that $\dot{V}_4(e_4) \leq 0$, we define the control u_1 by (5.41). This leads to have $\dot{V}_4(e_4) = -c_4e_4^2 \leq 0$, i.e. the subsystem is asymptotically stable from $e_4 = 0$ with c_4 a positive constant.

While working on the position control for this new model (5.36) (first subsystem of 3$^{\text{rd}}$ order), the similar steps as previously (in the case of the Y-λ control) are done.

Step 2: Using the position tracking error e_1 defined by (5.42), the control law is given by (5.44). With the Lyapunov function (5.45), it ensures the subsystem asymptotical stability from $e_1 = 0$ with $c_1 > 0$.

$$e_1 = y - y^d \tag{5.42}$$

$$\Rightarrow \dot{e}_1 = v - v^d \tag{5.43}$$

$$v = \alpha_0(e_1, v^d) = v^d - c_1e_1 \tag{5.44}$$

$$V_1(e_1) = \frac{1}{2}e_1^2 \tag{5.45}$$

$$\Rightarrow \dot{V}_1(e_1) = -c_1e_1^2 \leq 0 \tag{5.46}$$

We define the error e_2 (5.47) between the measured velocity and $\alpha_0(e_1, v^d)$ as follows:

$$e_2 = v - \alpha_0(e_1, v^d) \tag{5.47}$$

$$\begin{cases} \dot{e}_1 = e_2 - c_1e_1 \\ \dot{e}_2 = a - a^d + c_1(e_2 - c_1e_1) \end{cases} \tag{5.48}$$

The Lyapunov function candidate is chosen as

$$V_2(e_1, e_2) = V_1(e_1) + \frac{1}{2}e_2^2 = \frac{1}{2}e_1^2 + \frac{1}{2}e_2^2 \tag{5.49}$$

$$\Rightarrow \dot{V}_2(e_1, e_2) = e_1\dot{e}_1 + e_2\dot{e}_2 = -c_1e_1^2 + e_2(e_1 + a - a^d + c_1(e_2 - c_1e_1)) \tag{5.50}$$

Then, the control law (5.51) is applied for stabilizing the subsystem (5.48) with $c_2 > 0$.

$$a = \alpha_1(e_1, e_2, v^d, a^d) = a^d + (c_1^2 - 1)e_1 - (c_1 + c_2)e_2 \tag{5.51}$$

$$\Rightarrow \dot{V}_2(e_1, e_2) = -c_1e_1^2 - c_2e_2^2 \leq 0 \tag{5.52}$$

Considering finally the whole system (5.36), we introduce a new error e_3 between the measured acceleration and $\alpha_1(e_1, e_2, v^d, a^d)$. It is given by

$$e_3 = a - \alpha_1(e_1, e_2, v^d, a^d) = a - a^d - (c_1^2 - 1)e_1 + (c_1 + c_2)e_2 \tag{5.53}$$

The error variables lead to the following formulation:

$$\begin{cases} \dot{e}_1 = e_2 - c_1e_1 \\ \dot{e}_2 = e_3 - c_2e_2 - e_1 \\ \dot{e}_3 = \dot{a} - \dot{\alpha}_1(e_1, e_2, v^d, a^d) \\ \dot{e}_4 = \dot{P}_1 - \dot{P}_1^d \end{cases} \tag{5.54}$$

where $\dot{\alpha}_1(e_1, e_2, v^d, a^d) = \dot{a}^d - (c_1^3 - 2c_1 - c_2)e_1 + (c_1^2 + c_1c_2 + c_2^2 - 1)e_2 - (c_1 + c_2)e_3$.

In order to determine the stability of the system (5.54), the Lypunov function selected for the whole system is then as follows:

$$V_3(e_1, e_2, e_3, e_4) = V_2(e_1, e_2) + \frac{1}{2}e_3^2 + V_4(e_4) = \frac{1}{2}e_1^2 + \frac{1}{2}e_2^2 + \frac{1}{2}e_3^2 + \frac{1}{2}e_4^2 \tag{5.55}$$

$$\begin{aligned} \Rightarrow \dot{V}_3(e_1, e_2, e_3, e_4) &= e_1\dot{e}_1 + e_2\dot{e}_2 + e_3\dot{e}_3 + e_4\dot{e}_4 \\ &= -c_1e_1^2 - c_2e_2^2 - c_4e_4^2 + e_3\left(e_2 + \dot{a} - \dot{\alpha}_1(e_1, e_2, v^d, a^d)\right) \end{aligned} \tag{5.56}$$

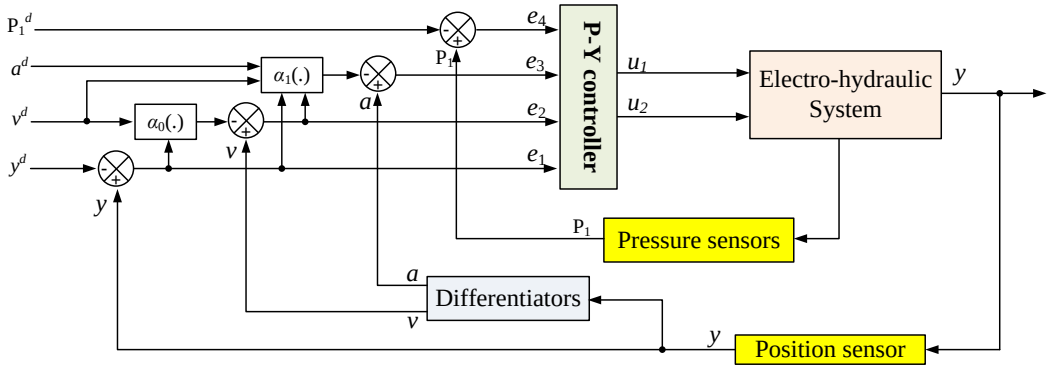

FIGURE 5.4: Schema of the P-Y control law

Thus, to guarantee the system stability, the command u_2 is then defined as

$$u_2 = -\frac{M}{A \cdot g_2}\left(-f - \frac{A \cdot g_1}{M} \cdot u_1 + \dot{a}^d + K_1 e_1 + K_2 e_2 + K_3 e_3\right) \tag{5.57}$$

where $\begin{cases} K_1 = 2c_1 + c_2 - c_1^3 \\ K_2 = c_1^2 + c_1 c_2 + c_2^2 - 2 \\ K_3 = -(c_1 + c_2 + c_3) \end{cases}$

and $\begin{cases} f = -\frac{b}{M} \cdot a - \frac{\partial F_{fs}(v)}{\partial v} \cdot \frac{a}{M} - \frac{A^2 \beta}{M}\left(\frac{1}{V_1(y)} + \frac{1}{V_2(y)}\right) \cdot v \\ g_2 = \frac{\beta}{V_2(y)} \cdot \phi_2(\cdot) \end{cases}$

In this expression, K_1 is a control gain associated with the position error, K_2 is indirectly related to the velocity error and K_3 involves the acceleration error. By adjusting these parameters, we can control the tracking precision, as well as the response time.

Note: To calculate the flow gain in the term g_2, the signs of u_2 is determined by the terms in the brackets of (5.57) as $-\frac{M}{A \cdot g_2}$ is always negative.

According to the control law defined by equations (5.41) and (5.57), we have

$$\dot{V}_3(\cdot) = -c_1 e_1^2 - c_2 e_2^2 - c_3 e_3^2 - c_4 e_4^2 \leq 0 \text{ with } c_{1,2,3,4}\text{: positive constants} \tag{5.58}$$

Hence, the whole system asymptotical stability is verified from $e_1 = e_2 = e_3 = e_4 = 0$. Figure 5.3 presents the block diagram of the P-Y control law.

5.4 Introduction to the adaptive higher order sliding modes differentiator

To implement the proposed control laws, it requires some system information including the piston position, velocity, acceleration, and chamber pressures. In conventional applications, these information is gathered by corresponding physical sensors. In our case, to eliminate some physical sensors and improve the system reliability, we tend to use a numeric differentiator to estimate the velocity and acceleration which is derived from the position information. Then, it needs only to install position and pressure sensors on the test bench. This section will give a brief introduction to the numeric differentiator used in this dissertation.

In recent decades, researchers and engineers in the industry make efforts to the on-line differentiation which can estimate accurately the derivative of a signal obtained form measurements. This type of numeric differentiator is an attractive solution for the cases where the physical sensor can not be used because of the lack of appropriate instrumentation, or environment constraints. Besides, the use of numeric differentiator is an ideal method to replace the physical sensors in industrial systems because it reduces the number of the sensors, and therefore decreases the installation cost and improves the system reliability by limiting the sensor failure.

However, the on-line differentiation is a difficult task to achieve since it requires a large bandwidth response while avoiding the corruption of the signal due to noise. These problem arise from the fact that information in a measured signal is limited. A possible solution for this problem is to develop suitable linear or nonlinear filters able to reduce the noise effect with the informative signal unchanged and little phase shift. Some approaches in the literature [Gauthier 1992] require a good knowledge of the system model for the synthesis of a differentiator. In this case, the differentiator is degraded to an observer and a filtering problem. However, lack of information about the system dynamics makes the implementation of nonlinear

state observers difficult. Thus, in some cases, the construction of a numeric differentiator is unavoidable, and in these cases, the sliding mode technique presents a good efficiency in dealing with this problem.

To design a sliding modes differentiator, let us consider the input signal of the differentiator defined by

$$f(t) = f_0(t) + \xi(t) \tag{5.59}$$

where

- $f_0(t)$ is an unknown base signal that is $(1+n)^{th}$ differentiable;
- $\xi(t)$ is a bounded noise function with unknown features, defined by $|\xi(t)| < \epsilon$ with ϵ sufficiently small.

In our case, $f(t)$ is the measured actuator position $y(t)$, $\dot{f}(t)$ and $\ddot{f}(t)$ correspond to the estimated velocity ($\hat{v}(t) = \hat{\dot{y}}(t)$) and acceleration ($\hat{a}(t) = \hat{\ddot{y}}(t)$) respectively. An infinite number of differentiator schemes is proposed in [Levant 2003]. It focuses on obtaining a robust estimate in real time of $\dot{f}_0(t), \ddot{f}_0(t), \ldots, f_0^{(n)}(t)$ which eliminates exactly the noise. With this general form, a second-order differentiator was developed by L. Sidhom in [Sidhom 2011a]. This differentiator is noted by DAO2 (Dérivateur Adaptatif d'Ordre 2) as the abbreviation, and enables the two first derivative of a signal to be computed. It induces adaptive laws that change the algorithm parameters on-line, guaranteeing the algorithm convergence whatever the signal spectra is. This second-order sliding modes differentiator is given by

$$\begin{cases} \dot{z}_0 &= v_0 \\ v_0 &= -\hat{\lambda}_0 |s_0|^{\frac{2}{3}} sign(s_0) - K_{d0} s_0 + z_1 \\ \dot{z}_1 &= v_1 \\ v_1 &= -\hat{\lambda}_1 |s_1|^{\frac{1}{2}} sign(s_1) - \hat{\lambda}_2 \int_0^t sign(s_1) dt - K_{d1} s_1 \end{cases} \tag{5.60}$$

where K_{d0} and K_{d1} are constant positive gains, and s_0, s_1 are the sliding surfaces defined by

$$\begin{cases} s_0 &= z_0 - f(t) \\ s_1 &= z_1 - v_0 \end{cases} \tag{5.61}$$

The dynamic gains $\hat{\lambda}_i, i \in \{0,1,2\}$ are defined by

$$\begin{cases} \dot{\hat{\lambda}}_0 &= \left[|s_0|^{\frac{2}{3}} sign(s_0)\right] s_0 \\ \dot{\hat{\lambda}}_1 &= \left[|s_1|^{\frac{1}{2}} sign(s_1)\right] s_1 \\ \dot{\hat{\lambda}}_2 &= s_1 \int_0^t sign(s_1) dt \end{cases} \tag{5.62}$$

Theorem: For $K_{d0}, K_{d1} > 0$ and with the dynamic gains $\hat{\lambda}_i, i \in \{0,1,2\}$ defined by (5.62), the trajectory system (5.60) converges locally asymptotically towards the equilibrium point $s_0 = s_1 = 0$ under the following assumption: there are unknown positive constants λ_0^* and λ_1^* defined by

$$\begin{cases} \dot{f}(t) &= -\lambda_0^* |s_0|^{\frac{2}{3}} sign(s_0) + z_1 \\ \ddot{f}(t) &= -\lambda_1^* |s_1|^{\frac{1}{2}} sign(s_1) - \lambda_2^* \int_0^t sign(s_1) dt \end{cases} \tag{5.63}$$

The convergence in finite time of the algorithm has been proved in [Sidhom 2011a]. In addition, the dynamic gains λ_i evolve over time according to the proposed adaptation law which has a bounded evolution and depends on the initial values of the algorithm gains.

5.5 Simulation validation and results

Before the implementation of the proposed control laws on the test bench, simulations are conducted on the virtual prototype of the system developed in chapter 4 for the sake of the preliminary analysis of the control performances.

According to the control design procedures illustrated in section 5.3, we develop a controller corresponding to the proposed control strategies in AMESim, and implement it into the virtual simulation system (see figure 4.7). The desired trajectory applied here is a signal defined by a 7^{th}-order polynomial function that enables a smooth velocity, acceleration, and jerk trajectory, namely the 1^{st}, 2^{nd}, and 3^{rd} derivative of the position respectively. All the simulations and experiments in the following sections take this trajectory as default test signal.

In order to facilitate the control strategy validation, during the simulation, the dynamic weight $\lambda(t)$ and the reference pressure $P_1^d(t)$ are defined as constants of which the derivatives are equal to zero. Experiments will be conducted with time-variant functions applied to these parameters in section 5.6. As the pressure without direct control in each actuator chamber is more than 110 bar, we apply here a relative low pressure of 80 bar as the reference one (P_1^d for the P-Y control and P_0 for the Y-λ control) to alternate the system stiffness in our multivariable controls.

Firstly, to validate the proposed control laws, the control gains applied in simulations are relatively low values defined as follows:
a) Y-λ : $c_1 = 500\,\mathrm{s}^{-1}, c_2 = 400\,\mathrm{s}^{-1}, c_3 = 400\,\mathrm{s}^{-1}, c_4 = 400\,\mathrm{s}^{-1}, \lambda = 0,5, P_0 = 80\,bar$;
b) P-Y : $c_1 = 500\,\mathrm{s}^{-1}, c_2 = 400\,\mathrm{s}^{-1}, c_3 = 400\,\mathrm{s}^{-1}, c_4 = 400\,\mathrm{s}^{-1}, P_1^d = 80\,bar$.

Figure 5.5 and 5.6 present the simulation results obtained by applying the proposed controls. It can be observed that both of them show a relative high accuracy in position tracking. The system trajectories obtained in simulations show a good agreement with the desired ones, except that the position error increase to around 0.3 mm on the rising edge of the trajectories and that a steady state error appears for the Y-λ control. For the Y-λ control, the static error in λ tracking is nearly 1 and the dynamic one reaches more than 2. This is probably due to the fact that in the process of pressure distribution, the pressure difference $\Delta P = P_1 - P_2$ is estimated by the function $\alpha_1(.)$ (5.26), whereas the calculation of λ (5.64) uses the actual pressure difference.

$$\lambda = \frac{P_1 - P_0}{\Delta P} \tag{5.64}$$

The pressure tracking errors for the P-Y control are around 1 bar at steady state and less than 5 bar in transient regime. It will be improved by increasing the control gain c_4 as in section 5.6.2. According to the simulations, we can notice that the proposed control laws have good dynamic performances with a high response speed. Besides, the error at equilibrium position is negligible, this is especially true for the P-Y control.

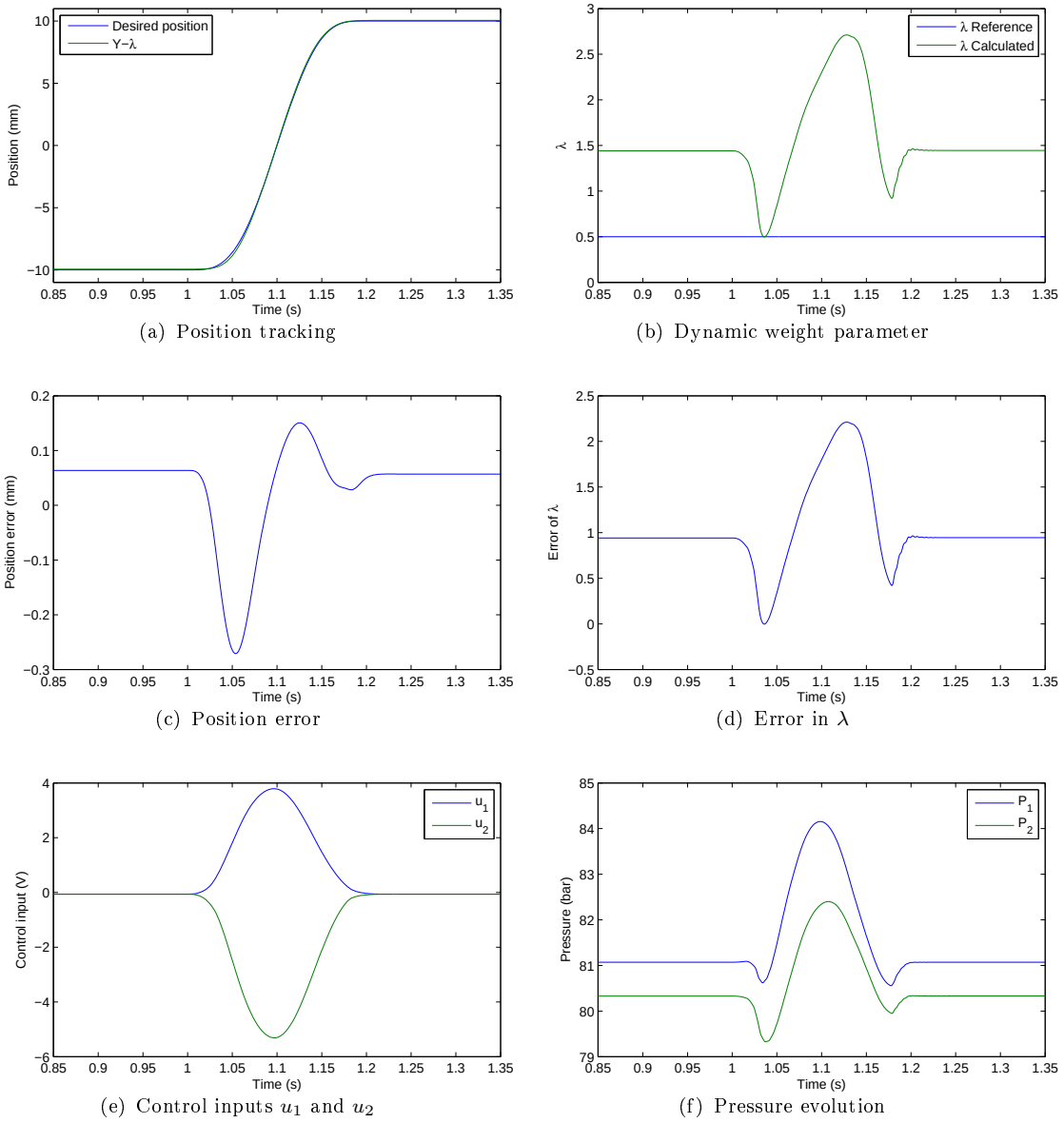

(a) Position tracking

(b) Dynamic weight parameter

(c) Position error

(d) Error in λ

(e) Control inputs u_1 and u_2

(f) Pressure evolution

FIGURE 5.5: Simulation results obtained by the Y-λ control based on the backstepping

5.6 Experimental validation and results

After the validation of the control performance in simulations, the proposed control laws have been implemented on the test bench. The position is given by a LVDT position sensor installed on the actuator rod. The sensor linearity is less than 0.1% and its sensibility is 4 mV/V/mm. The pressures in actuator chambers are measured from pressure sensors with a precision of $\pm 0.1\%$. All these signals are collected on an analog conditioning unit, and then digitalized at a sampling rate of

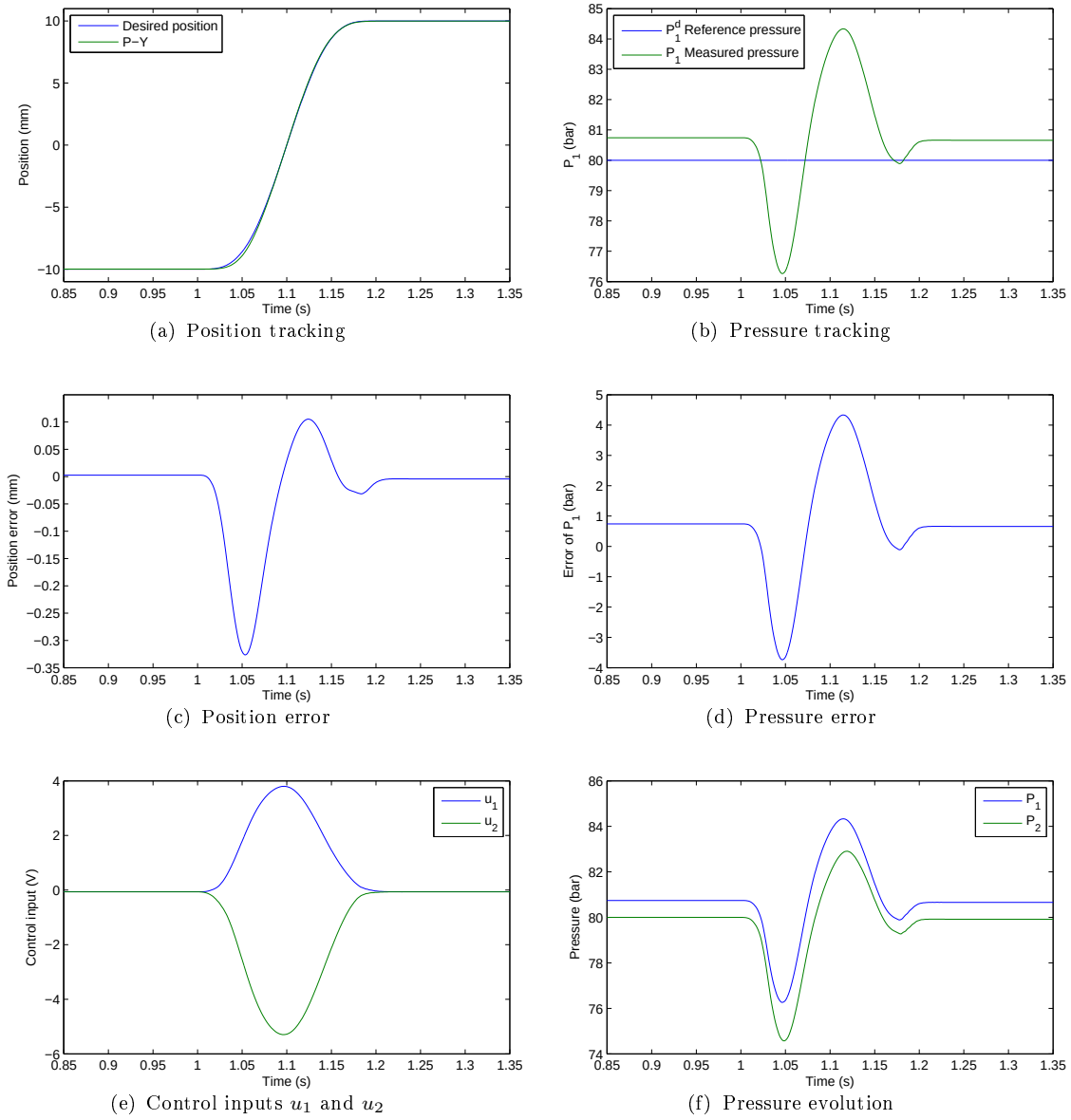

(a) Position tracking

(b) Pressure tracking

(c) Position error

(d) Pressure error

(e) Control inputs u_1 and u_2

(f) Pressure evolution

FIGURE 5.6: Simulation results obtained by the P-Y control based on the backstepping

1 kHz with 16 bits precision on a dSPACE acquisition board (DS1104). Velocity and acceleration are calculated from the on-line 2^{nd}-order adaptive differentiators [Sidhom 2011b, Sidhom 2011a] as described in section 5.4. The control gains of the differentiators are given by $K_{d0} = 200\,\text{s}^{-1}$ and $K_{d1} = 80\,\text{s}^{-1}$ as the default values if not specified in the following sections.

The experiments focus on the validation of the proposed control laws, and the control performance analysis. The desired position trajectory applied here is a

signal defined by the 7^{th}-order polynomial function as mentioned in section 5.5. The dynamic weight $\lambda(t)$ is chosen as constant while a brief discussion about different values is conducted in section 5.6.3. In the first two experiments in sections 5.6.1 and 5.6.2, the reference pressures $P_1^d(t)$ and $P_0(t)$ are constant, whereas they are defined by a time-variant function in section 5.6.3.

5.6.1 Experimental validation

Firstly, to validate the proposed control laws, we apply low gain values to both backstepping-based controls as in section 5.5:
a) Y-λ : $c_1 = 500\,\mathrm{s}^{-1}, c_2 = 400\,\mathrm{s}^{-1}, c_3 = 400\,\mathrm{s}^{-1}, c_4 = 400\,\mathrm{s}^{-1}, \lambda = 0,5, P_0 = 80\,bar$;
b) P-Y : $c_1 = 500\,\mathrm{s}^{-1}, c_2 = 400\,\mathrm{s}^{-1}, c_3 = 400\,\mathrm{s}^{-1}, c_4 = 400\,\mathrm{s}^{-1}, P_1^d = 80\,bar$.

Figure 5.7 presents the experimental and simulation results obtained with the backstepping-based controls. According to the figure, it can be noticed that the simulation and experiment results have a good agreement in the evolution of the studied variables, except for some obvious offsets in steady state and some amplitude differences in transient phase due to the precision of the parameter estimation and dynamic modelling. However, the tendency of the results concerning the comparison of both control methods is well respected between simulation and experiments. Hence, it is proved that the virtual prototype is able to obtain relatively accurate results when a sophisticated control law is implemented on it.

The experimental results (figure 5.7) show that there is a slight offset between the desired and measured trajectories in transient phase and at steady state, except at the beginning of the transient phase. The mean position error in steady state condition is about 2 μm for the Y-λ control and -79 μm for the P-Y control respectively, whereas the maximum position error in the transient part of the trajectory is nearly 660 μm for Y-λ and 664 μm for P-Y control.

Besides, it can be observed that the commands are smooth, which leads to a good energy efficiency. Similarly, the pressure varies smoothly without any sharp

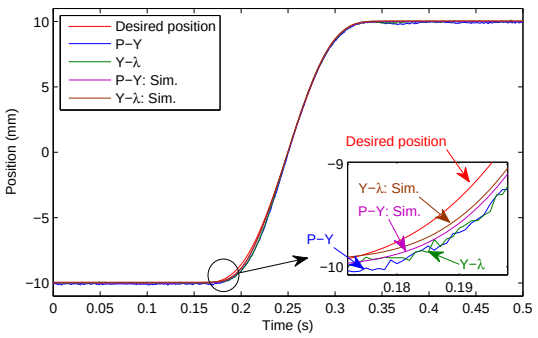

(a) Position tracking

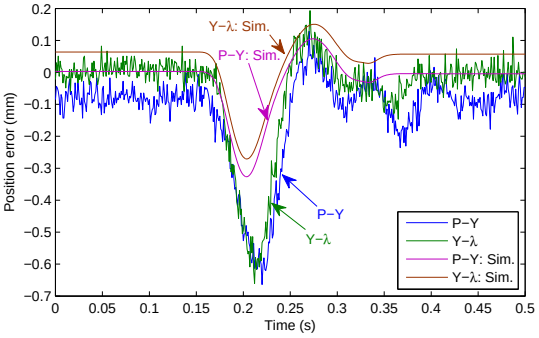

(b) Position error

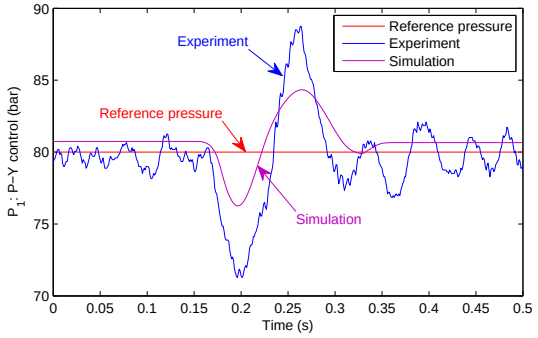

(c) Pressure tracking: P-Y

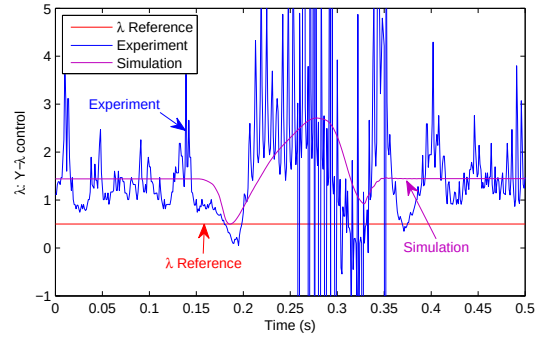

(d) Dynamic weight parameter: Y-λ

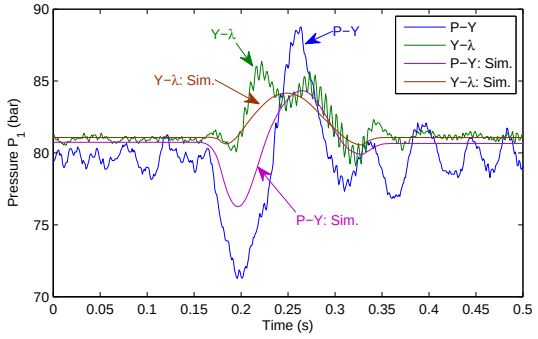

(e) Pressure P_1 evolution

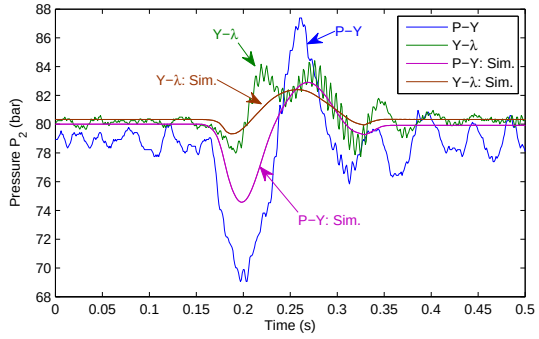

(f) Pressure P_2 evolution

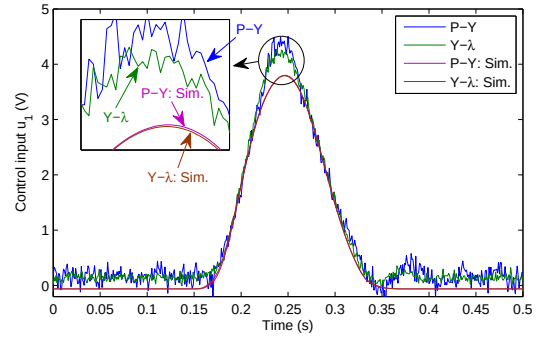

(g) Control input u_1

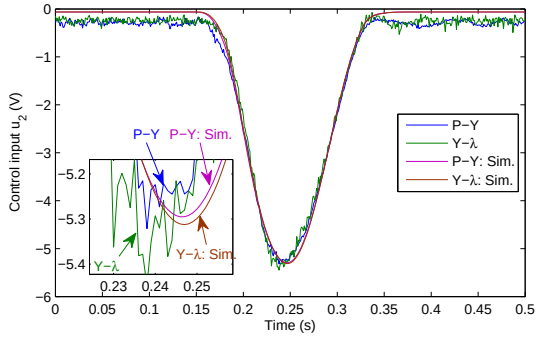

(h) Control input u_2

FIGURE 5.7: Experimental and simulation results obtained with the backstepping-based multivariable control using low gain values

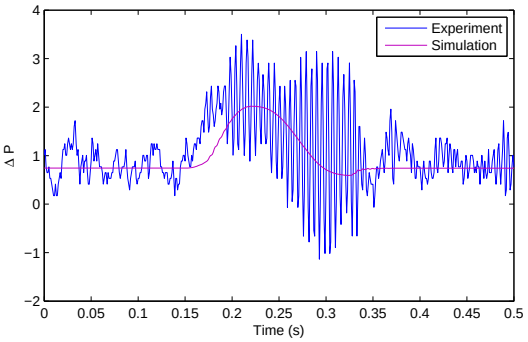

FIGURE 5.8: Pressure difference in the Y-λ control (low gains)

impulsion, but there are high frequency pressure oscillations in transient phase for the Y-λ control.

However, the evolution of the dynamic weight for the Y-λ control presents a violent fluctuation. This is caused by the pressure oscillations and the low precision of the pressure difference. This difficulty is increased due to the pressure sensors precision ($\approx \pm 0.2$ bar), while the pressure difference has a small mean value, e.g. 1 bar as shown in figure 5.8. Hence, the measurement incertitude for the pressure difference is $\pm 40\%$. On the other hand, in the dynamic weight calculation, the small pressure difference at the denominator in (5.64) will result in a low precision of the parameter estimation and great fluctuation.

5.6.2 Comparative experiments and results with high gains values

Low gain values do not enable the best performances to be achieved. Let us use higher gain values now:
a) Y-λ : $c_1 = 700\,\mathrm{s}^{-1}, c_2 = 600\,\mathrm{s}^{-1}, c_3 = 700\,\mathrm{s}^{-1}, c_4 = 700\,\mathrm{s}^{-1}, \lambda = 0,5, P_0 = 80\,bar$;
b) P-Y : $c_1 = 700\,\mathrm{s}^{-1}, c_2 = 600\,\mathrm{s}^{-1}, c_3 = 600\,\mathrm{s}^{-1}, c_4 = 700\,\mathrm{s}^{-1}, P_1^d = 80\,bar$.

As shown in figure 5.9, the tracking performance are significantly improved. Increasing the gains improves the response speed and reduces the tracking errors. The mean steady state error is now about -20 μm for the Y-λ control and -43 μm for the P-Y control. The maximum position error in the transient part is less than

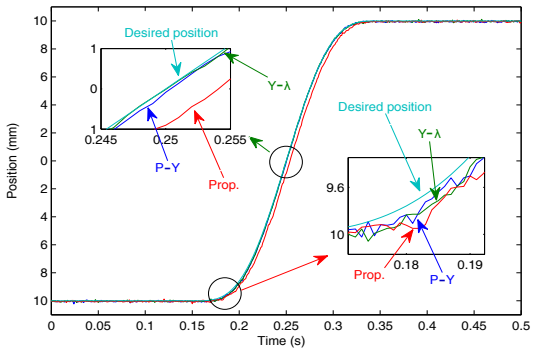

(a) Position tracking

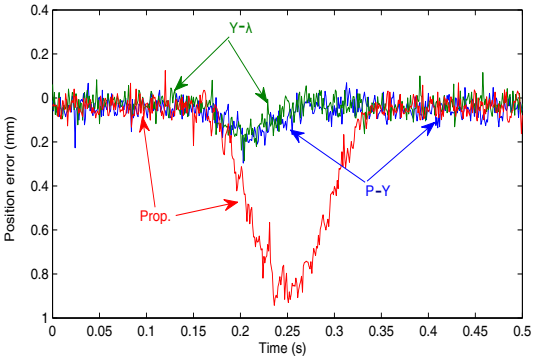

(b) Position error

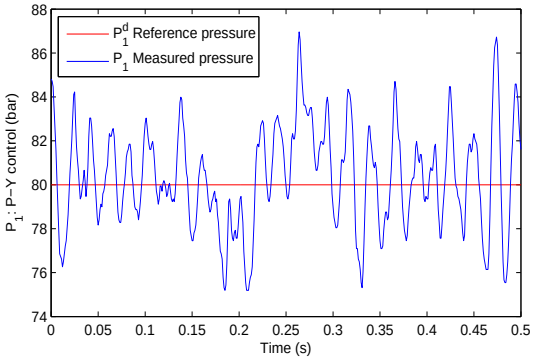

(c) Pressure tracking: P-Y

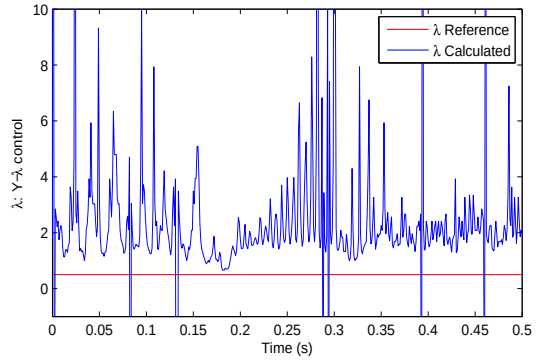

(d) Dynamic weight parameter: Y-λ

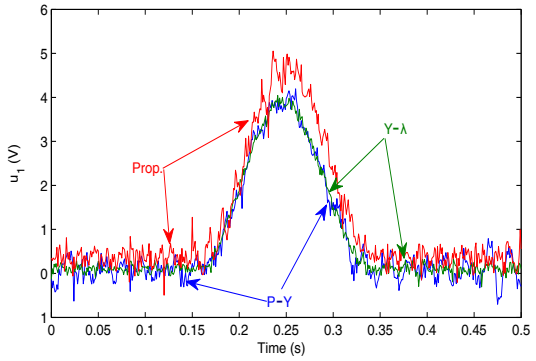

(e) Control input u_1

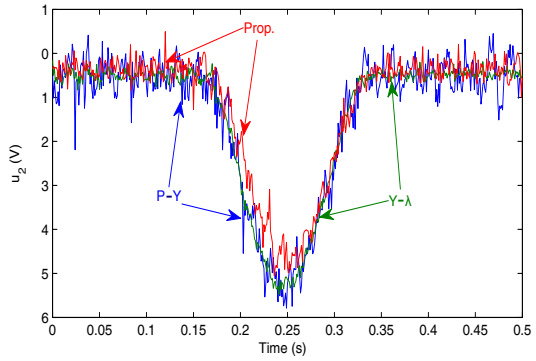

(f) Control input u_2

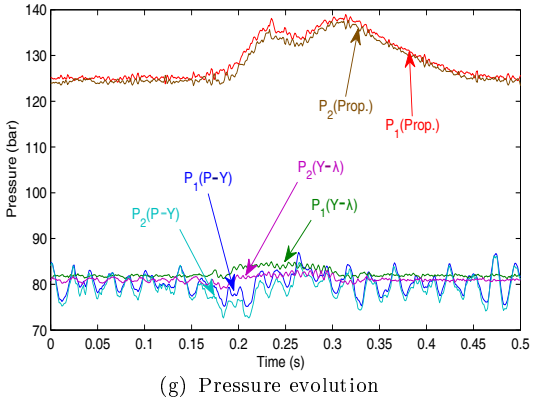

(g) Pressure evolution

FIGURE 5.9: Experimental results with high gain value; comparison with proportional control

286 μm for the Y-λ and 296 μm for P-Y control. Compared with the previous results (experiment with low gain values in figure 5.7), it can be noticed that the static position errors are not only reduced, mainly for the P-Y control, but present also much less oscillations. The dynamic errors are much more reduced by more than twice.

Besides, it can be observed that as the gain values increase, the SNR (Signal-to-Noise Ratio) of the commands decreases slightly; this introduces low frequency oscillations with a notable amplitude in pressure evolution for the P-Y control.

On the other hand, pressure offset and λ offset between the desired and measured results are reduced by increasing the control gains, particularly those related to the pressure control such as c_4 in P-Y, and c_3, c_4 in Y-λ. The Y-λ control presents a better performance on the pressure control (figure 5.9(g)). When a significant change in position occurs, e.g. at about 0.25 s in figures 5.7 and 5.9, the P-Y control results in a pressure variation with a large amplitude, whereas the Y-λ control introduces a smaller amplitude fluctuation for both gain values. This confirms the simulation results (figures 5.5 and 5.6).

For comparison, a proportional control (5.65) has also been implemented as a position feedback with the highest possible gain value until no significant performance improvement is observed. The final value of the proportional gain applied here is 5200 V/m.

$$u_1 = -u_2 = K_P \cdot (y^d - y) \tag{5.65}$$

Compared with the results obtained using a proportional controller, the backstepping based controls achieve better tracking performances with a higher response speed (figure 5.9). Besides, the conventional linear control focuses only on one control objective, namely the position control, and do not enable any other requirement to be fulfilled such as a pressure trajectory. Furthermore, for the position control, it uses only the position error, and not the velocity, or acceleration error which avoid any anticipation of the control.

TABLE 5.1: Position errors of backstepping-based controls and proportional control

Control strategy	Transient phase		Steady state	
	Max.(μm)	STD[a](μm)	Mean(μm)	STD[a](μm)
Y-λ (LG[b])	660	214	2	32
P-Y (LG[b])	664	205	-79	33
Y-λ (HG[c])	286	63	-20	36
P-Y (HG[c])	296	60	-43	36
Prop.	943	304	-41	35

a) STD: Standard deviation

b) LG: low gain values

c) HG: high gain values

A comparative summary is given in table 5.1. Here, the LVDT position sensor has a linearity error of 0.3 mm. Clearly, the proposed control laws based on the backstepping show better performances than the conventional proportional method in transient phase. In steady state, the improvement can not be clearly observed. However, both proposed backstepping-based control laws have identical performances whatever the initial conditions are (near cylinder's end for example); this is not the case for the linear control.

5.6.3 Experiments on pressure control

Instead of using a constant pressure set value as shown previously, the pressure can also be defined as a trajectory which can correspond to some application requirements. Thus, the pressure trajectory may vary as a function of time. Figure 5.10 shows the experimental results obtained when the desired pressure is a sinusoidal function at 0.5 Hz and 10 bar amplitude with an offset of 80 bar in the P-Y control. In the Y-λ control, this desired pressure function is applied as the reference pressure P_0 with the dynamic coefficient λ equal to 0.5. Firstly, let us analyze the experimental results when applying the low gain values (as in section 5.6.1).

Along with the evolution of the reference pressure P_0 and P_1^d, the pressures P_1 and P_2 follow the desired profiles. However, the effect of the position riding can

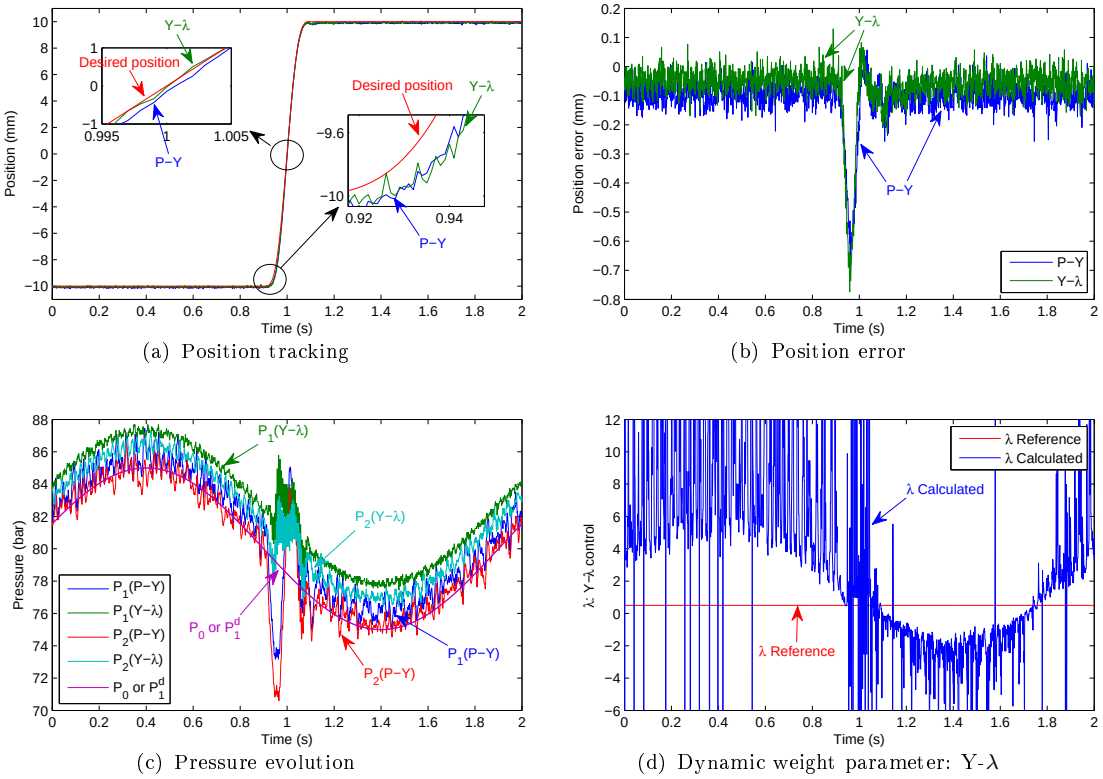

(a) Position tracking (b) Position error

(c) Pressure evolution (d) Dynamic weight parameter: Y-λ

FIGURE 5.10: Experimental results with sinusoidal pressure trajectory: 1) Y-λ: $\lambda = 0.5$, $P_0 = 80 + 10\sin(\pi t)$; 2) P-Y: $P_1^d = 80 + 10\sin(\pi t)$

more clearly be seen around 1 s on the P-Y control. The dynamic weight λ of the Y-λ control algorithm can precisely adjust the pressure distribution in the two chambers and attenuates the pressure changes when the position step occurs.

According to figure 5.10(b), the maximum error in transient phase increases to 672 μm for the P-Y control, and 774 μm for the Y-λ control. The amplitude of the error is not noticeably increasing by comparison to the results obtained with a constant pressure trajectory (figure 5.7(b)) when using the same gains values. Hence, the position tracking accuracy keeps the same level enven with a variable desired pressure.

Besides, it is interesting to remark that the Y-λ control is equivalent to the P-Y control in some particular cases. When λ equals to 1, the pressure trajectory in chamber P_2 is directly P_0, whereas it is the pressure trajectory P_1 which is equal to P0 when λ equals to 0. In this last case ($\lambda = 0$), the Y-λ control is equivalent to

the P-Y control. Figure 5.11 illustrates the experimental pressure evolution with different values of λ.

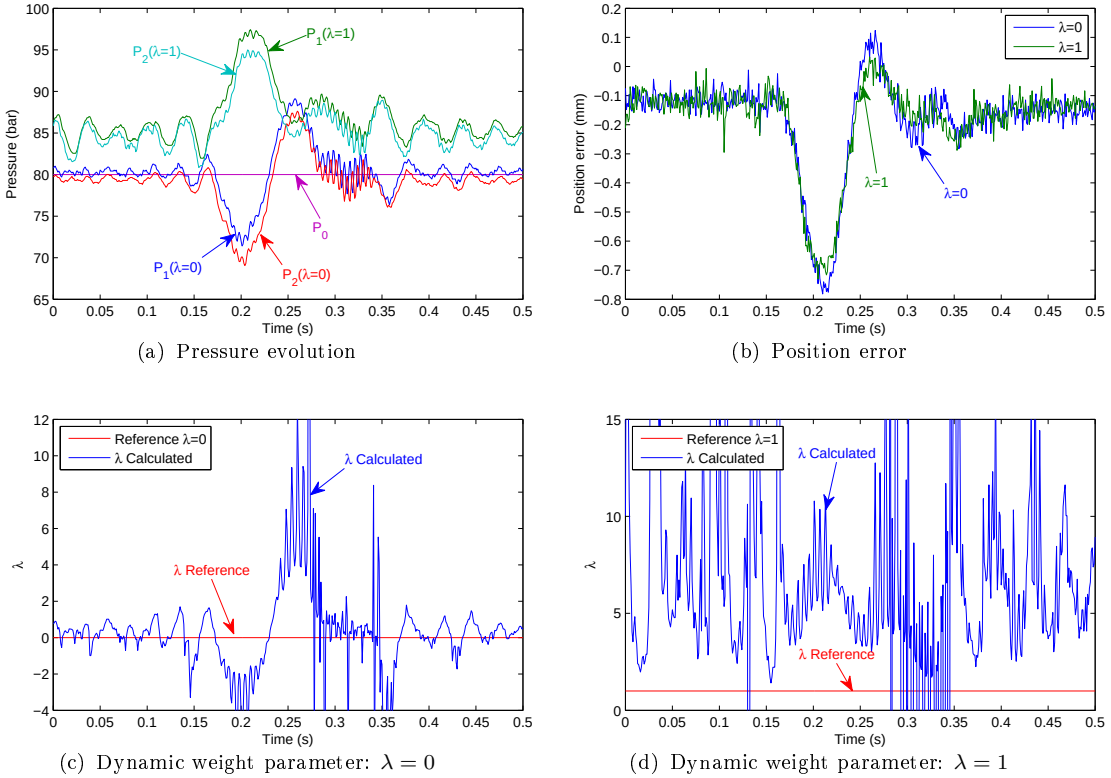

(a) Pressure evolution

(b) Position error

(c) Dynamic weight parameter: $\lambda = 0$

(d) Dynamic weight parameter: $\lambda = 1$

FIGURE 5.11: Experimental results with different λ

From figure 5.11, the mean value of P_1 at $\lambda = 0$ show a bias from the reference pressure P_0 of a slight amplitude of about 0.35 bar. At $\lambda = 1$, the offset of the mean value of P_2 rises 4.23 bar. Meanwhile, the error in λ is obviously less at $\lambda = 0$ where the direct control pressure is P_1 than at $\lambda = 1$ where P_2 is directly controlled. Trying to explain this, it is believed that the increase of the static error in pressure is related to the fact that the local geometric defects of the two servovalves leads to behaviour which are not exactly symmetrical; this results in a low precision at small opening.

Additionally, the maximum pressure shift are 8.96 bar for $\lambda = 0$ and 10.78 bar for $\lambda = 1$ in transient phase. When the position rising edge of the desired trajectory occurs, the same pressure tends to vary in two opposite directions for the two different values of λ ($\lambda = 0$ and $\lambda = 1$). It can be explained mathematically by

the following pressure expressions:

$$\text{a) For } \lambda = 0: \begin{cases} P_1 = P_0 \\ P_2 = P_0 - \alpha_1(e_1, e_2, v^d, a^d) \end{cases} \tag{5.66}$$

$$\text{b) For } \lambda = 1: \begin{cases} P_1 = P_0 + \alpha_1(e_1, e_2, v^d, a^d) \\ P_2 = P_0 \end{cases} \tag{5.67}$$

where $\alpha_1(\cdot)$ represents the estimation pressure drop $\Delta\hat{P} = \hat{P}_1 - \hat{P}_2$ from 5.64. This value increases when the position rises, which results in the pressure diminution of P_2 for $\lambda = 0$, and the pressure augmentation of P_1 for $\lambda = 1$. On the other hand, in order to guarantee the position tracking accuracy, the other modulated pressure P_1 ($\lambda = 0$) or P_2 ($\lambda = 1$) follows the pressure variation mentioned above until the system reaches the equilibrium state.

5.7 Conclusion

The electro-hydraulic system presents nonlinearities, which make difficult to implement controls with high accuracy by conventional linear method. This chapter proposes two nonlinear control strategies based on backstepping. These two strategies can achieve multiple-objective controls on our specific test bench on which the hydraulic actuator is equipped with 2 servovalves. The proposed controls were validated by simulation and experimentally, then they have shown good steady state and dynamic performances with a very short response time. Besides, according to those controls, the pressures can easily be modulated according to the application requirements (dynamic stiffness, efficiency etc.). Compared to conventional linear control, the proposed controls are more suitable for position tracking tasks. The dynamic weight λ in the Y-λ control allows a better tracking of pressures by comparison with the P-Y control.

Since a system model is required for the proposed backstepping-based control strategies, and in some cases, the model parameter is not accurate due to its estimation method or to the perturbation, it is also essential to evaluate if the control strategy can retain good performances against parameter incertitude perturbations. Therefore, a brief robustness analysis will be conducted for the backstepping-based control laws in chapter 7.

As it has been shown in this chapter, the backstepping approach provides a nice environment to design control laws which guarantee global stability of the system. However, the command model has to be put in a strict feedback form and this was possible on our test bench thanks to the two servovalve command inputs. In the case of position tracking control, this requires to define an additional trajectory, here pressure for P-Y or a pressure weight for Y-λ, which is not necessarily an obvious task in any context. Of course, energy consumption and actuation efficiency can be a research direction, but robustness performances can also be considered.

Besides, the controller gains introduced by the backstepping approach are not directly linked to a single physical variable and this makes the tuning of the gains difficult to achieved in an industrial context. Therefore, in the next chapter, we will explore a new control approach introduced recently called model-free control, which tackles the drawbacks of the linear controllers but keeps the ease of the controller gain tuning.

Chapter 6

Control of the test bench by the model-free method

Contents

6.1 Introduction

In the previous chapter, two nonlinear control laws based on the backstepping method have been developed. These methods show good performances in the

control of the hydraulic system. However, they have a certain complexity that could limit their application in industry as several control parameters are involved to tune the system performance. In this chapter, on the contrary, we will adopt a novel control strategy, the model-free control method, which allows good control to be achieved without considering an accurate system model.

Indeed, the model-free method does not require the use of a global system model. Instead, it introduces a common ultra-local model which aims at approximating the unknown system dynamics on a very short time interval. Moreover, its parameters are estimated rapidly by gathering the system state information from sensors, and will automatically be updated on every time interval. This means it can work automatically without manual intervention once well configured. Therefore, compared to the methods based on nonlinear control theory, it provides a new way to control a complex nonlinear system and it has the advantage to be easy to implement. The tuning of the control law coefficients is simplified compared to other nonlinear methods.

This approach is applied here on our hydraulic test bench for the position tracking control. Besides, an evolution of the model-free control, the control with a restricted model was also implemented. This technique is based on a limited model of the system to be controlled. For example, it can be a partial model, the unknown part being estimated by the mentioned method, i.e. the model-free control. In this case, since more information are known about the system, the control algorithm should provide better control performances.

Firstly, section 6.2 will give a review of the model-free control method. The implementation of the model-free based controls in the case of our hydraulic test bench will be illustrated in section 6.3. Then, simulations will be conducted with the virtual prototype developed in AMESim in section 6.4. Finally, experiments will be carried out with different control gain values in section 6.5.

6.2 Review of the model-free control algorithm

In industry, the most popular feedback design approach is still the PID controller even if it has modest performances. The reason is that it has a very simple structure and can be tuned according to a number of existing rules in the literature [Aström 2006, O'Dwyer 2006]. However, it is valid only for first and second order linear systems with constant coefficients. When dealing with nonlinear systems or those involving time-varying parameters, the classic PID controller becomes inadequate and will result in the deterioration of system performances and stability. Meanwhile, although a large number of nonlinear control strategies [Bartolini 2003, Smaoui 2006, Precup 2011, dos Santos Coelho 2011] arose during the last decades, they are rarely employed in industry because they require on one side mathematical modelling with some precision and on the other side complexity in implementation and controller parameter tuning. In [Riachy 2011], authors investigated a comparison between high-order sliding modes and model-free control with two concrete cases. The model-free control presents good control performances and is more robust with respect to noise.

This new control approach, called model-free control, was recently developed by Fliess and Join in [Fliess 2008, Fliess 2009, Fliess 2011]. This approach does not need any mathematical modelling. Instead, it introduces a simple local model which can approximate the unknown system dynamics on a very small time interval, avoiding the difficult task of developing a global system model. The controller parameters will be automatically estimated and updated according to the knowledge of the input-output behaviour. Because of its ease of implementation and its straightforward coefficient tuning, the model-free control method has been successfully applied in several domains, such as automobile [Choi 2009, Villagra 2009, d'Andréa Novel 2010a], electro-hydraulics [Join 2010], and applications of new technologies [Gédouin 2008, Gédouin 2009].

Consider a system in which the input-output behaviour is dominated by an unknown finite-dimensional differential equation (6.1) as follows:

$$\Phi_j(\boldsymbol{y}, \cdots, \boldsymbol{y}^{(N_j)}, \boldsymbol{u}, \cdots, \boldsymbol{u}^{(M_j)}) = 0 \tag{6.1}$$

where

- $\boldsymbol{u} = (u_1, \cdots, u_m)$ and $\boldsymbol{y} = (y_1, \cdots, y_p)$ are sets of input and output variables respectively;
- Φ_j, $j = 1, \cdots, p$ are polynomial functions.

Note that equations in (6.1) are not necessarily linear. Assume that the system is left invertible. If there are more output variables than input ones, namely $p > m$, take m output variables in order to get an invertible square system.

We introduce the following ultra-local model (6.2) to represent this unknown system, which is only valid during a very short time interval.

$$\begin{cases} y_1^{(n_1)} = F_1 + \alpha_{1,1}u_1 + \cdots + \alpha_{1,m}u_m \\ \vdots \\ y_p^{(n_p)} = F_p + \alpha_{p,1}u_1 + \cdots + \alpha_{p,m}u_m \end{cases} \tag{6.2}$$

where

- $n_j \geq 1$, $j = 1, \cdots, p$, are the differentiation order, usually $n_j = 1$ or 2;
- $\alpha_{j,i} \in \mathbb{R}$, $i = 1, \cdots, m$, are non-physical constant parameters chosen by user so that $\alpha_{j,i}u_i$ and F_j have the same magnitude;
- F_j are parameters representing the system structural information.

The value of F_j is derived from those of $\boldsymbol{u}$ and $y_j^{(n_j)}$. Algebraic loops can be avoided by applying the following expression to estimate F_j as the implementation is done at a given sampling time.

$$\widehat{F}_j(k) = \widehat{y}_j^{(n_j)} - \sum_{i=1}^{m} \alpha_{j,i}u_i(k-1) \tag{6.3}$$

where

- $\widehat{F}_j(k)$ and $\widehat{y}_j^{(n_j)}$ stand for the estimated value of F_j and $y_j^{(n_j)}$ at time step k;
- $u_i(k-1)$ is the control input at time step $k-1$.

Hence, the controller, called intelligent PID controller or i-PID, takes the following form:

$$\boldsymbol{u} = \boldsymbol{A}^{-1}(\tilde{\boldsymbol{y}}_d - \boldsymbol{F}) + \boldsymbol{K}_P \boldsymbol{e} + \boldsymbol{K}_I \int \boldsymbol{e} + \boldsymbol{K}_D \dot{\boldsymbol{e}} \tag{6.4}$$

where

- $\boldsymbol{A}$ is a $p \times m$ matrix with $(j,i)^{\text{th}}$ element $\alpha_{j,i}$. In fact, $p = m$ due to the invertible square system;
- $\tilde{\boldsymbol{y}}_d = [y_{1d}^{(n_1)}, \cdots, y_{pd}^{(n_p)}]^T$ are derivatives of the output reference trajectory;
- $\boldsymbol{F} = [F_1, \cdots, F_p]^T$;
- $\boldsymbol{e} = [y_1 - y_{1d}, \cdots, y_p - y_{pd}]^T$ are the tracking errors;
- $\boldsymbol{K}_P = [K_{P1}, \cdots, K_{Pp}]^T$, $\boldsymbol{K}_I = [K_{I1}, \cdots, K_{Ip}]^T$, $\boldsymbol{K}_D = [K_{D1}, \cdots, K_{Dp}]^T$ are classic PID tuning gains.

In (6.4), the last PID terms are introduced to complete a feedback loop and assure the system stability and performances.

For a monovariable system, the i-PID can be simplified to (6.5) when the differentiation order is equal to 2.

$$u = -\frac{F}{\alpha} + \frac{\ddot{y}_d}{\alpha} + K_P e + K_I \int e + K_D \dot{e} \tag{6.5}$$

If the differentiation order is equal to 1, the feedback loop i-PID can be replaced by a i-PI controller.

Hence, the model-free control strategy is able to bypass the difficult task of mathematical modelling and improve greatly the practical applicability and the performances of the classic PID controller [Fliess 2009]. The intelligent PID controller shows the following advantages over the classic ones [d'Andréa Novel 2010b]:

1) The gain tuning of the i-PID is straightforward since the unknown part is eliminated and the control design handles systems with only an integrator of order 1 or 2. Contrarily, the gain tuning is complex and difficult for classic PIDs despite the numerous existing rules in the literature [Aström 2006, O'Dwyer 2006].
2) The i-PID has better robustness performances against system perturbations, while the classic PID controller, when correctly tuned, is unable to deal with this kind of change such as heat effects, ageing processes, and characteristic dispersions due to mass production.
3) The intelligent controllers show a much better fault tolerant control than the classic ones.

6.3 Model-free control design

The configuration of the test bench is the same as the one used for the backstepping-based control described in the chapter 5. The bench works in mode 3, namely, the two servovalves work as 3-way components to control the flow in each actuator chamber. The model-free based controls are applied in the test bench to achieve the piston position control. The implementation of the control methods are described in the following part.

6.3.1 Model-free control

The electro-hydraulic system is here considered as a SISO (single input single output) system by taking the opposite command condition for the servovalves, namely,

$$u = u_1 = -u_2. \tag{6.6}$$

The output of the system is the actuator piston displacement. According to the model-free method, we do not need any information about the system model. In a very short time step (in practice, the sampling period ΔT) the system is modelled

by

$$\dot{y}(t) = F(t) + \alpha u(t) \tag{6.7}$$

where F represents the unmodelled or time-varying part of the system and will be updated automatically; α is a parameter chosen by the user such that αu and F have the same magnitude.

Then, the value of F is evaluated from those of u and $\dot{y}$ at any time step as the following:

$$\widehat{F}_k = \widehat{\dot{y}}_k - \alpha u_{k-1} \tag{6.8}$$

where $\widehat{F}_k$, $\widehat{\dot{y}}_k$ are the estimated values of F and $\dot{y}$ at time step k; u_{k-1} is the command at time step $k-1$. Moreover, $\widehat{\dot{y}}_k$ is obtained from position movement differentiation by applying the adaptive high-order sliding modes differentiator [Sidhom 2011b, Sidhom 2011a].

The controller is then developed from equation (6.7) as follows:

$$u_k = -\frac{\widehat{F}_k}{\alpha} + \frac{\dot{y}_k^d}{\alpha} + K_P e_k + K_I \sum (e_k \cdot \Delta T) \tag{6.9}$$

where u_k is the command at time step k; $\dot{y}_k^d$ is the desired velocity at time step k; $e_k = y_k - y_k^d$ is the tracking error; K_P, K_I are the classic PI tuning gains.

The block diagram of the model-free control is presented in figure 6.1. This controller is called the intelligent PI controller or i-PI in [Fliess 2008, Fliess 2009].

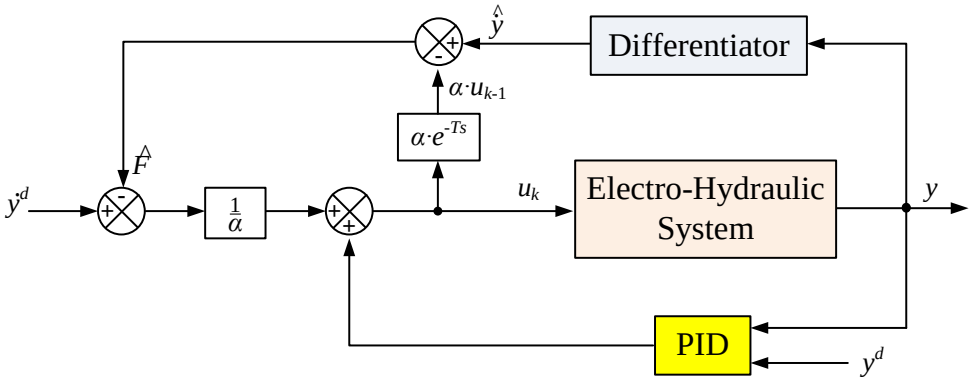

FIGURE 6.1: Scheme of the model-free control

The last PI part is required to assure the stability of the system and better performances. Compared with a classic PI controller, the i-PI controller contains a part involving the system structure information represented by the estimation of F. Therefore, the i-PI can improve the system robustness and tracking performance in comparison with the classical PI without requiring a complex tuning of the parameters as it is the case for nonlinear control laws.

6.3.2 Control with restricted model

A restricted model or an approximate model can be used to improve the precalculation of the open-loop command which is applied according to the desired position. In our case, the following assumptions are considered:

1) the internal and external leakages are ignored;

2) the dynamics of the servovalves is neglected;

3) the flow rates are considered proportional to the command.

This restricted model is given by (5.36) in chapter 5. As we consider only a SISO system with the model-free based controls, the pressures are not directly controlled. Instead, the opposite command condition as given by equation (6.6) is taken into account. Then, this system is degraded to a SISO one with an input command u and a position output y as described in (6.10).

$$\begin{cases} \frac{dy}{dt} = & v \\ \frac{dv}{dt} = & a \\ \frac{da}{dt} = & \frac{1}{M}\Bigg(-ba - \frac{\partial F_{fs}(v)}{\partial v}a - A^2\beta\left(\frac{1}{V_1(y)} + \frac{1}{V_2(y)}\right)v \\ & \quad + A\beta\left(\frac{\phi_1(\cdot)}{V_1(y)} + \frac{\phi_2(\cdot)}{V_2(y)}\right)\cdot u\Bigg) \end{cases} \tag{6.10}$$

$$\text{where } \phi_i = \frac{Q_n}{u_n}\sqrt{\frac{|P_P - P_i|}{\Delta P_n}}\frac{sign(u_i)+1}{2} + \frac{Q_n}{u_n}\sqrt{\frac{|P_i - P_T|}{\Delta P_n}}\frac{1-sign(u_i)}{2}$$

$$F_{fs}(v) = \left(F_C + (F_{sdyn} - F_C)\, e^{-C\left|\frac{v}{v_0}\right|}\right) tanh\left(\frac{v}{v_0}\right)$$

By inverting the dynamics model (6.10), an open-loop nominal command is given by

$$u^* = \frac{M \cdot j^d + b \cdot a^d + \frac{\partial F_{fs}(v^d)}{\partial v^d} \cdot a^d + A^2\beta\left(\frac{1}{V_1(y^d)} + \frac{1}{V_2(y^d)}\right) \cdot v^d}{A\beta\left(\frac{\phi_1(\cdot)}{V_1(y^d)} + \frac{\phi_2(\cdot)}{V_1(y^d)}\right)} \tag{6.11}$$

As the system model is incomplete and there exists some unknown effects, the control law can then be defined as

$$u = u^* + \Delta u \tag{6.12}$$

where Δu represents the compensation command of the unknown phenomena or unmodelled parts of the system and also the feedback controller.

We assume that the compensation command complies with the following relationship (6.13) with the system output.

$$\dot{y}(t) = F(t) + \alpha \Delta u(t) \tag{6.13}$$

Similarly to what was done in section 6.3.1, the function F is given by

$$\widehat{F}_k = \widehat{\dot{y}}_k - \alpha \Delta u_{k-1} \tag{6.14}$$

$$\text{where } \Delta u_{k-1} = u_{k-1} - u^*_{k-1} \tag{6.15}$$

u^*_{k-1} is the nominal command at time step $k-1$.

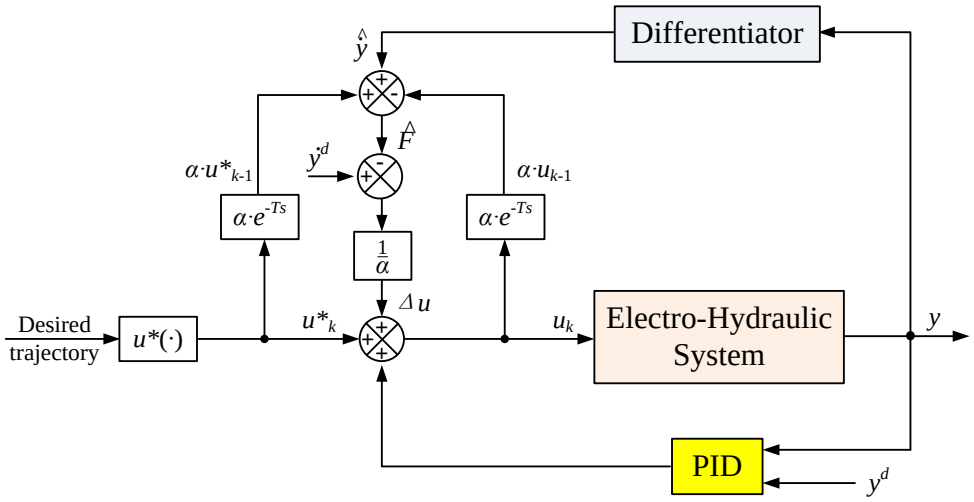

FIGURE 6.2: Scheme of the control with restricted model

The compensation command at time step k is then calculated by

$$\Delta u_k = -\frac{\widehat{F}_k}{\alpha} + \frac{\dot{y}_k^d}{\alpha} + K_P e_k + K_I \sum (e_k \cdot \Delta T) \tag{6.16}$$

Finally, the controller with restricted model is given in the following equation (6.17):

$$u_k = u_k^* - \frac{\widehat{F}_k}{\alpha} + \frac{\dot{y}_k^d}{\alpha} + K_P e_k + K_I \sum (e_k \cdot \Delta T) \tag{6.17}$$

The block diagram of the model-free control is presented in figure 6.2. With more information about the system, we will show that the control with restricted model can achieve better control performances than the model-free control, the i-PI being dedicated to the regulation along the tracked trajectory in this case. Some simulation and experimental results are presented in the following sections.

6.4 Simulation validation and results

According to the design approaches described in section 6.3, we have designed a submodel of the controller based on the model-free method in AMESim. In order to validate the control based on the model-free method, as well as to conduct a robustness analysis in simulation, this submodel is implemented into the AMESim

virtual prototype as for the backstepping-based controls presented in section 5.5. The desired trajectory is still the 7^{th}-order polynomial function that has been described in section 5.5. During the simulation, to calculate the value of F, we use directly the calculated velocity in AMESim, whereas in practice the velocity value is estimated by the on-line numeric differentiator (DAO2). If a problem occurs, this allows to distinguish the origin of the problem, from the controller from the differentiator.

Figures 6.3 and 6.4 show the simulation results obtained by the model-free control. Since the static error is very low, only the gain K_P is really required. We have tested different values of K_P, which showed that the proposed control laws are validated with good performances within values between 30 to 250 V/m. This gain is set here to a low value of 30 V/m in order to guarantee the control stability and modest performances.

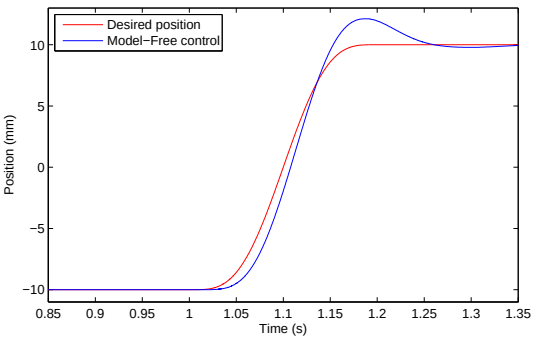

(a) Position tracking

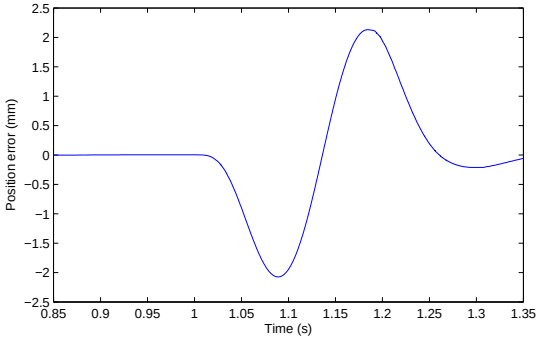

(b) Position error

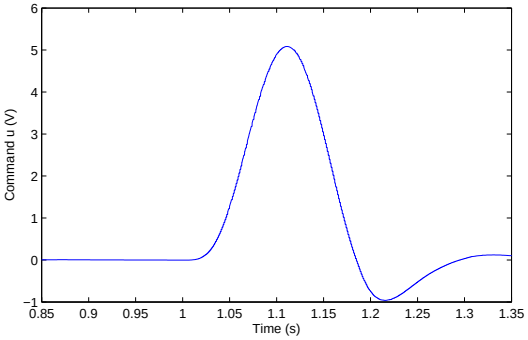

(c) Command u

FIGURE 6.3: Simulation results obtained by the model-free control

In figure 6.3, with a low gain value of 30 V/m, the position trajectory derived from the model-free control still follows the desired one, except that there is a notable

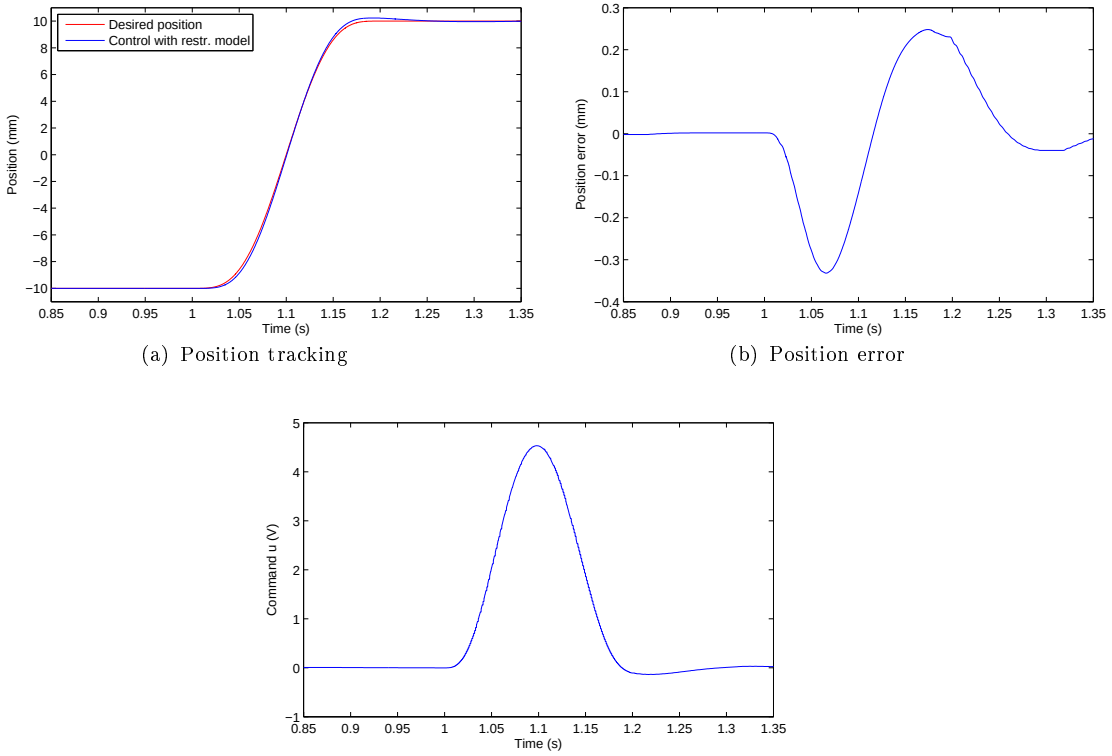

(a) Position tracking

(b) Position error

(c) Command u

FIGURE 6.4: Simulation results obtained by the control with restricted model

position error of about 2 mm in transient phase and an important overshoot occurs at the end of the position rising edge. These results with the virtual prototype in simulation show that the model-free control is applicable to the position tracking on our test bench. As more system information are used in the case of the control with restricted model, we can observed from figure 6.4 that this control strategy provides a shorter response time and a maximum error in transient phase less than 0.35 mm. Clearly, according to the simulation results, the control with restricted model has a better position tracking performance compared with the model-free control. This demonstrate the interest of introducing a pre-compensation term if we want to improve the model-free control.

6.5 Experimental validation and results

The experimental configuration is the same as the one used for the controls based on backstepping algorithm in section 5.6. The piston position is measured with a LVDT sensor. This position signal is collected into dSPACE acquisition board (DS1104) at a sampling frequency of 1 KHz. The velocity information is obtained by applying the online 2^{nd}-order adaptive differentiator (DAO2). The control gains of the differentiator are the same as previously that is $K_{d0} = 200\,\text{s}^{-1}$ and $K_{d1} = 80\,\text{s}^{-1}$. The desired trajectory is still the 7^{th}-order polynomial function as described in section 5.5.

Since the static error is not obvious, to simplify the gain tuning, only the proportional part of the i-PI is used in this experimental study. The parameter α is chosen to keep the magnitudes of αu and F at the same level. Because of the small value of the piston velocity (less than 0.3 m/s) in equation (6.7), the value of α can be set to 1 m/s/V in all experiments.

6.5.1 Experimental validation

In order to validate the model-free control strategy on our test bench, we implemented first a test with a low gain value K_P of 30 V/m as in simulation. Figure 6.5 presents the experimental and simulation results with this low gain value.

As in simulation, the model-free method shows a significant overshoot of 2.12 mm after the rising edge with this low gain K_P, while the control with restricted model maintains a good performance with high control precision not only in steady state, but also in transient phase even with the low value of the gain K_P. The maximum error of the control with restricted model is only 0.19 mm with the same gain value. The control with restricted model has a better performance on the position tracking. In both control laws, the commands are smooth and any critical noise can not be observed. Moreover, it can also be noticed that the simulation and experimental results obtained with the model-free control show a better coherence

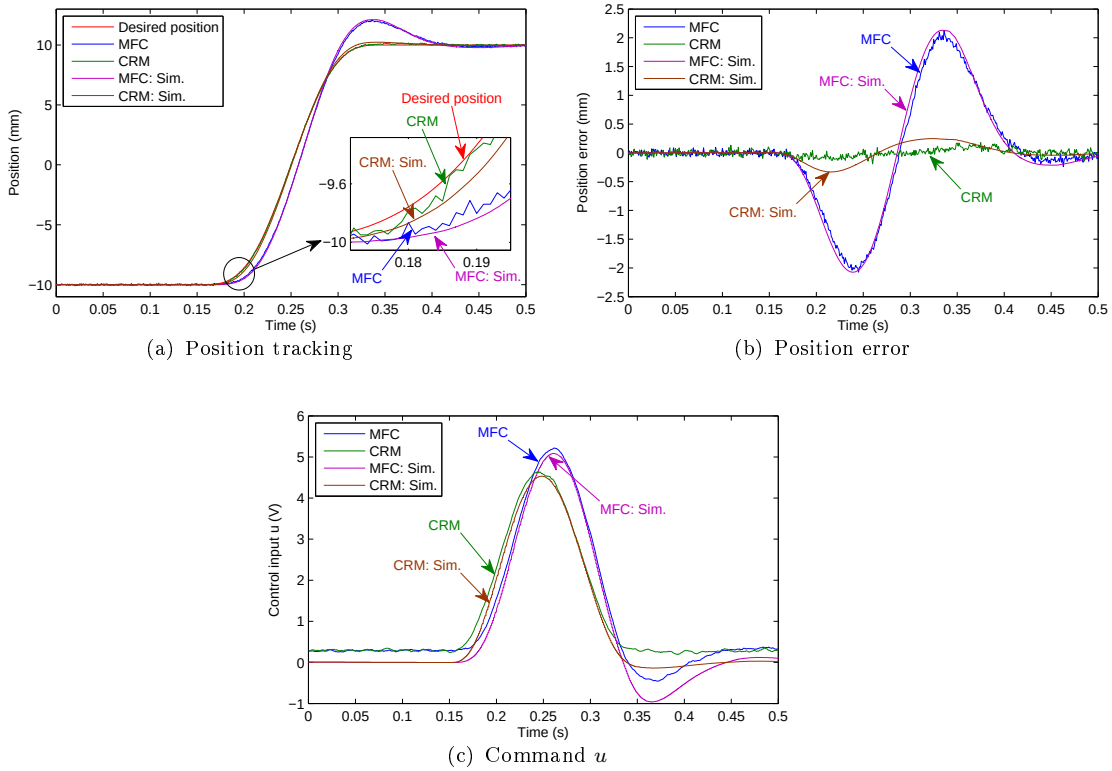

(a) Position tracking

(b) Position error

(c) Command u

FIGURE 6.5: Experimental and simulation results of the control laws based on model-free control with low gain values

than those obtained with the backstepping-based controls (figure 5.7) and the control with restricted model (figure 6.5). This can be explained by the fact that the model-free control is independent of the system model. While there exit some errors in the system modelling and parameter estimation, the results will present less differences than the model-dependent methods. In other words, the model-free control is more robust against the modelling perturbations.

In conclusion, with more information about the system, the control with restricted model provides a better position tracking precision, whereas the model-free control has a better robustness performance against the modelling perturbation due to its model-independence.

6.5.2 Comparative experiment results

As in chapter 5, for comparison, a proportional control has also been implemented with the highest possible gain value until no significant performance improvement is observed. Besides, we manage to increase the gain values of the proposed methods in order to observe how the control performance evolves. The experimental results are given in figure 6.6 with a high gain value K_P of 250 V/m for the model-free based controls.

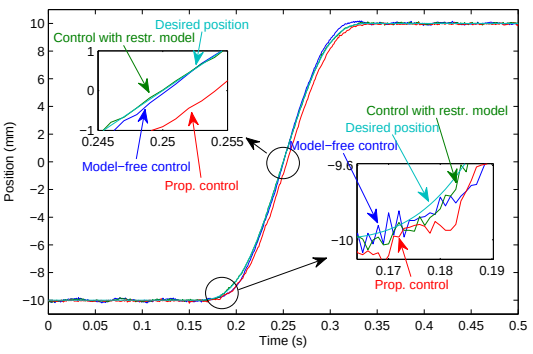

(a) Position tracking

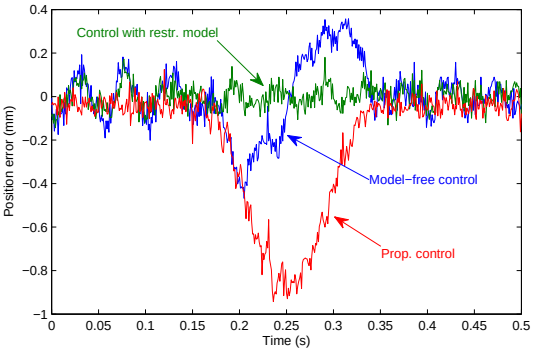

(b) Position error

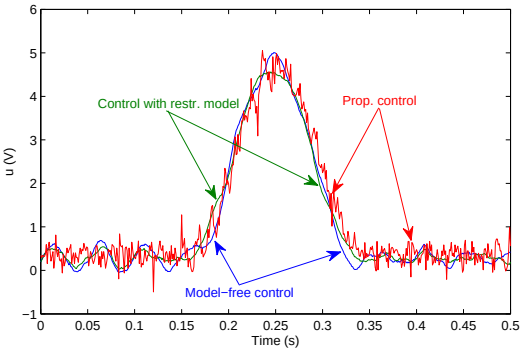

(c) Command u

FIGURE 6.6: Experimental results with high gain value; comparison with proportional control

As shown in figure 6.6, the tracking performance of the model-free control has been significantly improved, compared to figure 6.5, while the position error of the control with restricted model in transient phase has only a slight difference with the one obtained in steady state. However, the increasing of the gain leads to an obvious low amplitude fluctuation of the system response for both the model-free control and the control with restricted model. Compared with the results derived

from the proportional control, the proposed methods show a better tracking performance with a shorter response time. Besides, the control inputs of the proposed methods contain less noise than what is obtained with the proportional control.

Table 6.1 illustrates the position error comparison of the three control strategies for both K_P values. Here, the LVDT position sensor has a linearity error of 0.3 mm. The control with restricted model shows a better tracking performance than the other methods, despite the obvious fluctuation of the system response leading to an important STD value when the gain value is high. However, both proposed control strategies reach good performances.

TABLE 6.1: Comparison summary of the position errors in model-free control (MFC), control with restricted model (CRM), and Proportional control (Prop.)

Control strategy	Transient phase		Steady state	
	Max.(μm)	STD[a](μm)	Mean(μm)	STD[a](μm)
MFC (K_P : 30 V/m)	2122	1344	0.06	39
CRM (K_P : 30 V/m)	192	71	0.2	41
MFC (K_P : 250 V/m)	468	227	0.5	69
CRM (K_P : 250 V/m)	181	48	-0.1	66
Prop.	943	304	-41	35

a) STD: Standard deviation

6.6 Conclusions

In this section, the model-free control and the control with restricted model have been implemented on our high performance test bench. It has been shown that the two control laws can be easily applied to this nonlinear system. After validating these control laws with the developed virtual prototype, the experimental results show that they reach good performances in terms of dynamic property with a very short response time, as well as a high accuracy. Besides, the model-free control requires a higher gain to give nearly equivalent tracking performance as the control with restricted model. It can be explained by the fact that no information on the system are given contrary to the control with restricted model, where a

simple model is used. Compared to the conventional PID controller, the model-free based controls provide a simple way to tune the coefficients and obtain a better tracking precision. To conclude, the model-free based control methods are easy to implement as they do not require a precise model of the system and have good performances with high position tracking precision, and this shows its high potential for application in industry.

Chapter 7

Robustness analysis of the proposed control laws

Contents

7.1 Introduction

It can be expected that applications in real world are much more complex than models developed in laboratory because of certain unpredictable effects, such as changes of the environment temperature, vibration, etc.. Accuracy of the model

is possibly degraded due to the model mis-adjustment, or unavailability of some measurements, or also difficulty of tuning system parameters. When a control strategy is applied in practice, problems may occur and lead to a degraded even unpredictable result. The robustness of a control strategy is thus an important criterion of performance evaluation. Of course, one of the main difficulty of the robustness analysis is to define properly the parameters to check and their range of variation.

This chapter will concentrate on the robustness analysis through both simulation and experimental approaches. One of the main robustness criteria is related to the load mass change. Therefore, sections 7.2 and 7.3 respectively propose a robustness analysis against the mass change of the moving part. In section 7.3, different loads are used on the test bench to estimate the robustness performance of the control strategies. Finally, changes of the gain values of the differentiator are also explored in order to demonstrate the influence of the precision of the tracking performance.

7.2 Robustness analysis based on simulation

7.2.1 Controls based on the backstepping

In simulation, in order to study the influence of the mass change on the control performance, the parameters of the controller are maintained unchanged and the mass of the moving part is changed. The additional mass applied here are 20, 50, and 100 kg, while an initial mass of 6.9 kg. All other parameters take the same values as in section 5.5 (low gains). Figures 7.1 and 7.2 show the robustness simulation results obtained by the control strategies based on the backstepping technique.

According to the figures, we notice that the tracking precision presents a slight difference according to the mass change for the P-Y control, while the static error for the Y-λ control strategy becomes larger as the mass increases. For the Y-λ control, the λ error is reduced when the payload increases, whereas the pressure

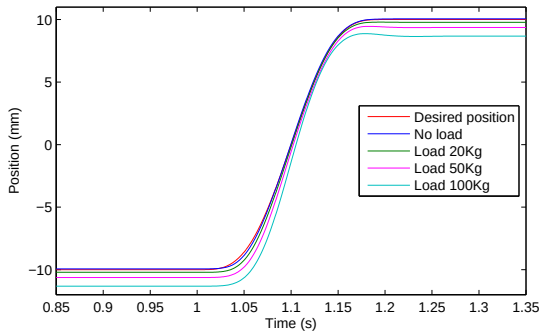

(a) Position tracking

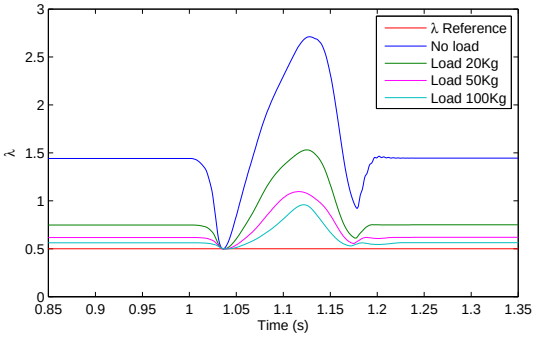

(b) Dynamic weight parameter

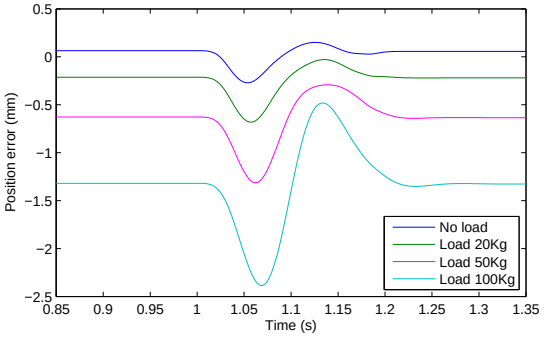

(c) Position error

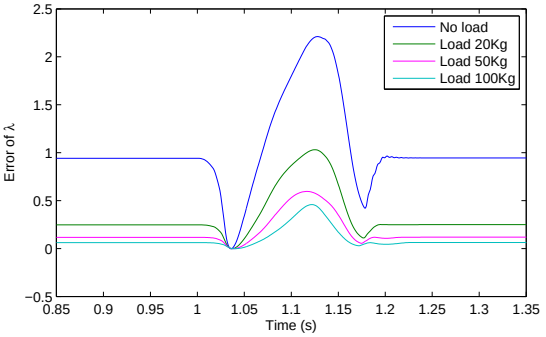

(d) Error in λ

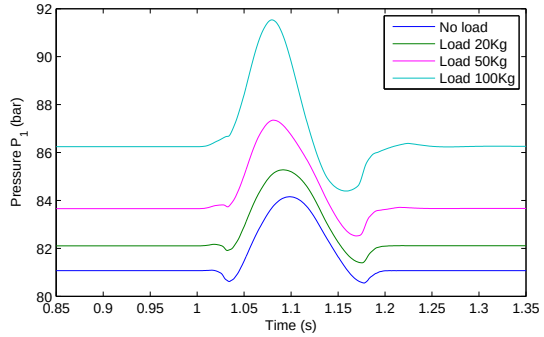

(e) Pressure P_1 evolution

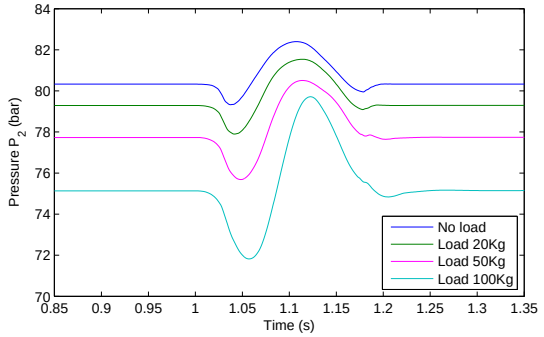

(f) Pressure P_2 evolution

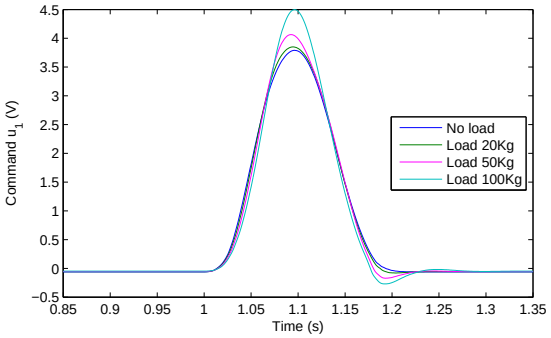

(g) Command u_1

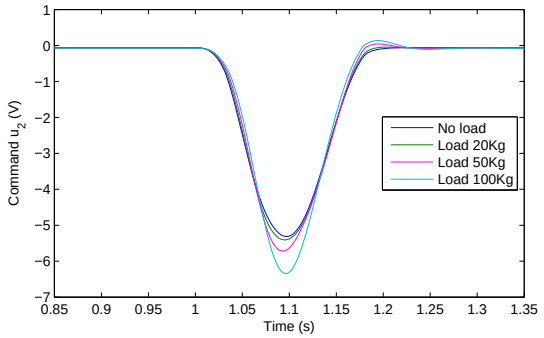

(h) Command u_2

FIGURE 7.1: Robustness simulation results obtained by the Y-λ control

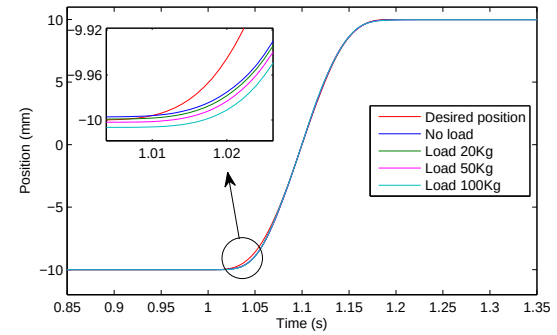

(a) Position tracking

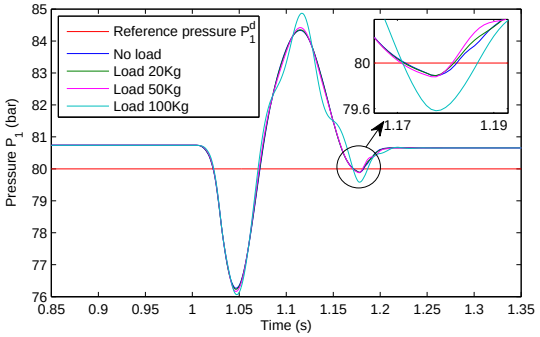

(b) Pressure tracking

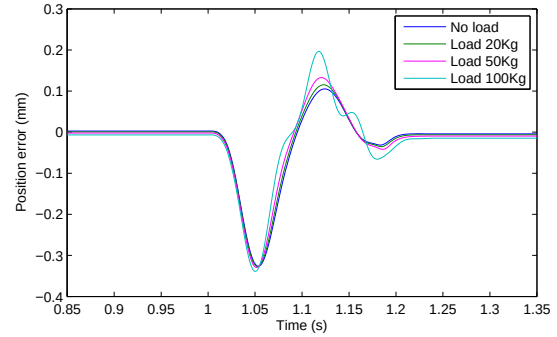

(c) Position error

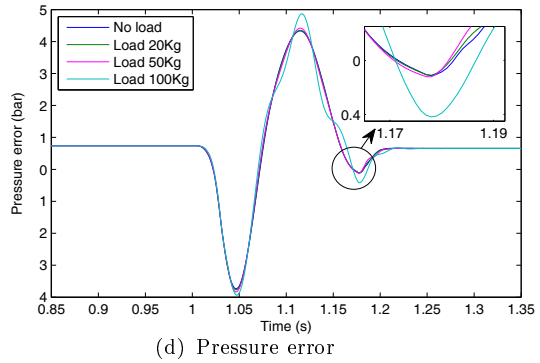

(d) Pressure error

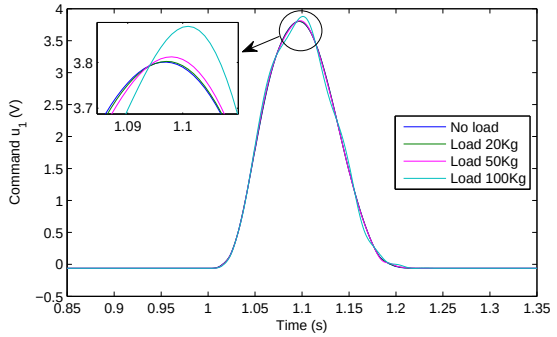

(e) Command u_1

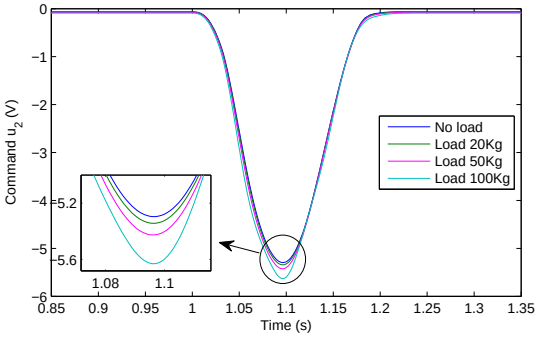

(f) Command u_2

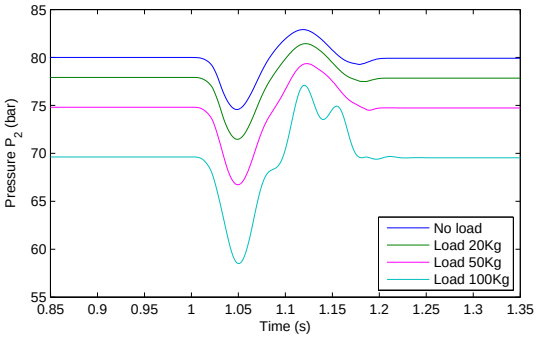

(g) Pressure P_2 evolution

FIGURE 7.2: Robustness simulation results obtained by the P-Y control

tracking error for the P-Y control nearly stays at the same level. Table 7.1 shows the static and maximum error obtained with the two control strategies. For the Y-λ control, the static error increase is nearly proportional to the mass, while all the results for the P-Y control consist well except that the maximum error fluctuates slightly along with the mass increase. However, when the mass reaches 100 kg, a slight oscillation appears in the pressure evolution for the P-Y control at the end of the position rising edge. For the Y-λ control, there are always stiff changes in pressure at the beginning and the end of the position riding edge where the spool of the servovalve arrive nearly its neutral position. This probably leads to the system instability while the gains of the controller increase or the perturbation becomes important. To conclude, the P-Y control shows better robustness performance than the Y-λ control.

TABLE 7.1: Summary of the position error obtained by two control strategies based on the backstepping in simulation

Added mass (kg)		0	20	50	100
Y-λ	Max. error (μm)	271	682	1314	2386
	Static error (μm)	64	-213	-628	-1320
P-Y	Max. error (μm)	327	327	330	339
	Static error (μm)	3	1	-2	-7

As it can be observed on figure 7.1, there are always static errors in Y-λ control. This is due to the shortcomings of the control design that can be explained as follows: in steady state, the system states do not vary as a function of time and the dry friction force is neglected due to the small friction of the hydraulic bearing. According to this condition, the system model (II.1) can be rewritten as

$$\begin{cases} \frac{dy}{dt} = v_{eq} = 0 \\ \frac{dv}{dt} = \frac{A}{M}\left(P_{1,eq} - P_{2,eq}\right) - g = 0 \\ \frac{dP_1}{dt} = \frac{\beta}{V_1(y_{eq})} \cdot \phi_1\left(\cdot\right) \cdot u_{1,eq} = 0 \\ \frac{dP_2}{dt} = \frac{\beta}{V_2(y_{eq})} \cdot \phi_2\left(\cdot\right) \cdot u_{2,eq} = 0 \end{cases} \tag{7.1}$$

$$\Rightarrow \begin{cases} P_{1,eq} - P_{2,eq} = \frac{Mg}{A} \\ u_{1,eq} = 0 \\ u_{2,eq} = 0 \end{cases} \tag{7.2}$$

Substituting (5.34) into the last two equations of (7.2) , yields

$$\begin{cases} -c_3 e_{3,eq} + \lambda \dot{\alpha}_{1,eq} - \frac{A}{M} e_{2,eq} = 0 \\ -c_4 e_{4,eq} + (\lambda - 1)\dot{\alpha}_{1,eq} + \frac{A}{M} e_{2,eq} = 0 \end{cases} \tag{7.3}$$

As the piston velocity is null at equilibrium, we have $e_{2,eq} = c_1 e_{1,eq}$. Besides, to guarantee the same pressure control precision, we set $c_3 = c_4$ in order that the pressures P_1 and P_2 are influenced in an identical way. Hence, according to (7.3), the difference of the pressure error variables can be written as

$$e_{3,eq} - e_{4,eq} = \frac{1}{c_3}\left(\dot{\alpha}_{1,eq} - \frac{2A}{\hat{M}} c_1 e_{1,eq}\right) \tag{7.4}$$

where $\hat{M}$ is the estimated mass of the moving part applied in the system controller.

At equilibrium, according to the expression of α_1 (5.26), we have

$$\alpha_{1,eq} = \frac{\hat{M}}{A}\left(g - (c_1 c_2 + 1) e_{1,eq}\right) \tag{7.5}$$

The derivative of α_1 leads to

$$\dot{\alpha}_{1,eq} = \frac{\hat{M}}{A}(c_1 c_2 + 1)(c_1 + c_2) e_{1,eq} - (c_1 + c_2)(e_{3,eq} - e_{4,eq}) \tag{7.6}$$

Substituting (7.6) into (7.4), yields

$$e_{3,eq} - e_{4,eq} = \frac{\hat{M}^2 (c_1 c_2 + 1)(c_1 + c_2) - 2A^2 c_1}{A\hat{M}(c_1 + c_2 + c_3)} e_{1,eq} \tag{7.7}$$

Then,

$$e_{3,eq} - e_{4,eq} = P_{1,eq} - P_{2,eq} - \alpha_{1,eq} \tag{7.8}$$

Substituting (7.5), (7.8) and the first equation of (7.2) into (7.7), yields

$$e_{1,eq} = -\frac{\hat{M}^2(c_1 + c_2 + c_3)}{2A^2c_1 + \hat{M}^2c_3(c_1c_2 + 1)}\left(\frac{M}{\hat{M}} - 1\right)g \tag{7.9}$$

By considering that $c_1c_2 \gg 1$ and $2A^2c_1$ is far less than $M^2c_1c_2c_3$ because of the small section area, (7.9) can be simplified as

$$e_{1,eq} = -\frac{c_1 + c_2 + c_3}{c_3c_1c_2}\left(\frac{M}{\hat{M}} - 1\right)g \tag{7.10}$$

Equation (7.10) implies that if $\hat{M}$ is not identical to the real mass M, the error in Y-λ is inevitable. This error decreases since at least one of the four control gains increases. If the gain values are increased, the position and the pressure control precisions will be improved. However, the increase of the control gains will introduce a problem of amplification of the signal noise, which will lead to instability, especially when increasing the pressure gains c_3 and c_4. The reason lies on that the signals derived from the pressure sensors contain a more important noise level with an amplitude up to 0.4 bar (precision of $\pm 0.1\%$ of the full measuring range), which has a dominating influence on the command calculation compared to the position noise at steady state.

7.2.2 Controls based on the model-free method

In order to test the robustness performance of the model-free based controls, simulations are conducted also with additional mass varying from 0 kg to 100 kg which corresponds to the mass change of the moving part. As previously, all other parameters remain unchanged. Figures 7.3 and 7.4 show the robustness simulation results obtained by the control strategies based on the model-free method.

From figure 7.3, we can not notice a great difference among the results obtained by the model-free control with different loads due to the model independence of the control strategy. This control law can adjust its local model to follow the load change at every sampling period by tuning automatically the parameter F

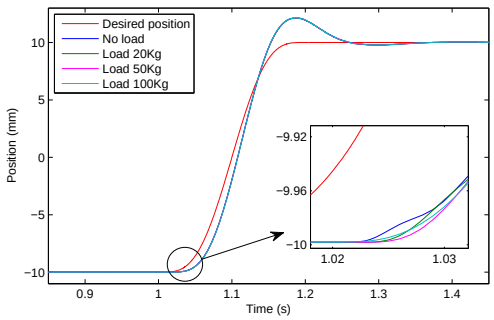

(a) Position tracking

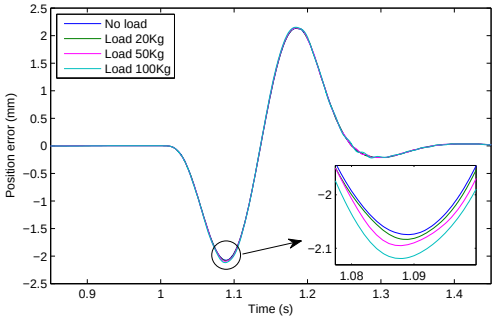

(b) Position error

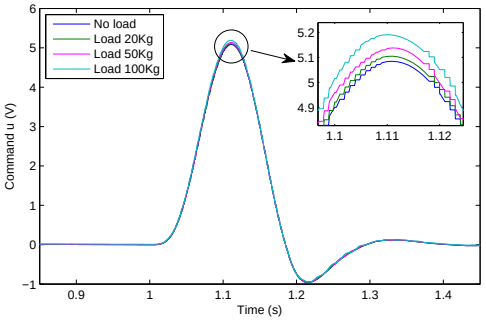

(c) Command u

FIGURE 7.3: Robustness simulation results obtained by the model-free control

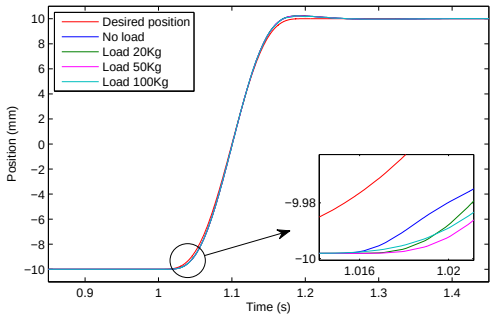

(a) Position tracking

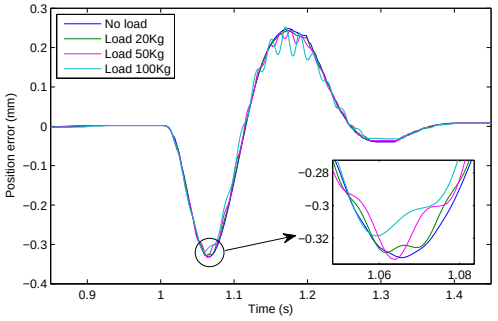

(b) Position error

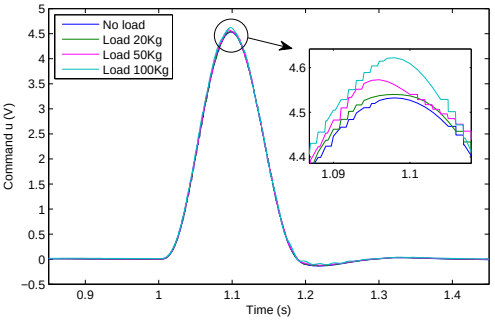

(c) Command u

FIGURE 7.4: Robustness simulation results obtained by the control with restricted model

(6.8). In figure 7.4, for the control with restricted model, slight fluctuations occur on the position errors which become gradually more important along when the mass increases. The reason lies on the fact that the approximate system model adopted in this control strategy involves a term (6.11) with respect to the mass of the moving part. The incoherence between the actual mass and the one used in the pre-compensation model induces an error. This error will be compensated by the feedback term Δu (6.16) that is introduced by the model-free method, which is automatically adjust with the model changes. During this self-tuning process, the fluctuations take place in position tracking. However, the tracking precision is kept at a high level with a maximum error of nearly 0.3 mm.

Table 7.2 gives a summary of the position error obtained by the model-free based controls. As we have seen in figures 7.3 and 7.4, the tracking position error presents slight changes in amplitude along with the increase of load. To conclude, the model-free control shows good robustness performances against the load changes. Despite slight fluctuations in position tracking error when a large load is applied, compared to the model-free control, the control with restricted model seems not sensible to payload changes.

TABLE 7.2: Summary of the position error in simulation obtained by the model-free control (MFC) and the control with restricted model (CRM)

Added mass (kg)		0	20	50	100
MFC	Max. error (μm)	2130	2135	2142	2152
	Static error (μm)	2	2	2	2
CRM	Max. error (μm)	332	329	333	319
	Static error (μm)	0.01	0.02	0.01	0.002

7.3 Robustness analysis based on experimentation

7.3.1 Experiments with different loads

In practical applications, the operating situation is always changing according to the task requirements, e.g. the load or temperature corresponding to different

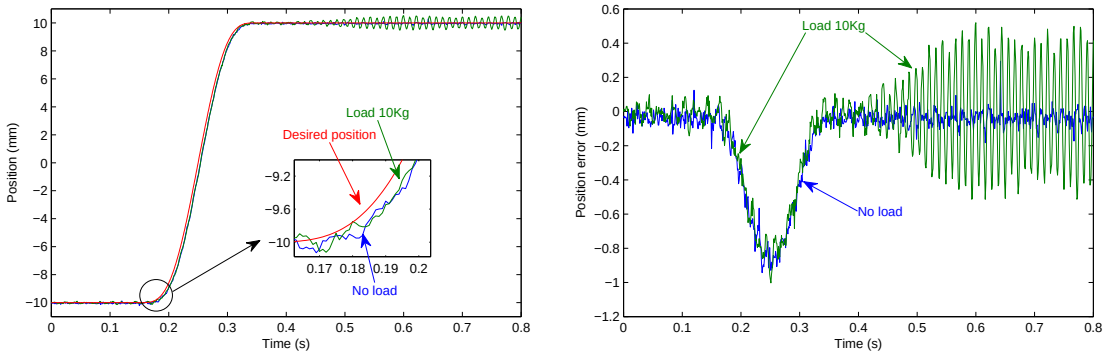

(a) Position tracking (b) Position error

FIGURE 7.5: Robustness experiment results obtained by the proportional control

tasks. A good control strategy with high performance should show insensibility to these changes. In this section, we will mainly discuss the influence of the payload change on the control performances. Experiments are conducted with different loads in order to investigate the robustness performance with respect to the mass perturbation. The load will vary from 0 to 20 kg, while the other experimental configurations are kept identical to those in sections 5.6.1 and 6.5.1. The parameters of the controller in this section remain unchanged and take the same low values as those in low gains experiment (sections 5.6.1 and 6.5.1).

7.3.1.1 Controls based on the backstepping

In order to make a comparison with the classic linear control strategy, we present firstly the experimental results obtained by a proportional control with different loads in figure 7.5. The experimental results of the proportional control with a load of 20 kg are not presented in the figure as its behaviour becomes unstable when the load reaches 20 kg. From this figure, we can observe that the position tracking curve in the experiment with a load of 10 kg presents already oscillations with an important amplitude up to 1 mm, which implied that the control tended to make the controlled whole system unstable.

Figures 7.6 and 7.7 show the experimental results obtained with the Y-λ and the P-Y control at different payloads. As it was underlined in simulation, the static

position error and the maximum error of the Y-λ control increases along with the payload. The P-Y control maintains the same position tracking precision whatever the payload is.

As the payload increases, the difference between the reference and calculated dynamic weight for the Y-λ control is getting less important despite the violent fluctuations due to the pressure oscillations. This is due to the fact that the calculation become more precise with an important pressure difference when the payload increases. Similarly, the pressure tracking precision for the P-Y control is also slightly improved for 20 kg. This can be explained by the fact that when the load increases, the mass dominates the control performances rather than the noise and the manufacture defects.

In figures 7.6(e) and 7.6(f), we can observe that for the Y-λ control, the pressures P_1 and P_2 present larger oscillations at the end of the transient phase when the load increases, compared to those obtained with the P-Y control in figures 7.7(b) and 7.7(g). The main reason probably lies on that the pressure terms involved in the position control calculation have an important weight on the Y-λ control calculation. However, the stability of the pressures is guaranteed in the P-Y control strategy because of the direct pressure stabilisation terms in this control law. Since there is a slight perturbation in pressures, such as the measurement noise and pressure variation due to the fluid dynamics that is not taken into account in the system control modelling, oscillations appear rapidly in the pressure evolution of the Y-λ control. If this effect reaches some limit, the control will probably become unstable.

According to figure 7.7 and as already observed in simulation, the P-Y control strategy shows good robustness performances. While the load changes, the position trajectories are always following accurately the desired ones. The position errors present a marginal fluctuation with loads of 10 kg and 20 kg. When no load applied, the static error has a slight negative offset due to the servovalve manufacturing defaults and the actuator leakages. These effects can be neglected while the mass of the moving part becomes important.

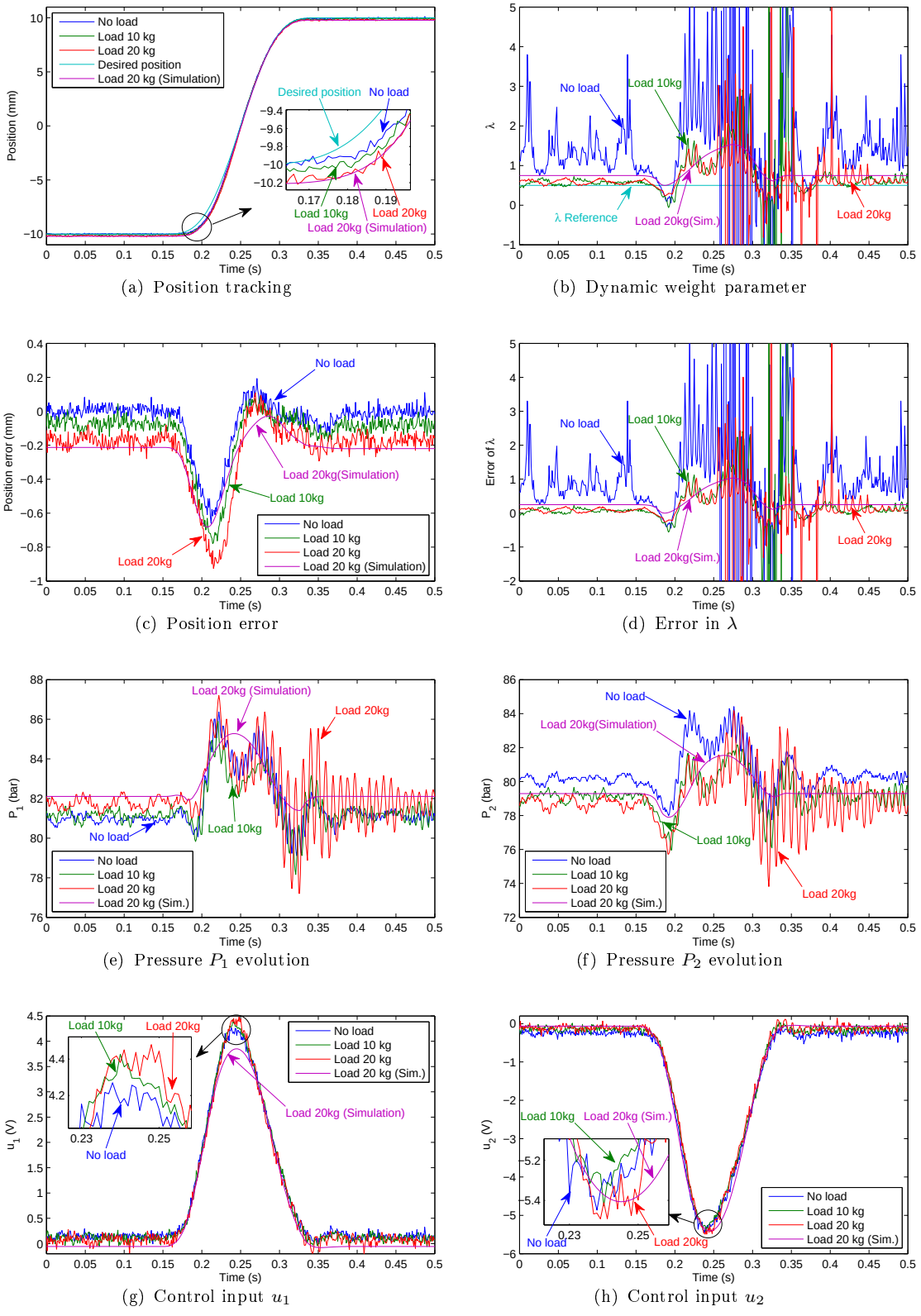

(a) Position tracking

(b) Dynamic weight parameter

(c) Position error

(d) Error in λ

(e) Pressure P_1 evolution

(f) Pressure P_2 evolution

(g) Control input u_1

(h) Control input u_2

FIGURE 7.6: Robustness experiment results obtained by the Y-λ control

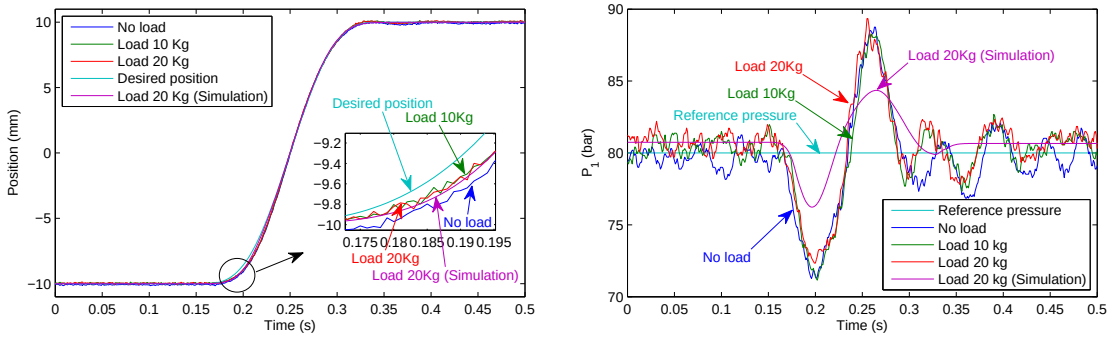

(a) Position tracking

(b) Pressure tracking

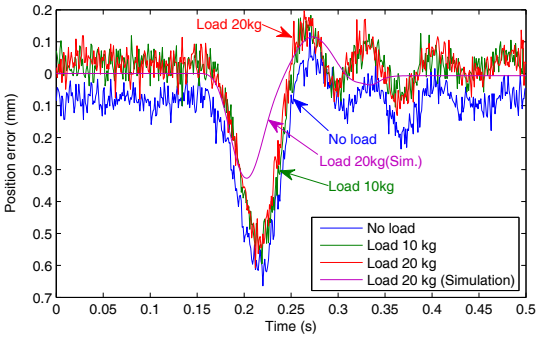

(c) Position error

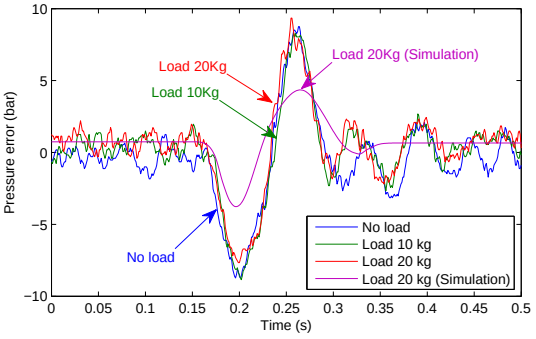

(d) Pressure error

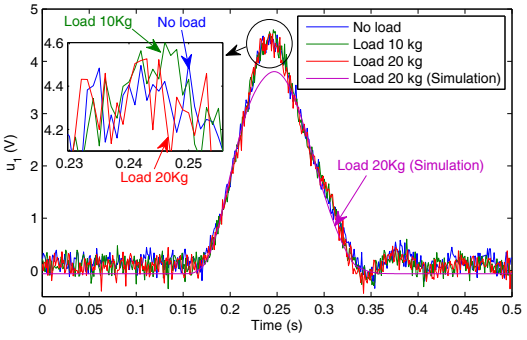

(e) Control input u_1

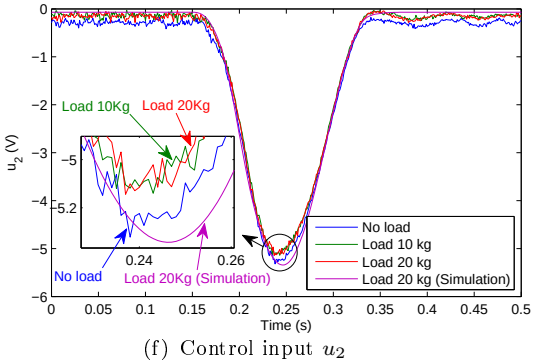

(f) Control input u_2

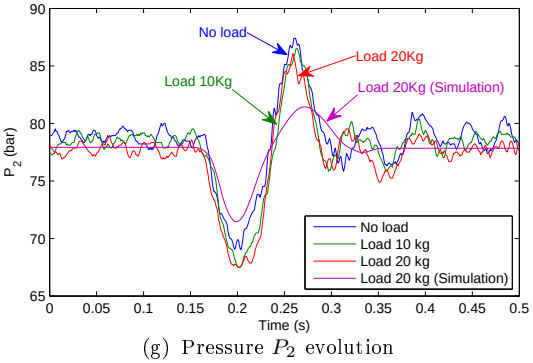

(g) Pressure P_2 evolution

FIGURE 7.7: Robustness experiment results obtained by the P-Y control

TABLE 7.3: Comparison summary of the position error with different payloads in control strategies based on the backstepping

Control strategy	Load (kg)	Transient phase		Steady state	
		Max.(μm)	STD[a](μm)	Mean(μm)	STD[a](μm)
Y-λ	0	660	214	2	32
	10	779	247	-72	31
	20	925	286	-170	31
	Sim.-20	682	-	-213	-
P-Y	0	664	205	-79	33
	10	595	207	25	33
	20	608	203	26	29
	Sim.-20	327	-	1	-
Prop.	0	943	304	-41	35
	10	1003	315	-10	52

a) STD: Standard deviation

Moreover, it can be noticed that the simulation results with a load of 20 kg still keep a good coherence with the experimental ones for both control laws, which proves again the good performance of the virtual prototype to implement novel control strategies.

Table 7.3 gives a summary of experimental performances of the three control laws. As observed in figures 7.5, 7.6, and 7.7, the position errors for the Y-λ control increase, whereas with the P-Y control, it is kept at the same level when the load increases. In agreement with the simulation results, the experimental results clearly comfirm that the P-Y control has better robustness performances against the load change than the Y-λ control.

7.3.1.2 Controls based on the model-free method

The same experimental analysis is now conducted for the model-free based control. The loads are 0, 10, and 20 kg, while the other system parameters remain unchanged and equal to those used in section 6.5. The low value (equal to 30 V/m) is used for the tuning gain K_P. Figures 7.8 and 7.9 present the experimental results obtained respectively by the model-free control and the control with restricted model.

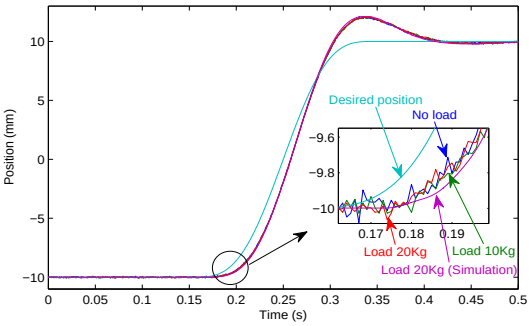

(a) Position tracking

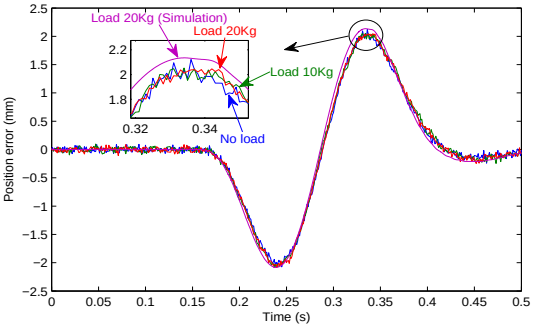

(b) Position error

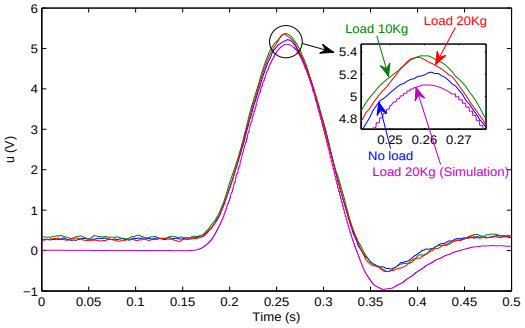

(c) Command u

FIGURE 7.8: Robustness experiment results obtained by the model-free control

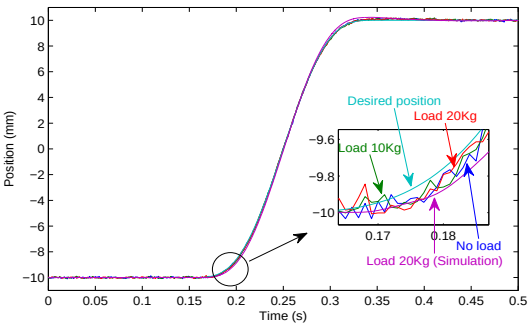

(a) Position tracking

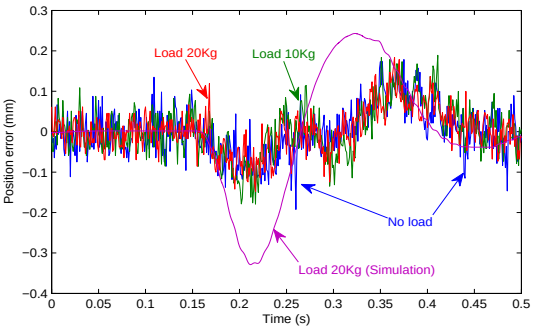

(b) Position error

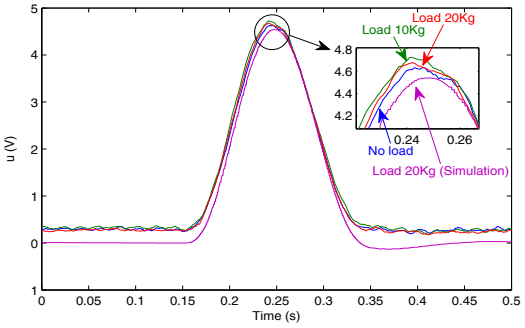

(c) Command u

FIGURE 7.9: Robustness experiment results obtained by the control with restricted model

TABLE 7.4: Comparison summary of the position error with different loads in model-free control (MFC), control with restricted model (CRM), and proportional control (Prop.)

Control strategy	Load (kg)	Transient phase		Steady state	
		Max.(μm)	STD[a](μm)	Mean(μm)	STD[a](μm)
MFC (K_P : 30 V/m)	0	2122	1344	0.06	39
	10	2082	1370	-0.2	40
	20	2079	1372	-0.02	34
	Sim.-20	2135	-	0	-
CRM (K_P : 30 V/m)	0	192	71	0.2	41
	10	189	77	-0.4	40
	20	184	66	0.02	33
	Sim.-20	329	-	0	-
MFC (K_P : 250 V/m)	0	468	227	0.5	69
	10	515	247	-0.2	61
	20	431	237	0.6	67
CRM (K_P : 250 V/m)	0	181	48	-0.1	66
	10	187	67	-0.6	52
	20	130	45	0.5	70
Prop.	0	943	304	-41	35
	10	1003	315	-10	52

a) STD: Standard deviation

Compared to the results obtained with the proportional control in figure 7.5 which becomes unstable at the end of the transient phase, the model-free based control strategies are keeping a good behaviour despite the load changes. Especially, it can be noticed that the accuracy of the position tracking is conserved with the control with restricted model when the payload is increased. No notable changes in the results with the different loads can be observed, this implies that the mass change has little influence on the tracking performance of the proposed strategies. This is consistent with the conclusion of the analysis in simulation (section 7.2.2). Besides, it can be observed that experiment and simulation results match well for the model-free control with a load of 20 kg, except for the command u which has an overall offset of about 0.25 V in experiment. This is certainly due to the internal and external leakages of the actuator and the manufacturing default of the servovalves.

Table 7.4 gives a comparison summary of the position errors obtained with both the model-free control and the control with restricted model when the loads and

gain values are changed. According to table 7.4, in all cases, the control with restricted model shows a higher precision in transient phase. The average static error changes obtained from the two model-free based methods can be negligible. In conclusion, according to the experimental results, the controls based on the model-free method show the best robustness performances against the mass perturbation of the moving part.

7.3.2 Experiments with different precisions of the estimated velocity

To conclude this robustness analysis, we will now study the effect of the differentiator on the control performance, since among the system perturbation parameters, it is easy to introduce some errors or noise for the signal measured by physical sensor or calculated by numeric differentiator.

7.3.2.1 Controls based on the backstepping

In expressions (5.34), (5.41), and (5.57), the calculation of the control input u_1 and u_2 uses the estimated value of velocity and acceleration obtained from the DAO2 algorithm. Hence, the control performances are associated with the estimation precision of the numeric differentiator which is influenced by the tuning gains K_{d0} and K_{d1} (5.60). Figures 7.10 and 7.11 present the results of experiments with different estimation precision. In the first one, the parameters are the same as in section 5.6.1 ($K_{d0} = 200\,\mathrm{s}^{-1}, K_{d1} = 80\,\mathrm{s}^{-1}$), whereas in the second one, the tuning gains of the differentiator are changed to lower values ($K_{d0} = 60\mathrm{s}^{-1}, K_{d1} = 25\mathrm{s}^{-1}$).

When the tuning gains of the DAO2 decrease, it can be noticed that the tracking precision declines notably in transient phase according to figure 7.10 and 7.11. The dynamic position error is almost doubled compared to the one obtained with high gain values. The position overshoot shows a slight oscillation at the end of the position rising edge (figure 7.11(a)). Figures 7.11(c) and 7.11(d) show that the phase shift of the estimated velocity and acceleration becomes significant when

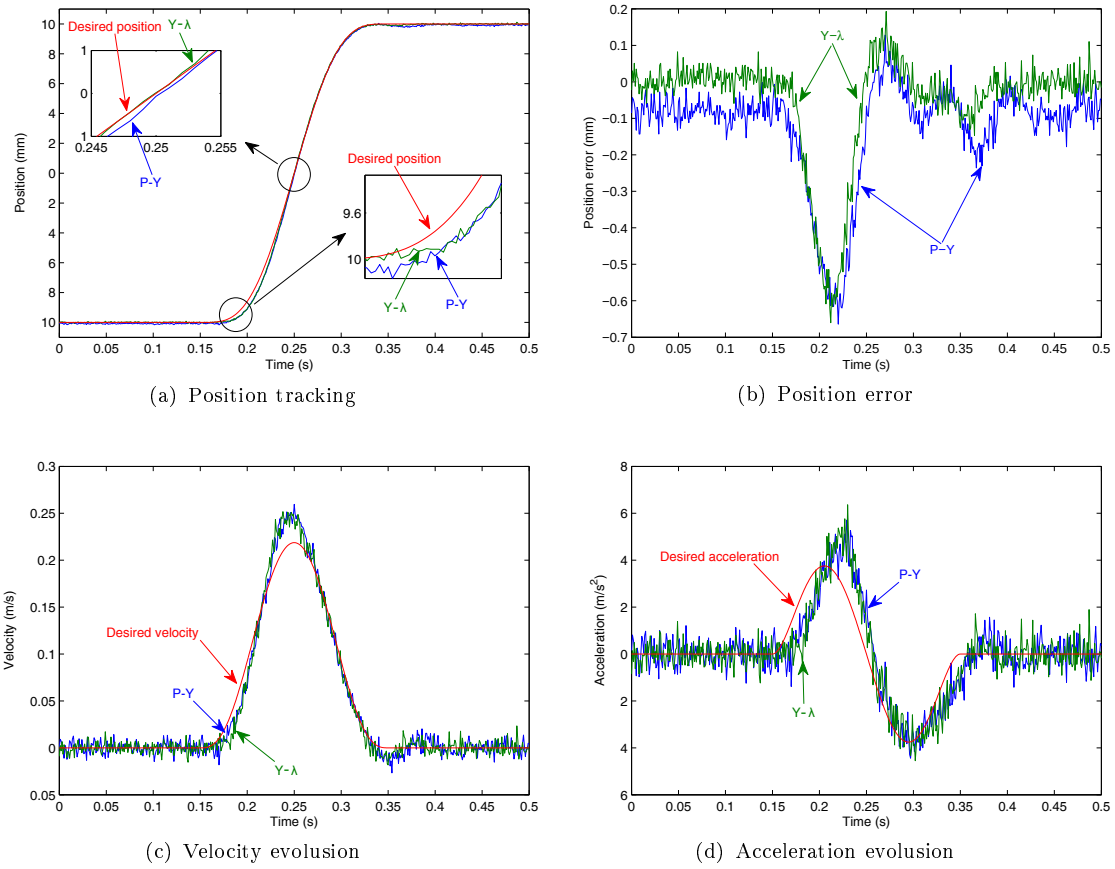

(a) Position tracking

(b) Position error

(c) Velocity evolusion

(d) Acceleration evolusion

FIGURE 7.10: Experimental results of the methods based on the backstepping with high gain values of DAO2

the DAO2 gains are decreased, this leads actually to the precision degradation. However, the noise is obviously reduced. Unfortunately, as no direct measurements of velocity and acceleration are available on the test bench, we are limited here to a qualitative analysis of the estimation precision and it is difficult to conclude on the estimation accuracy.

Table 7.5 summarizes the static and dynamic position errors for the two experiments. It can be found that the degradation on the control performances occurs mainly during the transient phase when the DAO2 gains decrease. The static error increases slightly, whereas the maximum dynamic error is doubled with low DAO2 gains. Hence, in order to obtain better results, higher gains of the differentiator are required but this is obtained to the detriment of noise.

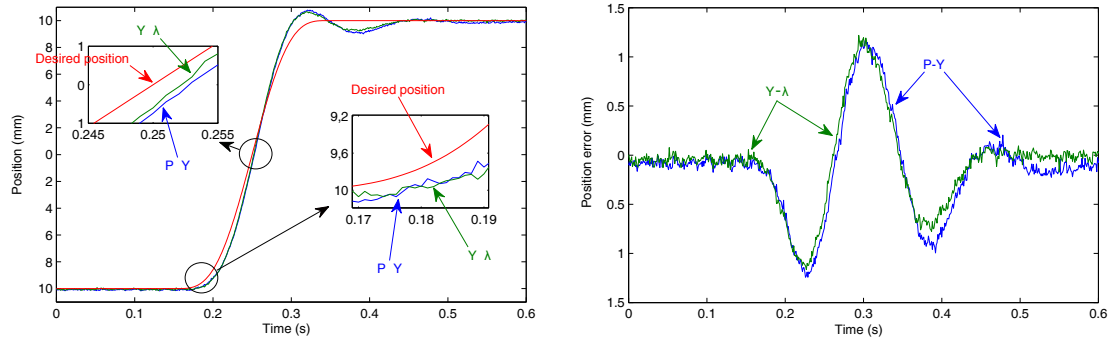

(a) Position tracking (b) Position error

(c) Velocity evolusion (d) Acceleration evolusion

FIGURE 7.11: Experimental results of the methods based on the backstepping with low gain values of DAO2

TABLE 7.5: Comparison summary of the experimental position error with different precisions of DAO2 for the control strategies based on the backstepping

Control strategy	Transient phase		Steady state	
	Max.(μm)	STD[c](μm)	Mean(μm)	STD[c](μm)
Y-λ (HG-DAO2[a])	660	214	2	32
P-Y (HG-DAO2[a])	664	205	-79	33
Y-λ (LG-DAO2[b])	1220	721	-51	38
P-Y (LG-DAO2[b])	1243	744	-83	37

a) HG-DAO2 : low gain values of DAO2

b) LG-DAO2 : high gain values of DAO2

c) STD: Standard deviation

7.3.2.2 Controls based on the model-free method

The same analysis is now conducted for the model-free based control methods. Figures 7.12, 7.13, and table 7.6 show the experimental results obtained with different precisions of the tuning gains of the DAO2 which is used here for velocity estimation. When these gains decrease, the estimated velocity will be less precise

but will be less noisy. The other experiment parameters remain the same as those in sections 6.5.1 and 6.5.2.

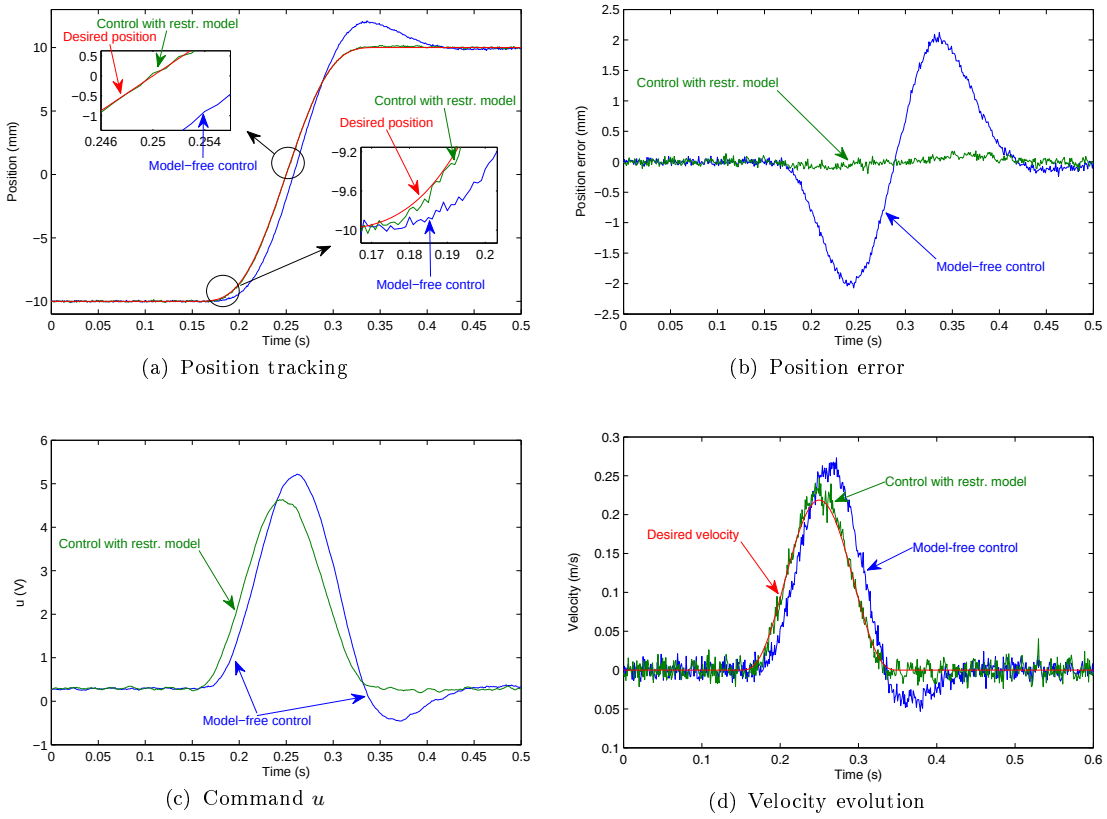

(a) Position tracking

(b) Position error

(c) Command u

(d) Velocity evolution

FIGURE 7.12: Experimental results of the methods based on model-free control with high gain values of DAO2

TABLE 7.6: Comparison summary of the experimental position error with different precisions of DAO2: model-free control (MFC), control with restricted model (CRM), and proportional control (Prop.)

Control	Transient phase		Steady state	
strategy	Max.(μm)	STD^c(μm)	Mean(μm)	STD^c(μm)
MFC (HG-DAO2^a)	2122	1344	0.06	39
CRM (HG-DAO2^a)	192	71	0.2	41
MFC (LG-DAO2^b)	1301	582	0.06	38
CRM (LG-DAO2^b)	1429	627	-0.3	44

a) HG-DAO2 : low gain values of DAO2

b) LG-DAO2 : high gain values of DAO2

c) STD: Standard deviation

For the model-free control (figure 7.13(a)), it can be noticed that the system needs more time to reach the high level position due to the degradation of the velocity

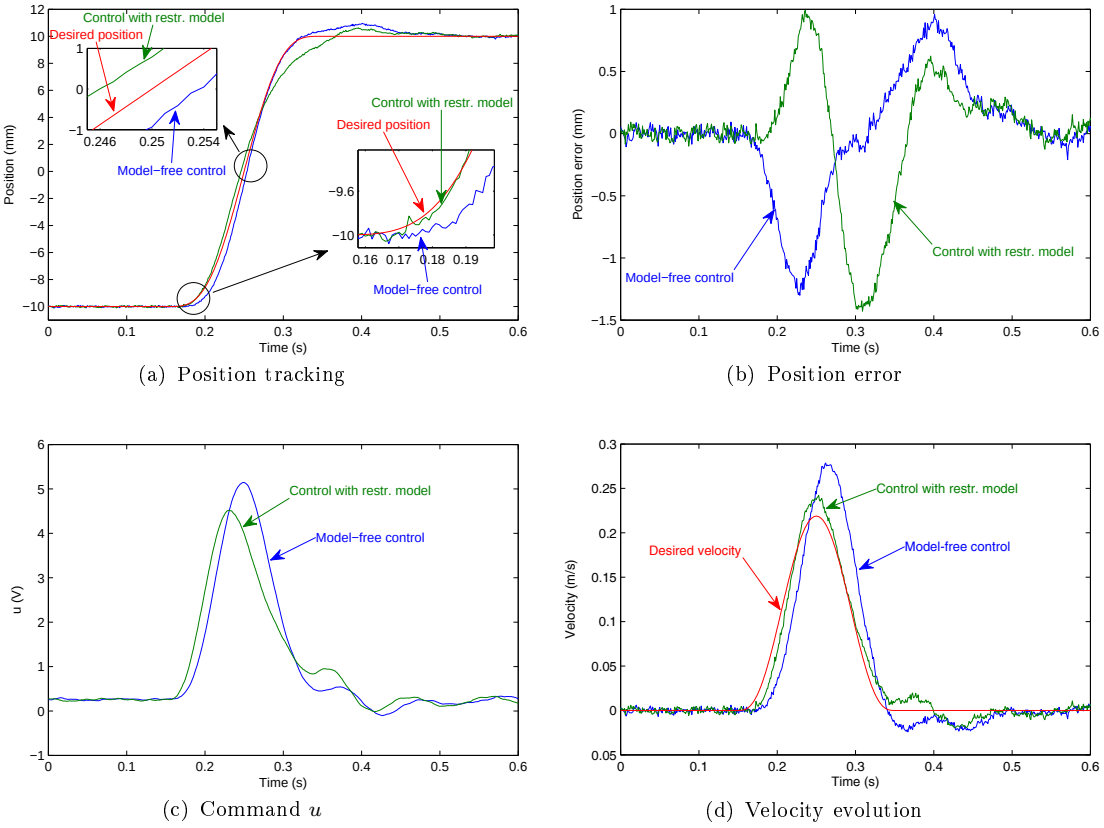

(a) Position tracking

(b) Position error

(c) Command u

(d) Velocity evolution

FIGURE 7.13: Experimental results of the methods based on model-free control with low gain values of DAO2

precision. Some oscillations at low frequencies occur in the steady state. By comparing figures 7.12(d) and 7.13(d), it can be observed that the estimated velocities have less noise as the gains of the DAO2 decrease, but the phase shift becomes significant, which leads to fluctuations in the command calculations (figures 7.12(c) and 7.13(c)). Decreasing the estimated velocity precision leads to a more significant degradation on the tracking performance for the control with restricted model because this control law uses an approximate system model involving a term function of the velocity. On the other hand, although the tracking error of the model-free control decreases for low gain values of the DAO2, the control performance is actually degraded according to the fluctuations in the command (figure 7.13(c)) which implies a degradation of the system stability. In conclusion, for the two proposed control strategies, the tracking performances are degraded as the velocity becomes inaccurate. The precision of velocity estimation is then a critical factor to improve the performances of this kind of control strategies.

7.4 Conclusions

In this chapter, we have conducted a robustness analysis of the control strategies proposed in the previous chapters. Their robustness to the load change and to the differentiator tuning is studied throughout simulation and experiments. Results show that compared to the proportional control, the proposed control strategies have good robustness performances when the payload is changed. The static tracking errors with the model-free based control and with the P-Y controls remain almost unchanged with the change of loads, whereas for the Y-λ control, it increases. With the model-free based controls, it should be noticed that in order to get accurate tracking, the velocity estimation accuracy is an essential factor. The backstepping based control strategies are more robust against the velocity and acceleration precision, only the dynamic errors are affected by the diminution of the estimation accuracy.

Conclusion on Part II

To conclude, this part concentrates on the control of the electro-hydraulic test bench. The main contributions lies on:

- Developing multivariable control strategies based on the backstepping technique in order to achieve precise position tracking and pressure control of the test bench, and analyzing the control performances and robustness of these methods;
- Implementing the model-free control and the control with restricted model on the test bench, and analyzing the control performances and their robustness to the perturbation.

However, there are still some interesting problems to be further studied:

- In this dissertation, all the simulations and experiments were conducted with the actuator operating around its neutral position where the natural frequency is relatively low in comparison with those at the other position (see chapter 3). It will be an interesting attempt to take experiments with the actuator piston near by the chamber ends;
- The backstepping-based conrols could apply different type of desired pressure or λ trajectories rather than a constant. This study will give interests to achieve the requirement of energy efficiency, system stiffness, etc.;
- The further study could be done to explore the servovalve dynamics in control design procedure, which will certainly result in better performances at high frequencies;

- As the model-free control is an interesting control approach which allows ease of implementation and good performances, it is worthwhile to realise a multivariable control with the model-free method.
- For the control with restricted model, we could try to reduce further the feedforward term related to the used model, e.g. only the mechanical part.

Chapter 8

Conclusion and perspectives

Contents

8.1 Conclusion

This dissertation investigates the modelling and the control of a high performance hydraulic test bench. A precise model derived from the analysis of physical phenomena was developed based on the Bond Graph representation. This model implemented in AMESim was validated by comparison of the experimental and simulation results. Besides, several nonlinear control strategies were synthesized and tested on the developed virtual prototype before being implemented on the test bench to be finally validated in practice.

The study of the test bench began with the analysis of its each main component, i.e. servovalves, manifold, actuator. Firstly, we proposed a new flow model of the two-stage servovalve from the analysis of its static characteristics. This enabled the improvement of the flow representation around the neutral position, that is the transient zone of the spool. Then, a dynamic study was conducted in order

to develop a physical model. Along with the establishment of the Bond Graph model of the MOOG D765 servovalve, we show that an accurate model for a large range of frequency and spool displacement can be obtained with a fully physical approach, that is the knowledge of all relevant constitutive equations and physical parameters. Besides, with a clear graphical architecture, the developed Bond Graph model can now be conveniently analyzed in regards with the system physical parameters, as well as improved by adding new phenomena when further effects are taken into consideration. Experimental and simulation results show that the model is valid in a large range and has a good precision.

The manifold was also carefully studied in this dissertation. It was modelled by considering its dynamic effects, including the compressibility effects, the fluid inertia, and the energy dissipation, which influence the performance of the hydraulic control system at high frequencies. Besides, an approach based on abacuses to determine the energy dissipation in each flow circuit has been proposed and the results have been validated by comparison with a CFD analysis. Moreover, the compressibility and inertia effects of the manifold were investigated and results of the theoretical calculation demonstrate that the manifold can cause an obvious decrease in the hydraulic natural frequency. After a brief study of the actuator, we established a global model of the test bench and develop a virtual prototype in AMESim. According to the simulation and experiment, we demonstrated that it makes sense to consider the effect of the manifold while modelling a hydraulic system to reach good agreement with the real system in wide frequency range and operating conditions.

In order to achieve good control performances with high accuracy in position tracking, we proposed two nonlinear control strategies based on backstepping, i.e. Y-λ control and P-Y control. These two strategies can realize multiple-objective controls on our test bench, i.e. position tracking and pressure control. The proposed controls were validated experimentally and by simulation. Compared to conventional linear control, they show good dynamic performances with a very short response time and a high position tracking precision. Moreover, several experiments illustrate their good robustness to velocity estimation precision. However,

the static tracking error of the Y-λ control increases with the load augmentation in spite of its flexibility in pressure control, whereas the P-Y control is quite robust to the load variation.

Although the backstepping approach can guarantee the global stability of the system, it requires that the system under study can be put in a strict feedback form. This condition was achieved in our test bench thanks to the two servovalve command inputs. In a multivariable control, the main control objective is normally position or force tracking . However, the additional trajectory is not quite obvious, here pressure for P-Y or a pressure weight for Y-λ. Usually, energy consumption and actuation efficiency can be an interesting research direction. Besides, the backstepping approach introduced a number of controlling gains. Each was not related to a single physical variable, which made the tuning of the gains difficult to achieved in industry.

Controls based on the model-free method were also implemented on our test bench in chapter 6. Compared to the nonlinear control strategies including the proposed backstepping control laws, these approaches present advantages as they enables good accuracy in trajectory tracking, but keeps the ease of gains tuning which constitutes the main advantage of linear controllers compared to nonlinear approaches. The model-free based controls have attractive dynamic properties with a short response time and high accuracy. Throughout some experiments, we notice that the model-free based control strategies have a good robustness against the load change. However, they are sensitive to the velocity estimation precision. Thus, in order to get an accurate result, the velocity estimation precision should be improved and an high sampling frequency is required.

This PhD work has realized a complete study process in automation which began with the modelling of each hydraulic component for an electro-hydraulic system. The virtual prototype based on the precise physical model was established and then validated. The control laws were synthesized and implemented on the virtual prototype. After the validation in simulation, experiments were conducted to

explore their control performances. Finally, their robustness performance was carefully studied through simulation and experiments.

8.2 Perspectives

Although we have studied the modelling and the control of the test bench in this dissertation, there are still some interesting problems which should deserve further research works. These problems include the following points:

- While conducting the analysis of our hydraulic system, we have not taken into account the temperature variation which has a significant effect on the fluid properties, such as the bulk modulus and viscosity. Thus, to reach a more precise model, the thermodynamic of the hydraulic system requires to be further studied.
- The model could also be improved by introducing a dynamic model of the piston friction phenomena in the actuator.
- Concerning the servovalve, it is clear that the electrical control loop has to be analyzed more carefully in order to take into account the real feedback, the LVDT sensor dynamics, and signal filtering implemented by the servovalve supplier.
- The control design in this dissertation does not consider the dynamics of the servovalves which is worthwhile for the future works and will give further interests into the improvement of the control performances.
- Rather than a constant signal of λ applied for the Y-λ backstepping control in this dissertation, the time-variant signal could be also taking into account.
- More experiments could be done to explore control performances with the actuator operating around the other positions in addition to the neutral one.
- It would be interesting to develop a strategy for alternating the servovalves in order to continue the tracking task if failure of a servovalve occurs.

- A further study on the application of two different servovalves (dynamics, flow characteristics) and the command distribution, could be conducted in order to achieve a better tracking precision and larger operating range, as well as to reduce the energy consumption.
- The model-free based controls can be advanced by testing them in the context of multiple-objective controls. The way to achieve this purpose is to add another state variable as a second control objective, e.g. the actuator pressure, instead of the opposite command limitation expressed in (6.6). The main challenge relies on dealing with problems of the derivative estimation of the control variable. For instance, in order to realize a pressure control, we should cope with the noise problem in the pressure derivative of which the large amplitude noise will degrade remarkably the control performances.
- It will be also interesting to develop a control law based on the model-free method to realise the force control.
- It should be an important aspect to consider some more trajectories with their dynamic increased.
- The robustness analysis in this dissertation concerned only two parameters separately, one related to the perturbation of the physical equipments, the other corresponding to the control parameter perturbation. Considering robustness performance with coupling these two types of perturbation parameters, or with additional perturbation sources, will give some more useful information.

Appendix A

Fluid properties

The fluid properties have a critical effect on the dynamic behaviour of hydraulic systems. In this appendix, density, compressibility, and viscosity properties of the fluid are introduced.

1. Mass density

The mass density is defined as mass per unit of volume (kg/m^3). It is considered as constant for a given fluid in practice, but actually varies in function of pressure and temperature. This function, usually called the equation of state for a fluid, can not be mathematically derived from physical principles. Due to only slight changes in density, it can be given by its first order Taylor approximation [Merritt 1967]:

$$\rho = \rho_0 + \left(\frac{\partial \rho}{\partial P}\right)_T (P - P_0) + \left(\frac{\partial \rho}{\partial T}\right)_P (T - T_0) \tag{A.1}$$

where ρ, T, and P are the density, temperature, pressure with their initial value ρ_0, T_0, and P_0.

In order to facilitate the analysis, (A.1) is reformulated as

$$\rho = \rho_0 \left(1 + \frac{1}{\beta}(P - P_0) - \alpha_P (T - T_0)\right) \tag{A.2}$$

with

$$\beta = \rho_0 \left(\frac{\partial P}{\partial \rho}\right)_T = -V_0 \left(\frac{\partial P}{\partial V}\right)_T \tag{A.3}$$

$$\alpha_P = -\frac{1}{\rho_0}\left(\frac{\partial \rho}{\partial T}\right)_P = \frac{1}{V_0}\left(\frac{\partial V}{\partial T}\right)_P \tag{A.4}$$

where V is the total volume with V_0 its initial value. β is the isothermal bulk modulus representing the fluid compressibility that will be discussed in the following section. α_P is called the cubical expansion coefficient which illustrates the fractional change in volume due to a change in temperature.

2. Compressibility

The compressibility is used to describe the phenomenon that the relative volume of fluid varies in response to a change in pressure. It is characterized by a parameter β, called the bulk modulus. This parameter determines the system stiffness and is the most important factor to illustrate the dynamic behaviour of hydraulic systems. At a constant temperature, the isothermal bulk modulus is given [Blackburn 1966, Merritt 1967, Faisandier 1999] by

$$\beta_T = -V_0 \left(\frac{\partial P}{\partial V}\right)_T \tag{A.5}$$

$$\text{or } \beta_T = \rho_0 \left(\frac{\partial P}{\partial \rho}\right)_T \tag{A.6}$$

where V_0 and ρ_0 is the initial volume and density respectively. The bulk modulus is usually positive because the volume decreases while the pressure increases.

In practice, a small amount of air entrained in the liquid will result in a sharp decrease of the bulk modulus. The effective bulk modulus is hence proposed in [Merritt 1967, McCloy 1980] and modelled in the following.

Consider a flexible container with a total volume V_t filled with a fluid mixture of liquid of volume V_l and gas of volume V_g as shown in figure A.1(a).

$$V_t = V_l + V_g \tag{A.7}$$

The movement of the piston towards the left leads to an increase in pressure ΔP and a variation of the volume ΔV_t that consist decreases of V_l and V_g and the augmentation of the container volume V_c as presented in figure A.1(b).

$$\Delta V_t = -\Delta V_l - \Delta V_g + \Delta V_c \tag{A.8}$$

The effective bulk modulus can be calculated according to the following expression (A.9).

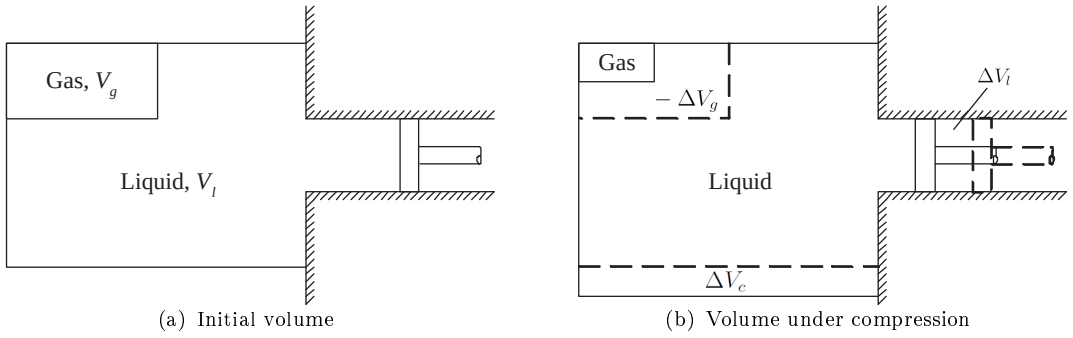

(a) Initial volume (b) Volume under compression

FIGURE A.1: Flexible container filled with gas-liquid mixture under compression [Merritt 1967]

$$\frac{1}{\beta_e} = \frac{1}{\beta_c} + \frac{1}{\beta_l} + \frac{V_g}{V_t}\frac{1}{\beta_g} \tag{A.9}$$

where β_l and β_g are the bulk modulus of the liquid and gas respectively, and β_c is the bulk modulus of the container with respect to the total volume. The calculation of these bulk modulus is given as follows:

$$\beta_c = V_t \frac{\Delta P}{\Delta V_c} \tag{A.10}$$

$$\beta_l = -V_l \frac{\Delta P}{\Delta V_l} \tag{A.11}$$

$$\beta_g = -V_g \frac{\Delta P}{\Delta V_g} \tag{A.12}$$

Figure A.2 shows the influence of the entrained air on the effective bulk modulus in the isothermal case [Watton 1989, Jelali 2003]. α is the ratio $\frac{V_g}{V_t}$. According

to this figure, we notice that the entrained air shows a significant effect on the effective bulk modulus mainly in the domain of low pressures.

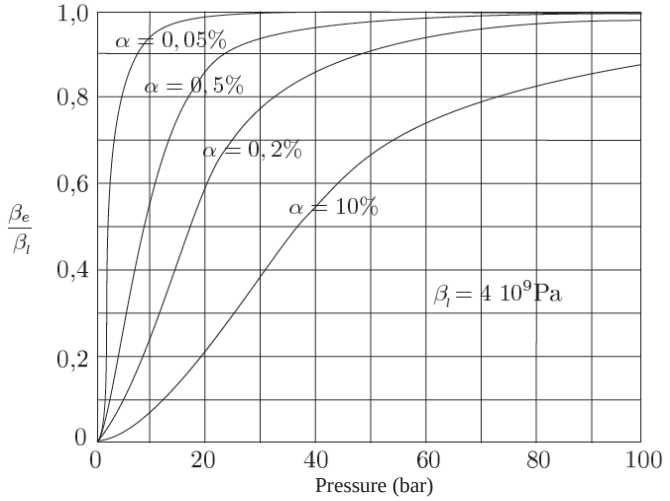

FIGURE A.2: Influence of the entrained air on the effective bulk modulus ($\beta_l = 4 \cdot 10^9$Pa) [Watton 1989, Jelali 2003]

3. Viscosity

The viscosity is an important physical property of a fluid to reflect the resistance of the fluid. This property is caused by the interaction of fluid molecules. For the laminar flow, the fluid is supposed to flow in a certain number of parallel layers with different velocities. According to the Newton's law, the internal friction between two parallel layers [Faisandier 1970] is given as

$$F = \mu A \frac{dv}{dz} \tag{A.13}$$

where

- v is the flow layer velocity, function of its vertical position z;
- μ is the absolute viscosity or dynamic viscosity in poise;
- A is the layer's surface area.

In hydraulics, the kinematic viscosity is often used to represent the fluid internal resistance, and it is easily obtained by the measurement of viscometers. This

parameter is derived from the absolute viscosity and the mass density:

$$\nu = \frac{\mu}{\rho} \tag{A.14}$$

This parameter illustrates the fluid resistance to the deformation. It depends substantially on fluid temperature and pressure. At a given temperature, the viscosity variation is a function of the pressure, given by the common Barus law [Faisandier 1970, Gupta 1981, Faisandier 1999, Tafraouti 2006]:

$$\mu = \mu_0 e^{C_{\mu p} P} \tag{A.15}$$

where

- μ_0 is the absolute viscosity at atmospheric pressure;
- $C_{\mu p}$ is a viscosity/pressure coefficient.

The relation between the kinematic viscosity and the temperature is revealed by the Mac Coull and Walther equation [Blackburn 1966, Faisandier 1970, Frene 1997, Faisandier 1999, Tafraouti 2006]:

$$\log(\log(\nu + a_1)) = a_2 \log T + a_3 \tag{A.16}$$

where

- T is the absolute temperature in Kelvin;
- a_1, a_2, a_3 are constants that must be determined for each fluid, in general a_1 has a value between 0.6 and 0.75 if ν is in centistokes.

Figure A.3 presents the viscosity evolution in function of the temperature at different levels of pressures. The diagram is plotted with abscissa $x = \log T$ and ordinate $y = \log(\log \nu)$, which was standardized by A.S.T.M. (American Society for Testing Materials). Compared to results in the case where the pressure decreases, the fluid viscosity decreases remarkably with the increase of the temperature.

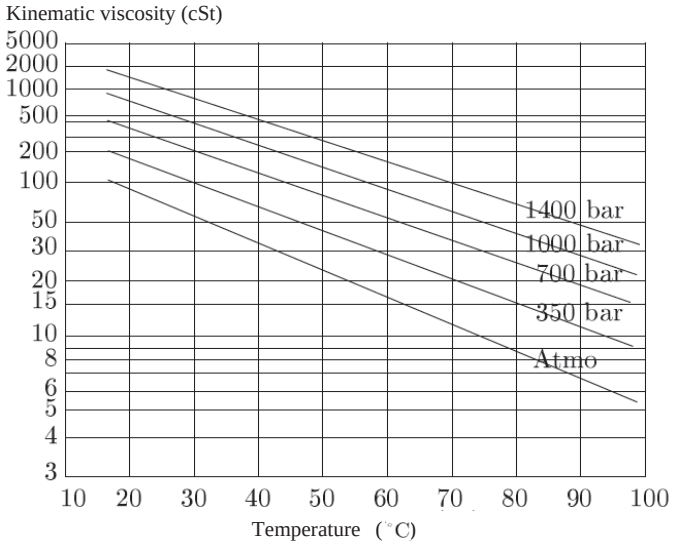

FIGURE A.3: Evolution of the viscosity in function of the temperature [Frene 1997]

Appendix B

Résumé en français

B.1 Introduction générale

Par rapport aux systèmes électromécaniques, les systèmes hydrauliques fournissent une puissance plus élevée à volume et poids identique. Les systèmes hydrauliques ont une bonne stabilité de mouvement et la régulation de vitesse peut être simplement réalisée dans une grande plage de variations (et même à des vitesses très faibles).

Depuis plus de 20 ans, l'un des domaines de recherche du Laboratoire Ampère est axé sur la modélisation, la conception et la commande des systèmes électro-hydrauliques et électro-pneumatiques. L'objectif de cette thèse est d'étudier la modélisation et la commande d'un système hydraulique hautes performances récemment acquis par le laboratoire.

Ce banc d'essai (figure 1.1) est composé d'un actionneur hydraulique contrôlé par un système complexe composé de 2 servodistributeurs hautes performances ayant une large bande passante et permettant de travailler à haute fréquence. Cette nouvelle technologie offre de nouvelles perspectives d'application dans les domaines de l'aérospatiale et de l'automobile comme les tests d'usure et de vieillissement

de composants dans des conditions réelles d'utilisation. Cela signifie que les composants doivent être excités par des signaux expérimentaux correspondant à différente situation de vie du véhicule (haute / basse vitesse, route/autoroute/tout terrain, ...). Un autre avantage de cette conception est de permettre différents modes de commande et différentes stratégies, visant efficacité énergétique et performances élevées.

La figure 1.2 montre le schéma du banc d'essai électro-hydraulique. Il est constitué d'une centrale hydraulique avec une pompe puissante, une embase spécifique qui relie deux accumulateurs, deux servovalves haute performance, et un vérin à double tige à piston symétrique auquel peut être fixé une charge externe. Le système d'acquisition et de contrôle et un ensemble de certains capteurs complète le banc d'essai permettant ainsi de valider le modèle proposé et d'implanter différentes lois de commande.

Les deux servovalves à hautes performances MOOG D756 peuvent travailler selon deux modes, à savoir les modes 3/2 ou 5/2. Elles modulent la puissance hydraulique fournie au vérin par variation des sections de passage correspondant au signal sortant du système d'acquisition (dSPACE).

Afin d'élaborer des lois de commande sophistiquées, le premier pas, objectif principal de la thèse, est de développer un prototype virtuel basé sur un modèle précis issu de considérations physiques et d'un travail expérimental afin d'identifier les paramètres et de valider le réalisme de ce prototype virtuel. Les difficultés sont ici principalement liées au besoin d'obtenir un modèle valide sur une large bande de fréquences et de grands déplacements. Ceci nécessite donc de prendre en compte les non linéarités des phénomènes physiques et les couplages entre les domaines mais aussi d'étudier et de modéliser des effets qui ne sont pas prépondérants dans les modélisations plus classiques. Ensuite, cette thèse se concentrera sur la conception de lois de commande sur le banc d'essai. Les commandes se baseront sur les cahiers des charges classiques, c'est-à-dire le contrôle mono-objectif tel que le suivi en position ou en effort dans une large bande de fréquence et de grands mouvements avec une bonne robustesse vis à vis des perturbations, et d'autre part

le contrôle multi-objectif tel qu'un contrôle position/raideur de l'actionneur, ou encore une commande de position/ efficacité énergétique.

Dans cette thèse, le travail se concentre sur les problématiques évoquées précédemment. Les contributions concernent les aspects suivants:

- L'analyse statique et dynamique des caractéristiques de la servovalve électro-hydraulique à deux étages, et l'établissement d'un modèle précis basé sur l'approche Bond Graph;
- La proposition d'un modèle d'écoulement pour le deuxième étage de la servovalve respectant les phénomènes physiques, à savoir le régime transitoire entre le découvrement et le recouvrement du distributeur à tiroir;
- L'étude des effets dynamiques de l'embase située entre les servovalves et le vérin, à savoir l'effet de compressibilité, l'inertie du fluide, et les pertes de charge: une méthode pour calculer les paramètres correspondant aux pertes de charge a été proposée;
- La validation du prototype virtuel du banc d'essai à l'aide du logiciel AMESim développé à partir de la représentation Bond Graph proposée;
- L'élaboration de lois de commande multivariables basées sur la technique du backstepping afin de réaliser un suivi en position précis et simultanément la modulation des pressions dans les chambres du vérin, ainsi que l'analyse des performances et de la robustesse des lois de commande proposées;
- La mise en œuvre de la commande sans modèle et de la commande avec modèle restreint sur le banc d'essai, et l'analyse des performances atteignables ainsi que la robustesse vis à vis des perturbations.

B.2 Analyse et modélisation de la servovalve haute performance

En tant qu'interface de puissance entre le système de commande et l'actionneur, la servovalve joue un rôle très important dans la chaine de contrôle de la puissance hydraulique. Ses performances ont un effet important sur les résultats de la commande. Nous étudierons d'abord les caractéristiques statiques de la servovalve afin de vérifier ses performances en régime stationnaire avant d'aborder les caractéristiques dynamiques de ce composant dans la section suivante.

L'étude des écoulements dans la servovalve peut généralement être décomposée en deux parties : la première concerne l'étage de pilotage et l'autre l'étage de puissance. Pour ces 2 parties, nous nous sommes largement inspirés de la bibliographie avant de proposer une amélioration du modèle d'écoulement dans l'étage de puissance qui représente plus précisément les écoulements de fuite au niveau des orifices de contrôle du débit de sortie.

La figure 2.5(a) présente le schéma de principe du système buse-palette. Dans ce système, la palette se déplace du fait du couple généré par le moteur couple. Cette force est issue du courant parcourant les deux bobines fixées autour de l'armature, elle-même liée à la palette. Du fait de ce mouvement, les sections de passage des orifices associées aux buses situées de chaque côté de la palette varient, ce qui entraine une variation des deux pressions aux extrémités du tiroir du deuxième étage. Du point de vue de l'écoulement, les restrictions fixes et variables du premier étage sont définies comme des orifices courts. De plus, nous supposons que les écoulements dans toutes les restrictions concernées sont en régime turbulent et donc que les coefficients de débit sont alors considérés comme constants. Pour chaque orifice fixe ou variable, les équations de débit sont décrites par les équations (2.1)-(2.7).

En tenant compte des hypothèses (2.8) et (2.9), nous pouvons obtenir les expressions de la différence de pression pilotée sur le tiroir du 2ème étage ((B.1)) et des

débits de fuite du premier étage ((**??**)):

$$\frac{P_L - P_R}{P_P - P_T} = \frac{\alpha_f^2(1+\delta_f)^2\dfrac{P_T}{P_P - P_T} + \dfrac{P_P}{P_P - P_T}}{\alpha_f^2(1+\delta_f)^2 + 1} - \frac{\alpha_f^2(1-\delta_f)^2\dfrac{P_T}{P_P - P_T} + \dfrac{P_P}{P_P - P_T}}{\alpha_f^2(1-\delta_f)^2 + 1} \tag{B.1}$$

$$\begin{cases} \dfrac{Q_{LE}}{C_f \pi d_n x_{f0}\sqrt{\dfrac{2}{\rho}(P_P - P_T)}} = \dfrac{1+\delta_f}{\sqrt{\alpha_f^2(1+\delta_f)^2+1}} \\ \dfrac{Q_{RE}}{C_f \pi d_n x_{f0}\sqrt{\dfrac{2}{\rho}(P_P - P_T)}} = \dfrac{1-\delta_f}{\sqrt{\alpha_f^2(1-\delta_f)^2+1}} \end{cases} \tag{B.2}$$

Les figures 2.7 représentent les surfaces décrivant le débit et la pression en fonction de δ_f et α_f pour une pression d'alimentation de 210 bar et une pression de retour de 5 bar.

- On remarque sur la figure 2.7(a) que plus α_f est petit, plus les variations du rapport de la différence de pression sont linéaires;
- Cependant, le domaine de pilotage de la différence de pression diminue lorsque α_f devient petit;
- On remarque également sur la figure 2.7(b) que plus δ_f est petit, plus l'évolution du débit de fuite sera faible.

La figure 2.5(b) présente le schéma de principe du distributeur à tiroir du deuxième étage. Le tiroir se déplace grâce à la différence de pression $(P_L - P_R)$. Ce déplacement entraine une variation des sections de passage des orifices associés, aux ports A et B de la servovalve, et par conséquent permet de faire varier les débits sur les voies A et B.

En tenant compte des défauts géométriques (figure 2.8), nous proposons un nouveau modèle d'écoulement (B.3) et (B.4) respectant l'effet du régime de transition. Pour le découvrement $(x_{si} \geq 0)$:

$$Q_{si,\text{underlap}} = \begin{cases} 4\dfrac{\delta_{\text{Re}}^2}{\mu} \cdot n \cdot wd_i^2(x_{si}) \cdot |\Delta P|, & \text{Re}_i \leq \text{Re}_t \\ C_{d\infty} \cdot n \cdot wd_i\sqrt{\dfrac{2}{\rho}|\Delta P|}, & \text{Re}_i > \text{Re}_t \end{cases} \tag{B.3}$$

Pour le recouvrement $(x_{si} < 0)$:

$$Q_{si,\text{overlap}} = \frac{n \cdot w \cdot e_s^3}{12\mu \left(k_s - x_{si} + k_I \tanh\left(-\frac{x_{si}}{L_t} \right) \right)} |\Delta P| \tag{B.4}$$

La figure 2.10 montre la comparaison des résultats de simulation et expérimentaux. Nous notons que la différence entre la valeur maximale mesurée et le modèle du débit de fuite est d'environ 0,005 l/min et que l'erreur maximale sur le débit de fuite se situe pour les grandes ouvertures (là où ce débit devient faible par rapport au débit en découvrement) et représente environ 0,08 l/min. De plus, les gains en pression mesurés et ceux obtenus à l'aide du modèle donnent respectivement 850 bars/V et 827 bars/V. La différence entre ces deux résultats est 23 bars/V, soit 2,7%. Les écarts de pression sur la figure sont inférieurs à 10 bars, ce qui montre que le modèle de débit proposé respecte bien les caractéristiques réelles du distributeur à une pression donnée.

D'ailleurs, les résultats CFD de la figure 2.14 montrent que l'évolution des débits correspond bien à l'expression classique du débit à grande ouverture. Ils confirment également l'augmentation des efforts hydrodynamiques avec la diminution de l'ouverture de l'orifice.

Enfin, pour caractériser les propriétés dynamiques de ce servodistributeur, nous avons ensuite étudié respectivement les dynamiques du moteur-couple, du système buse/palette et du distributeur à tiroir en précisant les approches mises en place au niveau des modèles Bond Graph, permettant ainsi de coupler les différents domaines: hydraulique, mécanique, et électro-magnétique, et facilitant l'interconnexion des différentes parties. Pour modéliser correctement le couplage entre les parties mécaniques et hydrauliques, des éléments R à 2 ports modulés par le déplacement du tiroir sont utilisés afin de représenter les pertes de charge dans le domaine hydraulique et la force hydrodynamique dans le domaine mécanique. Des éléments TF sont utilisés pour modéliser les couplages entre les parties hydrauliques et mécaniques au niveau des surfaces sur lesquelles s'appliquent les pressions. En outre, la servovalve étudiée comporte une rétroaction électrique correspondant à la mesure du déplacement du tiroir. Le modèle Bond Graph de la servovalve entière est finalement présenté à la figure 2.26.

Suite à l'approche Bond Graph, nous avons implémenté le modèle de la servovalve dans le logiciel AMESim en nous appuyant sur la phénoménologie retenue au niveau du Bond Graph (figures 2.27 et 2.28).

Pour les caractéristiques dynamiques, on note que l'amplitude et la phase obtenues en simulation montrent une bonne corrélation avec les résultats expérimentaux à basse fréquence. Toutefois, une erreur apparaît à haute fréquence, en particulier au niveau de la phase. L'erreur sur l'amplitude est de moins de 6 dB et celle sur la phase atteint 30°. Plusieurs raisons peuvent expliquer ces erreurs : (1) l'influence du mode de vibration transversale à haut fréquence ; (2) la méconnaissance de l'algorithme de commande du servodistributeur ; (3) le déphasage dû au capteur de position LVDT. Néanmoins, le modèle dynamique représente fidèlement les caractéristiques dynamiques de la servovalve sur une plage de 0 à 100 Hz. Malgré un certain décalage, il est encore valable jusqu'à 500 Hz, en particulier pour 100% du signal de commande.

En conclusion, nous avons d'abord analysé les caractéristiques statiques de la servovalve à deux étages. Les débits de l'étage de pilotage et ceux de l'étage de puissance ont été étudiés. Nous avons en particulier proposé un modèle du débit du distributeur pour l'étage de puissance en détaillant l'écoulement dans la zone de transition qui permet d'accroître la précision par rapport aux modèles précédents. Après avoir identifié les paramètres du modèle proposé, les résultats simulés du gain en pression et du débit de fuite sont bien corrélés avec les mesures. Nous avons proposé un modèle Bond Graph très complet de la servovalve. A l'aide de ce modèle, nous avons défini un modèle de simulation de la servovalve dans le logiciel AMESim en vue de valider expérimentalement l'approche proposée. La comparaison des réponses en fréquence obtenues en simulation et expérimentalement montre une bonne corrélation entre la réalité et le modèle que nous avons développé. Le modèle est très représentatif à basses fréquences et il présente peu de décalage à hautes fréquences.

B.3 Etude des effets dynamiques de l'embase

Dans un système hydraulique classique, le déplacement de l'actionneur est piloté par des éléments de contrôle tels que les servovalves qui sont reliées à l'actionneur via une embase. Dans notre cas, la plupart des autres dispositifs hydrauliques tels que les 2 accumulateurs, les deux électrovannes et les deux limiteurs de débit sont également installés sur cette embase. La figure 3.1 montre le schéma du circuit interne de l'embase utilisée sur notre banc d'essai. Le fluide en sortie de pompe hydraulique est filtré avant d'entrer dans l'embase pour être dirigé vers la servovalve qui ,odule la puissance hydraulique fournie à l'actionneur. Par ailleurs, cette embase est spécifique car elle a été conçue spécialement pour alterner entre les différents modes de fonctionnement du système via la commutation de deux électrovannes (V1 et V2) :

- Mode 1 : une seule servovalve 4-voies pour contrôler l'actionneur;
- Mode 2 : deux servovalves 4-voies en parallèle pour contrôler l'actionneur;
- Mode 3 : deux servovalves 4-voies avec chaque servovalve utilisée comme un composant à 3 voies pour piloter le débit au niveau de chaque chambre de l'actionneur.

Selon le mode de fonctionnement, le fluide s'écoule dans des circuits différents et traverse divers composants.

Le schéma de la figure 1.3 présente l'installation de notre banc d'essai. L'analyse hydraulique menée dans la thèse se concentre sur l'étude du circuit de l'embase qui relie les sorties des servovalves et les orifices d'entrée des chambres de l'actionneur. Cinq tronçons de circuit sont pris en considération (figure 3.2):

- Tronçon A_i-N_i : à partir de l'orifice A_i vers la servovalve SVi à la bifurcation N_i ;
- Tronçon N_i-V_i: à partir de la bifurcation N_i vers l'orifice V_i de la chambre de l'actionneur ;
- Tronçon B_i-C_i: à partir de l'orifice B_i de la servovalve SVi vers l'orifice C_i de l'électrovanne Vi ;

- Tronçon C_i-N_j: à partir de l'orifice C_i de l'électrovanne Vi (lorsque la vanne est ouverte) vers la bifurcation N_j ;
- Tronçon C_i-PT: à partir de l'orifice C_i de l'électrovanne Vi (lorsque la vanne est fermée) vers le réservoir (à travers le limiteur) ;

Pour la modélisation, nous supposons que les pertes de charge dans les limiteurs peuvent être négligées et que les électrovannes peuvent être considérées comme des composants idéaux sans perte de charge losqu'elles sont ouvertes.

Chaque tronçon de circuit (noté Z dans la figure 3.2) est modélisé par un Bond Graph en considérant trois effets : la dissipation d'énergie (les pertes de charge), la compressibilité, et l'inertie du fluide. Le modèle Bond Graph de l'embase est développé à partir de l'intégration des modèles de chaque tronçon du circuit, des bifurcations et des vannes. Le modèle final est donné à la figure 3.4. Dans ce modèle, les effets de compressibilité et d'inertie du circuit ZA0N0 sont négligés du fait de son faible volume (environ $2 \cdot 10^{-6}$ m^3).

La relation entre le débit et les pertes de charge est complexe dans un système hydraulique. Nous avons donc estimé les grandeurs à l'aide de deux approches: la méthode CFD et la méthode basée sur l'utilisation d'abaques (ABM). La dissipation d'énergie dépend non seulement de la géométrie locale et des propriétés du fluide, mais aussi du nombre de Reynolds fonction de la vitesse d'écoulement. Il n'existe pas de formulation unifiée valable dans tous les cas. Les résultats CFD sont utilisés ici seulement pour valider les résultats de la méthode ABM. Cette validation a été effectuée en comparant les caractéristiques de perte de charge en fonction du débit pour chaque circuit et chaque combinaison de circuit.

Pour l'approche ABM, chaque circuit à étudier est d'abord divisé en un réseau de résistances hydrauliques élémentaires, telles que des conduits, des coudes et des bifurcations. Les pertes de charge de chaque élément sont obtenues à partir de l'équation suivante [Idelchik 1994]:

$$\Delta P_{\text{total}} = \zeta_{\text{total}} \cdot \frac{\rho w_e^2}{2} = \zeta_{\text{total}} \cdot \frac{\rho}{2} \cdot \left(\frac{Q}{A_e}\right)^2 \tag{B.5}$$

Le coefficient global de perte de charge dépend la condition d'écoulement. Il est donc fonction du nombre de Reynolds, de la forme et des dimensions géométriques de l'élément hydraulique. Dans le calcul des pertes de charge, ce coefficient est un paramètre critique qui peut être obtenu à partir de formules empiriques ou d'abaques données par la littérature [Idelchik 1994, Filonenko 1948].

La figure 3.8 présente une comparaison des résultats obtenus par la CFD et par la méthode ABM pour les principaux circuits de l'embase. D'après la figure, nous remarquons que les deux méthodes introduisent approximativement la même évolution des pertes de charge en fonction du débit. A faible nombre de Reynolds, les résultats des deux méthodes sont bien en accord. Néanmoins, des différences apparaissent avec l'accroissement du nombre de Reynolds, surtout pour les modèles composés d'un petit nombre d'éléments, les différences deviennent alors non négligeables. Ceci peut s'expliquer de plusieurs façons :

1. L'orifice de sortie ou d'entrée de la géométrie 3D est proche de singularités qui peuvent changer la vitesse locale du fluide;
2. La distribution du champ de vitesse à l'orifice d'entrée n'est pas parfaitement configurée dans le modèle CFD pour correspondre à l'écoulement réel.
3. Les cas décrits dans la littérature ne correspondent parfois pas exactement à ceux que nous observons dans le circuit réel.
4. La précision de l'analyse CFD dépend de la finesse du maillage, de la méthode de calcul, et du régime d'écoulement.

Les volumes dans l'embase induisent un effet de compressibilité qui influence la dynamique de l'ensemble du système entraînant la diminution de la pulsation propre du système. Par rapport au volume du vérin au centre, soit $1,56 \cdot 10^{-}4$ m^3, les volumes dans l'embase représentent plus de la moitié de celui-ci, et ne peuvent donc pas être négligés.

On montre que la pulsation propre d'un vérin se calcule par:

$$f_H = \frac{1}{2\pi}\sqrt{\frac{k_{H1} + k_{H2}}{M}} \tag{B.6}$$

avec
$$k_{Hi} = \frac{2\beta \cdot A^2}{V_{Ti}}, \quad i = 1,\ 2 \tag{B.7}$$

La figure 3.10 présente l'évolution de la pulsation propre du vérin en fonction de la position du piston. Les résultats montrent que les volumes de l'embase ont un effet important sur l'évolution de la pulsation propre qui, dans notre cas, diminue de manière significative aux extrémités.

Malgré la faible masse de fluide dans l'embase, l'effet d'inertie ne peut pas être ignoré, en particulier pour un système à hautes performances avec une large bande passante, puisque la vitesse d'écoulement devient importante lors du passage du fluide dans de petites sections. La masse équivalente du fluide dans les conduits de l'embase s'écrit alors de la façon suivante:

$$m_{ei} = \rho V_{t1} \left(\lambda_{t1} \cdot \frac{A}{A_{t1}} \right)^2 \tag{B.8}$$

Comme l'effet de compressibilité, l'effet d'inertie provoque une diminution significative de la pulsation propre. Ainsi, les effets de volume et d'inertie influencent évidemment les performances dynamiques atteignables par le vérin. Les résultats montrent que l'effet de volume a une influence plus importante sur la pulsation propre à l'extrémité de la course du piston, tandis que l'inertie donne une diminution presque toute la course du vérin (voir figures 3.10 et 3.11).

En conclusion, ce chapitre a étudié la modélisation de l'embase en utilisant l'approche Bond Graph. Le modèle prend en compte les effets de compressibilité du fluide, d'inertie et de pertes de charge. Nous avons proposé une approche basée sur des abaques pour déterminer les pertes de charge dans chaque circuit. Elle a été validée par comparaison avec les résultats CFD. En outre, les effets de compressibilité et d'inertie de l'embase ont également été étudiés, et les résultats théorique prouvent qu'ils induisent une diminution importante de la pulsation propre du système, en particulier à hautes fréquences.

B.4 Modélisation et validation de l'ensemble du système

Pour compléter le modèle du banc d'essai, le vérin est modélisé en considérant qu'il est composé de deux volumes compressibles et d'une masse mobile (tige+piston). La partie mécanique du modèle est obtenue en appliquant la deuxième loi de Newton au solide en mouvement. Le modèle du vérin s'écrit alors:

Partie hydraulique:

$$\begin{cases} Q_1 = \dfrac{V_1(y)}{\beta}\dfrac{dP_1}{dt} + A\dfrac{dy}{dt} \\ Q_2 = \dfrac{V_2(y)}{\beta}\dfrac{dP_2}{dt} - A\dfrac{dy}{dt} \end{cases} \tag{B.9}$$

Partie mécanique:

$$M\frac{d^2y}{dt^2} = A(P_1 - P_2) - Mg - F_{fric}(y, \dot{y}, P_1, P_2) - F_{ext} \tag{B.10}$$

Le modèle de frottement utilisé se base sur le modèle de Tustin, c'est-à-dire:

$$F_{fs}(v) = \left(F_C + (F_{sdyn} - F_C)\, e^{-C\left|\frac{v}{v_0}\right|} \right) tanh\left(\frac{v}{v_0}\right) \tag{B.11}$$

Pour le modèle de commande du banc d'essai, nous négligeons la dynamique de la servovalve puisque les servovalves MOOG D765 présentent un temps de réponse de 2 ms négligeable devant celui du vérin. Le modèle de la servovalve adopté ici est restreint à une caractéristique statique en fonction de la pression d'alimentation P_P, de la pression de retour P_T, des pressions dans les chambres du vérin P_1 ou P_2, ainsi que de la commande u_1 ou u_2. De plus, les débits de la servovalve sont supposés proportionnels à la commande. Le modèle de commande du système est alors donné par:

$$\begin{cases} \frac{dy}{dt} = v \\ \frac{dv}{dt} = \frac{A}{M}(P_1 - P_2) - g - \frac{b}{M}v - \frac{F_{fs}(v)}{M} - \frac{F_{ext}}{M} \\ \frac{dP_1}{dt} = -\frac{\beta}{V_1(y)} \cdot A \cdot v + \frac{\beta}{V_1(y)} \cdot \phi_1\left(P_1, P_P, P_T, sign(u_1)\right) \cdot u_1 \\ \frac{dP_2}{dt} = \frac{\beta}{V_2(y)} \cdot A \cdot v + \frac{\beta}{V_2(y)} \cdot \phi_2\left(P_2, P_P, P_T, sign(u_2)\right) \cdot u_2 \end{cases} \tag{B.12}$$

$$\text{où } \phi_i = \frac{Q_n}{u_n}\cdot\sqrt{\frac{|P_P - P_i|}{\Delta P_n}}\cdot\frac{sign(u_i)+1}{2} + \frac{Q_n}{u_n}\cdot\sqrt{\frac{|P_i - P_T|}{\Delta P_n}}\cdot\frac{1-sign(u_i)}{2} \quad \text{(B.13)}$$

Après avoir établi les modèles pour tous les dispositifs constituant le banc d'essai, nous développons un prototype virtuel dans AMESim (figure 4.7) de façon à élaborer des lois de commande sophistiquées. Ce prototype virtuel tient compte de toutes les considérations physiques discutées dans les sections précédentes: servovalves, embase et vérin. Il est valable sur une large bande de fréquence de 0-200 Hz et de grands mouvements d'après la comparaison avec les résultats expérimentaux de réponse fréquentielle que nous avons réalisés.

Le travail expérimental concernant la validation de ce prototype à partir de sa réponse fréquentielle a consisté à appliquer une série de signaux sinusoïdaux de 0 à 200 Hz avec une amplitude de 3,5 mm en boucle fermée (commande proportionnelle en position). La comparaison des résultats de simulation et expérimentaux présentée aux figures 4.9, 4.10, et 4.11, montre l'intérêt du travail de modélisation réalisé.

Nous remarquons que le mode 1 présente un gain plus important en raison de sa capacité à fournir des débits plus importants. Nous notons également que les fréquences de résonance obtenues expérimentalement et en simulation sont bien en accord. La fréquence de résonance est d'environ 160 Hz. Cependant, il existe des différences importantes entre les résultats expérimentaux et de simulation vers 100 Hz. Ceci peut s'expliquer de différentes façons:

1. Le jeu entre le piston et la paroi interne du vérin peut changer en fonction du débit de fuite et des pressions. Le coefficient de frottement peut alors varier, surtout à haute fréquence ;
2. Les deux servovalves utilisées ne sont pas parfaitement identiques. Des erreurs peuvent être engendrées par l'hypothèse identité des servovalves dans le prototype ;
3. Les circuits liant les servovalves au vérin à l'intérieur de l'embase ne sont pas parfaitement symétriques. La dissymétrie géométrique de l'embase entraîne des pertes de charge différentes selon la chambre considérée.

4. Les capteurs de position LVDT dans le vérin et les servovalves comportent des déphasages que nous n'avons pas pris en compte dans notre prototype.

En conclusion, dans ce chapitre une brève étude du vérin a été réalisée avec un approfondissement sur la modélisation du frottement sec. Le prototype virtuel du banc d'essai, développé dans AMESim, a été validé par comparaison des résultats de simulation et expérimentaux. Les résultats montrent qu'il est nécessaire de considérer l'effet de l'embase pour améliorer le modèle à fréquences élevées.

B.5 Lois de commande nonlinéaires multivariable nonlinéaires

D'après l'équation (B.12), le système électro-hydraulique comporte deux entrées de commande qui permettent d'implanter des lois de commande multivariable. Dans ce chapitre, nous nous concentrons sur l'implantation des commandes basées sur la technique du backstepping. Leur schéma bloc correspond à celui de la figure 5.2. Puisque le banc d'essai comporte deux servovalves électro-hydrauliques, il est possible de développer des lois de commande multivariable. La commande peut viser le suivi simultané de deux trajectoires: l'une est classiquement la position, l'autre peut être choisie selon le cahier des charges imposé au système, tels que la raideur, l'énergie, la bande passante du système, etc. Nous proposons ici deux lois de commande basées sur la technique du backstepping qui s'intéresse pour la première notée P-Y, au suivi des trajectoires du déplacement du piston du vérin et de la pression dans une chambre du vérin, pour la seconde notée Y-λ, au suivi des trajectoires de déplacement du piston et d'une répartition dynamique des pressions dans chaque chambre du vérin. D'autre part, les deux lois de commande doivent assurer la stabilité asymptotique du système, sauf éventuellement en certains points singuliers.

Pour élaborer les lois de commande basées sur le backstepping, nous commençons par stabiliser un sous-système simple en utilisant une commande virtuelle. Puis,

par itération, nous proposons une autre commande virtuelle afin de stabiliser un nouveau sous-système qui comporte la commande virtuelle précédente, jusqu'à atteindre la commande externe voulue.

Finalement, la loi de commande Y-λ s'exprime par:

$$\begin{cases} u_1 = \frac{1}{g_1}\left(-f_1 + \dot{P}_0 + \lambda \cdot \dot{\alpha}_1(\cdot) + \dot{\lambda} \cdot \alpha_1(\cdot) - \frac{A}{M}e_2 - c_3 e_3\right) \\ u_2 = \frac{1}{g_2}\left(-f_2 + \dot{P}_0 + (\lambda - 1) \cdot \dot{\alpha}_1(\cdot) + \dot{\lambda} \cdot \alpha_1(\cdot) + \frac{A}{M}e_2 - c_4 e_4\right) \end{cases} \tag{B.14}$$

Selon cette méthode de contrôle, les deux pressions P_1 et P_2 peuvent être pilotées en fonction de la pression de référence P_0 et le coefficient de répartition dynamique λ.

En vue d'appliquer la méthode de commande P-Y, un difféomorphisme s'applique d'abord sur les variables d'état initiales du système (II.1) pour passer de (y, v, P_1, P_2) à (y, v, a, P_1). Dans le nouveau système de coordonnées, le modèle d'état s'écrit

$$\begin{cases} \frac{dy}{dt} = & v \\ \frac{dv}{dt} = & a \\ \frac{da}{dt} = & \frac{1}{M}\Bigg(- b \cdot a - \frac{\partial F_{fs}(v)}{\partial v} \cdot a - A^2\beta\left(\frac{1}{V_1(y)} + \frac{1}{V_2(y)}\right) \cdot v \\ & \quad + A\beta\left(\frac{\phi_1(\cdot)}{V_1(y)} \cdot u_1 - \frac{\phi_2(\cdot)}{V_2(y)} \cdot u_2\right)\Bigg) \\ \frac{dP_1}{dt} = & -\frac{\beta}{V_1(y)} \cdot A \cdot v + \frac{\beta}{V_1(y)} \cdot \phi_1\left(P_1, P_P, P_T, sign(u_1)\right) \cdot u_1 \end{cases} \tag{B.15}$$

La loi de commande P-Y s'exprime alors:

$$\begin{cases} u_1 = \frac{1}{g_1}\left(\frac{\beta}{V_1(y)} \cdot A \cdot v + \dot{P}_1^d - c_4 e_4\right) \\ u_2 = -\frac{M}{A \cdot g_2}\left(-f - \frac{A \cdot g_1}{M} \cdot u_1 + \dot{a}^d + K_1 e_1 + K_2 e_2 + K_3 e_3\right) \end{cases} \tag{B.16}$$

Ici, K_1 est un gain de contrôle relatif à l'erreur de position, K_2 à celle de vitesse, et K_3 à celle d'accélération. En réglant ces paramètres, nous pouvons contrôler la précision du déplacement, ainsi que le temps de réponse.

Les lois de commande proposées sont validées à la fois en simulation et expérimentalement. Les résultats expérimentaux (figure 5.7) montrent qu'il y a peu d'écart entre la position désirée et mesurée en régimes permanent et transitoire, excepté au début du régime transitoire où la position mesurée est en retard par rapport à la consigne. Par ailleurs, nous pouvons remarquer que les signaux de commande sont relativement lisses, ce qui permet d'avoir une bonne efficacité énergétique. Les pressions varient lentement avec aucune impulsion forte, mais il existe des oscillations à hautes fréquences en régime transitoire pour la commande Y-λ.

En comparaison avec les résultats obtenus à partir de la méthode linéaire classique (figure 5.9), les commandes basées sur la technique du backstepping offrent de meilleures performances avec un temps de réponse plus rapide. Par ailleurs, la méthode linéaire conventionnelle se concentre sur un seul objectif de contrôle, à savoir le contrôle de la position, et ne permet pas de satisfaire à l'autre exigence, telle que celle concernant les pressions.

Au lieu d'utiliser une valeur constante pour les pressions désirées comme dans les essais précédents, les pressions désirées peuvent suivre des trajectoires correspondant aux exigences de l'application (figure 5.10). L'augmentation d'erreur en position n'est pas notable par rapport aux résultats de la figure 5.7(b) où les mêmes valeurs de gains élevés s'appliquent. Le suivi en position garde donc une précision quasiment identique en dépit d'une pression désirée variable.

En outre, nous remarquons que lorsque λ est égal à 1, la trajectoire de la pression P_2 est modulée directement par P_0, alors que c'est la trajectoire de la pression P_1 qui est modulée directement par P_0 lorsque λ est égal à 0. Dans ce dernier cas ($\lambda = 0$), la commande Y-λ est équivalente à la commande P-Y. La figure 5.11 présente l'évolution des pressions pour différentes valeurs de λ.

En conclusion, ce chapitre propose deux méthodes de contrôle nonlinéaires basées sur la technologie du backstepping. Ces deux méthodes permettent de réaliser des contrôles multi-variables sur notre banc d'essai où l'actionneur hydraulique est équipé de 2 servovalves. Les méthodes de contrôle proposées sont validées et montrent une bonne stabilité que ce soit en simulation ou expérimentalement.

Avec les méthodes proposées, les performances dynamiques s'améliorent avec un temps de réponse très court par rapport à la commande proportionnelle. En outre, les pressions peuvent facilement se moduler en fonction des exigences de l'application (raideur dynamique, efficacité, etc.). Par rapport à la commande linéaire classique, les méthodes proposées sont plus efficaces pour des tâches de suivi en position. La coefficient dynamique λ dans la commande Y-λ permet un meilleur suivi de pression par rapport à la commande P-Y.

B.6 Contrôle du banc d'essai basé sur la commande sans modèle

Dans ce chapitre, nous utilisons la méthode de la commande sans modèle qui va permettre d'obtenir de bonnes performances en suivi de position sans prendre en compte un modèle précis. Il n'est pas nécessaire d'utiliser un modèle du système global pour la commande sans modèle. Au lieu de cela, elle introduit un modèle ultra-local qui consiste à se rapprocher de la dynamique inconnue du système sur un intervalle très court. En outre, les paramètres sont estimés rapidement à partir de la collecte de toutes les informations sur les états du système grâce aux capteurs, et le modèle est automatiquement mis à jour à chaque intervalle.

Pour appliquer la commande sans modèle sur notre banc d'essai, nous nous plaçons dans le cas des commandes opposées (B.17):

$$u = u_1 = -u_2. \tag{B.17}$$

Avec la commande sans modèle, nous n'avons pas besoin d'information concernant le modèle du système. Sur un intervalle très court, en pratique, il s'agit de la période d'échantillonnage ΔT, le système est modélisé par

$$\dot{y}(t) = F(t) + \alpha u(t) \tag{B.18}$$

Puis, la valeur de F est évaluée à partir de celles de u and $\dot{y}$ à tout instant à partir de:

$$\widehat{F}_k = \widehat{\dot{y}}_k - \alpha u_{k-1} \tag{B.19}$$

Le contrôleur est ensuite développé à partir de l'équation (B.18) avec:

$$u_k = -\frac{\widehat{F}_k}{\alpha} + \frac{\dot{y}_k^d}{\alpha} + K_P e_k + K_I \sum (e_k \cdot \Delta T) \tag{B.20}$$

Ce contrôleur est appelé régulateur PI intelligent ou i-PI dans [Fliess 2008]. Le comportement PI est utilisé pour assurer la stabilité du système et de meilleures performances. Par rapport à un régulateur PI classique, le régulateur PI intelligent contient un terme contenant l'information sur la structure du système représenté par une estimation de F. En conséquence, par rapport à un régulateur PI classique, le régulateur PI intelligent permet d'améliorer la robustesse du système et la performance du suivi en position sans un réglage complexe des gains.

Par ailleurs, la commande à modèle restreint a également été mise en place. Cette méthode est basée sur un modèle incomplet du système.

Le modèle restreint appliqué ici est donné par (B.15). Ce modèle est utilisé pour développer le pré-calcul de la commande en boucle ouverte qui sera appliquée sur le contrôle du suivi en position.

Le contrôleur de la commande à modèle restreint se compose d'une commande en boucle ouverte et d'une boucle de retour. Il est donné par:

$$u = u^* + \Delta u \tag{B.21}$$

où Δu représente la commande de compensation concernant l'effet inconnu ou non modélisé et le contrôleur de rétroaction. La commande en boucle ouverte se calcule à partir de (B.15) et s'écrit comme:

$$u^* = \frac{M \cdot j^d + b \cdot a^d + \dfrac{\partial F_{fs}(v^d)}{\partial v^d} \cdot a^d + A^2\beta \left(\dfrac{1}{V_1(y^d)} + \dfrac{1}{V_2(y^d)} \cdot v^d \right)}{A\beta \left(\dfrac{\phi_1(\cdot)}{V_1(y^d)} + \dfrac{\phi_2(\cdot)}{V_1(y^d)} \right)} \tag{B.22}$$

Enfin, le contrôleur de la commande à modèle restreint s'écrit comme suit:

$$u_k = u_k^* - \frac{\widehat{F}_k}{\alpha} + \frac{\dot{y}_k^d}{\alpha} + K_P e_k + K_I \sum (e_k \cdot \Delta T) \tag{B.23}$$

Puisque plus d'informations sur le système sont introduites par rapport à la commande sans modèle (contrôleur PI intelligent), cette méthode permet d'obtenir de meilleures performances sur le suivi en position.

Les lois de commande ont été validées à la fois en simulation et expérimentalement (figures 6.3, 6.4, et 6.5). En comparaison avec les résultats issus du contrôleur proportionnel, les méthodes proposées permettent d'attendre une meilleure précision en suivi en position avec un temps de réponse plus court (figure 6.6). En outre, les signaux de commande comportent moins de bruit que ceux de la commande proportionnelle.

En conclusion, la commande sans modèle et la commande à modèle restreint ont été mis en œuvre sur notre banc d'essai. Elles ont été validées en simulation et expérimentalement. Les résultats montrent qu'elles permettent de faciliter le réglage des gains et d'obtenir de bonnes performances de contrôle, et offrent une haute précision en suivi de position sans le connaissance précise du modèle. Cela permet donc d'envisager l'utilisation de ces types de loi de commande dans l'industrie.

B.7 Etude de la robustesse des lois de commande proposées

En raison des perturbations liées à l'environnement, l'implantation des lois de commande sur des bancs réels devient complexe. La précision du modèle est généralement dégradée en raison de la mauvaise configuration des paramètres lors du changement des conditions. Lors de l'implémentation d'une loi de commande, cela peut éventuellement conduire à la dégradation des performances de contrôle ou à l'instabilité du système. Ainsi, la robustesse d'une loi de commande est un critère important à évaluer.

Ce chapitre est consacré à l'analyse de la robustesse à la fois en simulation et expérimentalement. Nous étudions la robustesse des lois de commande proposées dans les chapitres précédents en faisant varier la charge du système et en considérant différents niveaux de précision sur la vitesse et l'accélération estimées.

Premièrement, nous discutons de l'influence de la variation de la charge sur les performances en commande. Des expérimentations sont réalisées avec différentes charges appliquées sur le système. Les résultats montrent que l'erreur statique en position dans le cas de la commande Y-λ augmente lorsque la charge augmente. Ceci est un désavantage de la commande Y-λ par rapport à la commande P-Y. Les erreurs en position de la commande P-Y, de la commande sans modèle, et de la commande à modèle restreint restent au même niveau lors de l'augmentation de la charge, ce qui démontre de bonnes propriétés de robustesse vis à vis de la perturbation de charge.

Les commandes étant évaluées à partir des valeurs de la vitesse et de l'accélération, la performance de ces loi de commande dépend de la précision des différentiateurs numériques qui est elle-même contrôlée par leurs gains K_{d0} et K_{d1} (voir l'équation (5.60)). Nous étudions ici l'influence de la précision des différentiateurs sur le suivi de trajectoire. Nous remarquons que la dégradation de la performance des commandes a lieu principalement en régime transitoire lors de la diminution des gains du DAO2, en particulier pour la commande sans modèle et pour la commande à modèle restreint. Quantitativement, les erreurs statiques ne changent pas beaucoup, alors que les erreurs maximales en régime transitoire sont environ deux fois plus importantes. En revanche, les bruits sont évidemment réduits par la diminution des gains du DAO2.

En conclusion, nous avons analysé la robustesse des lois de commande proposées par des simulations et par des expérimentations dans ce chapitre. Leur robustesse vis à vis de la variation de la charge et de la précision du différentiateur a été étudiée. Les résultats montrent que, par rapport à la commande proportionnelle, les lois de commande proposées conduisent à une meilleure robustesse lorsque la charge est changée. En appliquant la commande sans modèle, la commande à

modèle restreint, ou la commande P-Y, les erreurs en position restent presque inchangées lors de l'augmentation de la charge, alors que pour la commande Y-λ l'erreur en position augmente avec l'augmentation de la charge. Pour la commande sans modèle et la commande à modèle restreint, il faut noter qu'il est nécessaire d'améliorer la précision des valeurs estimées de la vitesse ou de l'accélération afin d'obtenir des résultats suffisamment précis. Les lois de commande basées sur le backstepping sont plus robustes vis à vis de la précision sur la vitesse et l'accélération, à l'exception des erreurs dynamiques qui augmentent avec la diminution de la précision du différentiateur.

B.8 Conclusion et perspectives

Le travail de cette thèse concerne un banc d'essai électro-hydraulique qui comporte trois composants hydrauliques principaux, à savoir deux servovalves haute performance, un vérin à double tige, et une embase spécifique qui relie les servovalves et le vérin. Ce banc d'essai a été conçu pour tester des composants aéronautique et automobile dans des conditions réelles (par exemple, tests d'usure ou de vieillissement). Cette thèse a étudié la modélisation et le contrôle d'un banc d'essai hydraulique à hautes performances. Un modèle précis a été développé à partir de l'analyse des phénomènes physiques à l'aide de la représentation Bond Graph. Il a été validé à partir de la comparaison des résultats expérimentaux et de simulation, et a montré une très bonne adéquation entre les résultats de simulation et les résultats expérimentaux non seulement en basses fréquences, mais également à fréquences élevées. En particulier, les performances en hautes fréquences sont nettement améliorées par l'introduction des effets dynamiques liés à l'embase. En outre, des lois de commande, respectivement basées sur le backstepping et sur la commande sans modèle, ont été élaborées et mises en œuvre sur le banc d'essai. Toutes les lois de commande proposées ont été validées à la fois en simulation et expérimentalement. Les résultats montrent qu'ils conduisent à de meilleures performances en suivi en position et en robustesse par rapport aux lois de commande classiques.

Bien que nous ayons étudié la modélisation et le contrôle du banc d'essai dans cette thèse, il reste encore quelques problèmes intéressants qui méritent de nouveaux travaux de recherche dans le futur. Ces problèmes concernent les aspects suivants:

- Pendant l'analyse du système hydraulique, nous n'avons pas tenu compte de la variation de température qui a un effet significatif sur les propriétés des fluides, tels que le module de compressibilité et la viscosité. Ainsi, pour obtenir un modèle plus précis, la thermodynamique du système devrait être étudiée de manière plus approfondie.
- L'élaboration des lois de commande dans cette thèse n'a pas tenu compte de la dynamique des servovalves. La prise en compte de celle-ci devrait permettre une amélioration des performances en commande.
- La commande sans modèle peut être poursuivie avec le développement de commande multi-objectifs.

Bibliography

[Alirand 2005] M. Alirand, N. Orand and M. Lebrun. *Model simplifications for nonlinear hydraulic circuits.* In Proc. of ASME IMECE2005, Orlando, pages 93 – 98, Nov. 2005.

[Alleyne 2000] A.G. Alleyne and Rui Liu. *Systematic control of a class of nonlinear systems with application to electrohydraulic cylinder pressure control.* Control Systems Technology, IEEE Transactions on, vol. 8, no. 4, pages 623 –634, Jul. 2000.

[Arcak 2000] M. Arcak, M. Seron, J. Braslavsky and P. Kokotovic. *Robustification of backstepping against input unmodeled dynamics.* Automatic Control, IEEE Transactions on, vol. 45, no. 7, pages 1358 –1363, Jul. 2000.

[Aström 2006] K.J. Aström and T. Hägglund. Advanced pid control. The Instrumentation, Systems, and Automation Society, 2006.

[Attar 2008] B. Attar. *Modélisation Réaliste en Conditions Extrêmes des Servovalves Electrohydrauliques Utilisées pour le Guidage et la Navigation Aéronautique et Spatiale.* PhD thesis, Université de Toulouse, 2008.

[Bai 2011] Y. Bai and L. Quan. *Principle and method to improve the dynamic stiffness of the electro-hydraulic servo system.* In Proceedings of the 8th JFPS International Symposium on Fluid Power, Okinawa, Oct. 2011.

[Bartolini 2003] G. Bartolini, A. Pisano and E. Usai. *A survey applications of second-order sliding mode control to mechanical systems.* International Journal of Control, vol. 76, no. 9, pages 875–892, June 2003.

[Blackburn 1966] J. F. Blackburn, G. Reethof and J. L. Shearer. Mécanismes et servomécanismes à fluide sous pression. Tome 1, Paris, 1966.

[Bo 1982] L.C. Bo and D. Pavelescu. *The friction-speed relation and its influence on the critical velocity of the stick-sleep motion.* Wear, vol. 3, pages 277 – 289, 1982.

[Brown 2002] F. T. Brown. *Simulating distributed-parameter multiphase thermodynamic systems using Bond Graphs.* In Proc. of AMSE IMECE2002, New Orleans, pages 545 – 553, Nov. 2002.

[Brown 2010] F. T. Brown. *Bond-Graph based simulation of thermodynamic models.* Journal of Dynamic Systems, Measurement, and Control, vol. 132, no. 6, Nov. 2010.

[Bryant 2011] M. D. Bryant and J. Choi. *Model based diagnostics for gearboxes.* In Proc. of ASME/STLE IJTC2011, Los Angeles, pages 361–363, Oct. 2011.

[Chen 2007] S.M. Chen. Hydraulic and pneumatic transmission. China Machine Press, 2007.

[Choi 2009] S. Choi, B. d'Andréa Novel, M. Fliess and H. Mounier. *Model-free control of automotive engine and brake for stop-and-go scenario.* In 10th IEEE Conf. Europ. Control Conf., Budapest, 2009.

[Choux 2010] M. Choux and G. Hovland. *Adaptive Backstepping Control of Nonlinear Hydraulic-Mechanical System Including Valve Dynamics.* Modeling, Identification and Control, vol. 31, no. 1, pages 35 – 44, Jan. 2010.

[Cornieles 2006] E. Cornieles, M. Saad, G. Gauthier and H. Saliah-Hassane. *Modeling and Simulation of a Multivariable Process Control.* In IEEE International Symposium on Industrial Electronics, volume 4, pages 2700 –2705, July 2006.

[d'Andréa Novel 2010a] B. d'Andréa Novel, C. Boussard, M. Fliess, O. El Hamzaoui, H. Mounier and B. Steux. *Commande sans modèle de vitesse longitudinale d'un véhicule électrique.* In 6e Conf. Internat. Francoph. Automatique, Nancy, 2010.

[d'Andréa Novel 2010b] B. d'Andréa Novel, M. Fliess, C. Join, H. Mounier and B. Steux. *A mathematical explanation via "intelligent" PID controllers of the strange ubiquity of PIDs.* In 18th Mediterranean Conference on Control and Automation, MED'10, Marrakech, Morocco, 2010.

[Dawson 1994] D.M. Dawson, J.J. Carroll and M. Schneider. *Integrator backstepping control of a brush DC motor turning a robotic load.* Control Systems Technology, IEEE Transactions on, vol. 2, no. 3, pages 233 –244, Sep. 1994.

[de Queiroz 1996] M.S. de Queiroz and D.M. Dawson. *Nonlinear control of active magnetic bearings: a backstepping approach.* Control Systems Technology, IEEE Transactions on, vol. 4, no. 5, pages 545 –552, Sep. 1996.

[dos Santos Coelho 2011] Leandro dos Santos Coelho and Mauro André Barbosa Cunha. *Adaptive cascade control of a hydraulic actuator with an adaptive dead-zone compensation and optimization based on evolutionary algorithms.* Expert Systems with Applications, vol. 38, no. 10, pages 12262 – 12269, 2011.

[Dransfield 1979] P. Dransfield and M. K. Teo. *Using bond graph in simulating an electro-hydraulic system.* Journal of the Franklin Institute, vol. 308, no. 3, pages 173 – 184, Sep. 1979.

[Ellman 1995] A. Ellman, K. Koskinen and M. Vilenius. *Through-flow in short annulus of fine clearance.* In Proc. of the ASME Dynamic Systems and Control Division, Atlanta, pages 813 – 821, 1995.

[Ellman 1998] A. Ellman. *Leakage Behaviour of Four-Way Servovalve.* In Proceeding of the ASME Fluid Power Systems and Technology, Anaheim, volume 5, pages 163 – 167, 1998.

[Eryilmaz 2000a] B. Eryilmaz and B. H. Wilson. *Combining Leakage and Orifice Flows in a Hydraulic Servovalve Model.* Journal of dynamic systems, Measurement, and Control, vol. 122, no. 3, pages 576 – 579, 2000.

[Eryilmaz 2000b] B. Eryilmaz and B. H. Wilson. *Modeling the Internal Leakage of Hydraulic Servovalves.* In International Mechanical Engineering Congress and Exposition, ASME, Orlando, pages 337 – 343, 2000.

[Ezal 2000] K. Ezal, Zigang Pan and P.V. Kokotovic. *Locally optimal and robust backstepping design.* Automatic Control, IEEE Transactions on, vol. 45, no. 2, pages 260 –271, Feb. 2000.

[Faisandier 1970] J. Faisandier. Les mécanismes hydrauliques et electrohydrauliques. Dunod, Paris, 1970.

[Faisandier 1999] J. Faisandier. Mécanismes hydrauliques et pneumatiques. Collection: Technique et ingénierie, série mécanique. Paris, 1999.

[Feki 2005] M. Feki and E. Richard. *Including leakage flow in the servovalve static model.* International Journal of Modelling and Simulation, vol. 25, no. 1, pages 51–55, 2005.

[Ferziger 1996] J.H. Ferziger and M. Peric. Computational methods for fluid dynamics. Springer, 1996.

[Filonenko 1948] G.K. Filonenko. *An expression for the coefficient of hydraulic resistance of smooth tubes.* Izv. VTI, vol. 162, no. 10, 1948.

[Fliess 2008] M. Fliess and C. Join. *Commande sans modèle et commande à modèle restreint.* e-STA, vol. 5, no. 4, pages 1–23, 2008.

[Fliess 2009] M. Fliess and C. Join. *Model-free control and intelligent PID controllers: towards a possible trivialization of nonlinear control?* In 15th IFAC Symp. System Identif., Saint-Malo, 2009.

[Fliess 2011] M. Fliess, C. Join and S. Riachy. *Rien de plus utile qu'une bonne théorie: la commande sans modèle.* In JN-JD-MACS, Marseille, 2011.

[Freeman 1993] R.A. Freeman and P.V. Kokotovic. *Design of 'softer' robust nonlinear control laws.* Automatica, vol. 29, no. 6, pages 1425 – 1437, 1993.

[Frene 1997] J. Frene, D. Nicolas, B. Degueurce, D. Berthe and M. Godet. Hydrodynamic lubrication: Bearings and thrust bearings. Elsevier Science Ltd., 1997.

[Gauthier 1992] J.P. Gauthier, H. Hammouri and S. Othman. *A simple observer for nonlinear systems applications to bioreactors.* IEEE Trans. On Automatic Control, vol. 37, no. 37, pages 875 – 880, 1992.

[Gédouin 2008] P.-A. Gédouin, C. Join, E. Delaleau, J.-M. Bourgeot, S. Arbab-Chirani and S. Calloch. *Model-free control of shape memory alloys antagonistic actuators.* In 17th IFAC World Congress, Seoul, 2008.

[Gédouin 2009] P.-A. Gédouin, C. Join, E. Delaleau, J.-M. Bourgeot, S. Arbab-Chirani and S. Calloch. *A new control strategy for shape memory alloys actuators.* In 8th Europ. Symp. Martensitic Transformations, Prague, 2009.

[Ghosh 1991] A. K. Ghosh, A. Mukherjee and M. A. Faruqi. *Computation of driving efforts for mechanisms and robots using Bond Graphs.* J. Dyn. Sys. Meas. Contr., vol. 113, no. 4, pages 744 – 748, Dec. 1991.

[Gupta 1981] P. K. Gupta, L. Flamand, D. Berthe and M. Godet. *On the Traction Behavior of Several Lubricants.* Journal of Lubrication Technology, vol. 103, no. 1, pages 55–64, 1981.

[Habibi 1994] S.R. Habibi, R.J. Richards and A.A. Goldenberg. *Hydraulic actuator analysis for industrial robot multivariable control.* In American Control Conference, volume 1, pages 1003 – 1007 vol.1, june-1 july 1994.

[Hibbeler 1997] R.C. Hibbeler. Mechanics of materials (3rd edition). Prentice Hall, Inc., New Jersey, 1997.

[Idelchik 1994] I.E. Idelchik. Handbook of hydraulic resistance (3rd edition). CRC Begell House, 1994.

[Jelali 2003] M. Jelali and A. Kroll. Hydraulic servo-systems: Modelling, identification and control. Advances in Industrial Control, London, 2003.

[Jiang 1997] Z.-P. Jiang and H. Nijmeijer. *Tracking control of mobile robots: A case study in backstepping.* Automatica, vol. 33, no. 7, pages 1393 – 1399, 1997.

[Jiang 2001] Z. P. Jiang, E. jiang and H. Nijmeijer. *Saturated stabilization and track control of a nonholonomic mobile robot.* Systems and Control Letters, vol. 42, pages 327 – 332, 2001.

[Join 2010] C. Join, G. Robert and M. Fliess. *Vers une commande sans modèle pour aménagements hydroélectriques en cascade.* In 6e Conf. Internat. Francoph. Automat., Nancy, 2010.

[Kanellakopoulos 1991] I. Kanellakopoulos, P.V. Kokotovic and A.S. Morse. *Systematic design of adaptive controllers for feedback linearizable systems.* Automatic Control, IEEE Transactions on, vol. 36, no. 11, pages 1241 –1253, Nov. 1991.

[Kang 2009] R.J. Kang, Z.X. Jiao, Maré J.-C., Y.X. Shang and S. Wu. *Nonlinear block diagram model and robust control of electro-hydrostatic actuator.* Acta Aeronautica et Astronautica Sinica, vol. 30, no. 3, pages 518 – 525, 2009.

[Karnopp 1972] D. Karnopp. *Bond Graph models in fluid dynamic systems.* Journal of Dynamic Systems, Measurement, and Control, vol. 94, no. 3, pages 222 – 229, 1972.

[Karnopp 1975] D. C. Karnopp and R. C. Rosenberg. System dynamics: a unified approach. John Wiley & Sons, New York, 1975.

[Karnopp 1985] D. Karnopp. *Computer simulation of stcik-slip friction in mechanical dynamic systems.* ASME, Journal of Dynamic Systems, Measurement and Control, vol. 107, no. 1, pages 100 – 103, 1985.

[Khalil 2001] H. K. Khalil. Nonlinear systems (3rd edition). New Jersey : Prentice-Hall, 2001.

[Kim 2000] D. H. Kim and T.-C. Tsao. *A linearized electrohydraulic servovalve model for valve dynamics sensitivity analysis and control system design.* Journal of Dynamic Systems, Measurement, and Control, vol. 122, no. 1, pages 179 – 187, 2000.

[Kokotovic 1989] P.V. Kokotovic and H.J. Sussmann. *A positive real condition for global stabilization of nonlinear systems.* Systems & Control Letters, vol. 13, no. 2, pages 125 – 133, 1989.

[Kokotovic 1992] P.V. Kokotovic. *The joy of feedback: nonlinear and adaptive.* Control Systems, IEEE, vol. 12, no. 3, pages 7 – 17, June 1992.

[Kristic 1995] M. Kristic, I. Kanellakopoulos and P. Kokotovic. Nonlinear and adaptive control design. New York : John Wiley & Sons, 1995.

[Kühnlein 2012] Michael Kühnlein, Hubertus Murrenhoff, René von Dombrowski, Andreas Koch and Guido Wüstenhagen. *Rapid parameterisation of a sealing friction model for hydraulic cylinders.* In 8th International Fluid Power Conference (8. IFK), volume 1, March 2012.

[Launder 1972] B. E. Launder and D. B. Spalding. Lectures in mathematical models of turbulence. Academic Press, London, England, 1972.

[Lebrun 1978] M. Lebrun. *Modélisation et Simulation d'Asservissements Electrohydrauliques, Application à l'Etude et à la Réalisation d'un Ensemble Destiné à la Mesure des Impédances en Biomécanique.* PhD thesis, Université Claude Bernard - Lyon 1, 1978.

[Lee 2001] T.-C. Lee, K.-T. Song, C.-H. Lee and C.-C. Teng. *Tracking control of unicycle-modeled mobile robots using a saturation feedback controller.* Control Systems Technology, IEEE Transactions on, vol. 9, no. 2, pages 305 –318, Mar. 2001.

[Leena 2008] G. Leena, K.B. Dutta and G. Ray. *A set of stabilizing PD controllers for multi-input-multi-output systems.* In International Conference on Electrical and Computer Engineering, pages 861 –866, dec. 2008.

[Levant 2003] A. Levant. *Higher-order sliding modes, differentiation and output-feedback control.* International Journal of Control, vol. 76, no. 9 - 10, pages 924 – 941, 2003.

[Li 1987] D. Li and J.-J. E. Slotine. *On Sliding Control for Multi-Input Multi-Output Nonlinear Systems.* In American Control Conference, pages 874 –879, June 1987.

[Lin 2000] F. J. Lin and C. C. Lee. *Adaptive backstepping control for linear induction motor drive to track periodic references.* IEE Proceedings-Electric Power Applications, vol. 147, pages 449 – 458, 2000.

[Liu 2012] X. Liu and Z. Lin. *On the backstepping design procedure for multiple input nonlinear systems.* International Journal of Robust and Nonlinear Control, vol. 22, no. 8, pages 918 – 932, 2012.

[Lozano 1992] R. Lozano and B. Brogliato. *Adaptive control of robot manipulators with flexible joints.* Automatic Control, IEEE Transactions on, vol. 37, no. 2, pages 174 – 181, Feb. 1992.

[Maré 1993] J.-C. Maré. *Contribution à la Modélisation, la Simulation, l'Identification et la Commande d'Actionneurs Electrohydrauliques.* PhD thesis, Université Claude Bernard - Lyon 1, 1993.

[Maré 1996] J.-C. Maré. *Estimation of effective parameters and accurate simulation of hydraulic valves.* In Proceeding of International Symposium on Fluid Machinery and Fluid Engineering, Beijing, pages 439 – 446, 1996.

[McCloy 1980] D. McCloy and H. R. Martin. Control of fluid power: Analysis and design. Ellis Horwood Limited, Chichester, U.K., 1980.

[Merritt 1967] H. E. Merritt. Hydraulic control systems. John Wiley & Sons, New York, 1967.

[MOOG] MOOG. *Servovalves with Integrated Electronics D765 Series.* Rapport technique, MOOG Inc.

[MOOG 1965] MOOG. *Transfer function for MOOG servovalves.* Rapport technique, MOOG Inc. Control Division, East Aurora, Ny 14052, 1965.

[Morse 1963] A.C. Morse. Electrohydraulic servomechanisms. McGRAW-HILL BOOK CO., New York, 1963.

[Nikiforuk 1969] P. N. Nikiforuk, P. R. Ukrainetz and S. C. Tsai. *Detailed analysis of a two-stage four-way electrohydraulic flow-control valve.* Journal Mechanical Engineering Science, vol. 11, no. 2, pages 168 – 174, 1969.

[O'Dwyer 2006] A. O'Dwyer. Handbook of pi and pid controller tuning rules. Imperial College Press, 2006.

[Pellicciari 2011] M. Pellicciari, G. Berselli and F. Leali. *Object-oriented modeling of industrial manipulators with application to energy optimal trajectory scaling.* In Proc. of IDETC/CIE2011, Washington DC, pages 997 – 1006, Aug. 2011.

[Precup 2011] R.-E. Precup and S. H. Hellendoorn. *A survey on industrial applications of fuzzy control.* Computer in Industry, vol. 62, pages 213 – 226, October 2011.

[Rabie 1981] G Rabie and M Lebrun. *Modélisation par les Graphes à Liens et Simulation d'une Servovalve Electrohydrauliques à Deux Etages.* RAIO Automatique/Systems Analysis and Control, vol. 15, no. 2, pages 97 – 129, 1981.

[Ray 1983] W.H. Ray. *Multivariable process control - A survey.* Computers & Chemical Engineering, vol. 7, no. 4, pages 367 – 394, 1983.

[Riachy 2011] S. Riachy, M. Fliess and C. Join. *High-order sliding modes and intelligent PID controllers: First steps toward a practical comparison.* In 18th IFAC World Congress, Milan, 2011.

[Samantary 2010] A. K. Samantary, S. S. Dasgupta and R. Bhattacharyya. *Bond Graph modeling of an internally damped nonideal flexible spinning shaft.*

Journal of Dynamic Systems, Measurement, and Control, vol. 132, no. 6, Nov. 2010.

[Sekhavat 2004] P. Sekhavat, N. Sepehri and Q. Wu. *Asymptotic Force Control of Hydraulic Actuators With Friction: Theory and Experiments.* In Proc. of ASME IMECE2004, Anaheim, USA, pages 405 – 412, Nov. 2004.

[Sidhom 2011a] L. Sidhom. *Sur la Dérivation Numérique : Algorithmes et Applications.* PhD thesis, Institut National des Sciences Appliquées de Lyon - INSA Lyon, 2011.

[Sidhom 2011b] L. Sidhom, M. Smaoui, D. Thomasset, X. Brun and E. Bideaux. *Adaptive Higher Order Sliding Modes for Two-dimensional Derivative Estimation.* In 18th World Congress of the International Federation of Automatic Control (IFAC), Milano, 2011.

[Smaoui 2006] M. Smaoui, X. Brun and D. Thomasset. *A study on tracking position control of electropneumatic system using backstepping design.* Control Engineering Practice, vol. 14, no. 8, pages 923–933, August 2006.

[Sohl 1999] G.A. Sohl and J.E. Bobrow. *Experiments and simulations on the nonlinear control of a hydraulic servosystem.* IEEE Transactions on Control Systems Technology, vol. 7, no. 2, pages 238 – 247, Mar. 1999.

[Sontag 1989] Eduardo D. Sontag and Héctor J. Sussmann. *Further comments on the stabilizability of the angular velocity of a rigid body.* Systems & Control Letters, vol. 12, no. 3, pages 213 – 217, 1989.

[Sorensen 1999] H.L. Sorensen. *Experimental and numerical analysis of flow force compensation methods for hydraulic seat valve.* In The Sixth Scandinavian International Conference on Fluid Power, Tampere, Finland, May 1999.

[Suzuki 1999] K. Suzuki, I. Nakamura and J. U. Thoma. *Pressure regulator valve by Bondgraph.* Simulation Practice and Theory, vol. 7, pages 603 – 611, Dec. 1999.

[Tafraouti 2006] M. Tafraouti. *Contribution à la modélisation et la commande des systèmes électrohydrauliques.* PhD thesis, Université Henri Poincaré - Nancy 1, 2006.

[Tustin 1947] S. Tustin. *The effects of backlash and of speed-dependent friction on the stability of closed-cycle controls system.* Journal of the Institution of Electrical Engineers, vol. 94, no. 2A, pages 143 – 151, 1947.

[Villagra 2009] J. Villagra, B. d'Andréa Novel, S. Choi, M. Fliess and H. Mounier. *Robust stop-and-go control strategy: an algebraic approach for non-linear estimation and control.* Int. J. Vehicle Autonomous Systems, vol. 7, pages 270–291, 2009.

[Wang 2002] W.-Y. Wang, T.-T. Lee and H.-C. Huang. *Evolutionary design of PID controller for twin rotor multi-input multi-output system.* In Proceedings of the 4th World Congress on Intelligent Control and Automation, volume 2, pages 913 – 917 vol.2, 2002.

[Wang 2011] L. Wang, J.-C. Maré, Y. fu and H. Qi. *Force equalization for redundant active/active position control system involving dissimilar technology actuator.* In Proceedings of the 8th JFPS International Symposium on Fluid Power, Okinawa, Oct. 2011.

[Watton 1984] J. Watton. *Servovalve flapper/nozzle dynamics with drain orifice damping.* Transactions of American Society of Mechanical Engineers, vol. 84-WA, no. DSC17, 1984.

[Watton 1987] J. Watton. *The effect of drain orifice damping on the performance characteristics of a servovalve flapper/nozzle stage.* Journal of Dynamic Systems, Measurement, and Control, vol. 109, no. 1, pages 19 – 23, 1987.

[Watton 1989] J. Watton. Fluid power systems. Prentice Hall International, New York, 1989.

[Xu 1998] J.-X. Xu, T. H. Lee, Q.-W. Jia and M. Wang. *On adaptive robust backstepping control schemes suitable for PM synchronous motors.* International Journal of Control, vol. 70, no. 6, pages 893–920, 1998.

[Yang 2001] Z. J. Yang and M. Minashima. *Robust nonlinear control of a feedback linearizable voltage-controlled magnetic levitation system.* Transactions of the Institute of Electrical Engineers of Japan., vol. 121, no. 7, pages 1203 – 1211, 2001.

[Yuan 2002] Q.H. Yuan and P.Y. Li. *An experimental study on the use of unstable electrohydraulic valves for control.* In Proceedings of the American Control Conference, volume 6, pages 4843 – 4848, 2002.

[Zeng 2008] H. Zeng and N. Sepehri. *Tracking Control of Hydraulic Actuators Using a LuGre Friction Model Compensation.* Journal of Dynamic Systems, Measurement, and Control, vol. 130, no. 1, pages 1 – 7, Jan. 2008.

[Zhang 2007] K. Zhang. *Dynamics design of a planar controllable five bar mechanism based on genetic algorithm.* In Proc. of ASME IDETC/CIE2007, Las Vegas, pages 821 – 827, Sep. 2007.

[Zhou 1991] F. Zhou and D. G. Fisher. *MIMO Sliding Mode Control: A Lyapunov Approach.* In American Control Conference, pages 1796 –1799, June 1991.

FOLIO ADMINISTRATIF

THESE SOUTENUE DEVANT L'INSTITUT NATIONAL DES SCIENCES APPLIQUEES DE LYON

NOM : XU
(avec précision du nom de jeune fille, le cas échéant)

DATE de SOUTENANCE : 11/06/2013

Prénoms : Yaozhong

TITRE : Modelling and Control of a High Performance Electro-hydraulic Test Bench

NATURE : Doctorat

Numéro d'ordre : 2013ISAL0039

Ecole doctorale : E.E.A.

Spécialité : Energie et Systèmes

RESUME :
Les systèmes électro-hydrauliques sont largement utilisés dans l'industrie pour des contrôles de position ou d'effort. Cependant, à cause des non-linéarités du système électro-hydraulique, il est difficile d'établir un modèle précis valable sur une large bande de fréquences et de grands mouvements. Le travail de cette thèse concerne un banc d'essai électro-hydraulique qui comporte trois composants hydrauliques principaux, à savoir deux servovalves haute performance, un vérin à double tige, et une embase spécifique qui relie les servovalves et le vérin. Ce banc d'essai a été conçu pour tester des composants aéronautique et automobile dans des conditions réelles (par exemple, tests d'usure ou de vieillissement). Le premier objectif principal de cette thèse concerne la mise en œuvre d'un prototype virtuel basé sur un modèle précis issu de considérations physiques et d'un travail expérimental afin d'identifier les paramètres et de valider le réalisme du prototype virtuel. Le deuxième objectif est d'élaborer des lois de commande non-linéaires sophistiquées avec une large plage de fonctionnement et une bonne robustesse aux perturbations. Le modèle proposé basé sur le Bond Graph montre une très bonne adéquation entre les résultats de simulation et les résultats expérimentaux non seulement en basses fréquences, mais également en fréquences élevées. En particulier, les performances en hautes fréquences sont nettement améliorées par l'introduction des effets dynamiques liés à l'embase. En outre, des lois de commande, respectivement basées sur le backstepping et sur la commande sans modèle, ont été élaborées et mises en œuvre sur le banc d'essai. Toutes les lois de commande proposées ont été validées à la fois en simulation et expérimentalement. Les résultats montrent qu'ils conduisent à de meilleures performances en suivi de position et en robustesse par rapport aux lois de commande classiques.
MOTS-CLES : Système électro-hydraulique, Haute performance, Modélisation, Bond Graph, Commande multivariable, Commande nonlinéaire, Backstepping, Commande sans modèle, Robustesse.

Laboratoire (s) de recherche : Laboratoire Ampère

Directeur de thèse: Prof. Eric BIDEAUX et Dr. Sylvie SESMAT

Président de jury :

Composition du jury :

Prof. Jean-Pierre Barbot	-	ENSEA (ECS)
Prof. Jean-Charles Maré	-	INSA de Toulouse (Inst. Clément Ader)
Dr. HDR. Edouard RICHARD	-	Univ. Henri Poincare (CRAN)
Prof. Andrew Plummer	-	University of Bath (CPTMC)
Prof. Rachid OUTBIB	-	Université d'Aix-Marseille (LSIS)
Prof. Eric Bideaux	-	INSA de Lyon (Ampère)
Dr. Sylvie Sesmat	-	INSA de Lyon (Ampère)
Invité :		
M. Ludovic Boisse	-	MOOG France
Prof . Daniel Thomasset	-	INSA de Lyon (Ampère)